Study of Catecholaminergic Cells in Murine Heart



Tianyi Sun

Wadham College

University of Oxford

A thesis submitted for the degree of

Doctor of Philosophy

Michaelmas 2021

Abstract

Cardiac conduction system (CCS) morphogenesis is essential for correct heart function yet is incompletely understood. During my D.Phil, I established the transcriptional landscape of cell types populating the developing heart by integrating single-cell RNA sequencing and high-resolution spatially resolved transcriptomics (SrT) analyses. This led to the identification of a previously unrecognized cardiomyocyte population expressing dopamine beta-hydroxylase (Dbh^{+}-CMs), which is closely associated with the CCS. To further comfirm, genetic fate mapping using Dbh^{Cre}/Rosa26-tdTomato reporters combined with SrT revealed that Dbh^{+}-CM lineage is Hcn4-independent, first emerged in the sinoatrial node at E12.5, then to atrial and ventricular CCS components at E14.5 and became prominent within CCS at perinatal stages. Dbh^{+}-CM populating CCS occurred concurrently with sympathetic innervation. Electrophysiological optogenetic mapping revealed a fast conduction in Dbh^{Cre}/ChR2-tdTomato hearts by selectively stimulating Dbh^{+}-CMs. Furthermore, catecholaminergic-type vesicles were identified in adult cardiomyocytes. Thus, by utilising advanced transcriptomic, genetic and functional analyses, my study provides new insights into mammalian CCS development and heterogeneity. Besides, by combining an improved heart tissue-clearing technique with high resolution light sheet fluorescence microscopy (LSFM), I conducted three-dimensional and multi-scale volumetric imaging of ultra-thin planes of murine hearts to visualize the specific cardiomyocyte subpopulations. This method provides a tool for further geometrical and topological analysis of these cell types and

the correlation with their physiological function in specific region of the murine heart.

Acknowledgements

First and most importantly, I would like to express my deepest gratitude to my supervisor, Prof. Ming Lei. He is the most helpful, supportive and considerate supervisor I have ever met. His enthusiasm, and persistence towards the academia and research greatly inspires me and encourages me to pursue and explore the unknowns. He was so kind and thoughtful to provide me a chance that allowed me to continue my D.Phil research in his collaborator's group during the pandemic in China. The time and efforts he spent in me, including daily meeting, countless email replies and discussions, are instrumental for me to go the extra mile and to make this thesis possible. Without his consistent guidance, patience and insightful suggestions, I would not engage in the research and achieve such a pleasant journey during my D.Phil.

I would like to pass my sincere thanks to the following people who offered great help to me during my D.Phil. My heartfelt appreciations pass to my second supervisor Prof. Nicola Smart for her strong support and guidance on my project. Without her help I cannot finish the lineage tracing and new mouse establishment smoothly. I owe thank to Prof. Paolo Tammaro and Prof. John Parrington (my two transfer and confirmation examiners), and Prof. Weinian Shou and Prof. Peter Somogyi who provided valuable insights and knowledge into the subject matter steered me through my research. Thanks Prof. Henggui Zhang and his group in the University of Manchester who supported me for the experiments. And special thanks to Dr. Andrew Jefferson and Dr. Niloufer Irani, two responsible staffs in Micron image center, about their endless help for imaging. In addition, I would like to thank Xinyu Guo, Yanru Ann and other staffs in BGI who offers great help for my project. Another appreciation goes to Prof. Xiaoqiu Tan, Dr. Xianhong Ou for help and guidance in Luzhou China during the Covid.

Thanks to my friendly group member Dr. Razik Bin Abdul Mu-u-min, Yu He, Yue Ren, Alexander Grassam-Rowe, Alexey Lipov, Shu Tu, Yongcheng Jin for all your significant

support. I am very fortunate and befriend with many kind people in Oxford, especially Danlei Li, Yuxuan Zhang, Wenyuan Zhang, Zun Chen, Shiyan Tang, Hang Zhou and Rui Lei. It was an unforgettable memory with you all. And my great thanks to my best friend, Fengyu Zhang for her support and company all the time.

Last but not the least, I would like to pass my biggest thanks to my family for all the unconditional support and unparalleled love. I am forever indebted to my family for giving me the opportunities and experiences that have made me who I am.

Statement of contributions

I am the author of this thesis and the work described in it with the following exceptions:

- The work described in Chapter 3.3 was analyzed by Alexander Grassam-Rowe.
- The work described in Chapter 5.3 was carried out by Prof. Henggui Zhang and his group from the University of Manchester.
- The work described in Chapter 7.4 was prepare by me and conducted by Dr. Zhidao Xia from Swansea University Medical School

Table of Contents

Abstract 1

Acknowledgement 3

Statement of contributions 5

Table of Contents 6

Abbreviations 9

Chapter 1 Introduction 12

1.1 The development of the murine heart 12
1.1.1 Formation of heart tube 12
1.1.2 Formation of chambers 16
1.1.3 Septation of outflow tract 18
1.1.4 Trabeculation 18

1.2 Electrophysiological properties of the heart 19
1.2.1 Functional organization of cardiac myocytes 19
1.2.2 Generation of cardiac action potentials 22
1.2.3 Mechanism of excitation-contraction coupling 26

1.3 Cardiac conduction system (CCS) 28
1.3.1 Components and anatomy of CCS 30
1.3.2 Current understanding of CCS development 32
1.3.3 Nervous system control in CCS 35

1.4 Intrinsic cardiac nervous system (ICNS) 36
1.4.1 Components of ICNS 36
1.4.2 The origin of ICNS 38
1.4.3 The anatomy of ICNS 40
1.4.4 The function of ICNS in the CCS 41
1.4.5 Catecholaminergic cells: ICA cells and Pnmt+ derived cardiomyocytes (PdCMs) 43

1.5 Development and application of single cell RNA sequencing technology in the heart 48

1.6 Development and application of spatial transcriptomic analysis 51

Chapter 2 Materials and Methods 55

2.1 Materials 55

2.1.1 Mouse models 55
2.1.2 Antibodies and RNAscope probes 58
2.2 Methods 59
2.2.1 Embryo dissection 59
2.2.2 Fixed frozen heart sample preparation 59
2.2.3 Immunofluorescence 60
2.2.4 Multiplex nucleic acid in situ hybridization (RNAscope ISH) 61
2.2.5 Transparent heart preparation 62
2.2.6 Lightsheet imaging 63
2.2.7 NE trace 64
2.2.8 3D reconstruction of the heart 65
2.2.9 Sample preparation for transmission electron microscopy (TEM) 68
2.2.10 Optical Voltage and Ca2+ mapping 69
2.2.11 Single-cell transcriptomic analysis using the 10X Genomics Chromium 70
2.2.12 Spatial transcriptomic analysis 75

Chapter 3 Single cell RNA sequencing analysis depicts developmental transcriptome of the murine cardiac conduction system and identifies *Dbh*$^+$ cells 80

3.1 Isolation of single cells from embryonic hearts for single-cell RNA sequencing analysis 81
3.2 Identification of cell types and CCS sub-clusters by each stage 91
3.3 Identification of cell types and CCS sub-clusters by merged stage data 114
3.4 Identification and characterization of *Dbh*$^+$ cells 121
3.5 Single cell RNA sequencing results revealing the potential role of *Dbh*$^+$ derived cardiomyocytes (*Dbh*$^+$-CMs) in the CCS 125

Chapter 4 Spatial transcriptomic analysis of development of murine cardiac conduction system by using high resolution *spatially resolved transcriptomics (*SrT*)* technology 128

4.1 Sample preparation for SrT analysis 129
4.2 Identification of cell types throughout each developmental stages by using different clustering methods 132
4.3 SrT analysis showing the spatio-temporal transcripts of *Dbh*$^+$-derived cardiomyocytes 147

Chapter 5 Lineage tracing analysis reveals the contribution of *Dbh*$^{+}$-derived cardiomyocytes (Dd-CMs) in developmental morphogenesis of murine heart 154

5.1 Lineage tracing fating the distribution of *Dbh*$^{+}$-CMs and Dd-CMs throughout different developmental stages and showing their association with CCS and sympathetic innervation 155

5.2 Anatomical characterization of *Dd-CMs* in the Purkinje fiber network 181

5.3 3D reconstruction of *Dbh*^{Cre}/R26-tdTomato mouse heart mapping the distribution of *Dbh*$^{+}$-CMs at P3 and adult stage 183

Chapter 6 Developing high-resolution three-dimension models of spatial distribution of cardiomyocyte subpopulation 189

6.1 Improvements of tissue clearing method and high-resolution light sheet fluorescence microscopy 189

6.2 Verification of improved method by 3D model reconstructions of Hcn4 expression pacemaker cells and Pnmt^{+} cell-derived cardiomyocytes 195

6.3 Technique validation for high-resolution three-dimension method 200

6.4 3D model reconstruction of *Dbh*$^{+}$ cells in murine heart 202

Chapter 7 Characterising electrophysiological and endocrine properties of *Dd-CM*s 207

7.1 Generation of mouse models 207

7.2 Optical mapping revealing fast conduction property of *Dd-CM*s 209

7.3 NE trace showing the potential endocrine functions 212

7.4 EM study indicating the structurally potential of endocrine functions 218

Chapter 8 Discussion and Conclusions 221

Publications 229

Bibliography 230

Abbreviations

ADP	Adenosine diphosphate
ATP	Adenosine triphosphate
AVC	Atrioventricular canal
AVN	Atrioventricular node
BB	Bundle branches
Bmp2	Bone morphogenetic protein 2
Bmp4	Bone morphogenetic protein 4
Bmp10	Bone morphogenetic protein 10
CANS	Cardiac automatic nervous system
CCS	Cardiac conduction system
CGRP	Calcitonin gene-related peptide
CM	Cardiomyocytes
DA	Dopamine
Dbh	Dopamine beta-hydroxylase
Dbh^{+}-CM	Dopamine beta-hydroxylase expressing cardiomyocytes
Dd-CM	*Dbh*$^{+}$-derived cardiomyocytes
DRAsGP	Dorsal right atrial ganglionated subplexuses
E	Epinephrine
eAM	Immature atrial cardiomyocytes
Emcn	Endomucin
Ephb3	EPH Receptor B3
eVM	Immature ventricular cardiomyocytes
FACS	Fluorescence-activated cell sorting
FFN270	Fluorescent false neurotransmitter 270
FHF	First Heart Field
Gja1	Gap Junction Protein Alpha 1
Gja5	Gap Junction Protein Alpha 5
GO	Gene Ontology
GPs	Ganglionated plexuses
HCN4	Hyperpolarization-activated cyclic nucleotide-gated channel 4
HDAC3	Histone Deacetylase 3
HIS	His bundle
ICA	Intrinsic cardiac adrenergic cells
ICNS	Intrinsic cardiac nervous system
Isl1	ISL LIM Homeobox 1
JSR	Junctional SR
LA	Left Atria
LCsGP	Left coronary ganglionated subplexus

LDsGP	Left dorsal ganglionated subplexuses
LSFM	Light sheet fluorescence microscopy
LV	Left Ventricle
MASH1	Mammalian achaete-scute homologue
MDsGP	Middle dorsal ganglionated subplexus
Myh6	Myosin Heavy Chain 6
Myh7	Myosin Heavy Chain 7
NE	Norepinephrine
NET	Norepinephrine transporter
Nppa	Natriuretic Peptide A
Nrg1	Neuregulin 1
OT	Outflow tract
PdCMs	$Pnmt^{+}$ derived cardiomyocytes
PFN	Purkinje fibers network
PHOX2B	Paired-like homeobox 2B
PKJ	Purkinje Fibres
Pnmt	Phenylethanolamine n-methyltransferase
RA	Right Atria
RCsGP	Right coronary ganglionated subplexus
RCTD	Robust cell type decomposition
RV	Right Ventricle
Ryr2	Ryanodine receptor 2
SAN	Sinoatrial node
Scn5a	Sodium Voltage-Gated Channel Alpha Subunit 5
scRNA-seq	Single cell RNA sequencing
Sh3bgr	SH3 Domain Binding Glutamate Rich Protein
SHF	Second Heart Field
Shox2	Short stature homeobox protein 2
SMASH	Scalable Marker (gene) Signal Hunter
SR	Sarcoplasmic Reticulum
SrT	Spatially resolved transcriptomics
SV	Sinus venosus
TAC	Transverse aortic constriction
Tbx18	T-box transcription factor 18
Tbx3	T-box transcription factor 3
Tbx5	T-box transcription factor 5
TEM	Transmission electron microscopy
Th	Tyrosine hydroxylase
Ttn	Titin
VMAT2	Vesicular monoamine transporter 2

VRAsGP	Ventral right atrial ganglionated subplexus

1. Introduction

1.1 The development of the murine heart

The heart is the first organ to form and function during the embryonic stage of development (Mantri et al., 2021). The development, maturation, and maintenance of the heart are crucial to the beginning of an organism's life and its continued survival. Heart development takes place first in almost all vertebrates ranging from small species such as zebrafish and mice to larger species such as dogs and pigs (Xia et al., 2020). The mouse has established itself as a popular animal model for research into both health and disease, due to not only the high similarity in structure and molecular profiles with humans but also the rapid development and widespread use of transgenic technologies (Cheng et al., 2003; J. Liu et al., 2007). Heart development is a finely tuned process requiring the collection of various cell types as well as the fidelity of cell migration and differentiation (Evans et al., 2010). However, the whole developmental process and related molecular signaling are not fully understood and need more investigation.

1.1.1 Formation of heart tube

The first signs of heart development were initially traced back to E7.5 in murine embryos(Savolainen et al., 2009). At embryonic day7.5 (E7.5) in mice, the cardiac precursors emerging from the splanchnic mesoderm start differentiation into cardiomyocytes through the formation of a bilateral structure from the midline called the cardiac crescent and assembly of contractile sarcomere function (Savolainen et al., 2009). At this time point, the cardiac region assumes a horse-shoe shape, above which is the cardiac crescent like a thick bent pillar with two thin poles (Ivanovitch et al., 2017)(Figure 1.1.1). The formation of the heart tube goes through three distinct temporal stages. Initially, the precursors in the cardiac crescent precursors show a rapid differentiation to cardiomyocytes and cellular morphogenesis (Ivanovitch et al., 2017). In the second phase, the differentiation pauses while the morphogenetic remodeling takes place and the cardiac crescent transforms to the primary heart tube with a dorsal opening (Bruneau, 2013). At E8.25, the cardiac precursors start recruitment followed by resumption of differentiation (Savolainen et al., 2009). The heart tube subsequently transforms into a linear tube with dorsal closure, which is also named a primitive tube (Evans et al., 2010; Kelly et al., 2014).

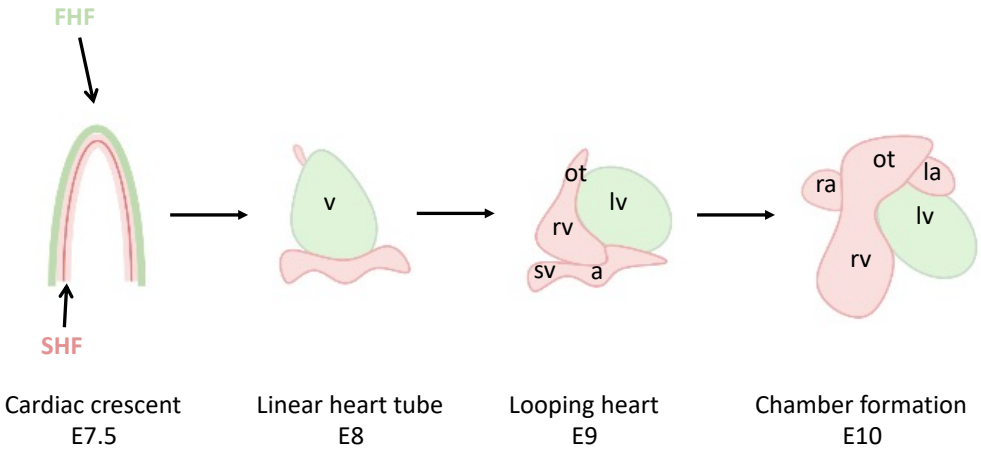

Figure 1.1.1 The major process of heart development (Bruneau, 2013). FHF: first heart field; SHF: second heart field; v: ventricle; lv: left ventricle; rv: right ventricle; ot: outflow tract; sv: sinus venosus; a: atria; la: left atria; ra: right atria. Created with BioRender.com.

It is reported that the left ventricle arises in the cardiac crescent and early heart tube exclusively whilst cardiac precursors in the dorsomedial region toward the cardiac crescent give rise to the outflow tract, right ventricle, and the atria (Bruneau, 2008, 2013; Zaffran et al., 2004). The canonical mechanism is that two cell populations contribute to the following heart developmental process. The first heart field (FHF) precursors, contribute cells to participate in the initial heart tube development and left ventricle construction. The second heart field precursors (SHF) contribute cells later and are responsible for the elongation of the heart tube (Ivanovitch et al., 2017). Currently, the origin and relationships of FHF and SHF remain controversial (Buckingham et al., 2005). One view suggests that the precursors in FHF and SHF are two unique and distinguishable cell populations with dedicated molecular pathways

(Devine et al., 2014a; Lescroart et al., 2014; Meilhac et al., 2004). Lescroart and co-workers proposed that the SHF precursors, unlike the FHF, share a common origin with the skeletal muscles of the neck and the head in the pharyngeal mesoderm, supported by clonal analysis (Lescroart et al., 2010, 2014, 2015). An alternative view suggests that heart development is a continuous process with a single rudimentary population of cardiac precursors and it is only the time of recruitment that is critical (Abu-Issa et al., 2004; Moorman et al., 2007). Evidence is available for this idea. The typical marker of SHF, Islet1, was once found to be transiently expressed in the FHF precursors, indicating the common characteristics would be shared in FHF and SHF or the inheritance would exist from FHF to SHF(Cai et al., 2003; Prall et al., 2007; S. Yuan & Schoenwolf, 2000). Interestingly, it has been identified that the cellular environment is important for the initial determination of cell identity during the developmental stage (Abu-Issa, 2014). The cell populations that contribute to heart development demonstrate some degree of plasticity. The cells isolated from either different locations or different developmental stages were shown to be able to contribute to heart development in certain cellular environments (Bruneau, 2013). There is yet no confirmed evidence for the argument of whether the origin of FHF and SFH precursors is the same (Bruneau, 2013). In part, the limitation of the experiments may account for that. So far, the spatial and temporal arrangements of these cardiac precursors and their differentiation patterns are based on the fixed samples from certain timepoints, which lack of the dynamic changes (Bruneau, 2013). With the help of lineage tracing and additional genetic mouse model, we might trace cells of interest. However, cell

fate and its respective molecular signature would likely not be fully recognized without a continuously dynamic record. Embryonic culture has been utilized in early developmental stages over short time scales but has not cover the entire development process. Live embryo tracking remains a big challenge.

1.1.2 Formation of chambers

The linear and tubular heart undergoes a series of transformations(Srivastava, 2006). These processes of expanding, lengthening and looping promote the movement of the heart tube from the midline to the right side of the embryo, shaping the asymmetric location of the heart in the body at E8.5(Savolainen et al., 2009). The fundamental structure of the heart, two atria, outflow tract, and two ventricles first becomes evident at this stage and becomes more recognizable in the following developmental process. Septation and valve formation also subsequently occur.

At E9.5, the outflow track elongates and bends(Savolainen et al., 2009). Unlike the slow proliferation in the distal outflow tract, the part close to the left ventricle proliferates quickly with the formation of trabeculae (Savolainen et al., 2009). An invagination but not clear septum is discernable between the ventricles which is the future interventricular septum (Savolainen et al., 2009.; Srivastava, 2006). At E11.5, the indentation between ventricles is more obvious and an apparent trabecular ridge

also develops (Savolainen et al., 2009). At E11.5, two endocardial cushions in the atrioventricular region appear, called the superior and inferior atrioventricular cushions (Bruneau, 2013; Savolainen et al., 2009). These two cushions fuse and then separate the atrioventricular canal into left and right canals, forming the atrioventricular septum (Bruneau, 2013). To allow the align the left and right canal to their corresponding ventricles, the atrioventricular septum moves in the direction of the interventricular septum (Bruneau, 2013). At E12.5, the fusion of the two cushions continues. The septation of the atria will complete at E14.5 while ventricular septation completes between E13 to E14 (Savolainen et al., 2009). These atrioventricular cushions are also involved in the formation of both left and right valves (left mitral bicuspid valve and right tricuspid) and their supporting structures (Savolainen et al., 2009).

It is notable that the atrial chamber is not divided until E14 into two separated atria(Savolainen et al., 2009; Webb et al., 2003). There is an inflow from the right atrium to the left atrium during the developmental stage through inter-atria ostia which become the foramen ovale (Webb et al., 1998, 2003). The foramen ovale normally closes after birth by the fusion of the atrial septum (Webb et al., 1998). A large amount of fresh oxygenated blood arrives from the placenta via the inferior vena cava into the right atrium, flows through the foramen ovale to the left atrium, and then through the atrioventricular canal to the left ventricle eventually(Webb et al., 2003). This blood will go to the systemic circulation via the ascending aorta. The

deoxygenated blood through the right superior vena cava shunts directly to the right ventricle rather than enter the left atrium first. The blood will then proceed into the pulmonary trunk. Only a small portion will move directly to the lungs since the lungs are not yet functional. While a large portion will pass to the abdominal aorta, supplying the tissue of the abdomen and lower limbs. The blood will be refreshed and oxygenated by traveling to the placenta(Kaufman & Bard, 1999).

1.1.3 Septation of outflow tract

The septation of the outflow tract begins at E11.5(Savolainen et al., 2009). The undivided outflow tract composes of three main parts, aortic sac, truncus, and conus, and they have different mechanisms of septation(Webb et al., 2003). The aortic sac divides from the neural crest-derived cells, which protrudes to the dorsal wall and further divide the distal outflow tract into aortic and pulmonary channels(Webb et al., 1998, 2003). The aorticopulmonary complex generates the septation in the truncus. The proximal part of the outflow tract is filled with the fusion of outflow tract cushions. By E12.5, the septation has been completed in the distal portion of the outflow tract whereas the proximal part starts to close in a zipper-like fashion from the distal region to the ventricles. Not until the E13.5 does septation complete in the outflow tract (Webb et al., 2003).

1.1.4 Trabeculation

During the differentiation and proliferation of the two ventricles, the trabeculated myocardium emerges from the luminal side of the ventricles while the outer side of the myocardium will later further differentiate into the compact myocardium(Bruneau, 2013). Although the trabeculated and compact myocardium are both from the ventricles, they do have their specific gene expression, suggesting different functions and differentiation modes (H. Chen et al., 2004a; Gassmann et al., 1995; Meyer & Birchmeier, 1995). The differentiation rate of trabeculae also varies, in which case it increases from the top to the base, and from the junction between outer wall to the inner(Grego-Bessa et al., 2007). This finding is further supported by the observation of abundant activated Notch signaling pathways at the base region, which regulates the differentiation and proliferation of the trabeculae.

1.2 Electrophysiological properties of the heart

1.2.1 Functional organization of cardiac myocytes

The heart is made up of myocytes, themselves outnumbered by other cell types like endothelial cells, smooth muscle cells in the vessels, and fibroblasts. The myocytes, especially ventricular myocytes, have unique morphology not only in size but also in

the delicate texture. Mature myocytes are rod-shaped, elongated cells with 80-150 μm in length and 20-35 μm in width. Myocytes usually have more than one nucleus and are packed with striated myofibrils which alternate the arrangement with the mitochondria. The myofibrils consist of cascaded sarcomeres in shape. Two major components of sarcomeres, thin filaments, and thick filaments interdigitate with each other. Thin filaments, composed of actin protein, extend from the edge of the Z band, crossing the I band, and reach the A band where they overlap and interact with the thick filaments. Thick filaments, made up of myosin, are limited to the A band at the middle of the sarcomere. One sarcomere is comprised of one Z-Z band while each myofibril contains 70 to 80 sarcomeres (Walker & Spinale, 1999).

In the thick filaments, the myosin consists of two pairs of light chains and two heavy chains. The myosin heavy chain is a dimer structure, made up of a tail and two bulbiform heads. The myosin tails are bundled to form the thick filament, whilst the heads extend from the thick filaments to reach the actin in the thin filaments. The thin filament is constituted by a dual-helical polymer made up of around three hundred spherical actin subunits. The actin has binding sites for myosin head interaction when contracting. The troponin complex and α-tropomyosin, involved in the muscle contraction, are located in the thin filament and conferred Ca2+ sensitivity.

On the surface of the plasma membrane, the transverse(T)-tubule is visualized, which presents a long and finger-like morphology from the superficial myofibrils to the deep

cell. T-tubules regulate the entry of extracellular Ca2+ into the cell through the L-type Ca2+ channels. Each myofibril is covered by an important feature, complex networking of tubules on the membranes called the sarcoplasmic reticulum (SR). This membrane network extends to form the junctional SR (JSR) whose membranes contain Ca2+ release channels which come into close proximity with tubular L-type Ca2+ channels while the opposite of which is the Ca2+ release channels. The JSR possesses Ca2+ binding protein through it acts as the main reservoir for Ca2+ whose cytoplasmic release produces the Ca2+ transient.

The myocytes described above are conventional working myocytes. Though myocytes distribute throughout the whole heart, they are distinct in morphology depending on different functions and locations. Myocytes in the sinoatrial and atrioventricular node regions are specifically small, with fortuitously arranged myofibrils and sparse gap junctions comprised of connexin 45. These characteristics lead to poor coupling and then slow conduction, which guarantee the propitious propagation of electrical impulse from atria to ventricles. The myocytes in the bundle branches and Purkinje network reveal a regular arrangement with large size of cells, ensuring promoting rapid action potential conduction into the ventricle leading to its contractile activation.

1.2.2 Generation of cardiac action potentials

The myocardial contraction starts from the generation of cardiac action potentials in the sinoatrial node, followed by a delay in the atrioventricular node and rapid propagation in both ventricles. Cardiac action potentials are distinct in the different sino-atrial, atrial, atrioventricular and ventricular conducting and contraction regions. The SAN action potentials have no resting potential after repolarization, followed by a spontaneously but gradual depolarization. The rate of upstroke in SAN is quite slow (1 to 10 V/sec) compared to atrial myocytes (100 to 200 V/sec) and ventricular myocytes (100 to 700V/sec)(CLAPHAM & KEATING, 2006). The pace of SAN is mediate by the I_{HCN} (human cyclic nucleotide gated) current and $I_{Kir2.1}$ (KCNJ2) which is an inward rectifying K+ channel relieving the opposition to depolarization. As a nonselective inward current, I_{HCN} (HCN2 is fast, I_f, HCN4 is slow I_s) is activated by the hyperpolarization to the pacing potential from -80 to -30mV and its activation in turns to lift potential to -20mV, thus allowing the entry of K+ and Na+. The inward Na+ depolarizing currents are named 'funny' currents. When the membrane is depolarized to -40mV, Ca2+ channel opening takes place, and this further boosts cell membrane depolarization. The lack of some Na+ channels and the reliance of slower inward Ca2+ channels account for the slow upstroke of SAN. $I_{CaV3.1}$ (CACNA1H) is the first Ca2+ current to open, driving the membrane potential while activating the L-type voltage-activated Ca2+ current ($I_{CaV1.2;}$ CACNA1C) around -30mV. An action potential is reached which is usually between -40mV and -30mV. Simultaneously, outwardly rectifying K+ currents I_{KVx} are fired during

the depolarization around -40mV. The balance is reached resulting from the inward conductance of $I_{CaV3.1}$, $I_{CaV1.2}$ and the Na+/Ca2+ exchanger $I_{Na/Ca}$ (NCX) to depolarization and outward conductance of I_{KVx}, eventually to the depolarization peak at +10mV. Action potential recovery involves outward K+ current including $I_{k2.1}$ promotion of repolarization. This efflux of K+ ions hyperpolarizes the membrane, triggering I_{HCN} initiating the next cardiac cycle.

When the ventricular myocyte is at resting potential, there is a potential difference around -80mV existing across the membrane, of which intracellular is negative. The negative potential mainly arises from open K+ channel resulting in a higher permeability of K+ relative to that of other ions in the plasma membrane. The intracellular concentration of K+ is about 140 mmol/liter, almost 35 folds of the outside the cell. Due to this concentration gradient, the K+ tends to flow out, leaving the intracellular environment more negatively charged. There is also Cl- movement across the membrane which passively balance the transmembrane charge.

The cardiac action potential can be divided into 5 phases. At phase 0, when the myocyte is electrically excited, Na+ channels open, allowing Na+ to flow in. At this stage, Na+ channel $I_{NaV1.5}$ takes the lead position in both atrial and ventricular myocytes for the generation of fast upstroke. The Na+ channel is sensitive to the potential difference across the membrane. This depolarizes the cell, causing more Na+ channels to open. The opening of the Na+ channel and abundant inflow of Na+ bring about a

positive current, which in turn leads to upstroke of the action potential. During this process, many Na+ channels close rapidly whereas the myocyte is still depolarized. The Na+ channels are now inactivated and cannot open until the repolarization.

At phase 1, the membrane potential shows a rapid transient recovery from the peak of depolarization at +47mV to +10mV due to the outflow of K+ ($I_{KV1.4+KV4.2/4.3}$, KCNA4+KCND2/KCND3) and the inactivation of voltage-dependent Na+ channel $I_{NaV1.5}$, rapidly and partially repolarizing the membrane(Oudit et al., 2001). During phase 2, plenty of different ion channels open and close, leading to a plateau phase 2. The low voltage-activated transient Ca2+ current ($I_{Ca.T,}$ $I_{CaV3.2}$) and high voltage-activated long-lasting Ca2+ current ($I_{Ca.L,}$ $I_{CaV1.2}$) are involved in the initial Ca2+ inward currents. $I_{CaV3.2}$ is mainly distributed in the conduction region including SAN, AVN and Purkinje fibers while it takes up one fifth the size of $I_{CaV1.2}$ thus contribute less to the effect of Ca2+ to excitation-contraction coupling process(Langdon et al., 1992). Unlike $I_{CaV3.2}$, $I_{CaV1.2}$ is found in all cardiac cells and it is predominant to Ca2+ current(Anderson, 2001). $I_{CaV1.2}$ takes a longer time to activate and inactivate compared with Na+ channel, opens at this stage to carry Ca2+ into the cells(Grant, 2009). L-type Ca2+ channel usually is activated at more positive potential (~-30mV) in contrast with Na+ channel(~-65mV). The influx of Ca2+ sustains the depolarization and initiates the Ca2+ induced C2+ release channels on SR, leading to more Ca2+ release and consequently myocyte contraction. During this stage, various K+ channels also open to cause an outflow of K+, some open at positive membrane potential and close at negative potential. The

outflow of K+ balances the inflow of Ca2+, contributing to a stable with the slightly decreased current. At phase 3, finally, the repolarization begins with the terminated influx of Ca2+ combined with the progressive growth of K+. There are more than four K+ currents participate during this process, among them I_{Kr} (rapid; I_{KHERG}, KCNH2), I_{Ks} (slow; I_{KLVQT1}, KCNQ1), and I_{Kur} (ultra-rapid; $I_{KV1.5}$, KCNA5). I_{Kur} is much more abudant in atria than in ventricle and is fifty times faster than I_{Kr} in activation(Carmeliet, 1999; Z. Wang et al., 1993). As a result, I_{Kur} plays a dominant role during this stage for the repolarization of the atrial action potential. In response to the increased concentration of Ca2+ inside the cell, the Na/Ca pump integrate to pump out on Ca2+ ion with three Na+ in, thereby prolonging the plateau and slowing down the repolarization. At phase 4, the recovery to resting potential is controlled mainly by the delayed rectifying K+ channel. During this stage, cardiac cells are unable to depolarize due to the inactivation of Na+ channel. The membrane potential is back to negative rest potential and cells are electrically silent waiting for the next event.

1.2.3 Mechanism of excitation-contraction coupling

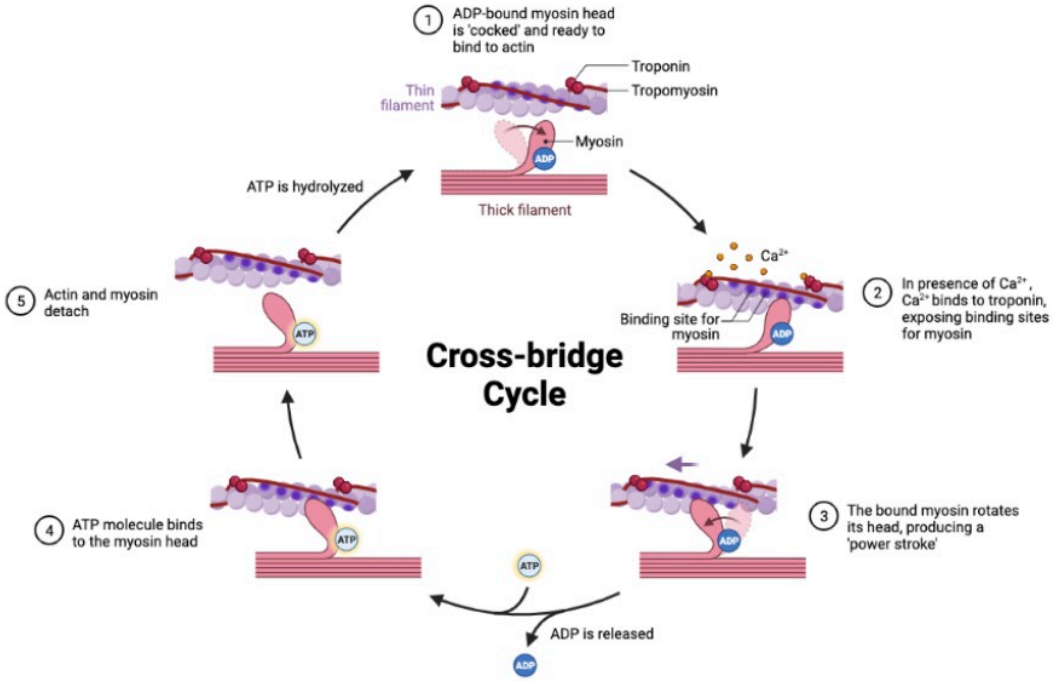

Figure 1.2.3 The mechanism of myocyte contraction. Created with BioRender.com

As mentioned above, the influx of Ca2+ fires the opening of Ca2+ induced Ca2+ release, which in turns open the ryanodine receptor (Ryr2) channels. A portion of released Ca2+ binds to the troponin C and then facilitating the myocyte contraction. To be specific, the cell contraction is a reflection of shortening and relaxation of numerous sarcomeres consistently, by the interaction of the myosin on the thick filament with the actin protein in the thin filament. The head of the myosin binds and sequentially hydrolyzes the ATP, leaving the ADP, phosphate (P), and trapping the free energy. Once the myosin-ADP-P complex attaches to the actin, the free energy is transiently released, causing a conformational change that moves the actin filament forward to the thick

filament which results overall in the shortening of the sarcomere. The Ca2+ is indispensable during this process. With the Ca2+ flowing into the cell, the Ca2+ induced Ca2+ release channels on the SR are activated, and a large amount of Ca2+ release. The increased concentration of cytoplasmic Ca2+ leads to muscle contraction finally. When released, Ca2+ binds to the troponin complex on the thin filament. There are three subunits of the troponin complex. The troponin C is a Ca2+ binding protein in which the Ca2+ binds to the N terminal of Troponin C to activate the thin filament. Troponin I is an inhibitory protein. When the muscle relaxes at a low concentration of Ca2+, the C terminal of Troponin I binds to the actin, thus preventing the interaction with myosin. When activated with high Ca2+ concentration, the Ca2+ binds to the N terminal of Troponin C and the C terminal of Troponin I binds to the N terminal of Troponin C, vacating this binding site for myosin, allowing myosin-actin interaction. The third subunit is Troponin T, which binds to Troponin C, Troponin I, and tropomyosin, anchoring the mediation complex in the thin filament. Eventually, the reuptake of Ca2+ to the SR terminates the contraction.

1.3 Cardiac conduction system (CCS)

The cardiac conduction system (CCS) plays an essential role in cardiac physiological function by initiating and coordinating cardiac contraction. The CCS comprises a set of distinct and specialized components, including the pacemaker sinoatrial node (SAN), the coordinating atrioventricular node (AVN) and the rapid transmission ventricular His–Purkinje system. Failure in correct development of CCS components leads to several fast (e.g. Wolff-Parkinson-White syndrome) and slow dysrhythmic (atrioventricular block and sick sinus syndrome) diseases(Mohan et al., 2018). Gaining insight into the morphogenesis and maturation of the CCS during the developmental process is critical for understanding the pathogenesis of these dysrhythmias(Mohan et al., 2018). However, our understanding of when and how diverse cell types arise to form different components of the CCS remains limited(van Eif et al., 2018).

In murine heart, the pacemaker activity can be detected as early as embryonic day (E)8.0(Cv Tyser et al., 2016). However, the formation of the CCS is not completed until perinatal stages(Meysen et al., 2007; van Eif et al., 2018). The origin of the cells, cellular differentiation, and the maturation of the various components of the CCS, in particular the ventricular CCS, is still in hot debate. A number of hypotheses have been proposed including: the neural crest-derived migration model(Gorza et al., 1988); the ingrowth model that suggests the CCS cells arise from common progenitors through endothelial derived signals(Gourdie et al., 1998, 2003); the outgrowth model

suggesting that CCS cells develop independently of the working myocardium from a pool of conductive progenitors at the crest of the interventricular septum in the early embryonic heart(Kitajima et al., 2006; Wessels et al., 1992). Recently, it has also been suggested that a polyclonal Purkinje fiber (PKJ) network forms by progressive recruitment of conductive precursors to this scaffold from a pool of bipotent progenitors(Choquet et al., 2020).

On the other hand, it has to be elucidated if cardiac sympathetic innervation plays any role in CCS development or functional maturation. Catecholamines, the canonical sympathetic neurotransmitter, are known to be essential for cardiac development: mice deficient in catecholamine synthetic enzymes (Zhou et al., 1995)tyrosine hydroxylase (Th) and dopamine beta-hydroxylase (Dbh)(Thomas et al., 1995, 1998), die in utero with cardiac developmental defects. There is also mixed evidence around the role of catecholamines in establishing and maintaining normal cardiac rhythm (Baker et al., 2012; Grassam-Rowe et al., 2020; HALL, 1957; Natarajan et al., 2004). However, the true importance and source of these catecholamines for the CCS development remains uncertain (Grassam-Rowe et al., 2020).

1.3.1 Components and anatomy of CCS

The heart is composed of several cell types including cardiomyocytes, fibroblasts, endothelial cells, and other cells. Among cardiomyocytes, working (contractile) cardiomyocytes make up to 98% CM while conducting cells only account for 2% and are responsible for the orchestration of generation and propagation of electrical impulses(Bhattacharyya & Munshi, 2020). The cardiac conduction system (CCS) is made up of distinct components including the sinoatrial node (SAN), atrioventricular node (AVN), His bundle, bundle branches (BB), and Purkinje fibers network (PFN). CCS is critical to the heart due to its essential roles and functions but is challenging for research because of the heterogeneity of cell types, small number of cells, wide anatomic distribution.

CCS is functionally classified as slow-conducting structures, including SAN and AVN, and fast-conducting structures, among them His bundle, BB and PFN. Although all the muscle cells are capable of rhythmic excitation without external stimulus, SAN takes advantage of their rapid intrinsic rate to control the whole beating rate of the rest of the cardiomyocytes. This is because SAN plays a role as pacemaker cells, which are highly specialized cells able to produce rapid depolarization and initiate electrical impulses. SAN locates in the gap between the superior vena cava and right atrium. Once the action potential is triggered and generated at SAN, it rapidly propagates to the atrial cells, inducing atrial systole. Before the onset of atrial systole, the AVN is

converged and initiated, which leads to a delay of impulse funnel. AVN is concentrated in the dorsal base of the interatrial septum. This delicate structure arranges the atrial contraction and blood filling in the ventricles before the ventricular systole, tuning up the regional beating sequentially. The propagation in the SAN and AVN is slow compared to the ventricular conduction system. Running out from the AVN, the propagation accelerates along with the His bundle, asymmetric BB, and finally reaches the PFN lying in the subendocardial layers of both ventricles, activating the ventricular contraction and blood pump via the outflow tract(Christoffels & Moorman, 2009).

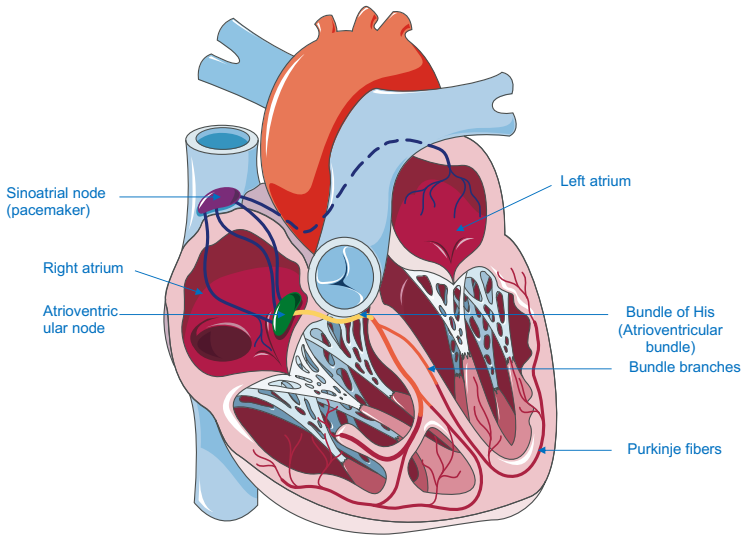

Figure 1.3.1 The anatomy of cardiac conduction system. Created with BioRender.com.

1.3.2 Current understanding of CCS development

Development of SAN

The origin of CCS varies for different constituents. The SAN progenitors are reported derived from the sinus venosus (SV) close to the right atrium, which is morphologically recognizable from around E10 in mice embryos(Bressan et al., 2013; Mommersteeg et al., 2010; Virágh & Challice, 1980). As the heart tube elongation and the addition of cardiac progenitors from the SFH, SAN cells start to express Hcn4(encoding potassium/sodium hyperpolarization-activated cyclic nucleotide-gated channel 4) and Tbx18(T-box transcription factor 18), the former is a necessity for the pacemaker activity and the latter is selectively expressed in the SAN and SV regions(Christoffels et al., 2006; Garcia-Frigola et al., 2003). Interestingly, Hcn4 is considered as a marker for FHF in the early heart tube(X. Liang et al., 2013). By contrast, a Cre-genetic lineage analysis demonstrated that SAN and SV cells are derived from Tbx18+ Nkx2.5- progenitors, given that *Nkx2.5* is widely expressed in the FHF, SHF, and other components(Christoffels et al., 2006). This is suggested that “a tertiary heart field” may exist before cardiac morphogenesis and support the differentiation of SAN(Burkhard et al., 2017). Many genes manipulate the development of SAN throughout the embryonic stages. *Tbx3* (T-box transcription factor 3) is expressed specifically to all the way mature the SAN by suppression of genes related to working myocardial like Gja1, Gja5, and Scn5a(Frank et al., 2012; Hoogaars et al., 2007). Tbx3 also conjugates with HDAC3 gene to repel the expression of NKx2.5 in SAN(Wu et al., 2014). Tbx5(T-box

transcription factor 5) regulates the expression of Bmp4, Tbx3, and Shox2, which are related the pacemaker development and maturation(Mori et al., 2006; Puskaric et al., 2010). Shox2(short stature homeobox protein 2) is vital for the SAN development which activates the expression of Isl1, Hcn4, and Tbx3(Blaschke et al., 2007; Espinoza-Lewis et al., 2009, 2011). Isl1 is a marker for the SHF with once transiently expressed in the FHF(Bhattacharyya & Munshi, 2020). Its expression is restricted in the SAN in adulthood and regulates the pacemaker programs involving Tbx3, Bmp4, Hcn4, and Shox2(Hoffmann et al., 2013; X. Liang et al., 2015; Tessadori et al., 2012; Vedantham et al., 2015).

Development of AVN

The AVN and AV ring bundles are all originated from the inferior atrioventricular canal (AVC), at which the pacemaker-like phenotypes are maintained like spontaneous depolarization and slow propagation until adulthood(Aanhaanen et al., 2009; Vicente-Steijn et al., 2011). The AVC is derived from the cardiac crescent from E7.5 in mouse embryos(Aanhaanen et al., 2009; Davis et al., 2001; de La Cruz et al., 2001; Domínguez et al., 2012). During that stage, the AVC expresses the Bmp2, the gene encoding bone morphogenetic protein 2 (BMP2), activating the expression of Tbx2 and Tbx3(Bhattacharyya & Munshi, 2020). There is a cell population that expresses Tbx2 in the caudal region of the cardiac crescent and the expressions of Tbx2 and Tbx3 contribute to the formation and functionalization of the AVC structure(Aanhaanen et al., 2011; Harrelson et al., 2004; Ma et al., 2005; Singh et al., 2012). The lineage tracing

analysis was reported to successfully fate map the Tbx2+ cells in the heart tube and label the inflow tract and AVC at E8.5 and E9.5 respectively(Aanhaanen et al., 2009; X. Liang et al., 2013; Mohan et al., 2018). In the mature heart, AVN and AV ring bundles express G1N2, a neural tissue antigen(Mohan et al., 2018). When tracing back to heart developmental stages, the interventricular ring, as well as the right part of AVC, also express the G1N2(Mohan et al., 2018). This colocalized expression pattern is consistent with the populations of AVN and AV ring bundles. All these findings indicate that the Tbx2+ cardiac precursors from the FHF sequentially form the embryonic inflow tract, the AVC, and the AVN and AV ring bundles eventually. In the AVN, cellular activity is modulated by the expression of Cx30.2, Cx45, and less Cx40(Bhattacharyya & Munshi, 2020). The expressions of Cx30.2 and Cx45 exert higher intrinsic rebellion and regulate the slow conduction in the AVN, AV ring bundle, and His bundle, exclusively(Bhattacharyya & Munshi, 2020).

Development of VCS

The His bundle, left and right bundle branches (LBB and RBB), and Purkinje fiber network (PFN) make up the ventricular conduction system (VCS), also known as fast conduction structures. The His bundle is proposed to derive from the Tbx3+ interventricular ring, the progenitors from the connection between the FHF and anterior SHF (Hoogaars et al., 2004; Wessels et al., 1992). The bundle branches differ bilaterally, LBB develops from the FHF whilst the RBB is from the progenitors expressing SHF markers(Aanhaanen et al., 2010; Devine et al., 2014b; Mohan et al.,

2018). Similarly, the PFN in the left and right ventricles also share these origins(Mohan et al., 2018). During heart formation, Tbx3, acts as a repressor in the VCS, to suppress fast conduction genes like Gja1 and Gja5 to inhibit cell proliferation and contribute to the slow conduction development (Bhattacharyya & Munshi, 2020). On the contrary, Tbx5 plays the role of activator to boost the expression of Gja5 and Scn5a (fast conduction genes)(Bakker et al., 2008; Bruneau et al., 2001; Hoogaars et al., 2007; van den Boogaard et al., 2012). In the early heart, the cells of the PFN highly express Bmp10, Nppa, Irx3, and Gja5. Bmp10 expression, stimulated by Notch signaling, promotes trabeculation by suppression of cell-cycle inhibitors(H. Chen et al., 2004a; Christoffels, Habets, et al., 2000; Christoffels, Keijser, et al., 2000; Delorme et al., 1997; Miquerol et al., 2010; Zhang et al., 2011). Moreover, endocardial Notch signaling induces the expression of Nrg1 (neuregulin 1) which in turn activates the fast conduction genes(Rentschler et al., 2002; Shekhar et al., 2016). The Irx3 gene is essential for VCS formation by inducing Gja5 expression and Gja1 inhibition(Bhattacharyya & Munshi, 2020).

1.3.3 Nervous system control of CCS

A study identified that all the components of CCS are innervated in different densities(Crick et al., 1996). CCS possesses a higher density of nerve fibers than working myocytes, whereas within the CCS not only the distribution but also the

density of cholinergic, adrenergic nerve fibers differ(Crick et al., 1996). So far, research has illustrated that the dorsal right ganglionated subplexuses and ventral right atrial ganglionated subplexus supply the SAN, though, the left and middle dorsal neural ganglionated subplexuses support the AVN region(Rysevaite, Saburkina, Pauziene, Noujaim, et al., 2011; Rysevaite, Saburkina, Pauziene, Vaitkevicius, et al., 2011). The nervous system, especially the cardiac intrinsic neurons system, is crucial to the CCS in the absence of external neural stimulus or hormone effect. 'Fight or Flight' is a good example. Activation on the β1 adrenergic receptors of the sympathetic neuronal system in the SAN and AVN, the heart rate increases, along with contractility and conduction rate in the AVN. The parasympathetic muscarinic M2 receptors are rich in nodal tissue but exiguous in ventricular myocytes. The stimulation causes adverse effects such as the slower rate of depolarization in SAN, heart rate, contraction, and atrial conduction velocity. Reducing the stroke volume of the heart, finally leads to a low cardiac output.

1.4 Intrinsic cardiac nervous system (ICNS)

1.4.1 Component of ICNS

The heart is a complex and sophisticated organ, that is under the control of the cardiac automatic nervous system (CANS). The CANS could be subdivided into three levels that

contribute to the regular functions of the heart. The first level is the central nervous system and comprises the neurons in the brainstem and spinal cord(Ardell & Armour, 2016). The second and third levels are both peripheral nervous systems, the former is composed of intrathoracic extracardiac ganglia while the latter one is the intrinsic cardiac nervous system(Ardell & Armour, 2016).

The intrinsic cardiac nervous system, acted as a “commander” or “little brain”, regulates and maintains the cardiac mechanical and electrophysiological activities in the heart(Armour, 2008). Three components consist of the ICNS, afferent sensory, interconnecting, and local efferent neurons. The ICNS including cardiac sympathetic and parasympathetic neurons locates in the atrial and ventricular ganglia and the disruption of ICNS has clinical implications causing various cardiac disorders like arrhythmia(JL et al., 2016; Wake & Brack, 2016b). The ICNS plays a crucial role in modulating the fundamental activities of cardiac muscle cells as chronotropism(automaticity), bathmotropism(excitability), intropism(contractility), and dromotropism(conductivity)(Cardiac Electrophysiology: From Cell to Bedside | ScienceDirect, 2017). To be specific, the sympathetic neurotransmitter Norepinephrine (NE) is released and acts on the cardiac adrenergic beta receptors to promote the opening of Ca ion channel to boost the rate of depolarization, in turn, to extend the slope of depolarization and finally increase the rate of SA node firing and heartbeats(Cardiac Electrophysiology: From Cell to Bedside | ScienceDirect, 2017.). Similarly, the sympathetic system could increase excitability, contraction, and

conductivity while the parasympathetic system works in the opposite way(Cardiac Electrophysiology: From Cell to Bedside | ScienceDirect, 2017).

1.4.2 The origin of ICNS

The development of innervation in the heart occurs in a stepwise fashion, concurrently appearing during heart development and maturation (Durães Campos et al., 2018a; Végh, Duim, Smits, Poelmann, Harkel, et al., 2016). The heart is reported to derive from mesoderm whereas the ICNS is originated from neuroectoderm. Before the formation of cardiac innervation, the heart activities rely on the catecholamine source generated by intrinsic cardiac adrenergic (ICA) cells(Ebert & Taylor, 2006; Huang et al., 2005). Not until E8.5 to E11 in murine embryos (around the fifth week in humans), does cardiac innervation begin to develop(W, 2013). The neural crest cells initially migrate to the dorsal aorta and differentiate into neurons. The aggregation of neuronal ganglia occurs, and the parasympathetic neuron ganglia are formed then(W, 2013). Cardiac innervation further differentiates, patterns, and projects to the whole heart. During development, the parasympathetic neurons take the lead to exert physiological functions before the differentiation of sympathetic neurons(Fedele & Brand, 2020).

The development of the sympathetic and parasympathetic neuron systems shows differences temporally and spatially. The neural crest cells migrate along the ventral

pathway to the dorsal aorta, afterward they migrate in rostral and caudal directions to form the paravertebral sympathetic chain(Fedele & Brand, 2020). During this process, neural crest cells orchestrate the migration route modulated by the repelling and attractive factors, among them Ephrins and semaphorins(SEMA)(W, 2013). EphrinB is a typical repulsive cue working on the EphB2 receptor expressed by neural crest cells(Kasemeier-Kulesa et al., 2006). SEMA family plays a principal role to determine the migration to form the sympathetic neuron system. SEMA3C is an attractive factor expressed in myocardial cuff cells located in the outflow tract to supporting the NCC migration, unlike the repulsive SEMA6B with an opposite manifestation in the dorsal neural tube. In accordance with that, researchers found the dysfunction in sympathetic ganglia occurred in Sema3a knock-out mice(Ieda et al., 2007). Parasympathetic ganglia are derived from not only a subset of vagal neural crest but also the nodose placode, migrating into the heart and forming at E12.5 in mice(ML, 1988; V et al., 2008).

The neural crest cells reach the dorsal aorta at E9.5 and then continue into the outflow tract at E10.5(Végh, Duim, Smits, Poelmann, Harkel, et al., 2016). Many cues trigger and modulate the specification for the identity of sympathetic and parasympathetic neurons, among them the Bone morphogenic protein (BMP) family and its signaling pathway. For example, BMP2 is conducive to sympathetic differentiation and sympathetic formation is found to cease after the inhibition of BMP4-7 in avian embryos(C et al., 1999; PM et al., 2001; Y et al., 2009). BMP signaling promotes the

expression of paired-like homeobox 2B(PHOX2B) and mammalian achaete-scute homologue (MASH1), which initiate the expression of PHOX2A in both sympathetic and parasympathetic pathways(A et al., 2006; F et al., 1993; Pattyn et al., 1999). PHOX2B and MASH1 also play a key role in the generation of catecholamine biosynthesis enzymes, TH and DBH(Pattyn et al., 1999; Végh, Duim, Smits, Poelmann, Harkel, et al., 2016). PHOX2B triggers the induction of TH via GATA3 while the MASH1 triggers the TH and DBH expression through the HAND2 in sympathetic neurons(Müller & Rohrer, 2002; Végh, Duim, Smits, Poelmann, Harkel, et al., 2016). PHOX2B is also involved downstream during the parasympathetic differentiation that induces the choline acetyltransferase and vesicular acetylcholine transporter expression(Enomoto et al., 2000; Végh, Duim, Smits, Poelmann, Harkel, et al., 2016). However, the differentiation of parasympathetic neurons is not fully understood and needs to be elucidated.

1.4.3 The anatomy of ICNS

Studies on cardiac innervation have been proceeding for a long time. The neurons and ganglia were visualized with the application of methylene blue staining which could mark the nerve fibers(B. -X Yuan et al., 1994). The high resolution of electron microscopy first revealed the neuron-cardiac network in both atrial and ventricle, through which the of the innervated heart was visualised (Choate et al., 1993;

FAWCETT & SELBY, 1958; PAUZIENE et al., 2000; Pauziene et al., 2017; PRICE et al., 1959; B. -X Yuan et al., 1994). The concept of ganglionated plexuses (GPs) was brought out for a cluster of ganglia in different locations(Wake & Brack, 2016b).

More research on GPs have demonstrated the anatomical distributions(Fedele & Brand, 2020). Interestingly, many of them concentrate on the supraventricular regions although the anatomy of GPs varies in different species(Batulevicius et al., 2008; Saburkina et al., 2010; Wake & Brack, 2016b). Various GPs fate the whole heart innervations(Fedele & Brand, 2020). The GPs that emerge from the left dorsal ganglionated subplexuses (LDsGP) innervate the anterior left atrial and posterior left and right ventricle. The GPs in the right atrial are from both the dorsal right atrial ganglionated subplexuses (DRAsGP) and the ventral right atrial ganglionated subplexus (VRAsGP). The middle dorsal ganglionated subplexus (MDsGP) innervates most vascular structures like left and right pulmonary veins. The left and right coronary ganglionated subplexus (LCsGP & RCsGP) make contributions to the ganglia in the left and right ventricle as well(Rysevaite, Saburkina, Pauziene, Noujaim, et al., 2011).

1.4.4 The function of ICNS in the CCS

The ICNS plays a fundamental role in the modulation of regional cardiac functions, among them the cardiac conduction system. Zarzoso's group employed the Langendoff

perfusion in mouse hearts and stimulated the hearts with the combination of propanol and atropine, which are adrenergic and cholinergic antagonists respectively(Allen et al., 2018; Zarzoso et al., 2013). This biphasic response of an acceleration of heartbeat after the initial slowdown was elicited and resulted from various reasons including the delayed sympathetic response, the complementary of parasympathetic reaction, and fast breakdown of Ach(Zarzoso et al., 2013). As shown in Sampaio's work, the SAN ganglia in rats were stimulated leading to bradycardia without the effect on the conduction whilst the stimulation in AVN ganglia slowed the heart conduction but not the heartbeats(Sampaio et al., 2003). Hou and coworkers also proved the interplay of various GPs have a role in regulation in the cardiac conduction system including SAN and AVN by ablation or inhibition of selective ganglia(Hou et al., 2007).

Cardiac innervation performs unique lateralization in both anatomy and functions, paired with the distribution of GP in the left and right heart. The right branches of innervation regulate the SAN whereas the left branches modulate the AVN downstream electrophysiological function in the left heart(Brack, 2015; Ng et al., 2001; Winter et al., 2012). Studies proved by the ablation and inhibition of the localized GPs point out that SAN is under the control of the GPs in the superior vena cava, right atrium, and right pulmonary vein whereas the AVN is regulated by the ganglia from the inferior vena cava and the inferior left atrium(Dickerson et al., 1998; Gatti et al., 1995; Gray et al., 2004; Hou et al., 2007). The interactions between sympathetic, parasympathetic ganglia and cardiac conduction system are not fully understood and

more research is needed in this regard.

1.4.5 Catecholaminergic cells – ICA cells and Pnmt+ derived cardiomyocytes (PdCMs)

Catecholamines, such as dopamine, Noradrenaline, and Adrenaline, play a crucial biological role in both physiological and pathological conditions within the heart. 'Fight and Flight' is a typical example. The catecholamines, working to regulate normal heart functions, are usually released from the chromaffin cells in the adrenal medulla tissue or cardiac sympathetic nerve system. By activating the β1 and β2 adrenergic receptors on the cell membrane, they modulate cardiac function including heart rate, conduction velocity, and contractility.

ICA cells

Heart development is a complex process that mobilizes different systems and organs. The catecholamines, such as norepinephrine (NE) and epinephrine (E), are important in cardiac development and function. Cardiac sympathetic innervation follows the development of the cardiac parasympathetic system and does not occur until E12.5 in the murine heart (Fedele & Brand, 2020). It is even later in other mammals, like rats (E16-E17), chick (HH stage 20), and humans (week 5-6)(de Boer et al., 2012; Shigenobu et al., 1988; Végh, Duim, Smits, Poelmann, ten Harkel, et al., 2016). The earliest

formation of adrenal medulla tissue can be traced to E13.5 in mouse hearts(de Boer et al., 2012). The expression of PNMT originating in the adrenal medulla was first detected in rats around E15.5(Teitelman et al., 1979). However, the heart shows reverse conditions. Specifically, adrenaline was first found by Thomas et al. at E10.5 in mouse heart(Thomas et al., 1995). The enzymes involved in the biosynthesis and metabolism of catecholamine also have been discovered in the early developmental chick heart. Tyrosine hydroxylase (TH), which acts as the first rate-limiting enzyme for catalyzing tyrosine to L-DOPA, presents in the early developmental stage in the chick heart before the formation of cardiac innervation(López-Sánchez et al., 2010). Likewise, Ignarro and Shideman group also confirmed the dopamine beta-hydroxylase (DBH), which is responsible for the conversion from dopamine to noradrenaline, was initially found in embryonic chick hearts(Ignarro & Shideman, 1968). Ebert et al. showed the first expression of PNMT in rat heart called back to E9.5 and E8.5 in mouse heart(Ebert et al., 1996, 2008a). Taken together, besides the supply from the sympathetic nervous system and adrenal medulla, the heart should have an intrinsic adrenergic resource that could probably produce the catecholamine and biosynthetic-related enzymes, which emerged from early developmental stages.

In keeping with the facts above, a novel discovery was revealed by Huang et al. that there are also distinct adrenergic cardiac cells and those cells constituted are called ‘Intrinsic Cardiac Adrenergic’ (ICA) cells(Huang et al., 1996). Adrenergic cells are known to be present in peripheral tissues and the central nervous system from which they

primarily regulate sympathetic response to stress stimuli like ‘fight or flight’. ICA cells are specialized non-neuronal cardiomyocytes localized originally in four chambers at the development stage of the heart in embryos but assembled in the left heart in adulthood(Ebert & Thompson, 2001b; Huang et al., 1996; Osuala et al., 2011). ICA cells are around 5-10 μm in diameter, often occurring in a clustered pattern(Huang et al., 2005). They possess catecholamine biosynthetic enzymes and transporters including tyrosine hydroxylase (TH), dopamine beta-hydroxylase (DBH), phenylethanolamine n-methyltransferase (PNMT), and norepinephrine transporter (NET)(Ebert et al., 1996; Huang et al., 1996). ICA cells can biosynthesize, release and uptake norepinephrine. Therefore, they are likely to alternatively contribute to contractile and pacemaker function(Abboud, 1996; Huang et al., 1996, 2005).

Interestingly, ICA cells in mammalian hearts maintain their morphology though they change the localization through from the fetal to the adult stage(Huang et al., 1996, 2005). Substantial explicit vesicles and extensive exocytosis were also observed in these cells under electron microscopy, evident to a secretory function(Huang et al., 1996, 2005; Tamura et al., 2016). It has been suggested that ICA cells may play a role in pathological conditions such as ischemia and left ventricular hypertrophy (Huang et al., 2009, 2010). Huang et al. demonstrated that ICA cells are capable of exclusively expressing and releasing Calcitonin gene-related peptide (CGRP), a type of neuropeptide beneficial to cardiovascular function, in both human and animal models (Huang et al., 2009). The dual stimulation of beta2 adrenergic receptor signaling and

CGRP receptor greatly reduce infarct size by triggering anti-apoptotic pathways during ischemia or reperfusion(Bell et al., 1995; Huang et al., 2007, 2010). A remarkable enhancement of this protective function could be achieved by stimulation of δ-opioid receptor expressed and released from ICA cells(Huang et al., 2009). Besides, ICA cells arose in mammalian hearts long before the formation of sympathetic innervation to serve for adrenergic activity in the embryonic stage and still exist in adulthood for some reason(Ebert et al., 2008b; Ebert & Taylor, 2006; Ebert & Thompson, 2001a; Zhou et al., 1995). Catecholamine-biosynthetic cells subsequently differentiated from neural crest stem cells activate the ICA system mediated by nerve growth factor. Based on these two facts, ICA cells may be involved in the regulation of heart homeostatic function through their capability to biosynthesize, release and uptake norepinephrine and other cytokines. On the other hand, it has been suggested that ICA cells can differentiate into a special group of cardiomyocytes during the embryonic stage(Ebert et al., 2004; Ni et al., 2017a; Osuala et al., 2011; Sun et al., 2019; Y. Wang et al., 2017a), but it is unknown whether adult ICA cells still have such capability.

Pnmt-derived Cardiomyocytes (PdCM)

Pnmt-derived cardiomyocytes (PdCMs) are a new subpopulation of cardiomyocytes reported by our group recently, they are designated as being distinct from ICA cells(Y. Wang et al., 2017b). PdCMs have immunoreactivity for the protein encoded by the pnmt gene, which is a biosynthetic enzyme responsible for conversion of norepinephrine to epinephrine in the last stage of the adrenergic biosynthetic pathway.

During the fetal stage, adrenergic-related enzymes appeared in those cells without expression of sarcomeric α-actinin, which is identified as a myocyte-specific marker. Accordingly, the major characteristic difference between PdCMs and ICA cells is that PdCMs are myocytes with sarcomeric α-actinin positive staining, while ICA cells are not myocytes, being sarcomeric α-actinin staining negative(Huang et al., 1996; Y. Wang et al., 2017b).

The distribution of PdCMs has been visualized by using a genetic mouse line expressing PnmtCre/ChR2-YFP to tracing pnmt expressing cells and their progeny(Y. Wang et al., 2017b). The genetically encoded fluorescence, as well as α-actinin immunofluorescence, provided compelling evidence that those PdCMs are highly concentrated on the left side of the heart as well as conduction system including the sinoatrial node and atrioventricular node(Ni et al., 2017a; Y. Wang et al., 2017b). Intriguingly, there is a notable overlap location between PdCMs and abundant sympathetic innervations, indicating some latent connection with the cardiac sympathetic nervous system(Kvetnansky et al., 2004, 2006; Osuala et al., 2011). Furthermore, PdCMs themselves display unique lateralization that suggests localized adrenergic signaling and cardiac regulation. However, those PdCMs have nearly lost their ability to express *Pnmt* gene by immunofluorescence of Pnmt antibody compared with genetic fluorescence in adulthood stage, which suggested that there was a transient surge of Pnmt expression, which underwent a great decline afterward. Fan et al. propose that PdCMs are possibly derived from ICA cells during the developmental

stage(Sun et al., 2019). However, it is still not clear either at which stages Pnmt expression peaks and declines to correspond with its endocrine function or the potent relationship between the origin of PdCMs and ICA cells.

1.5 Development and application of single cell RNA sequencing in the heart

To fully understand life, the cells that constitute the organs of the body need to be characterised for individual differences, cellular interaction, and coordination, as well as functional mechanism. RNA plays an indispensable role in various biological process, as the transcriptome provides important cues for cell phenotype. Thus, a multi-dimensional and thorough comprehension at the single cell RNA level would provide insights into molecular signatures that are important physiologically and pathologically. Single cell RNA sequencing is a powerful and informative tool for understanding the composition, characteristics and biological mechanism of an organ or tissue at the individual cellular level (Yamada & Nomura, 2020). Conventional bulk RNA sequencing examines average gene expression among the cells in one group and compares them with other groups in different conditions (Lafzi et al., 2018). This method can be usefully applied to samples with identical or similar cellular transcript, telling the attributes of different groups. However, this method covers up the heterogeneity

within one sample, lacking the cellular characteristics(Lafzi et al., 2018). Single cell RNA sequencing (scRNA seq) compensates and improves based on the traditional method. Without identifying cell types by rough morphology or molecules, scRNA seq facilitates accurate cell type identification based on the difference of transcriptional profiles between cells. The development of the heart is complex and elusive with continuous and changeable process. Cardiovascular disease is widely recognized as one of the leading killers that threatens our life. To have a clear understanding of the healthy heart and heart diseases is warranted.

The prerequisite of an effective scRNA seq is that isolation and collection of cells are performed well from the hearts. There are some common platforms used for cell collections. Fluorescence-activated cell sorting (FACS) is a popular and convenient for single cell sorting(Ibrahim & van den Engh, 2007). Scatter and fluorescence were used to sort cells into 96- or 384-plates, filtering dead cells and selecting the cells of interest. Due to the nozzle limit, it is able to filter cells less than 50 μm in diameter. The second platform is called integrated fluidic circuit (IFC) system(Yamada & Nomura, 2020). By isolating cells into individual reaction chambers, IFC automatically allows cell lysis and cDNA preparation. Compared to FACS, it can only isolate cells less 25 μm in diameters but up to 800 cells. Both Drop-seq and Chromium (10x Genomics) are droplet-based methods(Macosko et al., 2015; Yamada & Nomura, 2020). They can profile rapidly thousands of cells by encapsulating each of them into a small droplet, labelling each cell's RNA with a specific barcode and sequencing. The size limit for these two methods

is 30 μm in diameter. Given the high throughput, Drop-seq and Chromium outweigh FACS and IFC. However, compared to the plate-based method, droplet-based methods are poor in detecting genes due to low capture rate of mRNA and higher liability of doublets. Specifically, plate-based systems can capture around 1000-4000 genes, at least twice more than that of droplet-based systems, which is 500-1000 genes. The choice of platform really depends on the weight and balance between number of cells and expected genes for detection and analysis. However, adult cardiomyocytes present big size in morphology (20-40 in width and 80-120 in length), which may block the conventional nozzles and cause transformation and death on cells. Gladka et al. discovered a larger nozzle of FACS which is 130 μm in diameter to perform scRNA seq in murine adult heart and 1000-1500 genes were detected, though bending and death still occurred(Gladka et al., 2018). More training and investigation are needed for sorting larger adult cardiomyocytes.

Single cell RNA sequencing is widely used for murine heart discovery at different stages from embryos to adulthood under healthy and various disease condition models such as transverse aortic constriction (TAC) and ischemia/reperfusion (I/R) mouse models. For example, scRNA seq revealed that Nkx2-5 and Mesp1 play key roles in heart maturation(Lescroart et al., 2018; Xiong et al., 2019). ScRNA seq on TAC model illustrates that macrophage activation is a vital factor for cardiac hypertrophy(Ren et al., 2020; Yekelchyk et al., 2019). Besides the cellular interaction and biological mechanism, scRNA seq is also capable of delineating the temporal change of gene

expression in cellular level. By analyzing the transcriptional change between neighboring cells, developmental trajectory is inferred by pseudotime reconstruction. Trajectory analysis, combined with lineage tracing, shortens the distance between our understanding and the nature of heart development. To conclude, the rapid development of scRNA seq provides novel insight and prospective on how to explore both healthy and pathological hearts.

1.6 Development and application of spatial transcriptomic analysis

To achieve comprehensive molecular understanding of tissues and whole body in healthy and pathological conditions, single cell RNA sequencing technology is far away from providing more accurate information. Spatial transcriptomic approaches are highly complementary and aim to characterize genetic and molecular profiles while retaining the spatial context. The combination of two methodologies brings researchers closer to the expectation of reaching the transcriptome-wide scale at single cell resolution.

Currently there are two popular types of spatial transcriptomics, fluorescence in situ hybridization (FISH) and slide-based spatial transcriptomic sequence, while they both have pros and cons. The former technology is simply based on designated probes, including MERFISH (multiplexed error-robust FISH), seqFISH (sequential fluorescence

in situ hybridization), FISSEQ (fluorescent in situ RNA sequencing), and STARmap (spatially resolved transcript amplicon readout mapping)(K. H. Chen et al., 2015; Eng et al., 2019; Lee et al., 2014; X. Wang et al., 2018). This technology is feasible and operatable with relatively low cost but drawbacks like low capture throughput, limited resolution, and unstable accuracy of spatial information due to the experimental variability cannot be compromised. For example, in fluorescence in situ hybridization-based methods, pre-designed probes target and label the transcripts of interest directly in tissue sections, permitting the local visualization of transcripts in cellular and even subcellular level in a short time. This method provides a fast and effective way to either validate results from other experiments or discover novel cues. However, the number of probes and fluorescence for each slide and experiment is finite to avoid bewildering colors and genes. Slide-based spatial transcriptomics greatly makes up for this. There are also some techniques applied in this method such as Slide-seq, spatial transcriptomics (ST Visium) and DBiT-seq (deterministic barcoding in tissue for spatial omics sequencing)(Y. Liu et al., 2020; Rodriques et al., 2019; Ståhl et al., 2016). These methods adopt barcode-based probes to capture the transcripts in an unbiased mode, presenting wide RNA sequence on the slides. Nevertheless, this technique suffers from unbalance among the sequence resolution, average of gene/transcript per bin and capture rates, let alone the complex procedure and high cost. Moreover, a major bottleneck of scalability is that the sequence area is small and limited (e.g., Visium 42.5 mm2, Slide-seq/Slide-seqV2 7 mm2, and DBiT-seq 25 mm2), requiring a strict preparation for slides.

Recently, Chen et al (A. Chen et al., 2021)reported an improved spatially resolved transcriptomic technology, Stereo-seq (Spatio-Temporal Enhanced Resolution Omics-sequencing), combined billions of firmly packed barcodes in arranged locations with larger captured areas, high captured rate as well as high reproducibility, in which case they also decrease the effect of RNA diffusion(A. Chen et al., 2021). The DNA nanoballs are deposited in a flexible silicon chip on which randomly barcoded sequences are decorated with a series of grid-stacked array of spots where the DNA nanoballs are delicately docked in. Each spot is around 220 nm in diameter and arranged in a center-to center fashion of 500~715 nm. These creative DNA nanoballs enable larger chips involving barcoded probes in a much higher density than any other method reported before. The advancement of Stereo-seq method brings spatial transcriptomic analysis to nanoscale resolution and centimeter level field of view, increasing the sensitivity and minimizing the bin-bin space. Compared with other techniques, Stereo-seq is closer and more accurate to the individual cellular level with locational identity. This greatly and reliably helps for the evaluation of complex tissues and organs with high transcriptomic heterogeneity. Meanwhile, Stereo-seq is identified to increase the throughput and allow the systemic analysis of serial slides from the same tissue in a short time to potentially achieve the goal of 3D reconstruction of gene atlas in tissues and organs of interest. However, it is still a gap in the resolution and other regards between spatial transcriptomics and single cell RNA sequencing. More investigation is needed in this field.

The aim of this thesis is to study the molecular signature and potential physiological functions of catecholaminergic cells, especially *Dbh*$^{+}$ cells, during the development and maturation of murine heart and CCS by using advanced technologies including single cell RNA sequencing, spatial transcriptomic analysis and lineage tracing.

Chapter 2. Materials and Methods

2.1.1 Mouse models

All animal experiments were performed on neonatal or adult mice in accordance with the United Kingdom Animals (Scientific Procedures) Act 1986 and were approved by the University of Oxford Pharmacology ethical committee (approval ref. PPL: PP8557407) and the national guidelines under which the institution operates. Mutant mice (DbhCre/Rosa26-tdTomato, DbhCre/ChR2-tdTomato, DbhCre/ChR2-tdTomato /Cx40EGFP) and wild-type (WT) littermates used in this study were maintained in a pathogen-free facility at the University of Oxford. Mice were given ad libitum access to food and water.

2.1.1.1 Dbh-Cre/ tdTomato mouse model

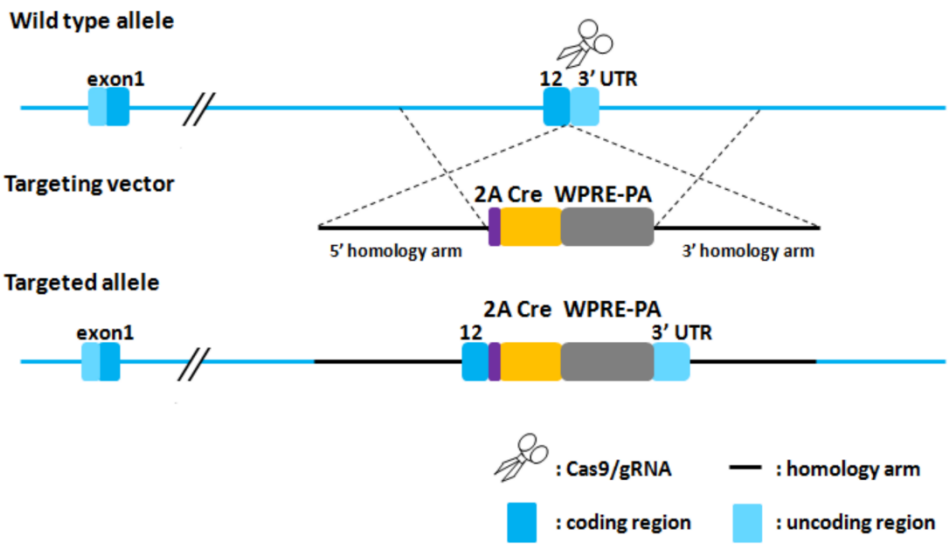

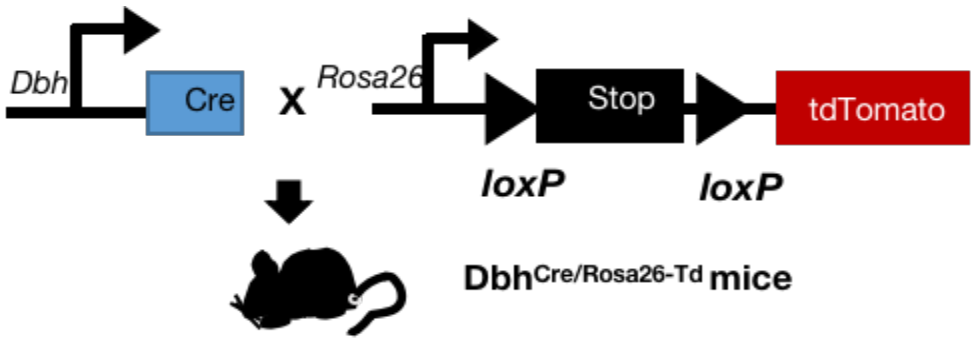

Figure 2.1.1.1 The design strategy of Dbh-Cre/ tdTomato mouse model

The Dbh-Cre mouse model was generated by the Shanghai Model Organisms and the 2A-iCre-WPRE-polyA expression box is knocked in by using CRISPR/Cas9 technology at the stop codon site of the Dbh gene through homologous recombination technology. The brief process is as follows: 1) Cas9 mRNA and gRNA are obtained by in vitro transcription; 2) homologous recombination vector is constructed by In-Fusion cloning method, which contains a 3.0 kb 5'homology arm, 2A-iCre-WPRE- polyA segment and 3.0 kb 3'homology arm; 3) Cas9 mRNA, gRNA and donor vector were microinjected into the fertilized eggs of C57BL/6J mice to obtain F0 generation mice. The positive F0 generation mice identified by PCR amplification and sequencing were mated with C57BL/6J mice to obtain F1 generation mice.

The existing mouse line was previously generated by crossing Dbh-Cre mice with B6.Cg-Gt(ROSA)26Sortm9(CAG-tdTomato)Hze/J strain (Stock No. 007909, Jackson Labs) provided by the Biomedical Service in the University of Oxford.

2.1.1.2 Dbh-Cre/ChR2-tdTomato mouse model

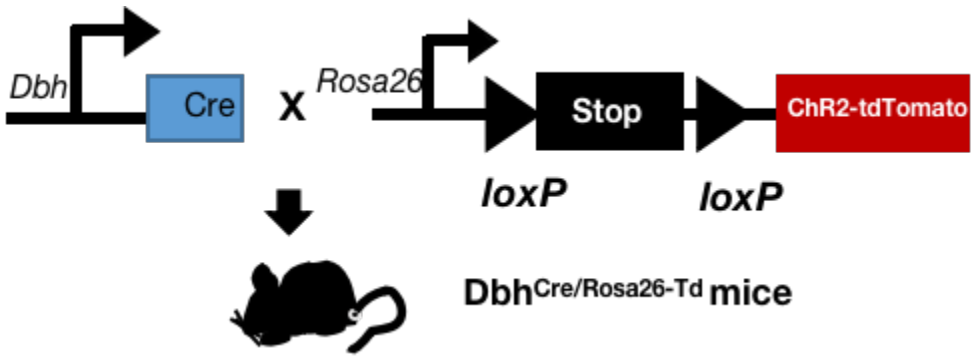

Figure 2.1.1.2 The design strategy of Dbh-Cre/ ChR2-tdTomato mouse model

To label and investigate cells that have expressed or are expressing Dbh gene, we crossed B6.Cg-Gt (ROSA) 26Sortm27.1(CAG-COP4*H134R/tdTomato) Hze/J strain (Stock No. 012567, Jackson Labs) with the above transgenic strain encoding Cre-recombinase under the control of Dbh promoter. The resulting offspring had the STOP cassette deleted in cardiomyocytes, driving the expression of ChR2 [hChR2 (H134R)-tdTomato fusion protein]. ChR2 gene was chosen because if most of Dbh+ cells are cardiomyocytes, optogenetics could be used for substantial evidence and for further cardiac electrophysiology studies.

2.1.1.3 $Dbh^{Cre/ChR2\text{-}tdTomato}$ /$Cx40^{eGFP}$ mouse model

Given that Cx40 protein has been shown to express in the atriums and the conduction system in both its bundle branches and His-Purkinje fibers (PF), plus vascular region,

we crossed our $Dbh^{Cre/ChR2\text{-}tdTomato}$ heterozygous positive mice with a $Cx40^{eGFP}$mouse strain(Miquerol et al., 2004).

2.1.2 Antibodies and RNAscope Probes

Application	Name	Source	Dilution
Immunostaining	Th	Abcam Ab6211	1:200
(antibody)	α-actinin	Abcam Ab9465	1:200
	Pnmt	Antibodies	1:50
	Donkey anti-Mouse 488	Abcam Ab150105	1:200
	Donkey anti-Rabbit 647	Abcam ab150075	1:200
	Mounting-Media Abcam	Abcam Ab104139	
RNAscope	Mm-Bmp10	415921-C1	
(Probe)	Mm-Hcn4	421271-C3	
	Mm-Th	317621-C4	
	Mm-Actn2	569061-C1	
	Opal 520	AKOYA BIOSCIENCES, FP1487001KT	
	Opal 690	AKOYA BIOSCIENCES, FP1497001KT	

2.2.1 Embryo dissection

The entire cardiogenic region was dissected at each time point, including all important developmental stages at E10.5, E11.5, E12.5, E14.5, E16.5, and neonatal stages. Due to the small size of embryos at E10.5, E11.5 and E12.5 stages, the whole embryo was microdissected to ensure complete retrieval of cardiac populations. Embryos were dissected from pregnant mice into cold PBS (Life Technologies, CAT# 14190250), de-yolked and placed in PBS on ice until dissociation. The embryos and cardiac regions were fixed with cold 4% paraformaldehyde (PFA) in 1X PBS for 15-20 minutes. After short fixation, the embryos and heart regions were either stored in 70% ethanol at 4°C for future use or embedded in OCT and frozen on isopentane-dry ice slurry and stored at −80°C. Coronal cryosections (10 µm) were collected on a cryostat (Leica), mounted onto superfrozen glass slides (VWR) and stored at -80°C.

2.2.2 Fixed frozen heart sample preparation

Neonatal or adult mice were transcardially perfused with ice-cold phosphate-buffered saline (PBS). The hearts were then dissected and rinsed with PBS. All tissue samples were fixed with cold 4% paraformaldehyde (PFA) in 1X PBS for no more than 30 min and moved into the 10% sucrose for 1 hour, transferred to 20% sucrose for 1 hour, and

then cryoprotected into 30% sucrose overnight at 4°C. The heart was then embedded in OCT and frozen on isopentane-dry ice slurry and stored at −80°C. Coronal cryosections (10 µm) were collected on a cryostat (Leica), mounted onto superfrozen glass slides (VWR) and stored at -80°C.

2.2.3 Immunofluorescence

Immunofluorescence staining was carried out using the following protocol. Specific chemicals used were shown above. The frozen sections were post fixed in 4% PFA fixation for 15 min at room temperature. The sections were washed in PBS three times and 5 minutes for each wash, followed by permeabilization in 0.1% TritonX-100/PBS for 30 min. After three washes in PBS, the tissue sections were blocked by 0.1% Tween20, 10% Normal serum for 1 hour at room temperature. The sections were then incubated in the primary antibody for overnight at 4°C. The slides were put at RT for 1 hour for recovery. After three washes, the sections were incubated in the secondary antibody for 2 hours. Finally, the mounting medium with DAPI was applied and nail polish was used to seal the slides with coverslips.

2.2.4 Multiplex nucleic acid in situ hybridization (RNAscope ISH)

Each in situ hybridization experiment was replicated at least twice for identifying spatial expression of genes. The fixed frozen tissue slides were thawed at room temperature for 15 min and baked at 60°C for 30 min. Afterwards, slides were post-fixed for 15 min in chilled 4% PFA, and serially dehydrated through 50%, 70%, 100%, and 100% ethanol for 5 minutes each. After drying for 5 minutes, the sections were treated with the RNAscope hydrogen peroxide for 10 minutes. 1X Target retrieval reagent covered the sections for 5 minutes at 95°C, followed by two washes in distilled water. Tissue sections were permeabilized using the protease digestion buffer (ACD Protease III) for 20 minutes. The probes in C1 and C3 channels were labeled by using Opal 520, and 690 fluorophores (Akoya Biosciences, diluted 1:200) respectively. The C4 probe was developed using TSA biotin (TSA Plus Biotin Kit, Perkin Elmer, 1:500). Nuclear staining was performed with DAPI. Imaging was performed on a Zeiss Black software in the Zeiss confocal LSM780 microscope using 10x or 20x air-immersion objectives or 63 water-immersion objectives. The excitation (Ex) laser and emission (Em) filter wavelengths were: DAPI (375nm; 435-480 nm), Opal 520(488 nm; 500-550 nm), Opal 690 (676 nm; 690-700 nm).

2.2.5 Transparent heart preparation

All mice were sacrificed via cervical dislocation in accordance with Schedule I of the Animals Scientific Procedures Act (1986). Before sacrifice, the mice were heparinized by intraperitoneal injection of heparin sodium physiological salt solution (Sigma-Aldrich, 500 U/mL) 0.2ml. The heart was excised, cannulated, and mounted onto a Langendorff system, then perfused (flow rate: 3 ml/min; Watson-Marlow Bredel Peristaltic pumps, model 505S, Falmouth, Cornwall, UK) with Krebs' Ringer (KR) (mM) (NaCl: 119, NaHCO3: 25, Glucose: 10, Na Pyruvate: 2, KCl: 4, MgCl2: 1, KH2PO4: 1.2, CaCl2: 1.8) warmed solution (37 ◦C) for 5-10 mins. Heart was removed from Langendorff system and then flushed with phosphate-buffered saline (PBS) briefly. The heart was fixed by 4% paraformaldehyde (PFA) (Sigma-Aldrich) for 15 mins, followed by PBS wash for 10 mins. The tissue clearing was carried out in dark conditions. 10 ml CUBIC-P (Tokyo Chemical Industry, Product No. T3782) was perfused gently through the aorta to pre-clear the heart tissue for 5 mins. The heart was then transferred to an Eppendorf tube for further clearing by 3 hours incubation in CUBIC-P solution at 4°C, then followed by 24-48 hours of slow perfusion via the coronary circulation system for obtaining a transparent heart with CUBIC-L solution (Tokyo Chemical Industry, Product No. T3740) at 37°C. The heart was washed with PBS for 2 hours. The heart was then immersed in 1:1 distilled water- CUBIC-R solution (Tokyo Chemical Industry, Product No. T3741) dilution with gentle shaking at rate of 50 rpm at room temperature for 24 hours for refractive index matching. Finally, the heart was

stored in CUBIC-R+ solution at room temperature for up to three months.

2.2.6 Lightsheet imaging

The imaging data was acquired by the Zeiss Light Sheet fluorescence microscope Lightsheet 7 (ZEISS Inc, Germany). 3D visualization and reconstruction were done using ZEN (ZEISS Imaging Software). The illumination objective EC Plan-Neofluar 5x/0.1 foc was used. Excitation of the fluorophore was done by using a 561 nm Laser with dual side successive illumination. Imaging objective was 5x/0.16 foc with 1.6x camera adapter, plus system optical zoom. The raw video was recorded directly after the illumination without using other processing software. The thickness for PdCM and HCN4 hearts are 6.113 mm and 8.352 mm respectively. The total magnification was 4.22. Emission filter band pass was 575~615 nm. The camera exposure time was 7.5 ms and pixel size was 1.54 × 1.54 × 4 µm3. The raw images were recorded and stitched together before 3D structure reconstruction. 3D iterative deconvolution was applied. By applying the maximum intensity, the reconstruction of whole cardiac architecture was achieved to present clearly Tdtomato fluorescence by contrast with background area in the transparent heart. The depth color code was employed to detect the depth of the signals which provided an accurate location of fluorescence in both epicardium and endocardium indicated by the color spectrum.

2.2.7 NE trace

Mice were sacrificed via cervical dislocation in accordance with Schedule I of the Animals Scientific Procedures Act (1986). Before sacrifice, the mice were heparinized by intraperitoneal injection of heparin sodium physiological salt solution (Sigma-Aldrich, 500 U/mL) 0.2ml. The heart was excised, cannulated, and mounted onto a Langendorff system, then perfused (flow rate: 3 ml/min; Watson-Marlow Bredel Peristaltic pumps, model 505S, Falmouth, Cornwall, UK) with Krebs' Ringer (KR) (mM) (NaCl: 128, NaHCO3: 21.98, Glucose: 11, KCl: 4.8, MgCl2: 1, CaCl2: 1, after 30 minutes oxygenation) warmed solution (37°C) for 5-10 minutes. The compound uptake was initiated by perfusion of experimental media (containing FFN270 probe prepared from a 10mM stock solution in DMSO, with a final probe concentration of 20 µM in the uptake assay) at 37°C. To investigate the inhibitory effect of nomifensine on uptake probe, the heart was perfused with Krebs solution containing the inhibitor (20 µM, prepared from a 10mM stock solution in DMSO) for 30 minutes, followed by the perfusion of experimental media for another 30 minutes at 37°C. After the perfusion, the heart was rinsed by Kreb's solution for 5-10minutes and dissected for imaging. The imaging was performed on a Zeiss Black software in the Zeiss confocal LSM780 microscope using 10x air-immersion objectives and the BFP channel was selected.

2.2.8 3D reconstruction of the heart

Three-dimensional image reconstruction was conducted to present the spatial architecture and morphology of cell distributions at the microscopic level (around μm) for the whole heart. The method was based on a modified procedure of our previous approach [1] to produce fluorescence images of multiple coronal slices of adult and neonatal murine cardiac tissue. To establish a 3D atlas of the whole heart with detail of spatial distribution of positively and negatively labelled cardiac cells, each two-dimensional (2D) fluorescence image was first pre-processed for registration, segmentation, and enhancement before final fusion for 3D reconstruction of the adult and neonatal hearts. The chart flow of the process is shown in Figure 2.2.8 for image preprocessing, contrast enhancement, image merge, frequency analysis, and 3D reconstruction.

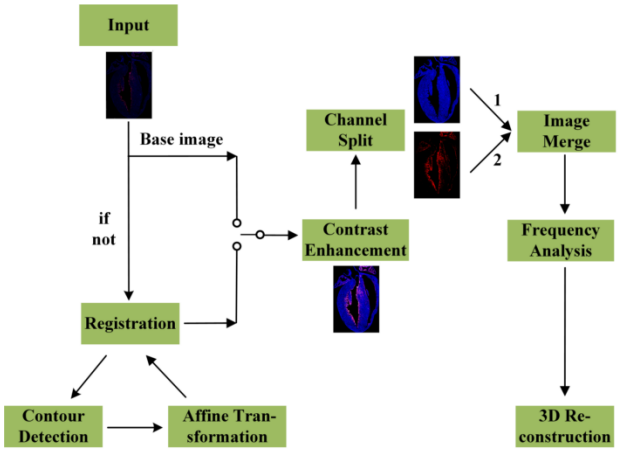

Figure 2.2.8. Chart flow of the 3D reconstruction process. All raw fluorescence images were set as the input. Except for the base image, all other images were registered to the base image first before contrast enhancement. Then informational signals for different fluorescence colours were split into different channels for characterising their

specific spatial distribution before frequency analysis and 3D reconstruction were made. Label 1: Hole Filling and Pixels Unification; Label 2: Pixels Unification.

Input: Raw 2D fluorescence images from adult and neonatal mouse heart slices were used after spatial resolution between the two groups were unified (the resolution of the adult mouse cardiac images was downsized as they are about 20-fold of those of the neonate ones).

Registration: Registration involves two steps: the contour extraction and the affine transformation. To account for the distinctively dispersed cell spatial distribution in the raw images, the Flood Fill algorithm was used to calculate numerous limited bounded regions, which corresponded to the position of holes. Once the positioning process was completed, a bitwise NOT inverted operation was performed to generate a new matrix, which was then logically computed with the raw image matrix to achieve the hole filling target. Finally, the Sobel operator method was utilized to construct a base-image emphasizing edge, following which the new edge was then added to the former layer of each image to execute the affine transformation (rotation and translation) process.

Contrast Enhancement: By modifying relative parameters gain (γ) and bias (β) in the following equation, we were able to optimize image features and boost color contrast using a common linear transformation method:

$$g(x,y) = \gamma f(x,y) + \beta$$

In this equation, $f(x,y)$ is the input pixel value, $g(x,y)$ is the processed pixel value, the gain parameter γ is used to increase contrast ratio, and the bias parameter β is

used to control brightness. The gain variable in this section was chosen from 1 to 3 depending on multiple visual attributes, whereas the bias factor was typically higher than 50. The performance of enhanced method is illustrated for adult mouse heart and neonatal mouse heart in chapter 5.3.

Channel Split: Once the multiple RGB images were enhanced, channel split measures were taken to separate them into red, green, and blue channels to implement the pixel aggregation operation.

The specific procedures are the following: On the one hand, repeated the Hole Filling method (see the registration method) based on the blue channel and reassign all pixel values to 40 to create the basic contour. On the other hand, extracted red and blue channels and rewrite these pixel values separately to 180 and 10, and then clear the green channel values.

Image Merge: To construct the processed image and carry out a series of canonical images, we further merge these images with the same weight mechanism. Each image has a light grey base color for the heart profile and a bright color for a positive fluorescence cell, as seen in Fig.3B.

Frequency Analysis: With the purpose of quantifying the pretreatment process, in this study we implemented the frequency analysis before 3D model building.

3D Reconstruction: Finally, all images were written to the same data file of VTK format. For this section, we used Matlab to build the adult and neonatal anatomical results, which have been exhibited in Chapter 5.3

2.2.9 Sample preparation for transmission electron microscopy (TEM)

The Dbh-Cre/tdTomato positive (week8) mouse heart and adrenal tissue were harvested and examined under a fluorescent microscope to select the region showing tdTomato fluorescence. The tissues were fixed in 5% potassium dichromate/chromate pH 5.6 with the addition of formaldehyde to 4% for 48 hours at 4°C. Samples were then extensively washed in running deionized water overnight to remove any unstained solution, and stored at 4% formaldehyde before fully dehydrated through graded propan-2-ol (15 minutes each in 50%, 70%, 90%, 2 × 100%), infiltrated with LR White acrylic resin (30 minutes each in 50% LR White in propan-2-ol, 4 × LR White) and polymerized at 50 °C for 24 hours.

For light microscopy, 0.35 µm thick sections were stained with 0.1% toluidine blue in borax buffer. Sections were examined with an Olympus BX51 research light microscope (Olympus Optical Co Ltd., London, U.K.) and images captured with a Zeiss Axiocam digital camera and Axiovision software (Carl Zeiss Vision GmbH, Hallbergmoos, Germany).

For TEM examination, 100 nm thick sections were collected onto 150 mesh formvar/carbon-coated copper grids, stained with 2% uranyl acetate, and coated with a few nanometers layer of evaporated carbon to eliminate charging. For metal particle morphology, the samples were observed by a JEOL JEM2000 TEM (JEOL, Welwyn

Garden City, UK), with STEM and EDAX Genesis 4000 Energy Dispersive X-Ray Spectrometry (EDAX, Leicester, UK) using 100 kV. Images were collected using a Getan Orius (11 megapixels) in-line digital camera (Gantan Inc. Abingdon, UK).

2.2.10 Optical voltage and Ca2+ mapping

To investigate the global Ca2+ and voltage characteristics of atrial tissue or ventricle, either Langendorff perfused heart or atria were prepared. Blebbistatin, a myosin II inhibitor, was applied to stop contractions and avoid movement artefacts. Tissue was incubated with blebbistatin at a concentration of 10 μ M for 45 min. After cessation of contractions, tissue was loaded with the acetoxymethyl (AM) ester of rhod-2 (45 min loading of 4 μ M dye in static, oxygenated solution) to measure cellular Ca2+, and with RH237 (applied to tissue by bolus of 36 μ l at 2 mM concentration over 5–7 mins) to measure membrane voltage. Ca2+ and voltage dyes were both excited by light at 530 nm, and emitted light at 581 nm and 782 nm respectively. Signals were filtered to separate Ca2+ and voltage channels with a 570 nm long pass optical filter and a 625 nm long pass dichroic mirror and, followed by analysis using Metamorph software (Molecular Devices). Light pacing pulses were delivered to the epicardial surface of the atrium and pacing protocols were applied. Tissues were imaged at a frame rate of 1 kHz for 2–3 s during and immediately after each pacing interval is applied. A temperature of 37 °C was maintained throughout this method. Image files were

analyzed to assess wave-speed, changes in action potential and calcium transient characteristics.

2.2.11 Single-cell transcriptomic analysis using the 10X Genomics Chromium

The single cells were either isolated from embryos at E8.5 and E10.5 stages, or embryonic hearts at E12.5, E14.5 and E16.5 stages, and neonatal mouse cardiomyocytes (from P3) using the standard enzymatic method described previously (Liu et al., 2011). Single-cell suspension samples were quality tested, quality control standards: cell activity > 80%, cell concentration 700-1200 cells / sL, cell diameter 5-40 m, the total number of cells up to 500,000. Single cells were prepared following the protocol from 10× Genomics, Inc (Pleasanton, CA). The protoplast suspension was loaded into Chromium microfluidic chips with 30 (v3) chemistry and barcoded with a 10× Chromium Controller (10× Genomics). RNA from the barcoded cells was subsequently reverse-transcribed and sequencing libraries constructed with reagents from a Chromium Single Cell 30 v3 reagent kit (10× Genomics) according to the manufacturer's instructions. Sequencing was performed with Illumina HiSeq according to the manufacturer's instructions (Illumina). FastQC was used to perform basic statistics on the quality of the raw reads.

Raw reads were demultiplexed and mapped to the reference genome by 10× Genomics Cell Ranger pipeline (https://support.10xgenomics.com/single-cell-geneexpression/) using default parameters. All downstream single-cell analyses were performed using Cell Ranger and Seurat(Macosko et al., 2015; Satija et al., 2015) unless mentioned specifically. In brief, for each gene and each cell barcode (filtered by CellRanger(Macosko et al., 2015), unique molecule identifiers were counted to construct digital expression matrices in detail: cellranger count takes FASTQ files performs alignment, filtering, barcode counting, and UMI counting. It uses the Chromium cellular barcodes to generate feature barcode matrices.

Initial cell typing in single-cell RNA sequencing data

To ensure robust and reliable transcriptomic signal-to-noise ratios, without impairing sensitivity to small signals, we filtered out all cells with unique RNA counts (nUMI) <300, or distinct genes (nFeatures) <270 to remove under-sampled cells and simple cells such as erythrocytes. The ratio of mitochondrial transcripts to nuclear genome-derived transcripts is often used as a metric of cell stress or quality in single-cell RNA sequencing. 5% is typically used as a ceiling, but this is not supported across cell types and can fail to identify damaged cells, particularly cardiomyocytes, which can reach ~30% [Osorio 2021 Systematic determination of the mitochondrial proportion in human and mice tissues for single-cell RNA-sequencing data quality control] and exclude particular cardiomyocyte populations(Galow et al., 2021). Given the changing nature of mitochondrial biogenesis across the embryonic to postnatal mouse

heart(Zhao et al., 2019), we utilized a dynamically changing filter for mitochondrial transcript ratios: E8.5: 5%, E10.5: 5%, E12.5: 7.5%, E14.5: 10%, E16.5: 15%, P3: 20%. We normalized cell libraries through SCTransform, which accounts for preservation of differential variation between highly variant and lowly variant genes(Hafemeister & Satija, 2019). We utilized Uniform Manifold Approximation and Projection (UMAP), following principal component analysis (PCA) and PCA dimension selection, to enable human-interpretable visualization of the transcriptomic space through dimensionality reduction. We visually examined the data for differences between batches of cells collected at each stage. Only P3 had significant batch differences. There are extensive suggested solutions for 'correcting' batch differences(Tran et al., 2020). However, from a statistical fundamentals perspective both a priori and empirically, such methods have been shown to produce aberrant downstream results(Nygaard et al., 2016). We visualized UMAP in 3D and used Louvain clustering, and labelled clusters based on expression profiles. Further sub-clustering was performed as necessary, and a small number of cells were manually assigned where appropriate. The above was done using Seurat functions unless specified(Satija et al., 2015).

Identification of Dbh^{+} cardiomyocytes

To improve the discrimination of cardiomyocyte-lineage specific cell types in the transcriptomic space, we isolated the cardiomyocyte-lineage cell types identified transcriptomically: Cardiac Progenitors, Early Cardiomyocytes, Immature Atrial Cardiomyocytes, Immature Ventricular Cardiomyocytes, Cardiac Conduction System,

ECM Atrial Cardiomyocytes, ECM Ventricular Cardiomyocytes, Atrial Cardiomyocytes, Ventricular Cardiomyocytes, and Myh6^{+} Ventricular Cardiomyocytes. We then re-normalised their raw nUMI counts, using SCTransform, and used PHATE(Moon et al., 2019) for dimensionality reduction and clustering. PHATE preserves global and local structure in the transcriptomic space of genes observed across cells: enabling intuitive interpretation of datasets, particularly so for 'lineage' type datasets in our experience. Cell types were assigned by comparison with literature expression profiles. We used the parallel implementation of Seurat's FindMarkers[https://github.com/vertesy/Seurat.multicore], implemented with min.pct =0.2, logfc.threshold=0.5, and test.use='bimod' to compare differential gene expression between cell types. In selecting Dbh^{+} cells from this lineage, we isolated all cells from the cardiomyocyte lineage with a raw nUMI for Dbh > 0. We then re-normalised these cells, using SCTransform, and performed PHATE dimensionality reduction. We used cell labels identified from the cardiomyocyte-lineage. To identify whether Dbh expression (defined as UMI>0 or UMI=0) was independent of cell type, we performed a two-tailed Chi Squared test for independence, using only cardiomyocyte lineage cell types composed primarily of cells beyond E10.5, as before this Dbh expression was extremely limited in cell types. Therefore, we excluded Heart fields, Endocardial-gene rich cardiomyocytes, Developing cardiomyocytes, and Primary heart tube from testing.

Gene Ontology analysis

For each of the cardiomyocyte lineage CCS cell types (Sinoatrial Node, Atrial Conduction System, Atrioventricular Node, and Purkinje Fibres), we used SCTransform to identify the top 9000 most highly variable genes in each cell type and used these for downstream analysis. For each cell type, we split the cells between those with a raw nUMI Dbh >0, and Dbh =0, which we labelled as Dbh^+ and Dbh^- as previously. We used the parallel implementation of Seurat's FindMarkers[https://github.com/vertesy/Seurat.multicore], implemented with min.pct =0, logfc.threshold=0, and test.use='bimod' to compare differential gene expression between the Dbh^+ and Dbh^- groups in each cell type. For each cell type we then used the TopGO implementation within the ViSEAGO package(Brionne et al., 2019), with a node size of 5 annotating 'biological processes' to the differentially expressed genes. We than used the TopGO implementation of the Kolmorgorov-Smirnov test, using the 'classic' algorithm argument, and a significance cut-off value of 0.01, to test for enrichment. We then merged the enrichment results and identified semantic similarity between terms, using the ViSEAGO implementation of the Wang gene ontology graph topology-based method. We then used ViSEAGO visualization functions and ggplot2 to visualise the data.

2.2.12 Spatial transcriptomic analysis

Tissue Collection

Hearts at different stages (E12.5, E14.5, P3, and adult (week 8)) were dissected from the wild type or Dbh^{Cre}/Rosa26-tdTomato mice and washed with PBS quickly, for adult heart dissection, the mice were killed by schedule 1, the heart was dissected and perfused with PBS solution through the aorta and rings collected after embedding in Tissue-Teck OCT (Sakura, 4583). The samples were embedded in OCT and frozen on isopentane-dry ice slurry and stored at −80°C. Cryosectioning was performed with Leica CM1950 cryostat and the sections were cut with 10 μm thickness. Then the tissue sections were adhered to Stereo-seq chips immediately for the following experiments. Adjacent sections would be adhered to a glass slide to check tdTomato fluorescence.

Stereo-seq experiment

Stereo-seq library preparation and sequencing were previously described(A. Chen et al., 2021). After tissue sections were adhered, Stereo-seq chips were incubated at 37 ℃ on a slide dryer for 3 min. Then the chips were immersed in prechilled methanol for 30 min. After fixation, tissue sections were stained with ssDNA reagent (Invitrogen, Q10212) for 5 min, and then washed using 0.1× SSC buffer (Ambion, AM9770) supplemented by 0.05 U/μl RNase inhibitor (0.1× SSC+RI). The ssDNA images were captured with Ti-7 Nikon Eclipse microscope using FITC channel. After imaging, tissue permeabilization was performed with 0.1% pepsin (Sigma, P7000) in 0.01 M HCl buffer

(pH = 2) at 37 ℃ incubator for optimal time, which is 6 min for E12.5, E14.5 and P3 heart sections, and 18 min for adult heart sections. After washing with 0.1× SSC+RI, Reverse transcription was performed with SuperScript II (Invitrogen, 18064014, 10 U/μL reverse transcriptase, 1 mM dNTPs, 1 M betaine solution PCR reagent, 7.5 mM MgCl2, 5 mM DTT, 2 U/μL Rnase inhibitor, 2.5 μM Stereo-TSO and 1× First-Strand buffer) at 42 ℃ incubator for overnight. After washing twice with 0.1× SSC buffer, tissues on the chip surface were digested with Tissue Removal Buffer (10 mM Tris-HCl, 25 mM EDTA, 100 mM NaCl, 0.5% SDS) at 37 ℃ incubator for 30 min. After washing with 0.1× SSC buffer for two times, the chips were treated with Exonuclease I (NEB, M0293L) at 37 ℃ incubator for 1 h. After washing once with 0.1x SSC buffer, cDNA was amplified using KAPA HiFi HotStart Ready Mix (Roche, KK2602) with 0.8 μM cDNA-PCR primer. For library preparation, cDNA products were further fragmented using in-house Tn5 transposase, amplified with KAPA HiFi HotStart Ready Mix, and purified using AMPure XP beads (Beckman Coulter, A63882). The purified PCR products were used to make DNBs (DNA nanoballs) which were sequenced with a MGI DNBSEQ-Tx sequencer.

Stereo-seq data analysis

Raw data processing method was carried out as previously described(A. Chen et al., 2021). Briefly, CID and MID were extracted from the forward reads, and the cDNA sequences were extracted from the reverse reads in the FASTQ files from MGI DNBSEQ Tx sequencer. CID mapping allows 1 base mismatch. MID reads with N bases or more than two low quality score bases (score < 10) were removed. The remaining DNA reads

were aligned using STAR against the reference mouse genome (mm10) supplemented with WPRE sequences obtained from transgenic plasmid. To each gene of each CID, reads with same MIDs were only kept one for counting. After annotation and count, gene expression matrices with CID were generated.

Unsupervised clustering.

Gene expression matrices were divided into bins with 20 × 20 DNBs for E12.5, E14,5, and P3 hearts, and 50 × 50 DNBs for adult heart. Density plotting was used to visualize the gene count distribution in each bin, and the minor peak containing bins with low gene counts were excluded. Genes expressed in fewer than 5 Bins were also discarded. After obtaining the final gene expression matrices of bin20 or bin50, data for all slices including three E12.5 slices, six E14.5 slices, and six P3 slices were merged to do the unsupervised clustering using Seurat. Briefly, SC Transform function was used to normalize the data and variable genes were identified. Then Run PCA was used for dimension reduction and run UMAP was used to indicate the two-dimensional projection with dims= 30. FindNeighbors and FindClusters were further used to identify clusters. Find All Markers was used to identify the differentially expressed genes for each group with the parameters: min.pct = 0.1, logfc.threshold = 0.25. Each cluster was annotated using several known cell type-specific marker genes. We assigned cluster labels using gene expression profiles and bin location. For grouping as ‘AM’, ‘AM-CCS’, ‘VM’, and ‘VM-CCS’, the following cell labels were combined respectively: atrial myocardium, atrioventricular junction; sinoatrial node,

atrioventricular node; ventricular myocardium, compact ventricular myocardium, trabecular ventricular myocardium, ventricular septum myocardium; His fibres and bundle branches.

Integration of single cell and spatial transcriptomic data

To elucidate probabilistic spatial distributions of our cell types identified in our single -cell RNA sequencing data; we combined cells identified from the cardiomyocyte lineage with those identified in the wider dataset, to give a representative transcriptional reference library of potential cell types in the developing murine heart from E12.5 to P3. We combined: Atrial Cardiomyocytes, Ventricular Cardiomyocytes, Immature Atrial Cardiomyocytes, Immature Ventricular Cardiomyocytes, Immature Trabecular Ventricular Cardiomyocytes, Trabecular Ventricular Cardiomyocytes, Sinoatrial Node, Atrioventricular Node, Purkinje Fibres, Fibroblast-like, Smooth Muscle-like, Endothelium, Epicardium, Endocardium, Neural Crest, Haematopoetic Precursors, Immune Cells, and Platelets. We re-normalised the raw nUMI of this library using SCTransform. To identify specific and robust marker genes for each cell type, we used SMASH(ME et al., 2021), and in brief, kept the top 50 genes that contributed most to the classification of each cell type through identifying gene-wise Gini importance from the trained supervised ensemble machine learning classifier algorithm.

For grouping as ‘AM’, ‘AM-CCS’, ‘VM’, and ‘VM-CCS’, the following cell labels were combined respectively: atrial cardiac conduction system; sinoatrial node,

atrioventricular node; trabecular ventricular cardiomyocytes; Purkinje fibres.

Chapter 3. Single cell RNA sequencing analysis depicts the developmental transcriptome of the murine cardiac conduction system and identifies *Dbh*+ cells

The cardiac conduction system (CCS) plays an essential role in cardiac physiological function by initiating and coordinating cardiac contraction. The CCS comprises a set of distinct specialized components including pacemaker sinoatrial node (SAN), the coordinating atrioventricular node (AVN) and the rapid transmission ventricular His–Purkinje system(van Eif et al., 2018). Failure in correct development of CCS components leads to several fast (e.g. Wolff-Parkinson-White syndrome) and slow dysrhythmic (atrioventricular block and sick sinus syndrome) diseases(Mohan et al., 2018). Gaining insight into the developmental processes and the cell populations involved in the morphogenesis of the CCS is critical for understanding the pathogenesis of these dysrhythmias(Mohan et al., 2018). However, our understanding of when and how diverse cell types arise to form different components of the CCS remains limited(van Eif et al., 2018).

Recent refinement of transcriptomic technologies including Single-cell RNA sequencing (scRNAseq) and spatial transcriptomics has facilitated the interrogation of cell populations with increasing classification power, revealing and characterizing novel cell types. Given the complexity and incomplete understanding of CCS morphogenesis, it is important to establish a molecular approach that enables

simultaneous analysis of global organ-wide spatial gene expression patterns and without biasing against cellular heterogeneity.

In this chapter, by using single cell RNA sequencing technology, I established the transcriptional landscape of cardiac cell types, especially the cardiac conduction system, populating the developing murine heart from E8.5 to postnatal stages. And a previously unreported catecholaminergic cardiomyocyte populations was revealed which contributes to the developing and mature murine cardiac conduction system. The molecular signature and potential functions are discussed in this chapter.

3.1 Isolation of single cells from embryonic hearts for single-cell RNA sequencing analysis

We isolated and collected the single cells from embryos or hearts at six developmental stages including E8.5, E10.5, E12.5, E14.5, E16.5 and postnatal P3. E8.5 and E10.5 embryos were dissected from the uterus of pregnant mice and were digested by 0.25% trypsin after removing head and limbs. The hearts from the stages of E12.5, E14.5, E16.5 and P3 were dissected directly from the embryos and postnatal mice, followed by the trypsin digestion. During the preparation of single cell suspension, cell activity and concentration were detected by staining with 0.4% trypan blue. After primary

quality control, cell activity was adjusted to the appropriate concentration for 10x single-cell transcriptome sequencing. ScRNA-Seq was done by 10x Genomics Nova-Seq (Fig 3.1.1). After pre-processing and library quality control, the raw sequencing data was obtaining as BCL format and the FastQC was used to evaluate the quality of the original data. Cell Ranger used the star comparison software to compare the previously generated FastQ sequencing data to the reference genome for Cell and UMI counting to generate the cell-gene expression matrix.

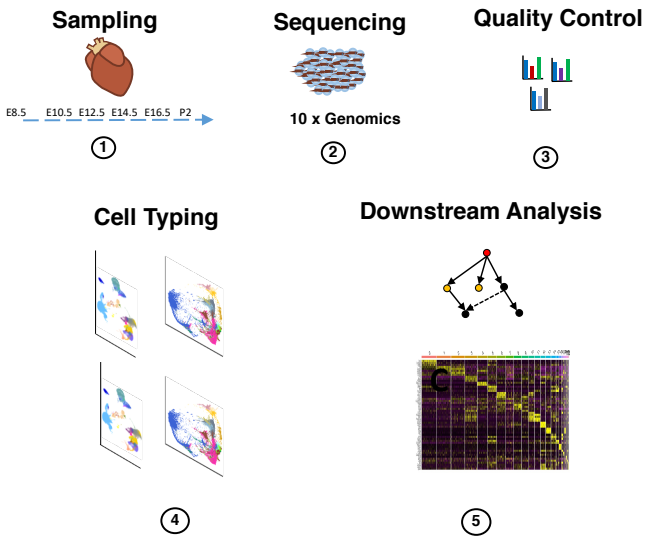

Figure 3.1.1 Summary of workflow. Whole embryos (E8.5, E10.5) or whole hearts (E12.5, E14.5, E16.5, P3) were sampled for single cell RNA sequencing, followed by clustering based on gene expression and a range of downstream analyses.

Figure 3.1.2 A-F showed the fastq quality control for the raw data. The horizontal axis represents the location of the base, and the read length of sequences is 150bp. The vertical axis represents the quality of sequencing, from top to bottom are green, yellow, and red, corresponding to best, good, and poor quality. Shown from Figure 3.1.2, the

quality for six stages is all of good condition, which is generally acceptable. The quality of base content was also checked. As illustrated in Figure 3.1.3A-F, the x axis represents the base content and y axis represents the percentage of base content. Green, red, blue, and black correspond to bases A, T, C, and G, respectively. Reads were basically stable during the entire sequencing process, and no large separation appeared between A-T and G-C, in which case the base content distribution of all samples is normal and acceptable. A total of 175237 cells were isolated and sequenced from either whole embryos (E8.5 and E10.5, n=10 embryos x 2 batches for each stage) or whole hearts (E12.5 to P3, n =10 hearts x 2 batches for each stage), which generally correspond to mid-to-late developmental stages of murine heart.

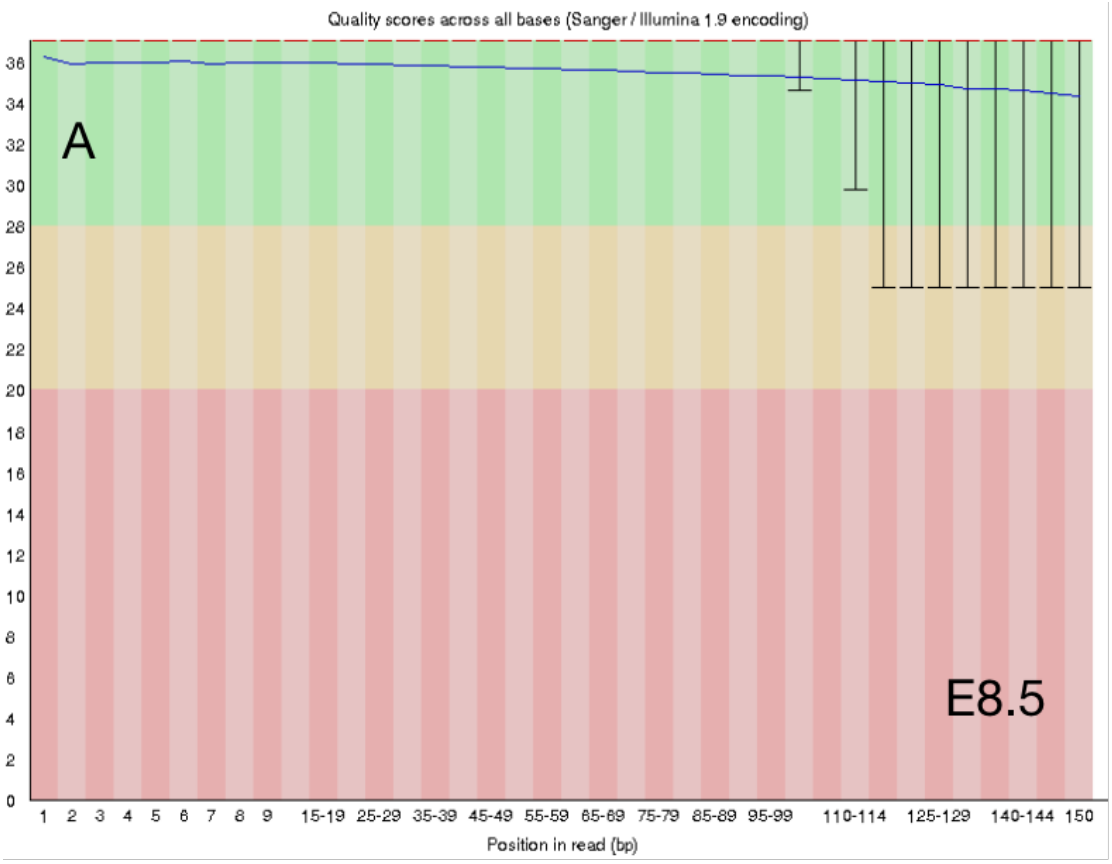
Quality scores across all bases (Sanger / Illumina 1.9 encoding)
A
E8.5
Position in read (bp)

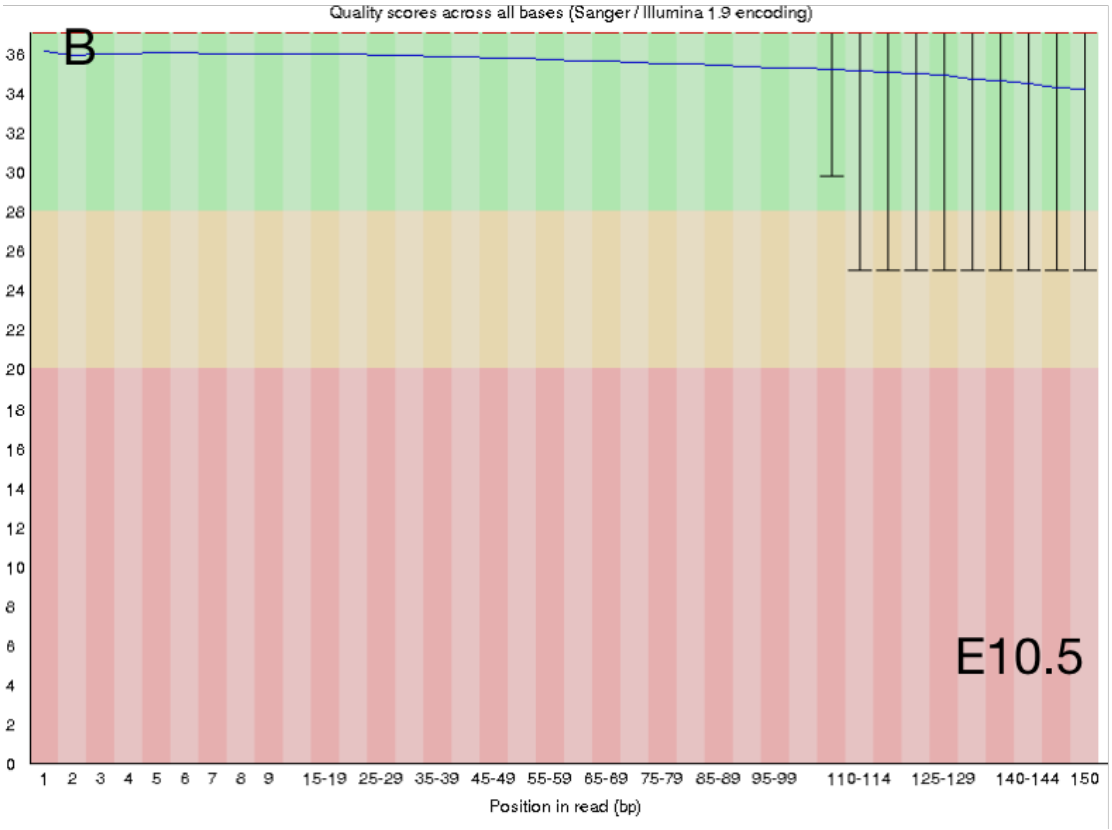
Quality scores across all bases (Sanger / Illumina 1.9 encoding)
B
E10.5
Position in read (bp)

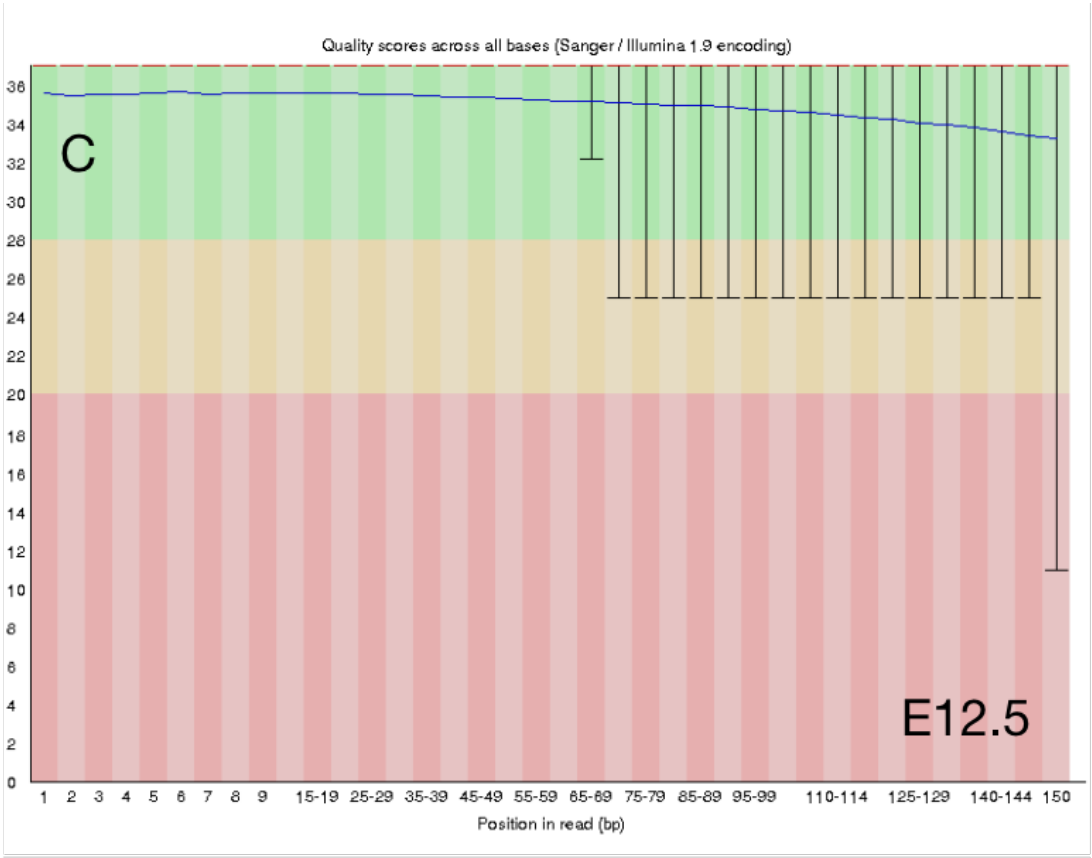
Quality scores across all bases (Sanger / Illumina 1.9 encoding)
C
E12.5
Position in read (bp)

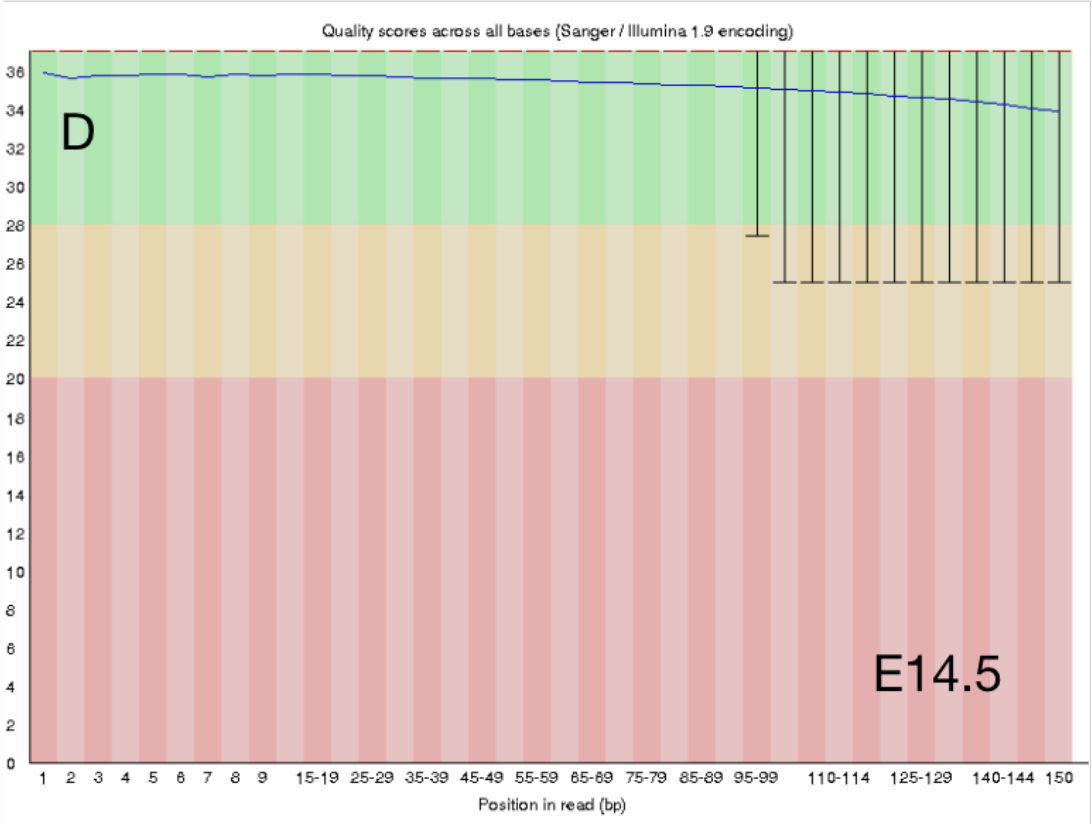
Quality scores across all bases (Sanger / Illumina 1.9 encoding)
D
E14.5
Position in read (bp)



Figure 3.1.2 The distribution of base quality of raw data at different stages. A: E8.5; B: E10.5; C: E12.5; D: E14.5; E: E16.5; F: Postnatal P3. The X axis is the position of bp from

1 to 149. The Y axis is the quality score (Q = -10*log10 (error P)). The red line is median and blue line is mean value. The green, yellow and pink areas represent good, moderate and poor quality.

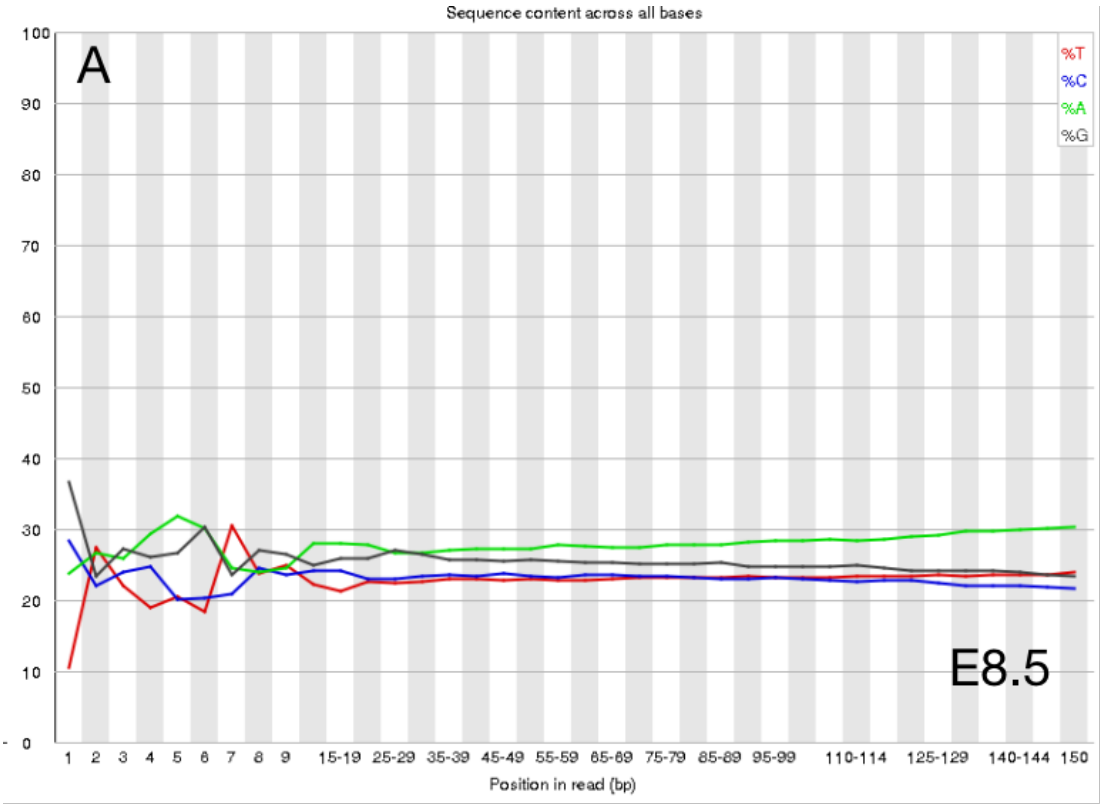
Sequence content across all bases
A
%T
%C
%A
%G
E8.5
100
90
80
70
60
50
40
30
20
10
0
1 2 3 4 5 6 7 8 9 15-19 25-29 35-39 45-49 55-59 65-69 75-79 85-89 95-99 110-114 125-129 140-144 150
Position in read (bp)

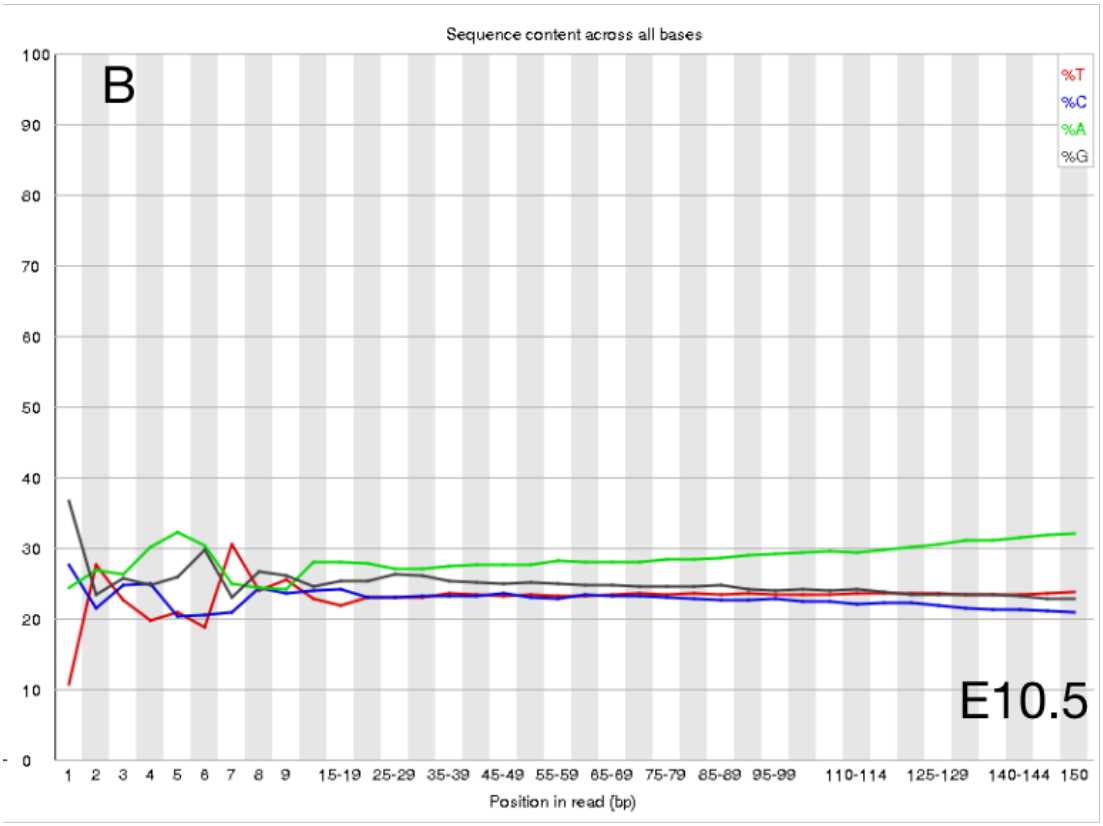
Sequence content across all bases
B
%T
%C
%A
%G
E10.5
100
90
80
70
60
50
40
30
20
10
0
1 2 3 4 5 6 7 8 9 15-19 25-29 35-39 45-49 55-59 65-69 75-79 85-89 95-99 110-114 125-129 140-144 150
Position in read (bp)

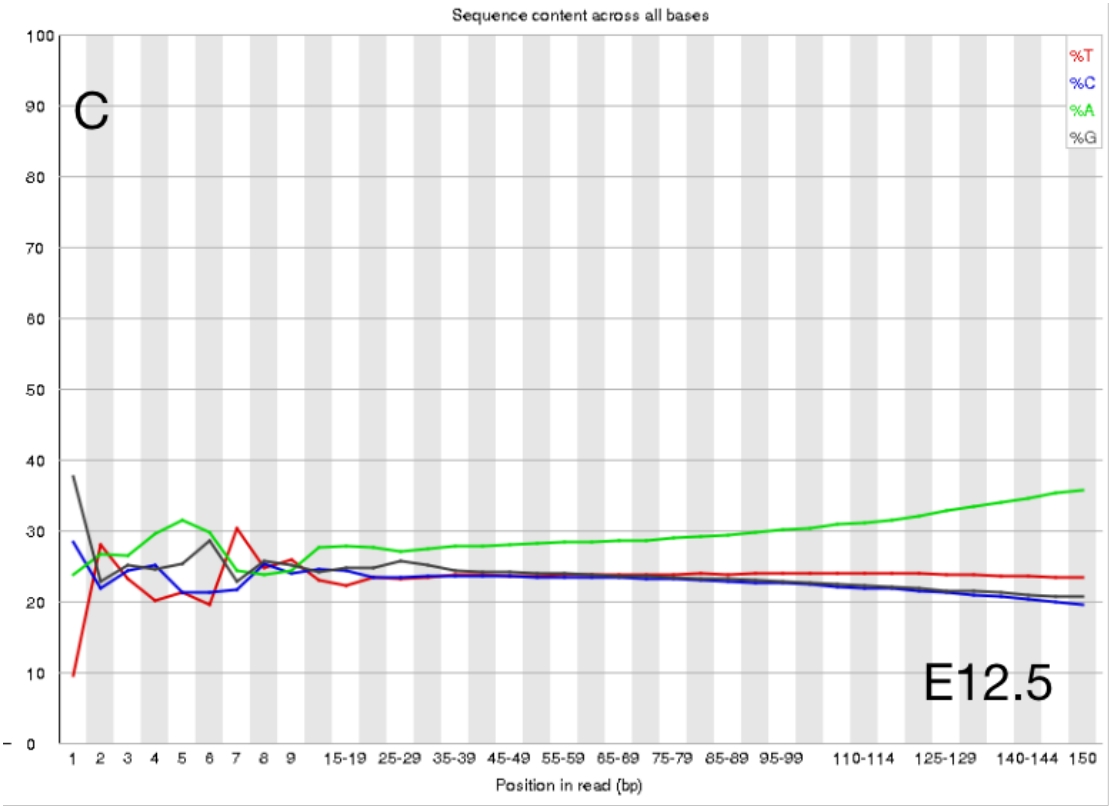
Sequence content across all bases
C
E12.5
%T
%C
%A
%G
100
90
80
70
60
50
40
30
20
10
0
1 2 3 4 5 6 7 8 9 15-19 25-29 35-39 45-49 55-59 65-69 75-79 85-89 95-99 110-114 125-129 140-144 150
Position in read (bp)

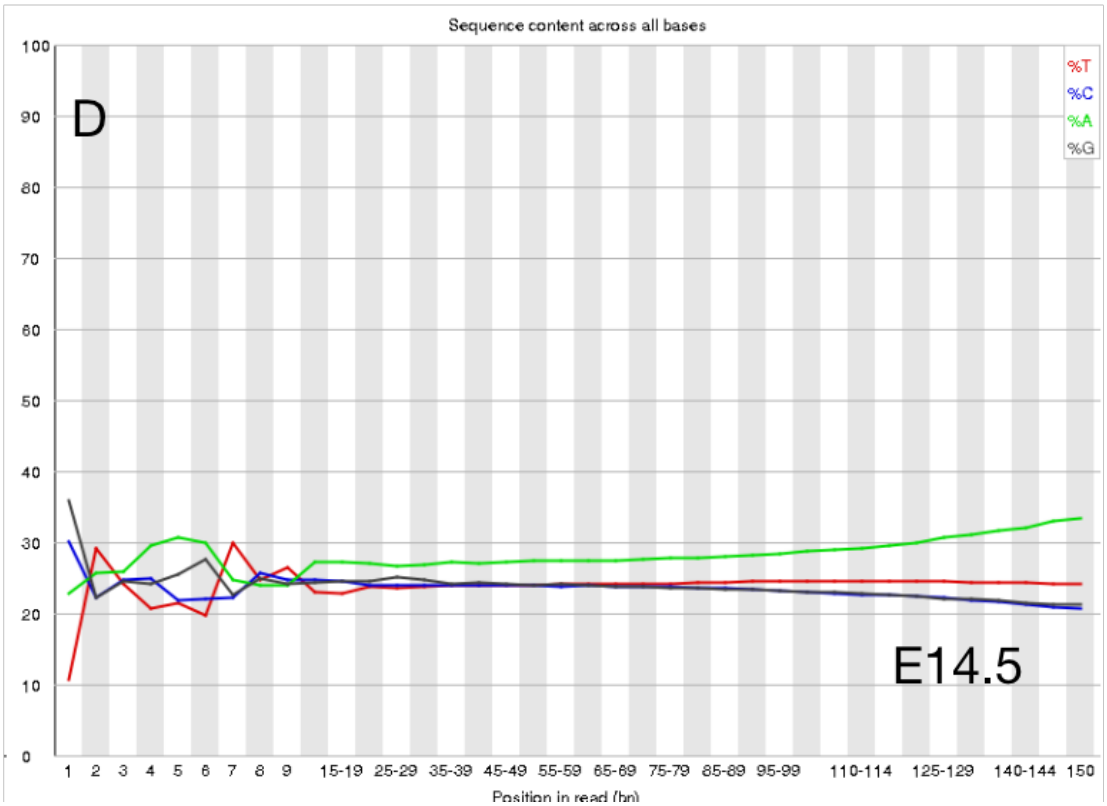
Sequence content across all bases
D
E14.5
%T
%C
%A
%G
100
90
80
70
60
50
40
30
20
10
0
1 2 3 4 5 6 7 8 9 15-19 25-29 35-39 45-49 55-59 65-69 75-79 85-89 95-99 110-114 125-129 140-144 150

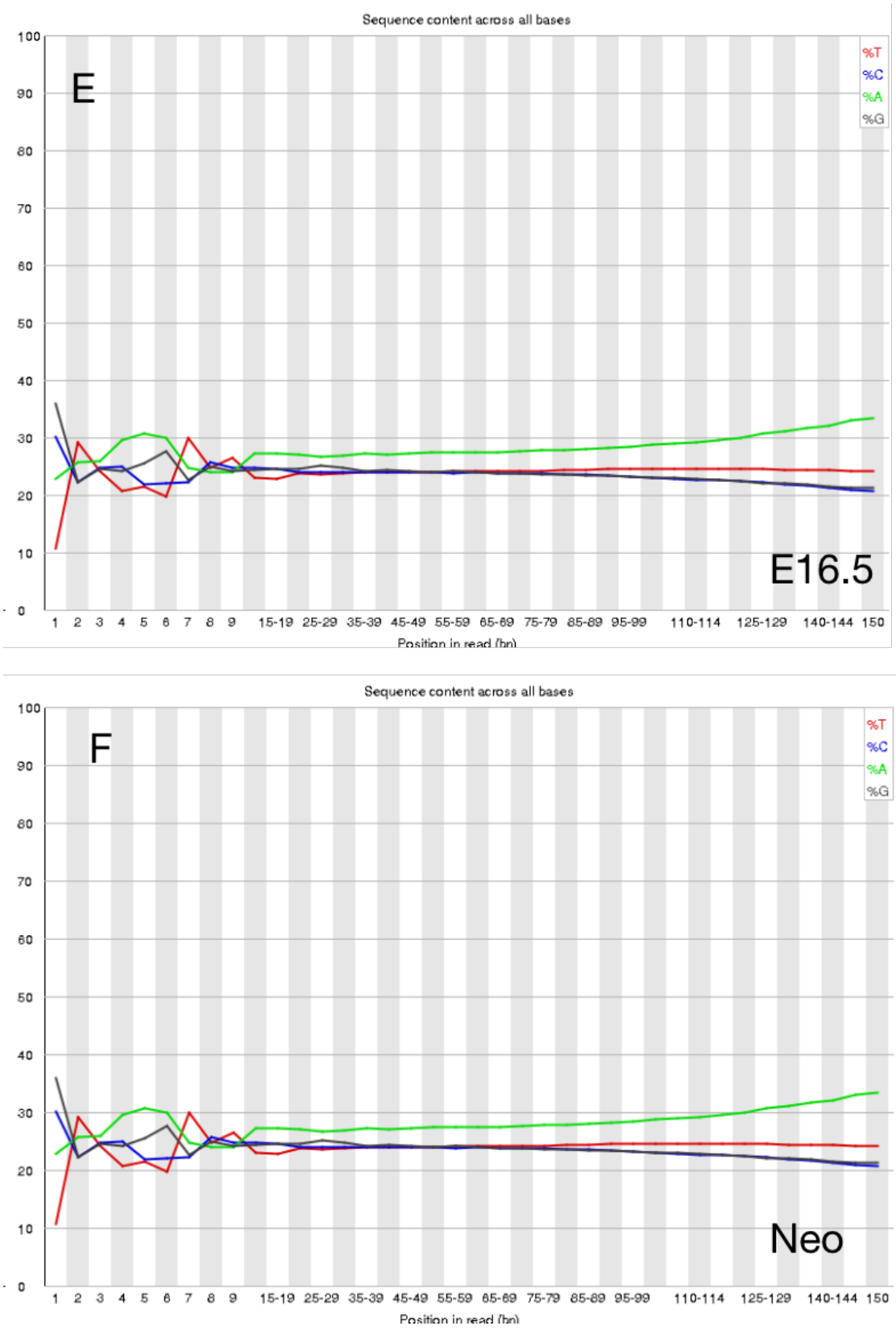

Figure 3.1.3 The distribution of base content of raw data at different stages. A: E8.5;

B: E10.5; C: E12.5; D: E14.5; E: E16.5; F: Postnatal P3. The X axis is the position of bp

from 1 to 149. The Y axis is the percentage of bp. Red, blue, green and grey represent to adenine (A), cytosine (C), guanine (G), and thymine (T).

3.2 Identification of cell types and CCS sub-clusters by each stage

After the quality control, data analysis was processed. Cell filtering, data normalization and unsupervised analysis were carried out by Seurat 3.0. Briefly, gene number, UMI number and the percentage of mitochondria genes are taken as criteria for cell filtering. The threshold for each one is that gene number range from 200 to 75,000; UMI number ranges from 1,000 to 5,000,000; percentage of mitochondria ideal is lower than 10%. Higher threshold may include some duplicate cells which cause some artifacts, whilst lower threshold fails to filter poor cells. The 'LogNormalize' method was employed in a global-scale fashion to normalize the feature expression measurements for each cell by the total expression, multiplies this by a scale factor (default:10,000), and log-transforms the result. Afterwards, all the variable genes detected were applied to perform the principal component analysis. Furthermore, 'FindAllMarker' function was used to identify the genes differentially expressed in each cell cluster. To be detectable, the genes should express in at least 25% of cells in one of the two clusters compared and the differential expression level also should be higher than 25%.

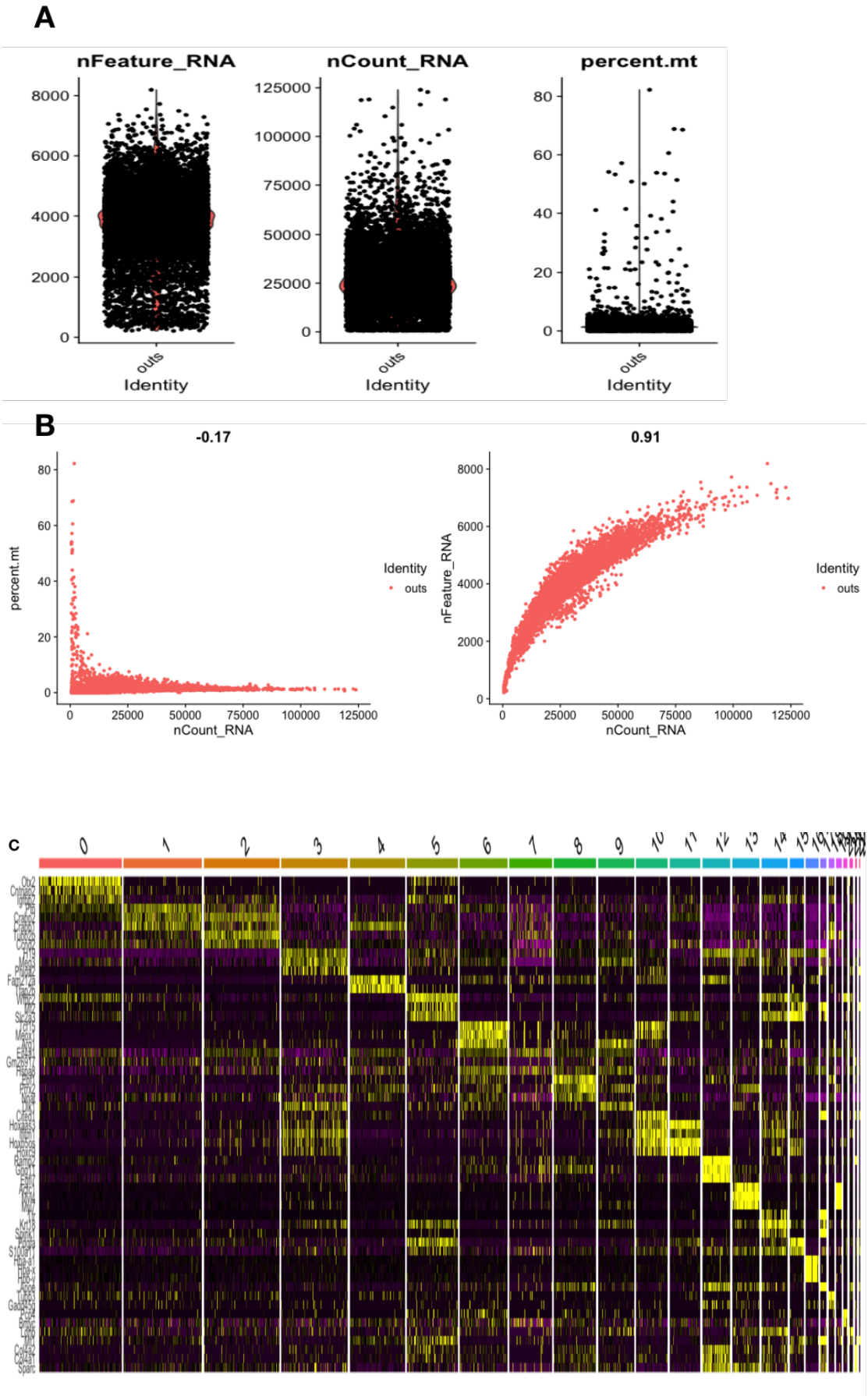
A
nFeature_RNA
nCount_RNA
percent.mt
Identity
outs
B
-0.17
0.91
percent.mt
nFeature_RNA
nCount_RNA
Identity
outs
C

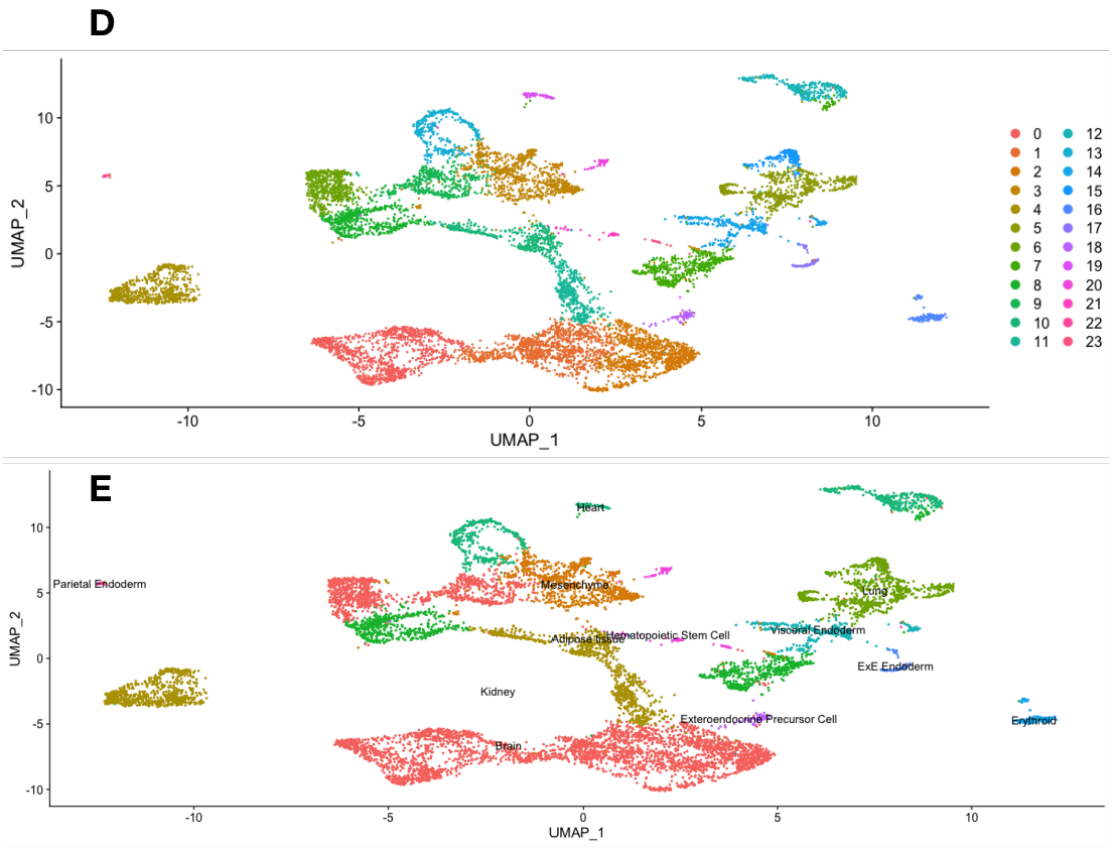

Figure 3.2.1 Quality control and clustering of E8.5 single cell RNA sequencing.

A. Quality control and cell filtering for E8.5 dataset. nFeature, nCount and Percent.mt refer to the number of genes detected in each cell, the total number of molecules detected within a cell, and the percentage of mitochondrial genes. Low nFeature indicates there are some dead cells or cells with poor quality. High nFeature or nCount indicate cells may be doublet or multiple ones. B. Visualization of feature-feature relationship. C Heatmap of differentially expressed genes for each cluster of cells. D. UMAP plot visualizing cluster assignments of cells. Cluster assignments of cells are defined by the FindCluster function using Seurat R package. Clustering is denoted as distinct colors. E. Major cell populations identified after unsupervised clustering. Each point depicts a single cell, colored according to cluster designation. Dimensionality was reduced by PCA, used a graph-based approach to cluster cells, and performed spectral

UMAP to reduce the data to 2 dimensions for visualization.

The analysis was carried out by stage. At E8.5, after quality check and cell filter (Figure 3.2.1A-B), the gene number, UMI, and percentage of mitochondrial gene were cut off from 200 to 7,000 and from 1,000 to 75,000, and 5% below, respectively. I processed the dimension reduction and unsupervised clustering, after which finally I got 24 raw clusters shown in Figure 3.2.1C-D. Identification of each cell population were based on the distinct cell marker reported in previous literature and UMAP with the labelling of each cell type was shown in Figure 3.2.1E. Compared to t-Distributed Stochastic Neighbor Embedding (tSNE) plot, which is a common technique for dimensionality reduction for visualization, Uniform Manifold Approximation & Projection (UMAP) have several advantages over it, among them high speed and better preservation of global structure on data. Due to the nature of cells undergoing the process of differentiation and proliferation at E8.5, cell type cannot be well distinguished to specifically functional cells and progenitor cells. Three markers, Ryr2, Myh6 and Emcm, were used to identify the cardiomyocytes (Figure 3.2.2). Due to the development of heart at this stage, the identification may show error just based on the differential gene expression and limited markers.

Cardiomyocytes

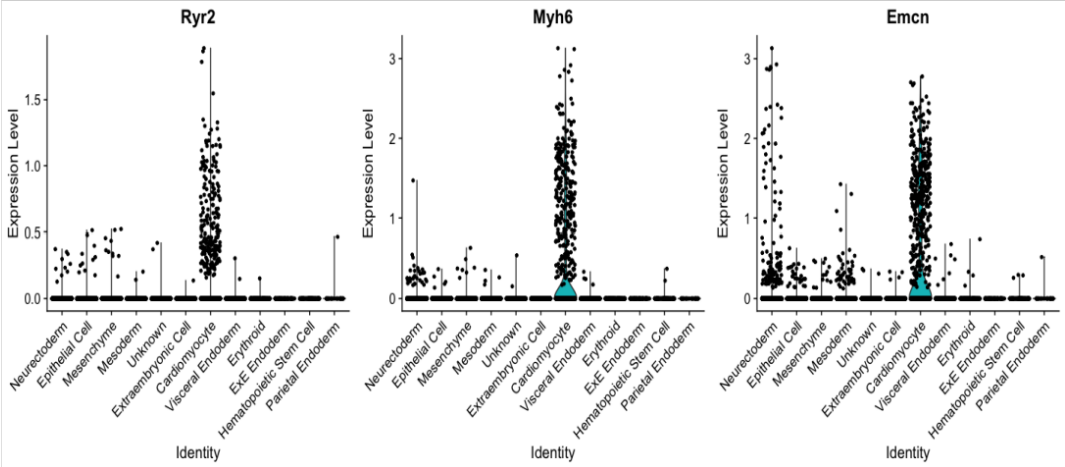

Figure 3.2.2 Violin Plots indicating the expression of selected, well-established cellular markers Ryr2, Myh6 and Emcn in cell populations identified as cardiomyocytes at E8.5 stage.

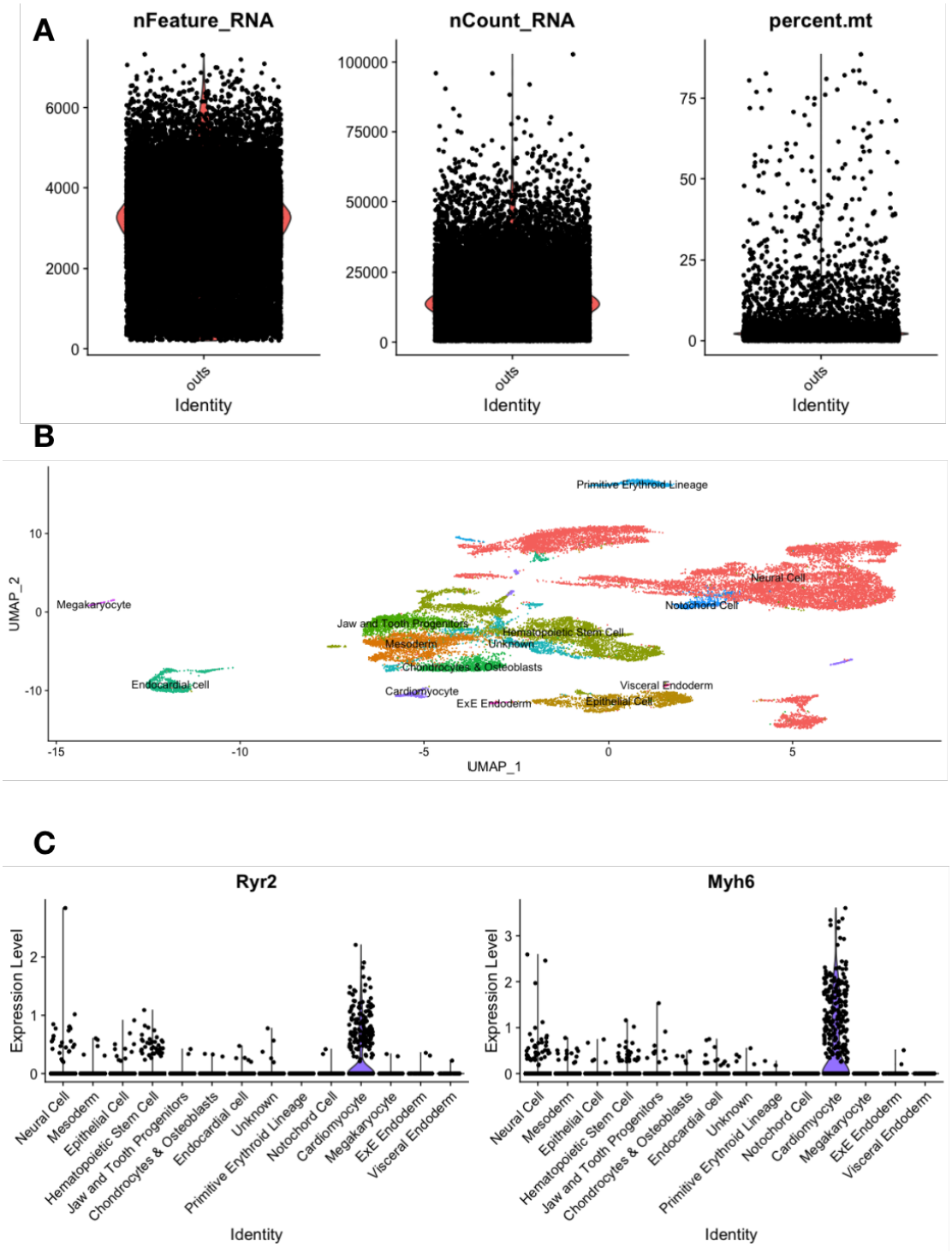

Figure 3.2.3 Quality control and clustering of E10.5 single cell RNA sequencing. A. Quality control and cell filtering for E10.5 dataset. B. Major cell populations identified after unsupervised clustering. Each point depicts a single cell, colored according to cluster designation. C. Violin Plots indicating the expression of selected, well-

established cellular markers Ryr2 and Myh6 in cell populations identified as cardiomyocytes at E10.5 stage.

Similarly, E10.5 data was processed to get 25 raw clusters and later these clusters were assigned into typical cell types (Figure 3.2.3A-B). Ryr2 and Myh6 were used to identify the cardiomyocytes Figure 3.2.3C). Since embryos rather than embryonic hearts were dissected for single cell RNA sequence, the results show diverse cell types from different organs. The percentage of cells from heart is low compared to other organs at this stage, let alone the identification of cardiac conduction system. It is difficult to recognize the cells from cardiac conduction system though it develops shortly after E10.5.

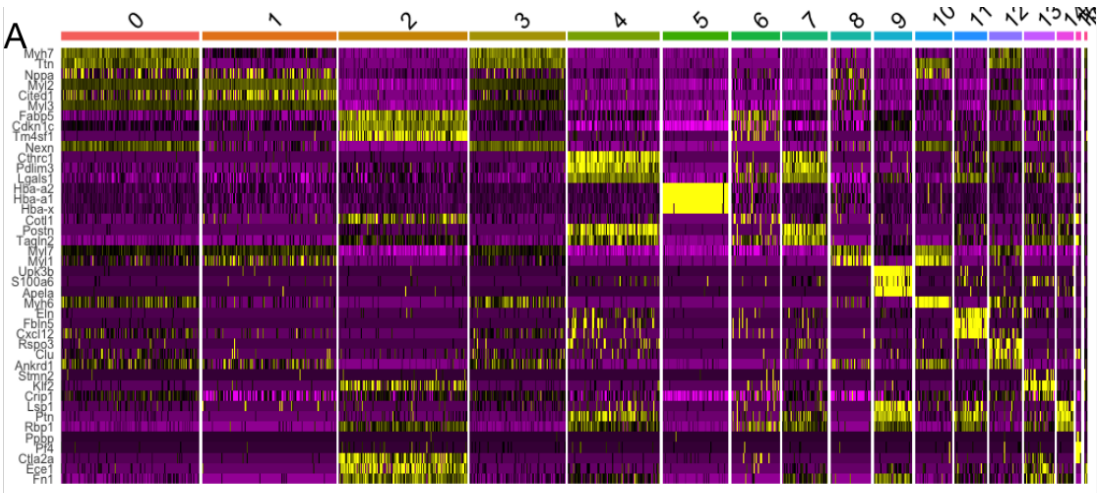
A
0
1
2
3
4
5
6
7
8
9
10
11
12
Myh7
Ttn
Nppa
Myl2
Cited1
Myl3
Fabp5
Cdkn1c
Tm4sf1
Nexn
Chrc1
Pdlim3
Lgals1
Hba-a2
Hba-a1
Hba-x
Cotl1
Postn
Tagln2
Myl7
Myl1
Upk3b
S100a6
Apela
Myh6
Eln
Fbln5
Cxcl12
Rspo3
Glu
Ankrd1
Stmn2
Klf2
Crip1
Lsp1
Ptn
Rbp1
Phpn
Ppp1r14a
Cfl4
Ctla2a
Ece1
Fn1

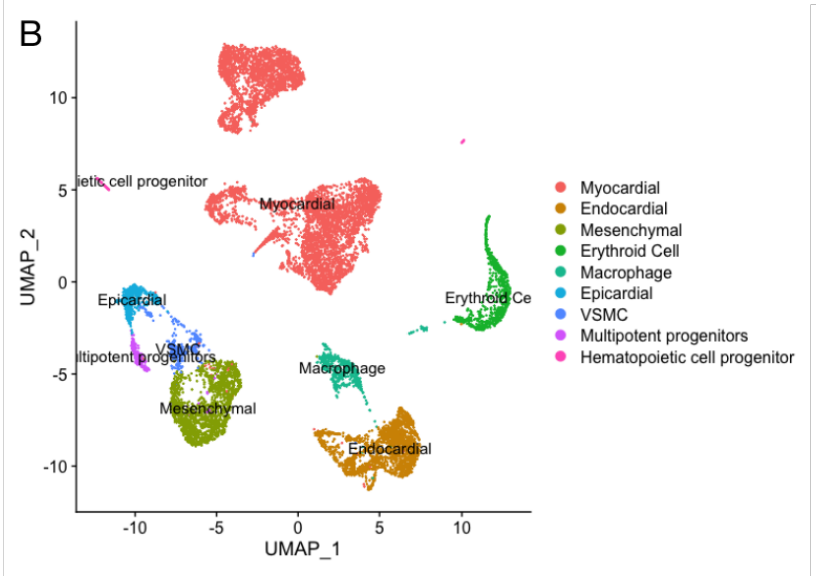
B
10
5
0
-5
-10
UMAP_2
ietic cell progenitor
Myocardial
Epicardial
VSMC
ltipotent progenitors
Mesenchymal
Macrophage
Erythroid Ce
Endocardial
-10
-5
0
5
10
UMAP_1
Myocardial
Endocardial
Mesenchymal
Erythroid Cell
Macrophage
Epicardial
VSMC
Multipotent progenitors
Hematopoietic cell progenitor

C

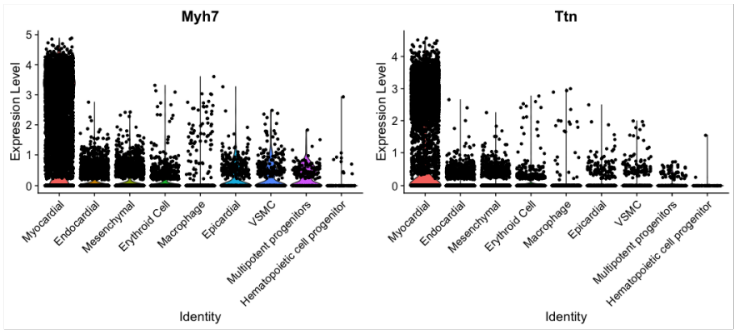
Myh7
Ttn
Expression Level
Myocardial
Endocardial
Mesenchymal
Erythroid Cell
Macrophage
Epicardial
VSMC
Multipotent progenitors
Hematopoietic cell progenitor
Identity

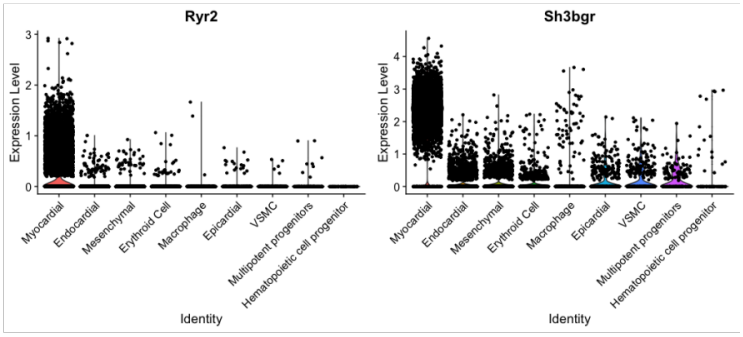
Ryr2
Sh3bgr
Expression Level
Myocardial
Endocardial
Mesenchymal
Erythroid Cell
Macrophage
Epicardial
VSMC
Multipotent progenitors
Hematopoietic cell progenitor
Identity

Figure 3.2.4 Clustering and violin plot for E12.5. A. Heatmap of differentially expressed genes for each cluster of cells. B. Major cell populations identified after unsupervised clustering at E12.5. Each point depicts a single cell, colored according to cluster designation. C. Violin Plots indicating the expression of selected, well-established cellular markers Myh7, Ttn, Ryr2 and Sh3bgr in cell populations identified as cardiomyocytes at E12.5 stage.

From E12.5, hearts from one littler were dissected for sequencing so that high cell counts from heart were available for analysis. After quality control and dimensionality reduction, 17 raw clusters were achieved by running the 'FindAllMarker' function in Seurat version 3 and the heatmap demonstrated the gene expression difference among them (Figure3.2.4A-B). 9 cell populations were annotated depending on their distinct gene expression, which are myocardial, endocardial, mesenchymal, erythroid cell, macrophage, epicardial, vascular smooth muscle cell (VSMC), multipotent progenitor, hematopoietic cell progenitor. Myocardium was identified with evident expression of Myh7, Ttn, Ryr2, and Sh3bgr (Figure3.2.4C). At this stage, the atrial and ventricular regions are just possible to recognize but still difficult at the sequencing level since they share transcript profiles.

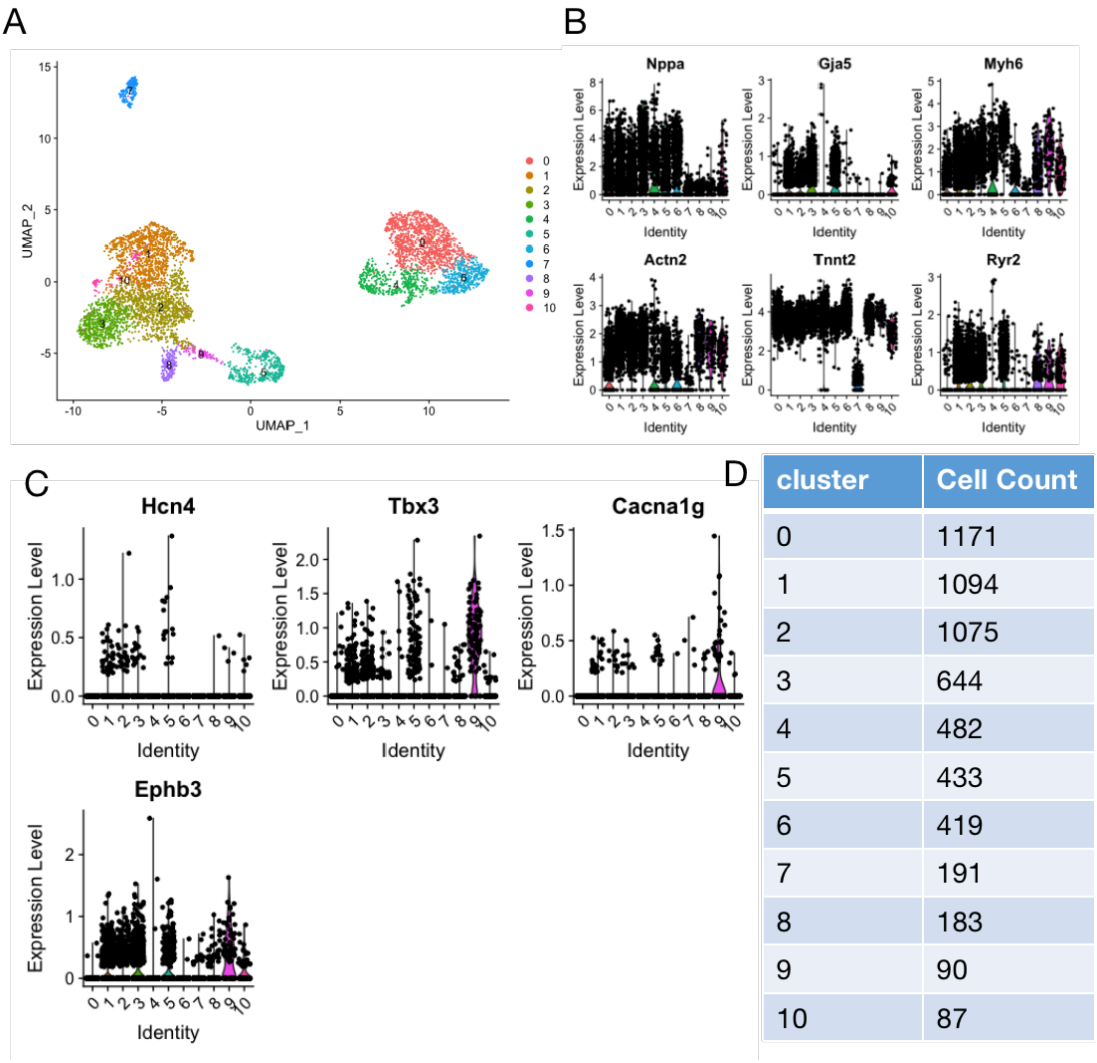

cluster	Cell Count
0	1171
1	1094
2	1075
3	644
4	482
5	433
6	419
7	191
8	183
9	90
10	87

Figure 3.2.5 A. UMAP plots of cardiomyocyte subpopulations at E12.5. B, Violin plots of the distribution of marker genes for the atrial myocytes (Nppa, Gja5), ventricular myocytes (Myh6, Actn2, Tnnt2 and Ryr2). C. Violin plots of the distribution of marker genes for the CCS cells (Hcn4, Tbx3 and Ephb3) in different myocyte subtypes, a higher expression of CCS cell marker genes can be seen in cluster 5 and cluster 9. D. The cell number per cluster is shown at bottom.

To explore the myocardial cells, I subclustered the myocardial cells and obtained 11 clusters in a total of 4901 cells (Figure3.2.5A). More expected myocardial markers like

Nppa, Gja5, Myh6, Actn2, Tnnt2 and Ryr2 were applied, and they were typically expressed in most of these clusters, which validates their classification as myocardium. At E12.5, Hcn4 downregulated in the atrial and ventricular chamber but increased in the cardiac conduction regions. Tbx3 expression was detected in SAN exclusively compared to the expression of Ephb3 in AV canal, prospective AV bundle as well as trabecular myocardium. Like Ephb3, Cacna1g also expressed at AV canal and AV cushion from E12.5. The violin plot illustrates the expression of these four markers in the myocardial subclusters. Interestingly, cluster 9 stands out from the others which is not due to its lower cell numbers (Figure 3.2.5C-D). However, these markers labelled different components of the cardiac conduction system, combined with the heterogeneity and development process, cardiac conduction system cannot be defined as a distinct cluster at this stage. A violin plot is performed to show the expression of well-defined genes that are involved in the development and function of cardiac conduction system (Figure3.2.6). Apart from cluster 9, cluster 5 has remarkable expression of Tbx5, Cacna2d2, Cpne5, and Tbx20. This indicates that cardiac conduction cells are most likely distributed in cluster 5 and cluster 9, although other cell types also have some expression.

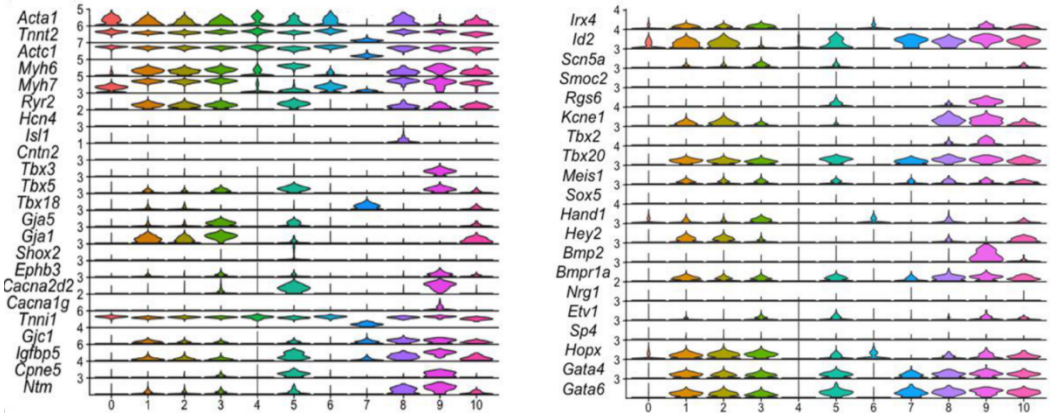

Figure 3.2.6 Stack violin plot showing the expression profile and abundance of CCS related genes in different cardiomyocyte subsets. Tbx5, Cacna2d2 and Cpne5 are expressed at relatively high levels in clusters 5 and 9. Bmp2 and Tbx2 are abundant in cluster 9.

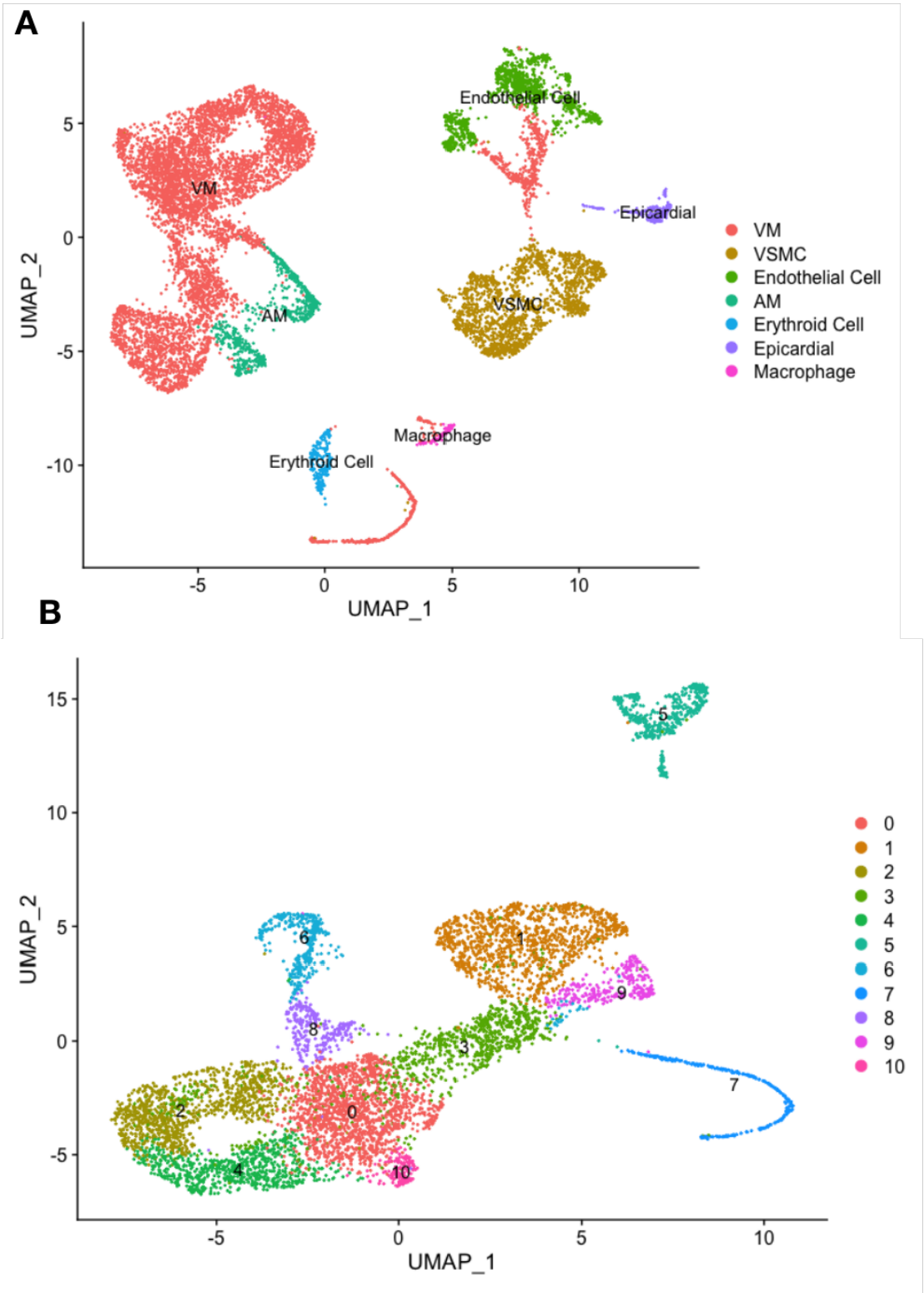
A
Endothelial Cell
VM
Epicardial
VSMC
AM
Macrophage
Erythroid Cell
UMAP_2
UMAP_1
VM
VSMC
Endothelial Cell
AM
Erythroid Cell
Epicardial
Macrophage
B
UMAP_2
UMAP_1
0
1
2
3
4
5
6
7
8
9
10

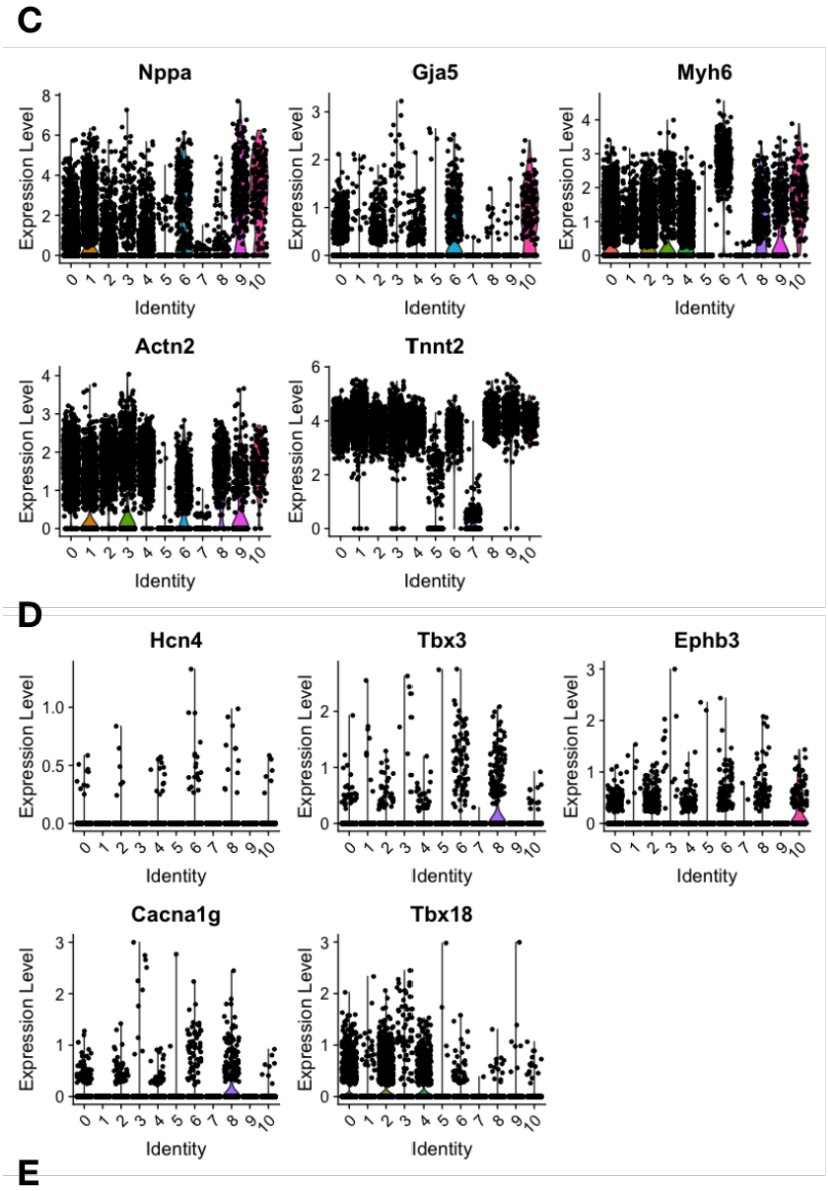

Cluster	0	1	2	3	4	5	6	7	8	9	10
Cell counts	1504	1165	1026	919	754	457	378	306	283	277	143

Figure 3.2.7 scRNA-seq analysis at E14.5 revealing the presence of distinct cell types in the heart and bioinformatic analysis of cardiac conduction cells. A. UMAP plots of all cell types in the heart. B. UMAP plots of cardiomyocyte subpopulations. C. Violin plots of the distribution of marker genes for atrial myocytes (Nppa, Gja5), ventricular myocytes (Myh6, Actn2 and Tnnt2). D. Violin plots of the distribution of marker genes for CCS cells (Hcn4, Tbx3 and Ephb3) in different myocyte types. A higher expression

of CCS cell marker genes is seen in clusters 0, 2, 4, 6, 8 and 10. E. The cell number in each cluster.

At E14.5, atrial and ventricles are characterized based on their structure and transcriptional profiles. 18 raw clusters were processed and attributed to 7 major cell populations in the heart including atrial myocyte, ventricular myocyte, endothelial cell, erythroid cell, macrophage, epicardial, and vascular smooth muscle cell (VSMC) (Figure 3.2.7A-B). The difference of clusters identified throughout the stages depicts the developmental changes within the heart. Subclustering was performed within the combined atrial and ventricular myocytes to get 11 subclusters. The distribution of atrial and ventricular myocyte markers was demonstrated in the violin plot among different myocyte subtypes (Figure 3.2.7C). At E14.5, Hcn4 contributes to the precursors of AV bundle, bundle branches and Purkinje fiber network, as well as Gja5. Critically, Tbx3 is fully confined to cardiac conduction components. Cacna1g and Tbx18 also participate in the formation of ventricular conduction. Indicated by the violin plot, cardiac conduction cells are abundant in clusters 0, 2, 4, 6, 8 and 10. Stack violin plots further verify that the above clusters have distinct expression of genes that related to development and function of cardiac conduction system (Figure3.2.8). The wide anatomic distribution of cardiac conduction cells possibly accounts for the fact that several subtypes rather than one contain abundant conduction cells.

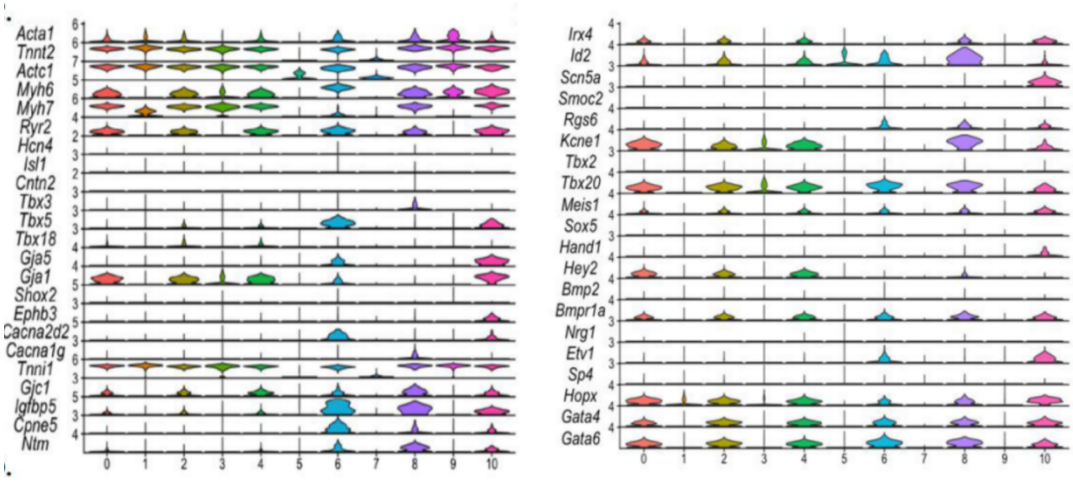

Figure 3.2.8 Stack violin plot showing the expression profile and abundance of CCS related genes in different cardiomyocyte subsets. Tbx5 marks the fast conduction system, which is expressed at relatively high level in clusters 6 and 10, and Igfbp5 is expressed at relatively high levels in clusters 6, 8, and 10.

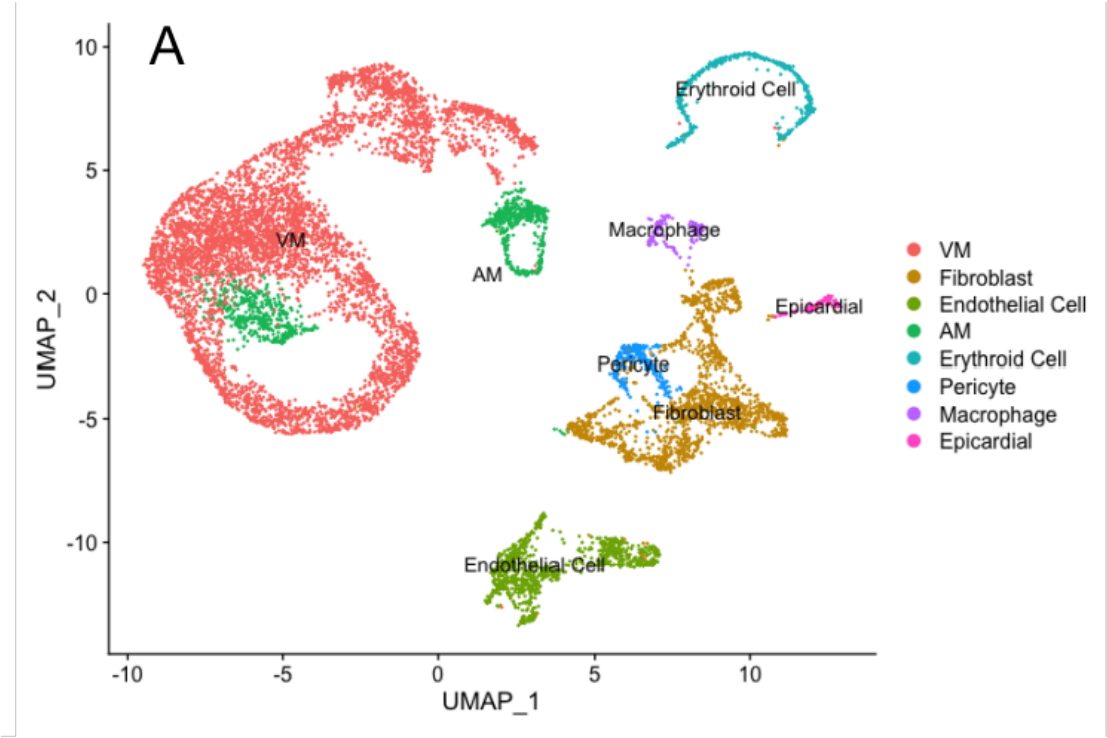
A
Erythroid Cell
VM
AM
Macrophage
Epicardial
Pericyte
Fibroblast
Endothelial Cell
UMAP_2
UMAP_1
VM
Fibroblast
Endothelial Cell
AM
Erythroid Cell
Pericyte
Macrophage
Epicardial

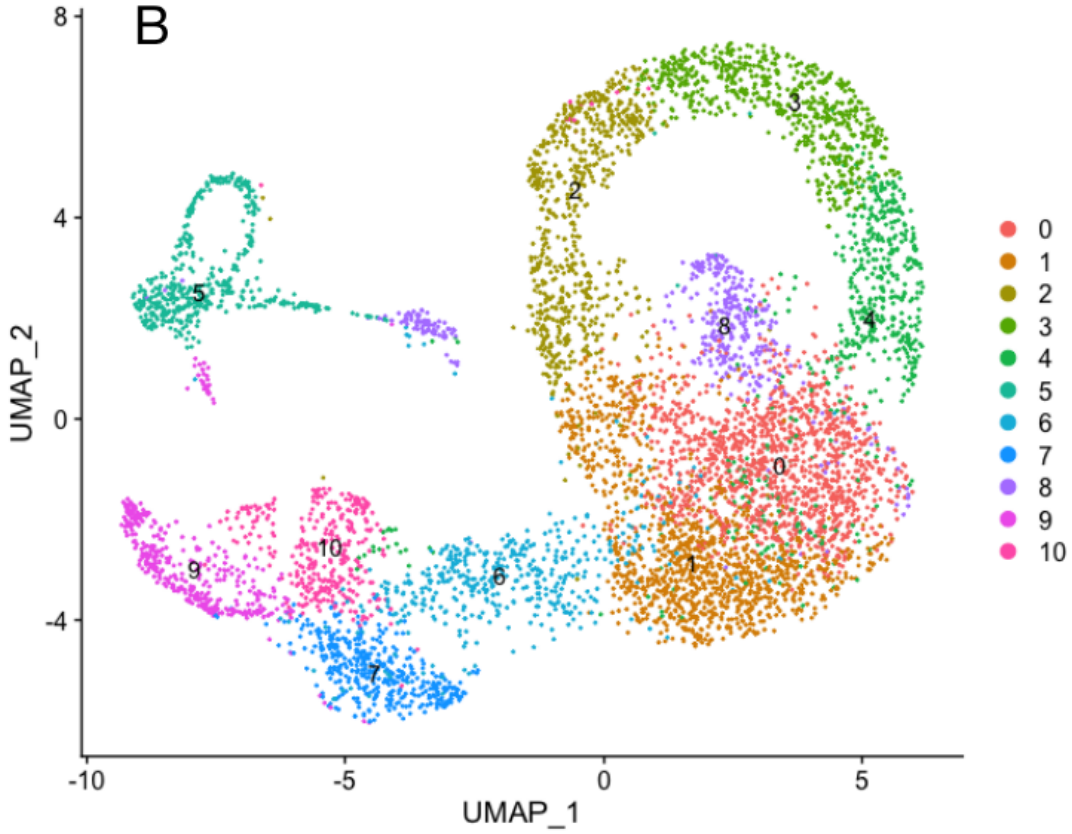
B
UMAP_2
UMAP_1
0
1
2
3
4
5
6
7
8
9
10

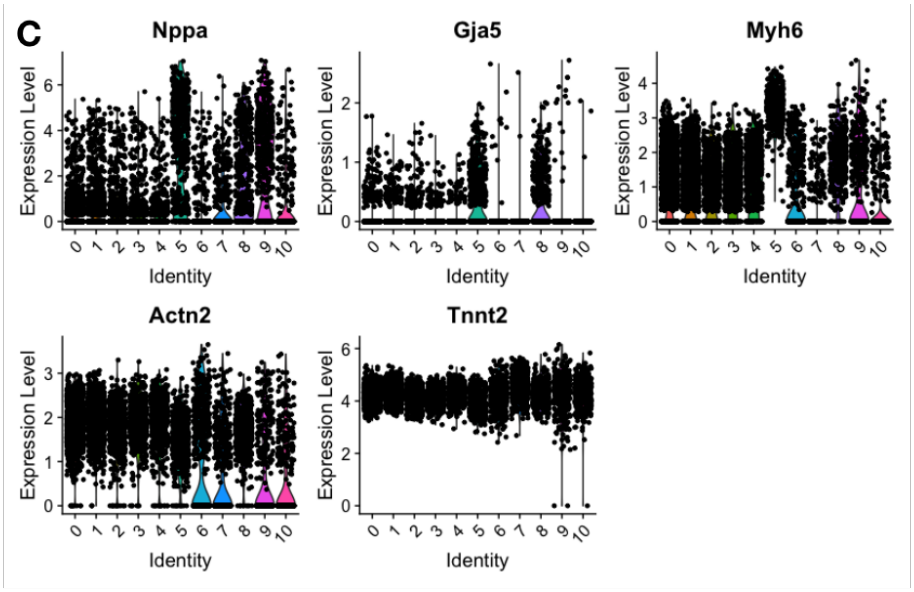

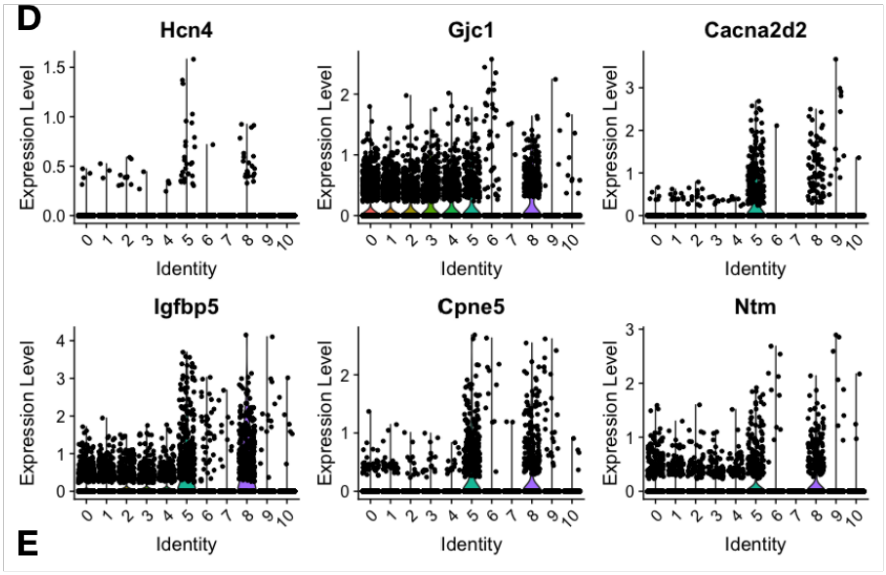

Cluster	0	1	2	3	4	5	6	7	8	9	10
Cell count	1263	1189	664	609	545	470	455	414	402	390	338

Figure 3.2.9 scRNA-seq analysis at E16.5 revealing the presence of distinct cell types in the heart and bioinformatic analysis of cardiac conduction cells. A. UMAP plots of all cell types in the heart. B. UMAP plots of cardiomyocyte subpopulations. C. Violin plots of the distribution of marker genes for atrial myocytes (Nppa, Gja5), ventricular myocytes (Myh6, Actn2 and Tnnt2). D. Violin plots of the distribution of marker genes for CCS cells (Hcn4, Gjc1, Cacna2d2, Igfbp5, Cpne5 and Ntm) in different myocyte types.

A higher expression of CCS cell marker genes is seen in clusters 5 and 8. E. The cell number in each cluster.

Similar to the previous stages, unsupervised clustering was conducted and assigned to 8 cell populations. At E16.5, fibroblasts were detected apart from other existing cell types (Figure3.2.9 A). Subclustering was performed in the cardiomyocytes including atrial and ventricular myocytes and 11 subtypes were classified (Figure 3.2.9B). Interestingly, clusters 5 and 8 are distinguishing from other subtypes in both Gja5, which is not only an atrial but also a Purkinje fiber marker, and other cardiac conduction system related markers like Cacna2d2, Igfbp5 and Cpne5 (Figure 3.2.9 D). Igfbp5 is reportedly rich in the SAN region while Cpne5 is abundant in the AVN and bundle brunch region. Cacna2d2 occurs in the bundle brunch as well as Purkinje fiber region. More gene expression data are shown in the stack violin plot in which cluster 5 and 8 also highly express the Tbx5 and Etv1 (Figure3.2.10). At E16.5, gene expression profiles indicate that cardiac conduction cells become distinct and recognizable from all the myocytes though they still share transcripts with working myocytes. However, central and peripheral cardiac conduction system are still highly similar and cannot be identified.

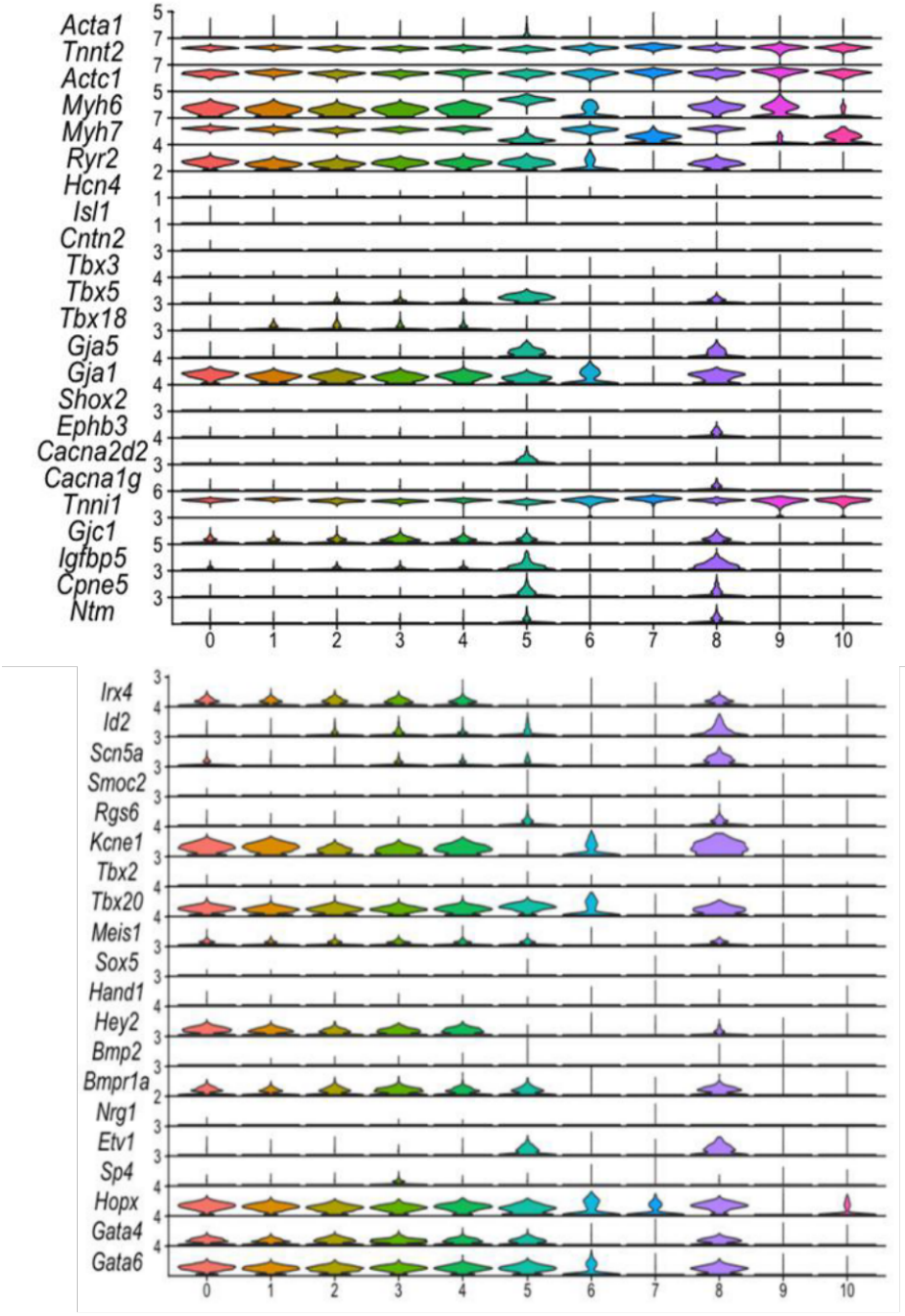

Figure 3.2.10 Stack violin plot showing the expression profile and abundance of CCS related genes in different cardiomyocyte subsets. Most CCS marker genes such as Tbx5 and Cacna2d2 have relatively high expression in Cluster 5 and 8.

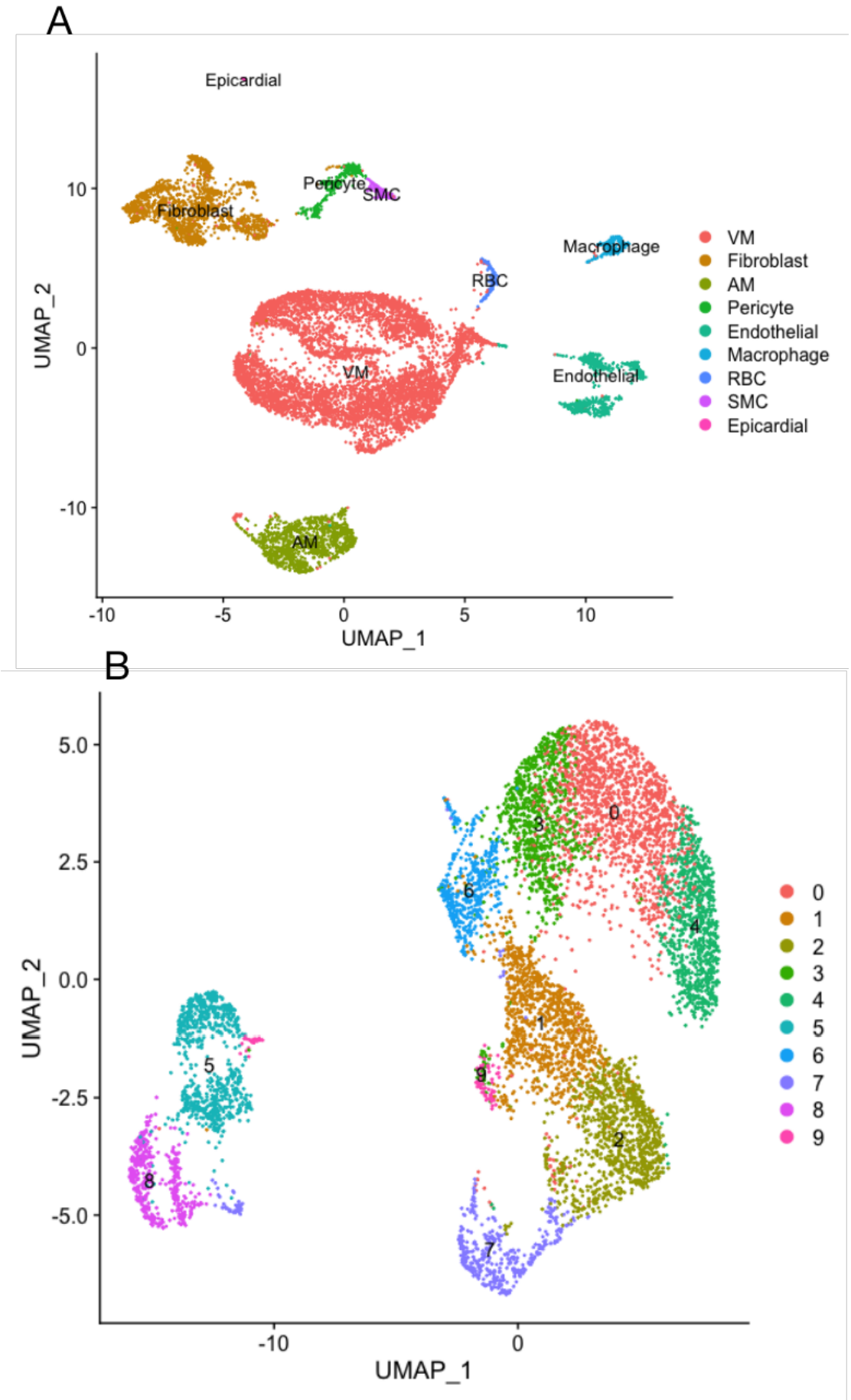
A
Epicardial
Pericyte
SMC
Fibroblast
Macrophage
RBC
VM
Endothelial
AM
UMAP_2
UMAP_1
10
0
-10
-10
-5
0
5
10
VM
Fibroblast
AM
Pericyte
Endothelial
Macrophage
RBC
SMC
Epicardial
B
5.0
2.5
0.0
-2.5
-5.0
-10
0
0
1
2
3
4
5
6
7
8
9

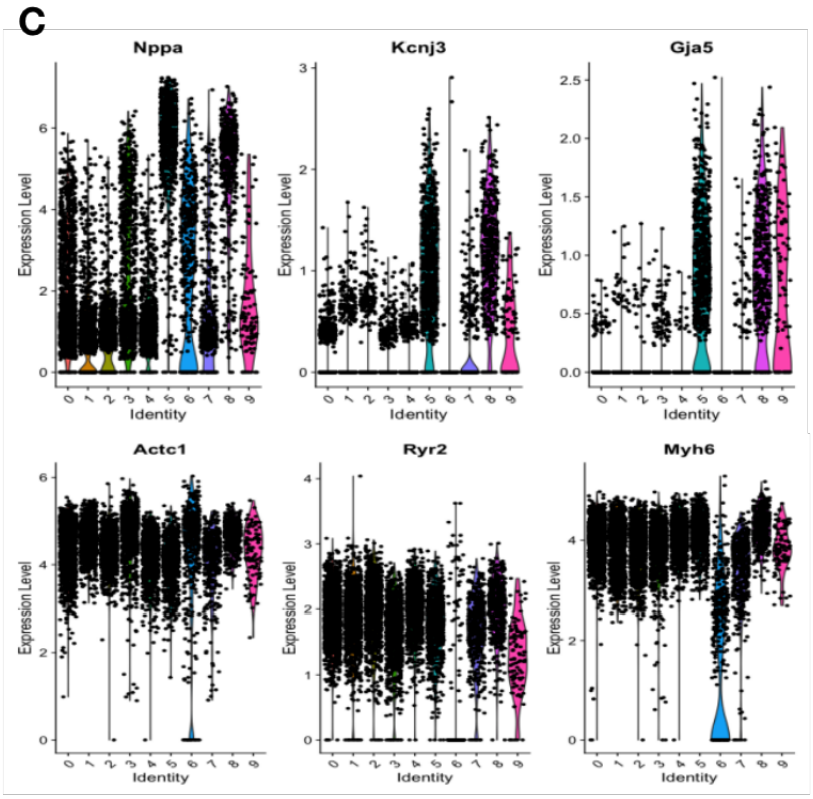

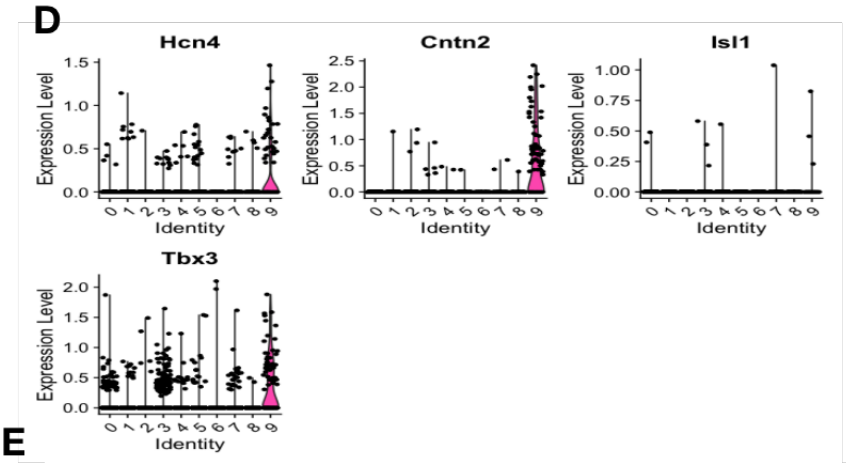

E

cluster	0	1	2	3	4	5	6	7	8	9
Cell Count	1508	978	947	896	850	717	450	442	430	97

Figure 3.2.11 scRNA-seq analysis at P3 revealing the presence of distinct cell types in the heart and bioinformatic analysis of cardiac conduction cells. A. UMAP plots of all cell types in the heart. B. UMAP plots of cardiomyocyte subpopulations. C. Violin plots of the distribution of marker genes for atrial myocytes (Nppa, Gja5 and Kcnj3), ventricular myocytes (Actc1, Ryr2 and Myh6). D. Violin plots of the distribution of

marker genes for CCS cells (Hcn4, Cntn2, Isl1 and Tbx3) in different myocyte types. A higher expression of CCS cell marker genes is seen in cluster 9. E. The cell number in each cluster.

The heart becomes increasingly more mature at postnatal stage and typical cell types are identified (Figure 3.2.11A). Atrial and ventricular cells retain identity in subclusters shown in Figure 3.2.11 B-C. Each dot in UMAP represents one cell and the distance between two dots reflect the similarity of transcript between cells. It is obvious that cluster 5 and 8 are close to each other but far from the majority of other cell types. As shown in the violin plot, cluster 5 and 8 predominantly express atrial markers like Nppa, Kcnj3 and Gja5 (Figure 7.2.11C). Compared to well-established markers of cardiac conduction system like Hcn4, Cntn2, Isl1 and Tbx3, cluster 9 have a better performance among all subclusters (Figure 3.2.11D). Combined with the expression level of cardiac conduction related genes in stack violin plot, cluster 9, together with part of cluster 5 and 8, have a higher number of conduction cells (Figure 3.2.12).

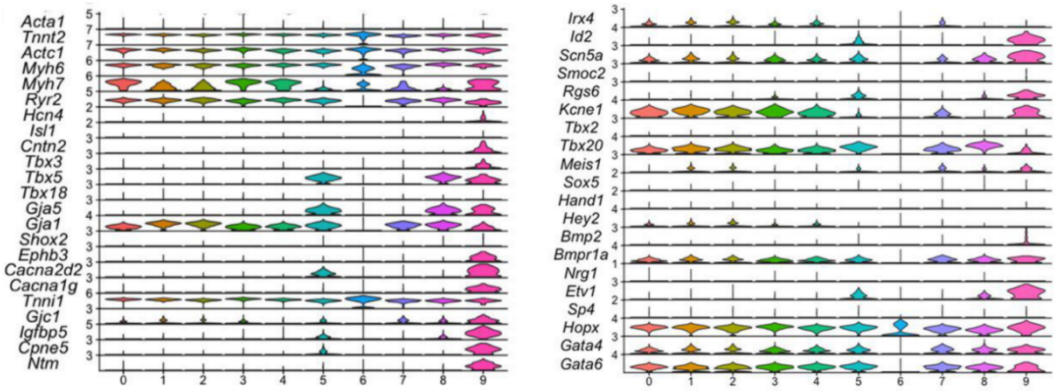

Figure 3.2.12 Stack violin plot showing the expression profile and abundance of CCS related genes in different cardiomyocyte subsets. Most CCS marker genes such as

Cntn2, Tbx3, Tbx5, Shox2 and Cacna2d2 have relatively high expression in Cluster 9.

Analysis separately on each stage showed the temporal expression profiles of each cell type. However, some drawbacks are exposed during the analysis. First, due to the low number of each cell types at each stage, certain transcript profiles between cells fail to be significantly captured and characterized. Second, as we know, heart development is a dynamic and changeable process containing continuous signaling pathways. The locus of genes and cell type of interest are not able to connect chronologically to show the trend in an individual stage. Especially, take cardiac conduction system as an example, it is hard to distinguish the conduction cell type completely at each stage due to not only to the natural heterogeneity and wide distribution in whole heart but also its similarity with myocytes. A combination of different stages gives the possibility to achieve the differential genes in cell types and subtypes, as well as to trace out the development trajectory of cell lineage by alteration of the transcript signature.

3.3 Identification of cell types and CCS sub-clusters by merged stage data

We performed initial unsupervised clustering to identify a range of putative cell types across the developing heart. For scRNAseq, by 10x Genomics Illumina HiSeq PE150, following pre-processing and library quality control, our data had mean UMI and gene

counts of 6417 and 1482 respectively across 175237 cells in our scRNAseq (Figure 3.3.1). UMAP dimensionality reduction suggested that the scRNA-Seq identified 4 overarching populations – early embryonic tissue, mixed mesenchymal tissue, and ventricular and atrial cardiomyocyte populations. 26 distinct cell types were identified following iterative unsupervised clustering and re-clustering (Figure 3.3.2). The constitution of cells from each developmental stages were also demonstrated in Figure 3.3.2. The distinct stage-dependent clusters indicate the changeable genetic profiles throughout development.

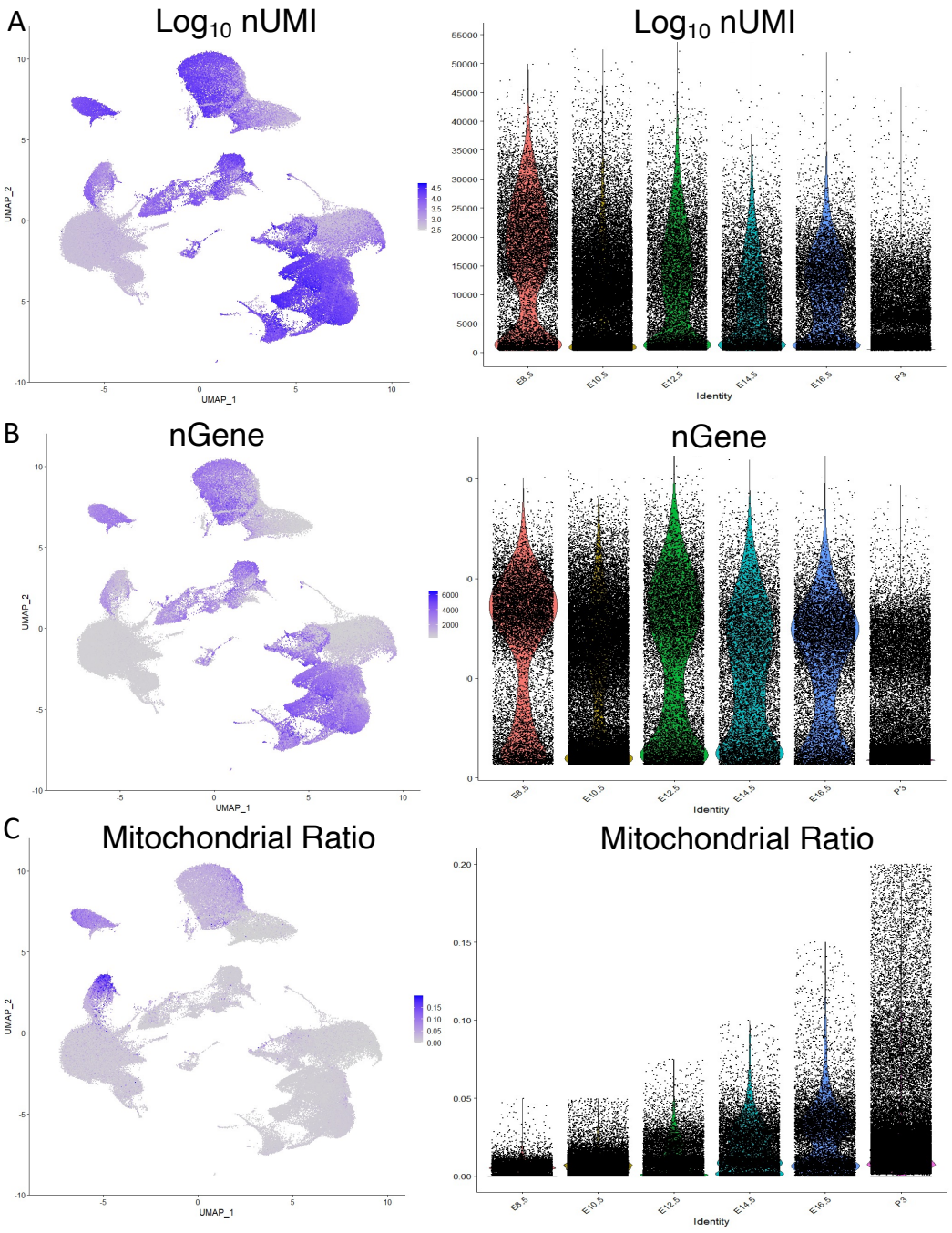

Figure 3.3.1 Quality control metrics for merged single-cell data. A. A UMAP plot of all initial cells post-quality control, coloured by Log10(nUMI) and a violin plot demonstrating the same across different stages. B. A UMAP plot of all initial cells post-quality control, coloured by nGene and a violin plot demonstrating the same across different stages. C. A UMAP plot of all initial cells post-quality control, coloured by the ratio of mitochondrial nUMI to total nUMI and a violin plot demonstrating the same

across different stages.

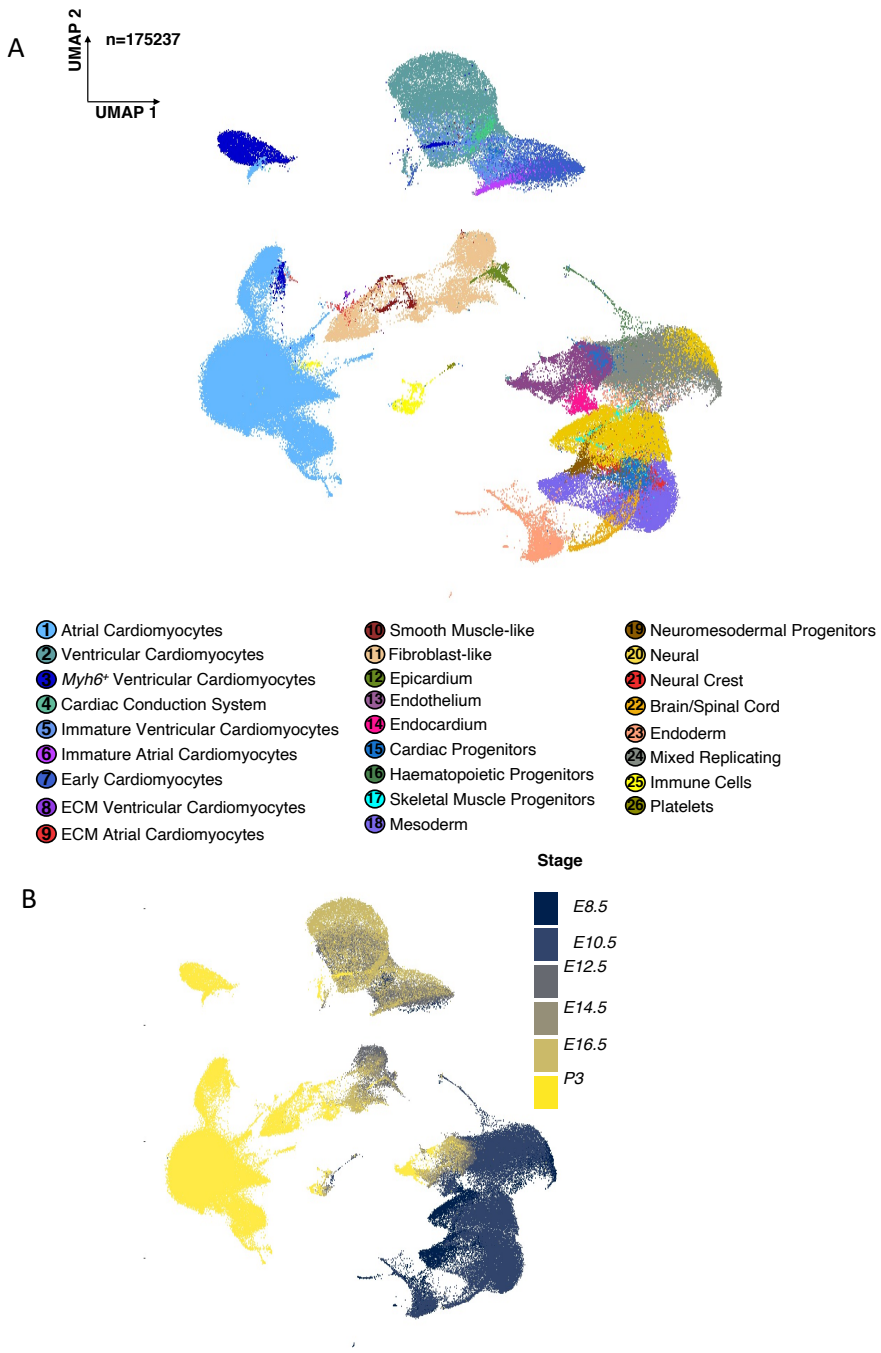

Figure 3.3.2 The cellular landscape of the developing mouse heart and mid-stage embryo. A. A UMAP plot of cells identified from 10 x Genomics single cell RNA sequencing of E8.5 and E10.5 embryos, and E12.5, E14.5, E16.5, and P3 isolated hearts.

Cells are coloured by corresponding cell type as the labels below. B. A UMAP plot of cells coloured by isolated stages.

To better understand cardiomyocyte populations in the developing heart, more extensive analysis of the cardiomyocyte lineage was undertaken. The dataset was predominated by the heart-specific lineages of the later (>E10.5) sampling stages, with a rich range of cardiomyocyte subpopulations identified in this initial interrogation of the data (Fig 3.3.3). However, dimensionality reduction and clustering algorithms must balance local and global transcriptional differences: local discrimination of transcriptional differences within cell types may be obscured by preservation of global differences. To focus on identifying cardiomyocyte-lineage heterogeneity, we selected cell types mapping the expected developmental lineage of cardiomyocytes, from mesoderm through to neonatal 'mature' cardiomyocytes. A novel method was used which is a local and global structure-preserving dimensionality reduction technique called PHATE and it 'spectral-like' unsupervised clustering to identify 17 cardiomyocyte lineage cell types over n=106461 cells (Fig 3.3.3). The expected lineage was able to be discriminated from earlier cardiac progenitors across to more mature cardiomyocyte cell types over the 3-dimensional PHATE space, which can be taken as an approximation of pseudotime, given the structure-preserving nature of the PHATE algorithm(Moon et al., 2019). We observed the 'development' from the mesodermal cardiogenic heart fields, through the primary heart tube formation, to immature ventricular and atrial cardiomyocytes, and then through into more mature atrial and

ventricular cardiomyocytes (Figure 3.3.4). Interestingly, we saw that much of the CCS formed clusters distinct in 3D PHATE space from their respective most similar working cardiomyocyte populations. For example, Purkinje Fibres (PKJs) compared with the trabecular ventricular myocardium. With use of the 'spectral-like' clustering algorithm (Moon et al., 2019), and cluster labelling based on gene expression profiles (Figure 3.3.4) the CCS was identified from scRNAseq, whereas many prior scRNAseq studies (Goodyer & Wu, 2018a; Lescroart et al., 2018; G. Li et al., 2016; Tyser et al., 2021; Xiong et al., 2019)did not discriminate separate CCS populations apart from those using CCS-biased sampling techniques(Goodyer et al., 2019; D. Liang et al., 2021).

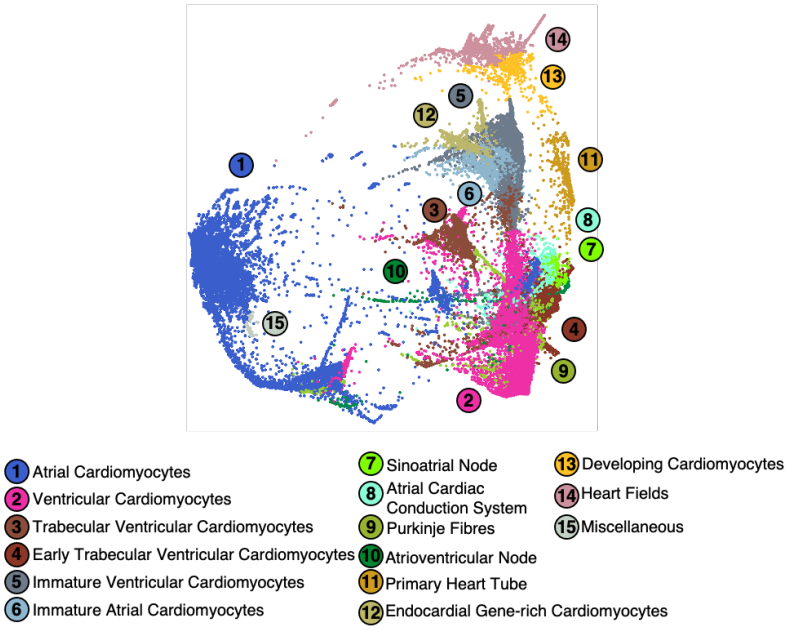

Figure 3.3.3 A PHATE plot of the cellular landscape of the cardiomyocyte lineage. Numbered labels indicate the cell type with the corresponding colour on the PHATE plot, with full names below.

A

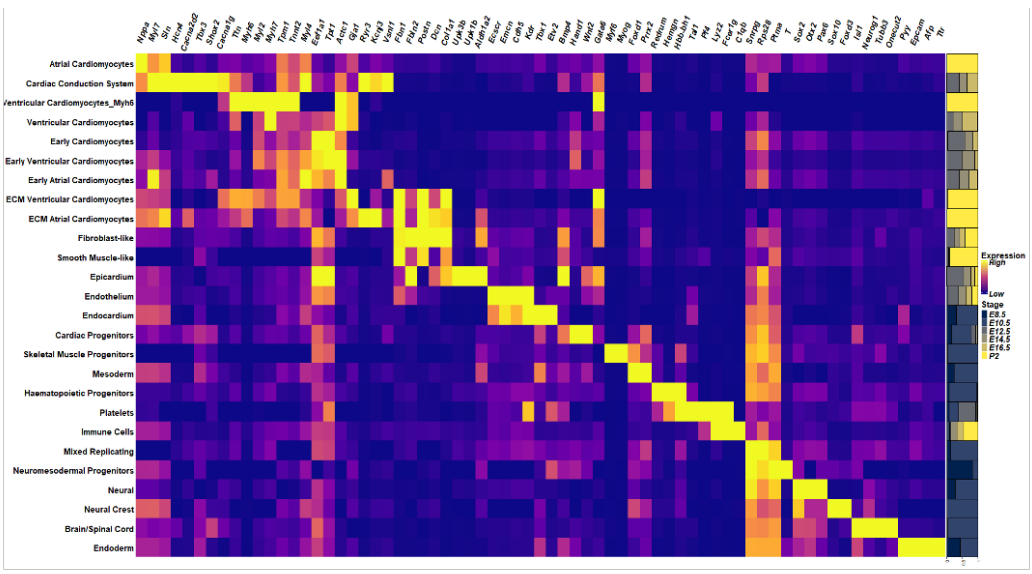

B

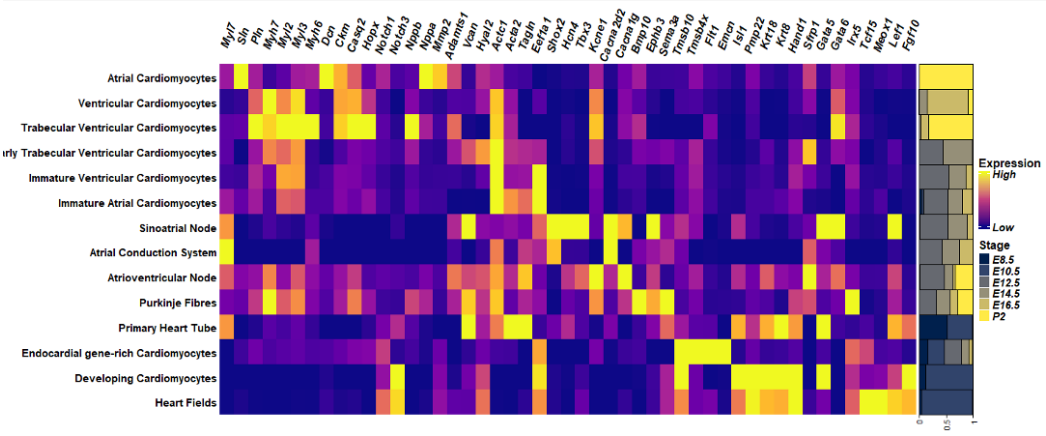

3.3.4 Cell types display a range of associated biologically defining marker genes in our single-cell RNA sequencing analyses. A. Heatmap showing the typical markers for all cell types identified across the developmental stages. Values for expression are normalised by row and then by column. B. Heatmap showing the typical markers for cardiac cell types identified in terms of developmental stages. Values for expression are normalised by row and then by column.

3.4 Identification and characterization of *Dbh*$^{+}$ cells

We identified previously unreported dopamine beta-hydroxylase (Dbh) expressing cardiomyocytes (*Dbh*$^{+}$-CMs) populations from the cardiomyocyte lineage (Figure 3.4.1). We observed *Dbh* expression across both working and non-working (i.e., pacemaker/conducting) cardiomyocyte populations (Figure 3.4.1). The major *Dbh*$^{+}$-CMs cell types were: atrial and ventricular cardiomyocytes; early and more mature ventricular trabecular cardiomyocytes; sinoatrial and atrioventricular nodal cardiomyocytes; and non-specific atrial cardiac conduction system and Purkinje fibers, although we did identify a small number of cells that belonged to earlier developing cardiomyocyte populations. Overall, there were n=2591 *Dbh*$^{+}$-CMs, at 2.43% of all cardiomyocyte lineage cells from E8.5, through to P3. However, significant numbers of *Dbh*$^{+}$ cells only became apparent beyond E10.5. We confirmed expression of expected specific cardiomyocyte markers such as Tnnt2 and CCS-specific markers (Figure 3.4.3), within the *Dbh*$^{+}$ population. Strikingly, although *Dbh*$^{+}$-CMs represented only small percentages of the total working cardiomyocyte populations (AM: 2.13%, VM: 3.90%, VM-trab: 4.18%, and eVM-trab: 2.26%) (Table 3.4.2), the CCS appeared to be over-represented in *Dbh*$^{+}$ cardiomyocytes as percentages of their respective total cardiomyocyte lineage numbers (PKJ: 12.76%, AVN: 12.14%, SAN: 8.39%, and AM-CCS: 3.82%) (Table 3.4.2). A two-tailed Chi-Squared test for independence confirms that cell type, within cardiomyocytes, and *Dbh* expression (positive or negative) are not independent (p= 1.4934E-238).

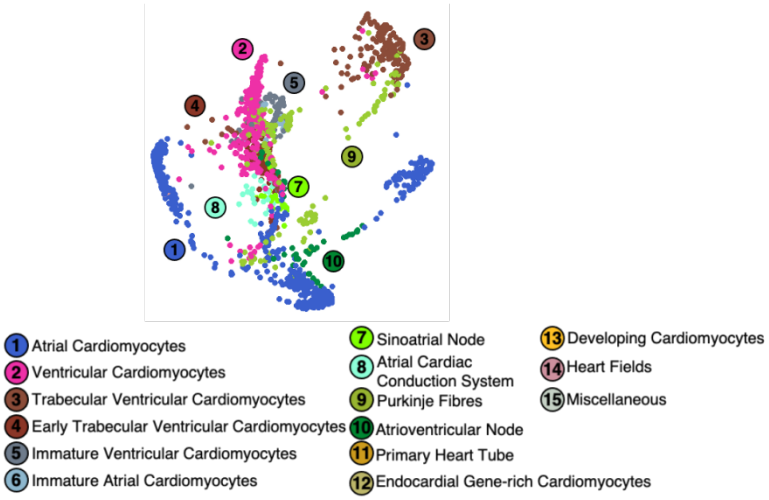

Figure 3.4.1 A PHATE plot of the *Dbh*$^{+}$ cardiomyocyte subpopulation in the developing murine heart. Numbered labels indicate the cell type with the corresponding colour on the PHATE plot.

Cell type	Cell Number that are Dbh+	Percentage of cell type that is Dbh+
Atrial CMs	1575	2.13
Atrial CCS	29	3.82
AVN	59	12.14
Developing CMs	5	0.63
Endocardial gene-rich CMs	2	0.14
Early Trabecular Ventricular CMs	123	2.26
Heart Fields	5	0.72
Immature Atrial CMs	17	0.97
Immature Ventricular CMs	72	1.04

Primary Heart Tube	5	0.89
Purkinje Fibres	205	12.76
SAN	24	8.39
Trabecular Ventricular CMs	170	4.18
Ventricular CMs	300	3.9

Table 3.4.2 The number of *Dbh*$^{+}$ cells and their percentage in each cell type based on the scRNA-seq analysis.

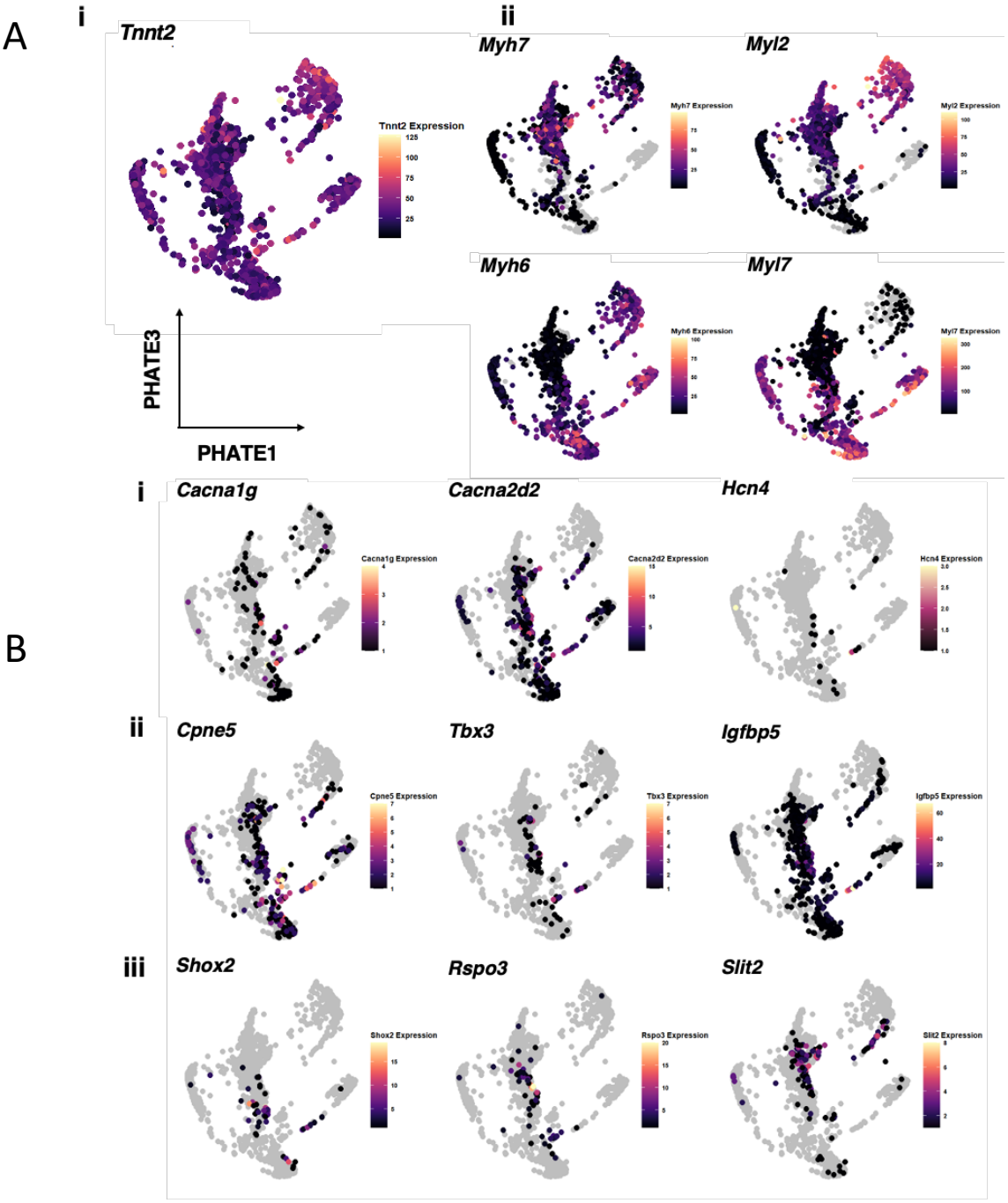
A
i
Tnnt2
Tnnt2 Expression
125
100
75
50
25
PHATE3
PHATE1
ii
Myh7
Myh7 Expression
Myl2
Myl2 Expression
Myh6
Myh6 Expression
Myl7
Myl7 Expression
B
i
Cacna1g
Cacna1g Expression
Cacna2d2
Cacna2d2 Expression
Hcn4
Hcn4 Expression
ii
Cpne5
Cpne5 Expression
Tbx3
Tbx3 Expression
Igfbp5
Igfbp5 Expression
iii
Shox2
Shox2 Expression
Rspo3
Rspo3 Expression
Slit2
Slit2 Expression

C

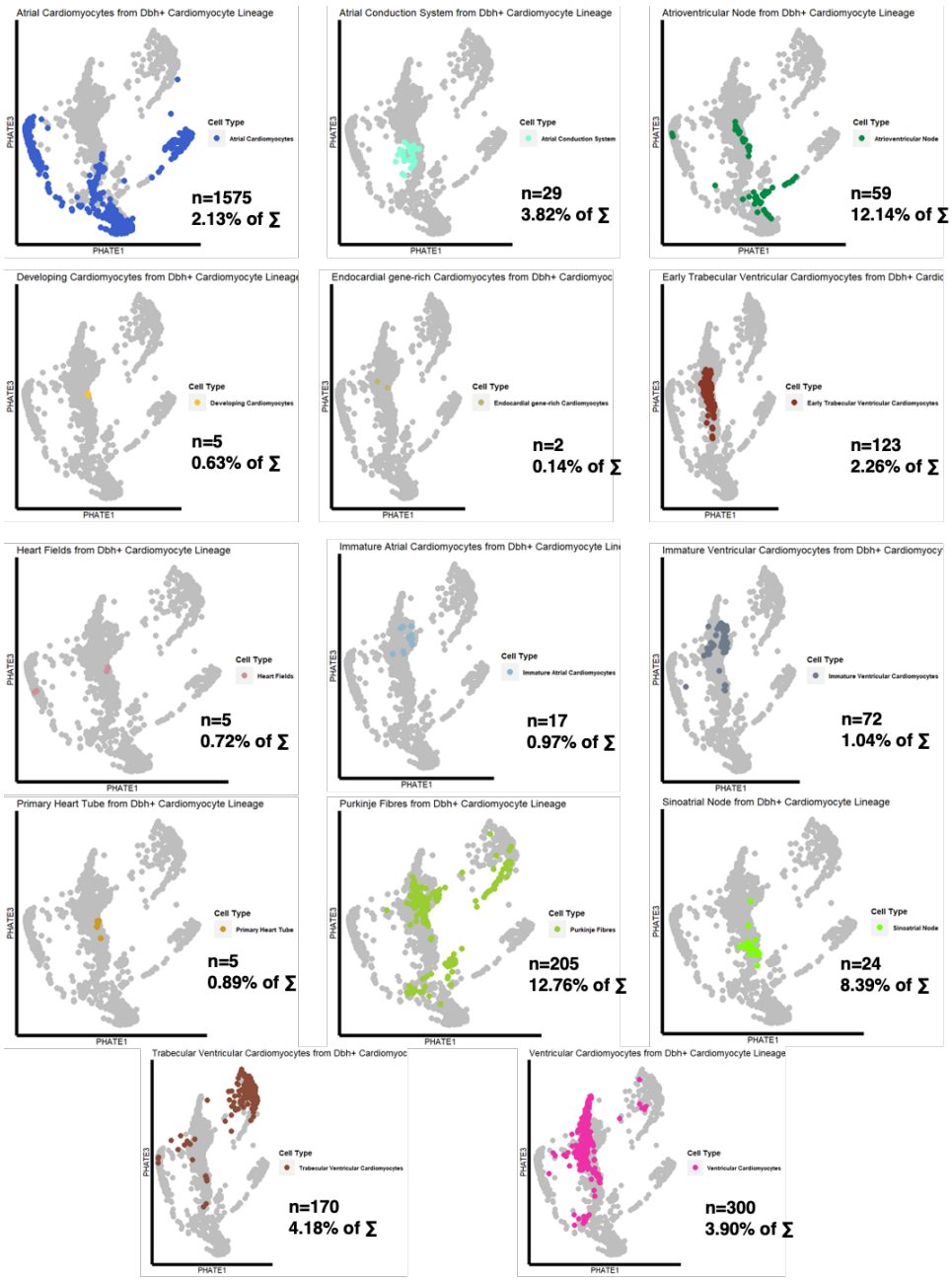

Figure 3.4.3 *Dbh*$^{+}$ cardiomyocytes express the expected general cardiomyocyte markers, and more specific cardiac conduction system-associated genes. A. *Dbh*$^{+}$ cardiomyocytes express general cardiomyocyte (i) and specific atrial and ventricular cardiomyocyte genes (ii). B. *Dbh*$^{+}$ cardiomyocytes widely express cardiac conduction system associated markers in terms of ion channels (i), developmental marker genes and transcription factors (ii & iii). C. Cell types and percentages from *Dbh*$^{+}$

cardiomyocytes. Each panel displays a single cell type highlighted in colour and displaying the number of this cell type identified in the *Dbh*$^{+}$ cardiomyocyte population. The percentage given is the number of *Dbh*$^{+}$ cardiomyocytes for that given type, over the total number of cardiomyocytes of that type. ∑ defines the total number of cells of a given type.

3.5 Single cell RNA sequencing results revealing the potential role of *Dbh*$^{+}$-CM in CCS

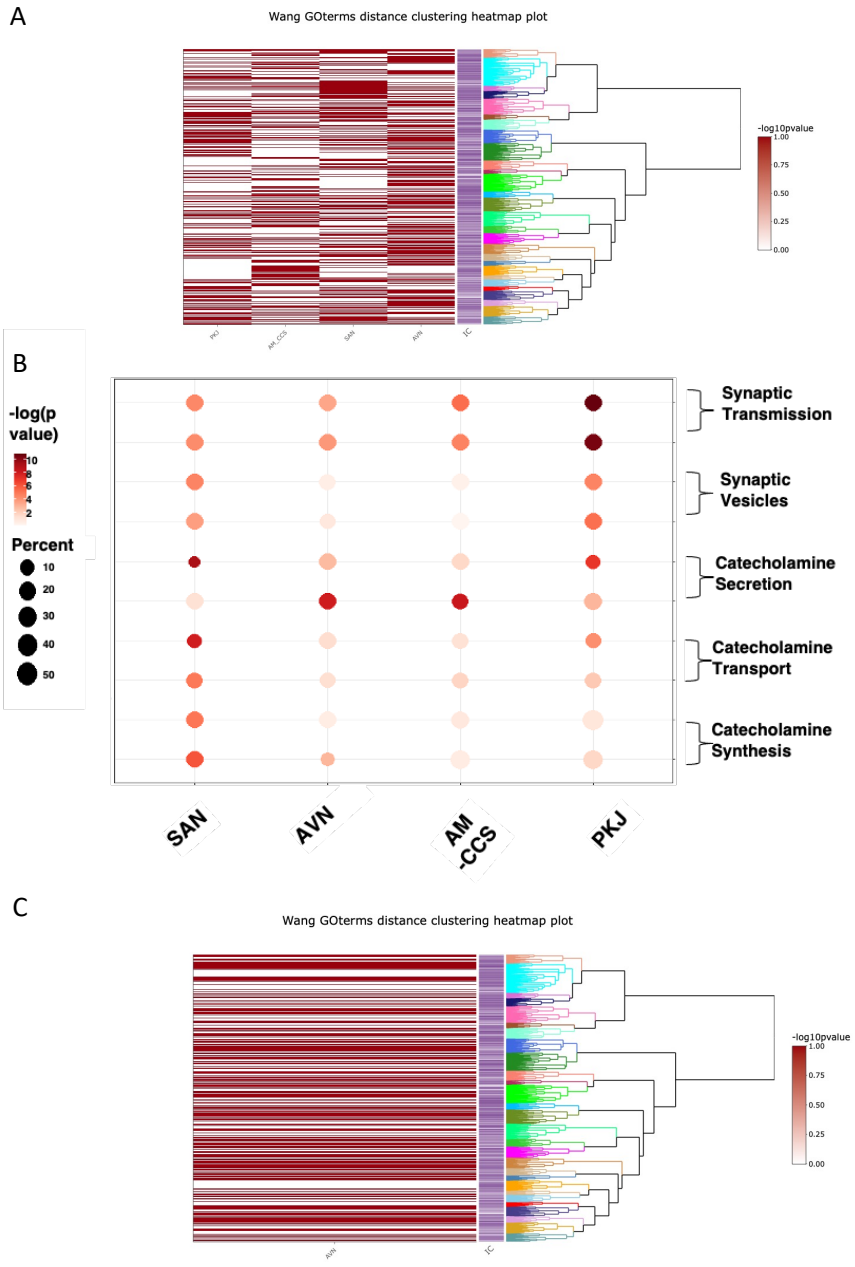

Figure 3.5.1 GO analysis for *Dbh*$^{+}$ and *Dbh*$^{-}$ cells in the cardiac conduction system. A. Heatmap plot showing the Wang GO terms between *Dbh*$^{+}$ and *Dbh*$^{-}$ cells. B. Selected GO terms enriched in differential gene expression results between *Dbh*$^{+}$ and *Dbh*$^{-}$

cardiac conduction system. Percent is the percent of genes enriched that are associated with each GO term. p-values are unique to each row, as the precise background used for testing enrichment was specific to each cell type. C. GO terms in the AVN region.

To determine whether *Dbh* expression in *Dbh*$^{+}$-CMs is associated with any functional differences to conventional cardiomyocytes, we utilised the bioinformatic data mining technique of Gene Ontology (GO), assessing for enrichment of shared functions across genes differentially expressed by the *Dbh*$^{+}$-CMs within the CCS shown in Figure 3.5.1A-C. The analysis suggested that within the CCS, *Dbh*$^{+}$ and *Dbh*$^{-}$ CMs differentially expressed genes related to functions like cardiac development, heart contractile function and catecholaminergic function. Overall, the analysis indicated that within the most component of CCS including SAN, AVN and PKJ, *Dbh*$^{+}$ and *Dbh*$^{-}$ CMs differentially expressed genes related to catecholamine synthesis (GO:0042423, GO:0042415), transport (GO:0090493, GO:0015872), and secretion of catecholamines (GO:0046879, GO:0050432), concurrently with genes related to vesicular storage (GO:0099003, GO:0099504), and synaptic transmission (GO:0007268, GO:0099537) (Figure 3.5.1). The potential catecholaminergic related functions exerted by *Dbh*$^{+}$-CMs in CCS play an important role in cardiac conduction and heart contraction. To be specific, *Dbh*$^{+}$-CMs in AVN is highly related to the cardiac development including atrial cardiac muscle tissue development (GO:0003228), Trabecula formation (GO:0060343), muscular septum morphogenesis (GO:0003150), ventricular septum morphogenesis

(GO:0060412), regulation of heart morphogenesis (GO:2000826) and cardiac pacemaker cell development (GO:0060926). Compared to *Dbh*$^{-}$ CMs, it is suggested that *Dbh*$^{+}$-CMs participate in and even play an important role in heart morphogenesis and cardiac pacemaker development. Also *Dbh*$^{+}$-CMs contribute to cardiac contractile function as implied by the GO analysis such as regulation of the force of heart contraction (GO:0002026), regulation of cardiac muscle cell contraction (GO:0086004), and regulation of cardiac conduction (GO:1903779). Although these are all the cells located in the AVN region, *Dbh*$^{+}$-CMs weigh higher than *Dbh*$^{-}$ CMs in terms of the physiological contractile function. Moreover, *Dbh*$^{+}$-CMs perform well in the catecholaminergic related functions including catecholamine uptake (GO: 0090493), dopamine secretion (GO: 0014046), catecholamine secretion (GO:0050432) and norepinephrine (NE) secretion and transport (GO0048243, GO0048241). As we know, Dbh is a key enzyme responsible for the conversion from dopamine to NE in the process of catecholamine biosynthetic pathway. The GO analysis indicates that with the existence of *Dbh* gene, *Dbh*$^{+}$-CMs are involved in the process of biosynthesis, uptake and release of catecholamines. And this further explains the potential contractile function of *Dbh*$^{-}$ CMs above that undergoing the activities with catecholamine activates the PKA and triggers the phosphorylation cascade to eventually support physiological muscle contraction.

Chapter 4: Spatial transcriptomic analysis of development of murine cardiac conduction system by using high resolution spatially resolved transcriptomics (SrT) technology

Measurement of the spatial expression of molecules in tissue is essential for understanding organ and tissue formation and function. Given the complexity and incomplete understanding of cardiac development such as its morphogenesis and maturation, it is important to establish powerful molecular technologies that enable simultaneous analysis of organ-wide spatial gene expression patterns and cellular heterogeneity at cellular resolution. Current rapid development of transcriptomic technologies such as single-cell RNA sequencing (scRNA-seq) have facilitated our study on heart development by revealing and characterizing previously uncharacterized cell types including cardiogenesis, focusing on subpopulations of cells isolated using predefined gene(Goodyer & Wu, 2018b; Lescroart et al., 2018; G. Li et al., 2016; Tyser et al., 2021; Xiong et al., 2019). However, scRNA-seq does not provide spatial information, and thus has a disadvantage in studying the complex cellular interplay and intercellular communications and tissue morphogenesis spatially. Recent emerging spatial transcriptomic technology presents a major advance in high-throughput profiling of in situ gene expression spatially towards the systematic understanding of the development and homeostasis of complex tissue molecular architecture. BGI scientists(A. Chen et al., 2021) developed a spatio-temporal enhanced resolution omics-sequencing (Stereo-seq) that combines DNA nanoball (DNB) patterned array

chips and in situ RNA capture. This approach allows high throughput sample transcriptomic profiling of histological sections at unprecedented nanoscale (200 nm size per spot and 500 or 700 nm spot-spot space distance) to achieve cellular and even subcellular spatial resolution. In this chapter, I applied this advanced Stereo-seq technology with the help of BGI group, aiming to conduct a systemic analysis of the molecular architectures for understanding of cardiac morphogenesis and maturation as well as characterisation of Dbh+ derived cardiomyocytes.

4.1 Sample preparation for SrT analysis

To validate the identification of *Dbh*$^{+}$-CMs, a new nanoscale spatially resolved transcriptomic technology (SrT) was used called Stereo-seq(A. Chen et al., 2021), to analyse this *Dbh*$^{+}$ cardiomyocyte population, including its spatial distribution, in the developing and mature murine hearts. A *Dbh*$^{+}$ cell lineage tracing reporter line was established by crossing the *Dbh*-Cre line with B6.Cg-Gt(ROSA)26Sortm9(CAG-tdTomato)Hze/J strain (Stock No. 007909, Jackson Labs) for genetic fate mapping of *Dbh*$^{+}$-CMs (Figure 4.1.1a). Following sampling, library preparation, and quality control, we had at least n = 3 sections for embryonic hearts from *Dbh*Cre/R26-tdTomato mice at E12.5, E14.5, and P3, with mean UMI and genes respectively of 4053, 1399 (E12.5), 1940, 746 (E14.5), and 1291, 562 (P3) per 20 x 20 DNA-labelled nano ball (14 × 14 μm) bin (Figure 4.1.1b). The ssDNA images of mouse heart tissue from each stage were

captured before the Stereo-seq analysis (Figure 4.1.1c). The gradual decrease in mean UMI and genes across stages likely reflects the decrease in cell number captured per bin, as cells grow in size across stages. TdTomato-coding sequences in our generated libraries were not readily detectable due to the use of 3'-end sequencing, thus the expression levels of Wpre (expressed at 3'-end of the TdTomato reporter cassette construct) (Figure 4.1.1a) were used as a proxy for TdTomato expression in our sequencing data, which is used to distinguish *Dbh*$^{+}$- and *Dbh*$^{+}$-derived cells.

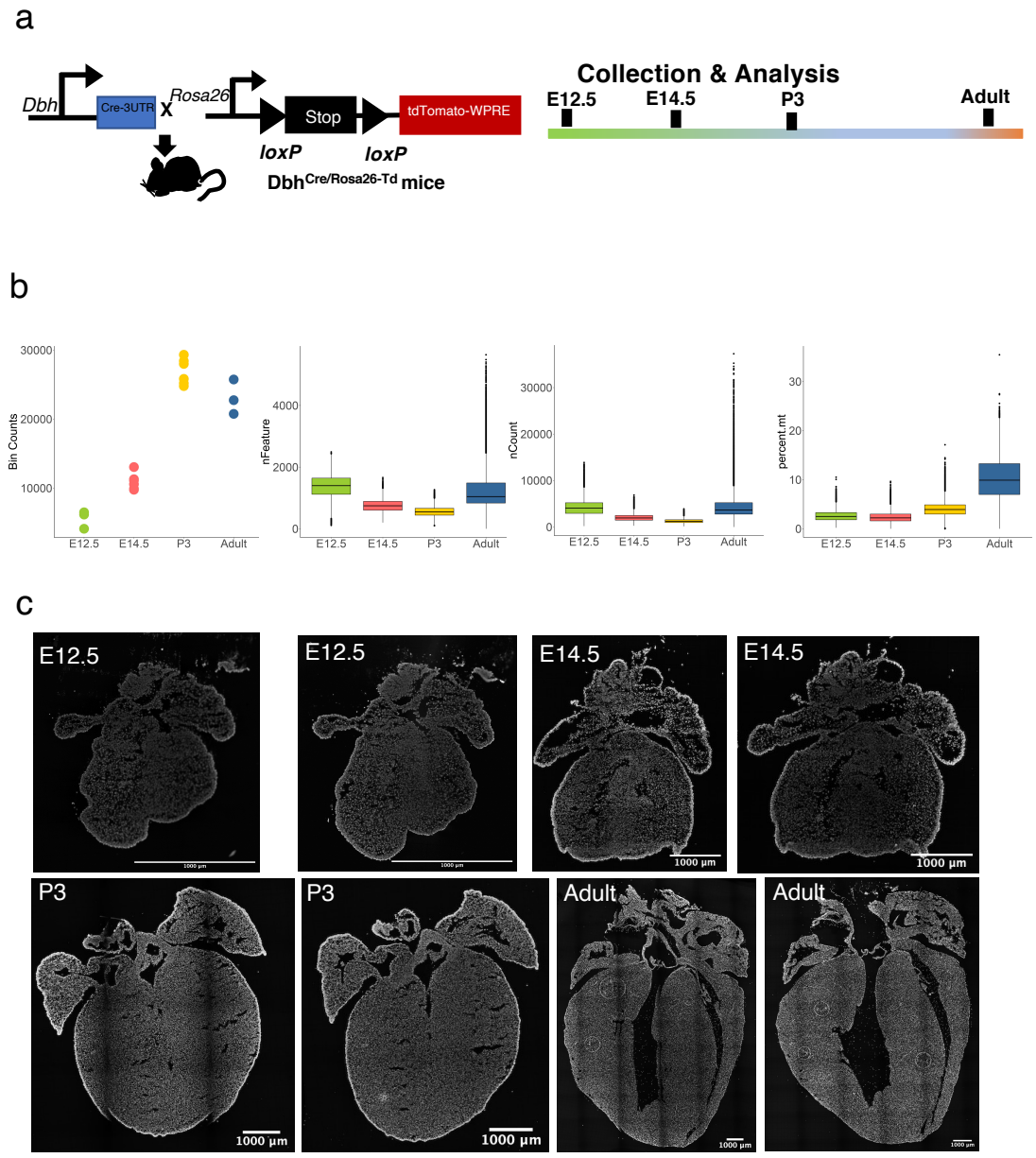

Figure 4.1.1 a. Schematic of Dbh-tdTomato reporter line creation and analysis for spatial transcriptomics. b. Total bin number, nFeature, and mitochondrial percentage across different stages. c. ssDNA staining images of mouse heart tissue sections analyzed by Stereo-seq across different stages. Scale bar: 1000 μm.

4.2 Identification of cell types throughout development by using different clustering methods

Unsupervised clustering was used to identify sub-populations at each stage. Overall, a range of working and non-working cardiomyocyte populations were identified in the unsupervised analysis (Figure 4.2.1). All sections underwent the quality control test and the removal of batch effect. After a series of preliminary analysis, over fifty raw clusters from each stage were identified and major cell types were then assigned to each raw clusters depending on their differential gene expression. UMAP visualized the assignment of clusters to each cell type throughout the developmental stages to P3 demonstrated in Figure 4.2.1. It is worth noting that the subpopulations of CCS were unveiled including SAN, AVN, nodal and PKJ shown in Figure 4.2.1. Finally, major cell populations were identified and the expression profiles of key markers for each cell type were displayed by a dot plot in Figure 4.2.2.

The performance of cell types identified in previous scRNA-seq was sought to ascertain, which could be computationally integrated with the Stereo-Seq dataset. The selection of marker genes for cell types identified in scRNA-seq data prior to integration remains vital for accurate and meaningful integration. The marker genes were identified through a supervised learning pipeline implemented in SMASH(Nelson et al., 2021) (Figure 4.2.3), and then the top 50 genes per cell type were used as a reference library for computational probabilistic cell-type assignment in identifying probable major cell

types for each Stereo-Seq bin (Figure 4.2.4-Figure 4.2.6)(Cable et al., 2021; Loher & Karathanasis, 2020). In Figure 4.2.4a, 4.2.5a and 4.2.6a, the major cell types were integrated, assigned and visualized throughout different developmental and postnatal stages. Besides, typical CCS cell types including SAN, AVN and PKJ were specifically assigned, that is consistent with their anatomical locations shown in Figure 4.2.4b-c, 4.2.5b-c, 4.2.6b-c.

Overall, the integrated assignments were mostly consistent with prior expectations. However, it is noted that 'AM-CCS', mapped in a non-specific manner across the atrial myocardium, likely reflecting the weaker expression of CCS markers in AM-CCS, compared to the SAN/AVN, but with expression of more generic atrial markers (Figure 3.3.4) leading to the AM-CCS being interpreted as this wider atrial fate. Those cell types with imperfect integration often appear to have mapped to cell types with expectedly similar transcriptomic signals, and analysis of the robust cell type decomposition (RCTD) scores for certain populations suggests that these cell types may still be identified by this supervised learning technique, but that the final highest predictive score for each cell might be obscuring this complexity (Figure 4.2.7).

a

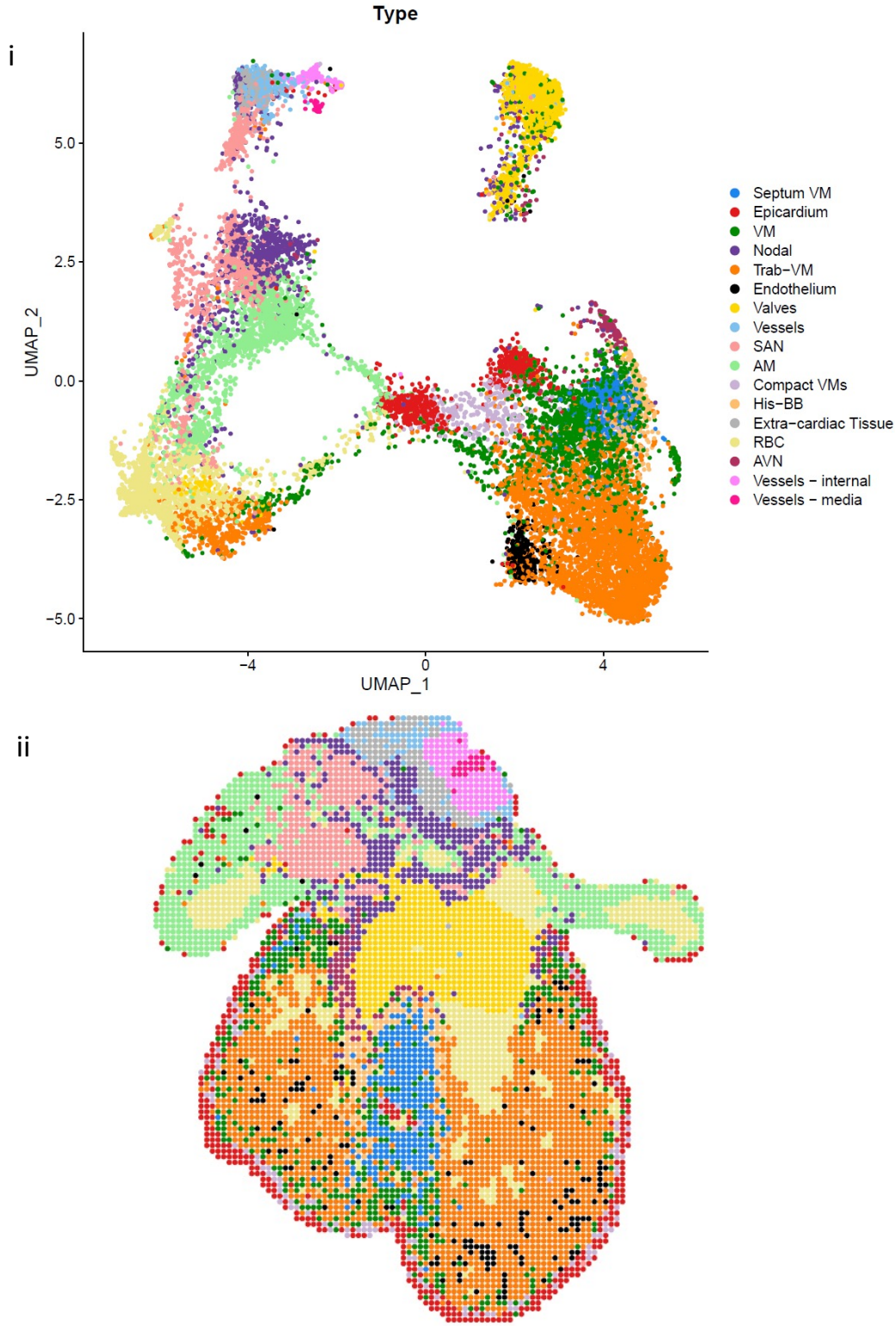
Type
i
5.0
2.5
0.0
−2.5
−5.0
UMAP_2
−4
0
4
UMAP_1
Septum VM
Epicardium
VM
Nodal
Trab−VM
Endothelium
Valves
Vessels
SAN
AM
Compact VMs
His−BB
Extra−cardiac Tissue
RBC
AVN
Vessels − internal
Vessels − media
ii

b

i

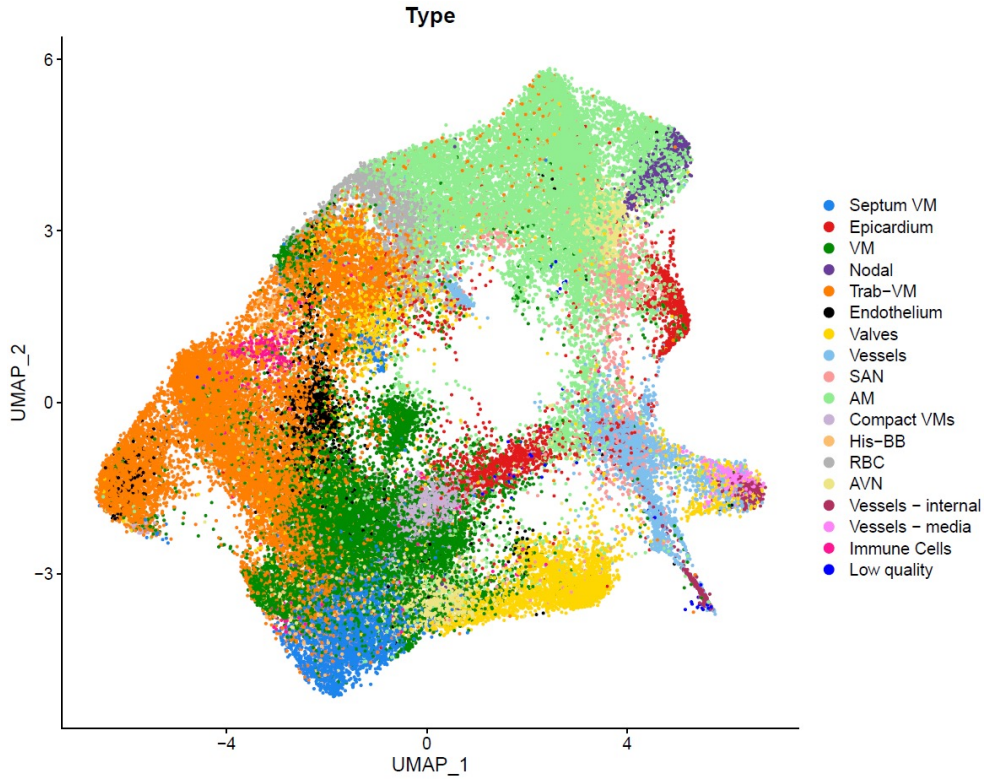
Type
UMAP_2
UMAP_1
6
3
0
−3
−4
0
4
Septum VM
Epicardium
VM
Nodal
Trab−VM
Endothelium
Valves
Vessels
SAN
AM
Compact VMs
His−BB
RBC
AVN
Vessels − internal
Vessels − media
Immune Cells
Low quality

ii

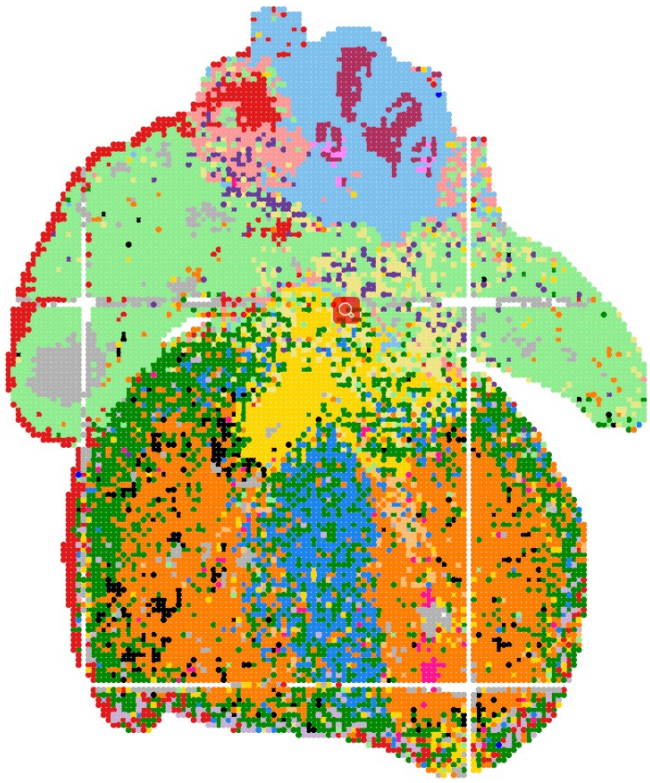

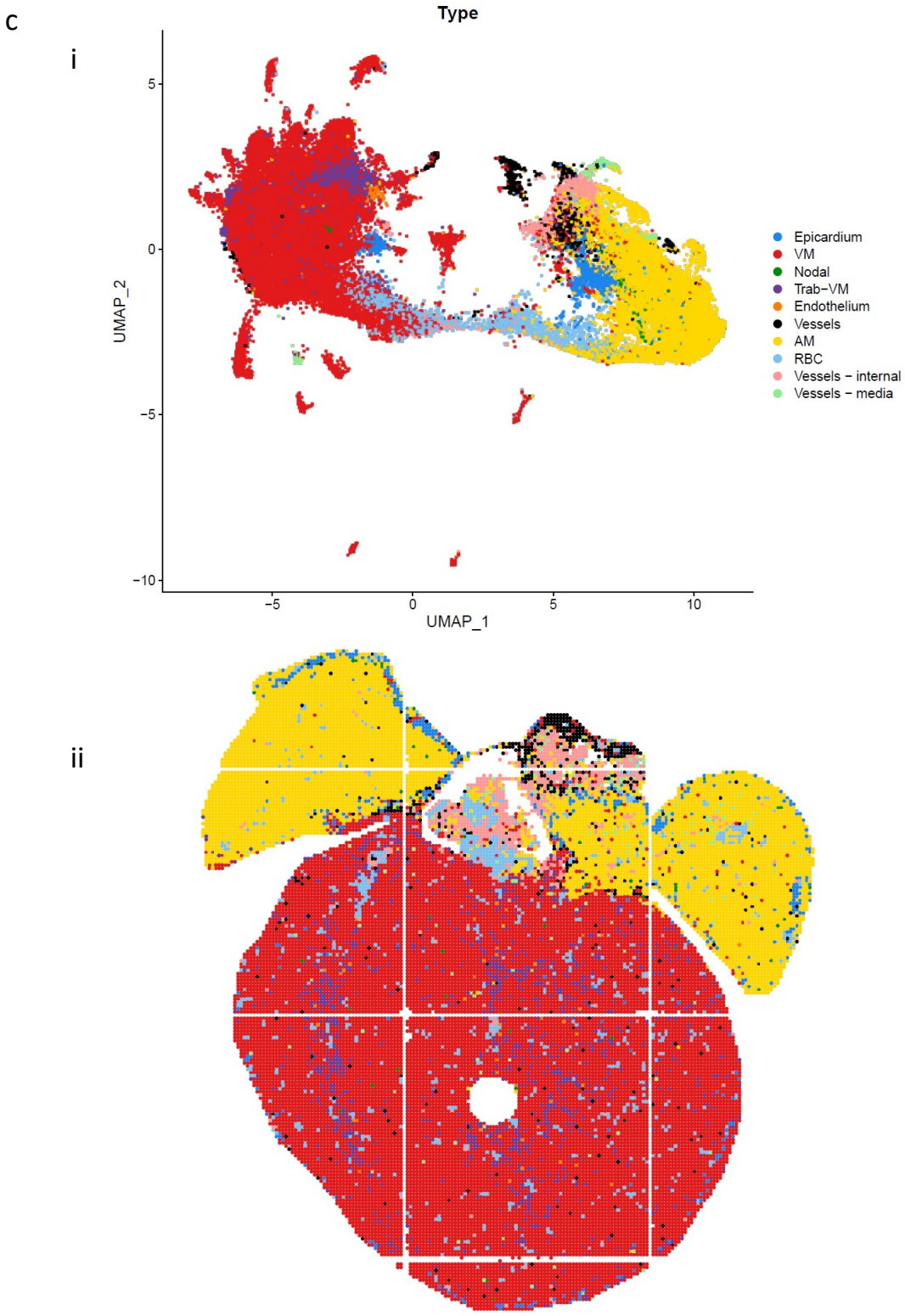

Figure 4.2.1. Unsupervised clustering identified cell types across the developing murine heart.

a. (i) UMAP visualized the cluster assignment for each cell type at E12.5.

(ii)The slices from E12.5, coloured by cell type identified through unsupervised cluster and corresponding to cell labels at the figure base.

b. (i) UMAP visualized the cluster assignment for each cell type at E14.5.

(ii) The slice from E14.5, coloured by cell type identified through unsupervised cluster and corresponding to cell labels at the figure base.

c. (i) UMAP visualized the cluster assignment for each cell type at P3.

(ii) Two representative slices from P3, coloured by cell type identified through unsupervised cluster and corresponding to cell labels at the figure base.

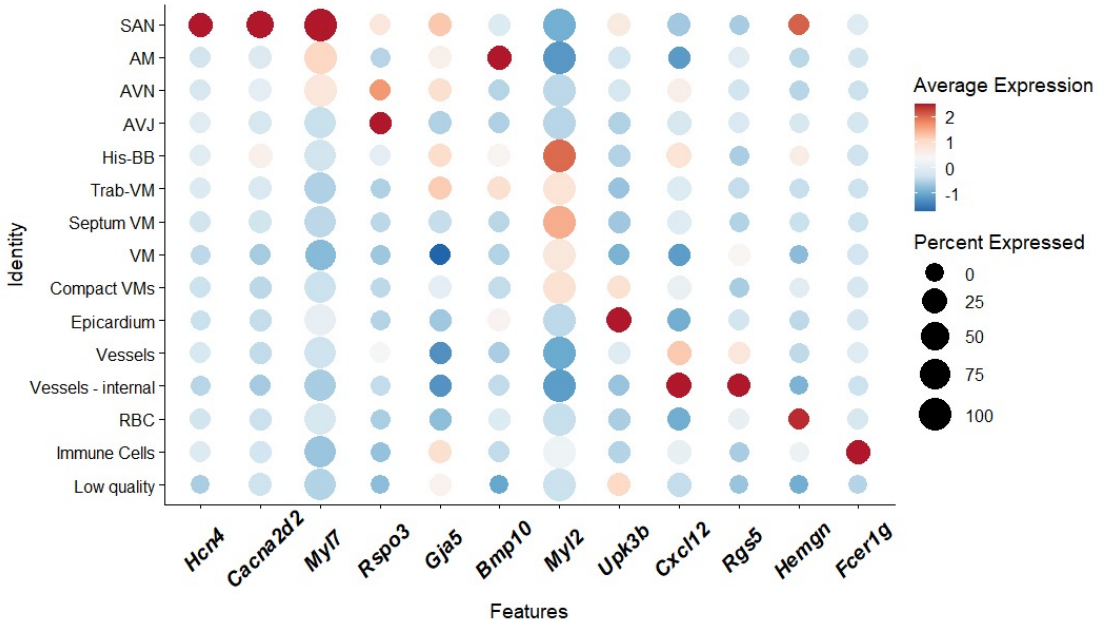

Figure 4.2.2. Unsupervised clustering of spatial transcriptomics data enables robust identification of underlying anatomy at an oligo-cellular and tissue-level high resolution. A dot plot displays the z-scored expression of a range of key marker genes across different populations identified across 3 stages of heart slices collected (E12.5, E14.5, and P3).

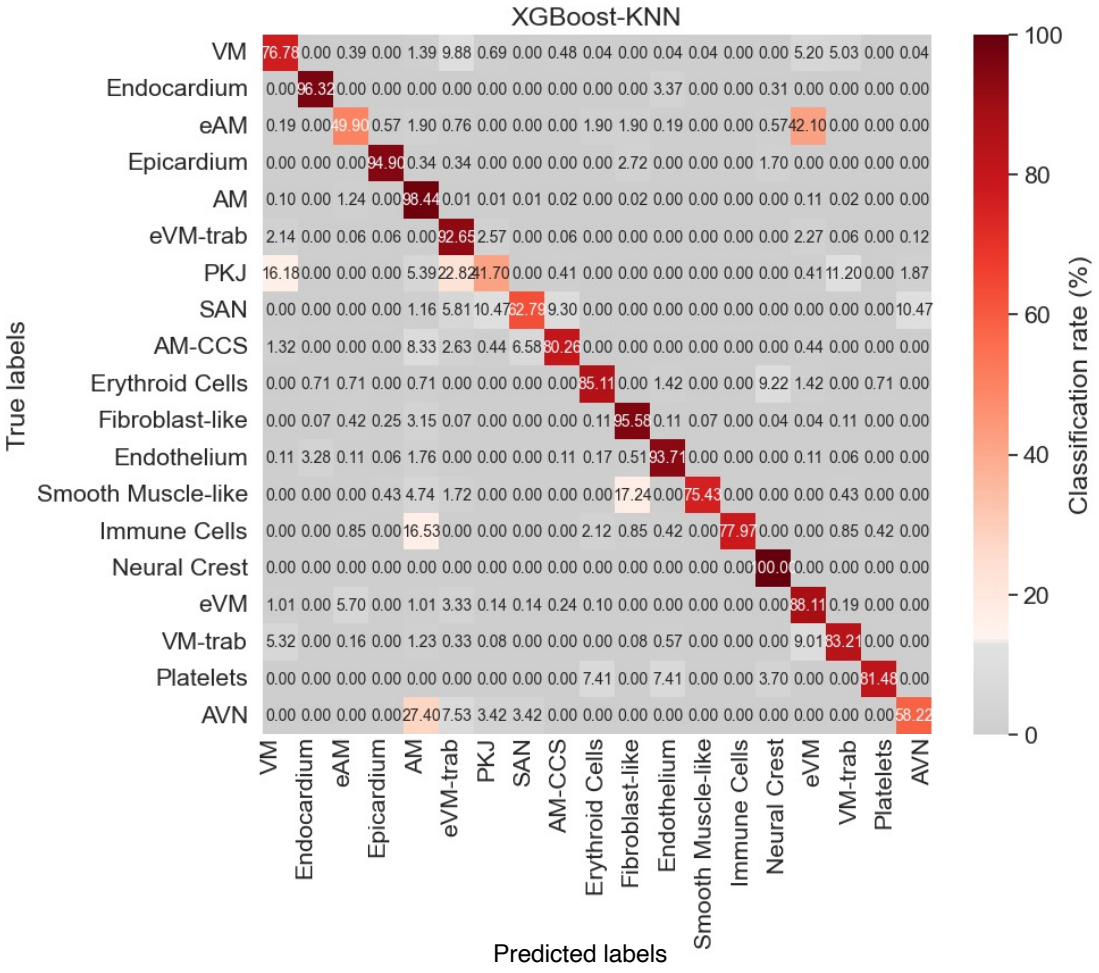

Figure 4.2.3. Supervised machine learning techniques can produce accurate classifiers for cell type based on gene expression and marker gene selection.

SMASH (Scalable Marker (gene) Signal Hunter) is applied to identify biologically relevant marker genes with robust computational signatures sufficient to facilitate cross-dataset and cross-platform supervised learning-based classification of pixels within our spatial transcriptomics data with maximally informative, but interpretable, unique gene sets per cell type as classification label. This matrix demonstrates the highly accurate classification of cell types by a trained classifier, on our separate test data, for subsequent identification of cell type marker genes in single-cell RNA sequencing data by SMASH. Y-axis true labels refers to the set of cell-wise labels

provided for our dataset, based on our initial analysis. The x-axis predicted labels are the same labels, with a high number (dark red) at the intersect of the two in the main body of the matrix indicating that the trained classifier was able to correctly identify the cell label. The scale shows the percentage of classification, with dark red indicating a higher percentage of the true label on y, was predicted to be the cell type on the x axis. Each row sums to 100.00, representing all the cells within the given cell type label on the y-axis, have been classified with predicted label(s).

Abbreviations: VM – ventricular cardiomyocytes; eAM – immature atrial cardiomyocytes; AM – atrial cardiomyocytes; eVM-trab – early trabecular ventricular cardiomyocytes; PKJ – Purkinje fibres; SAN – sinoatrial node; AM-CCS – atrial cardiac conduction system; eVM – immature ventricular cardiomyocytes; VM-trab – trabecular ventricular cardiomyocytes; AVN – atrioventricular node.

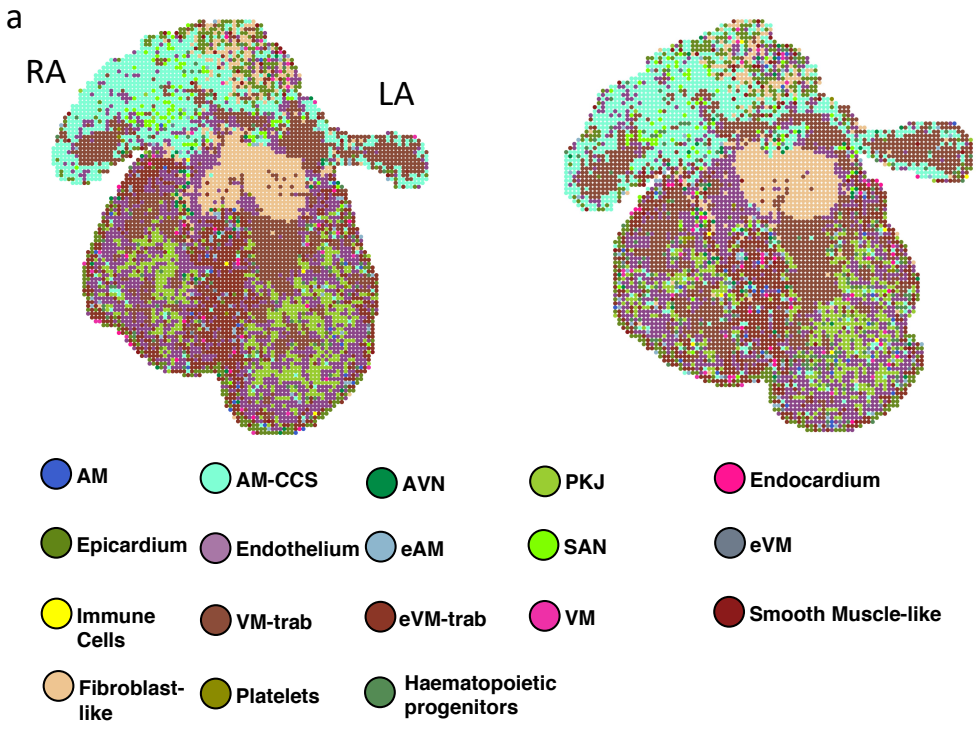

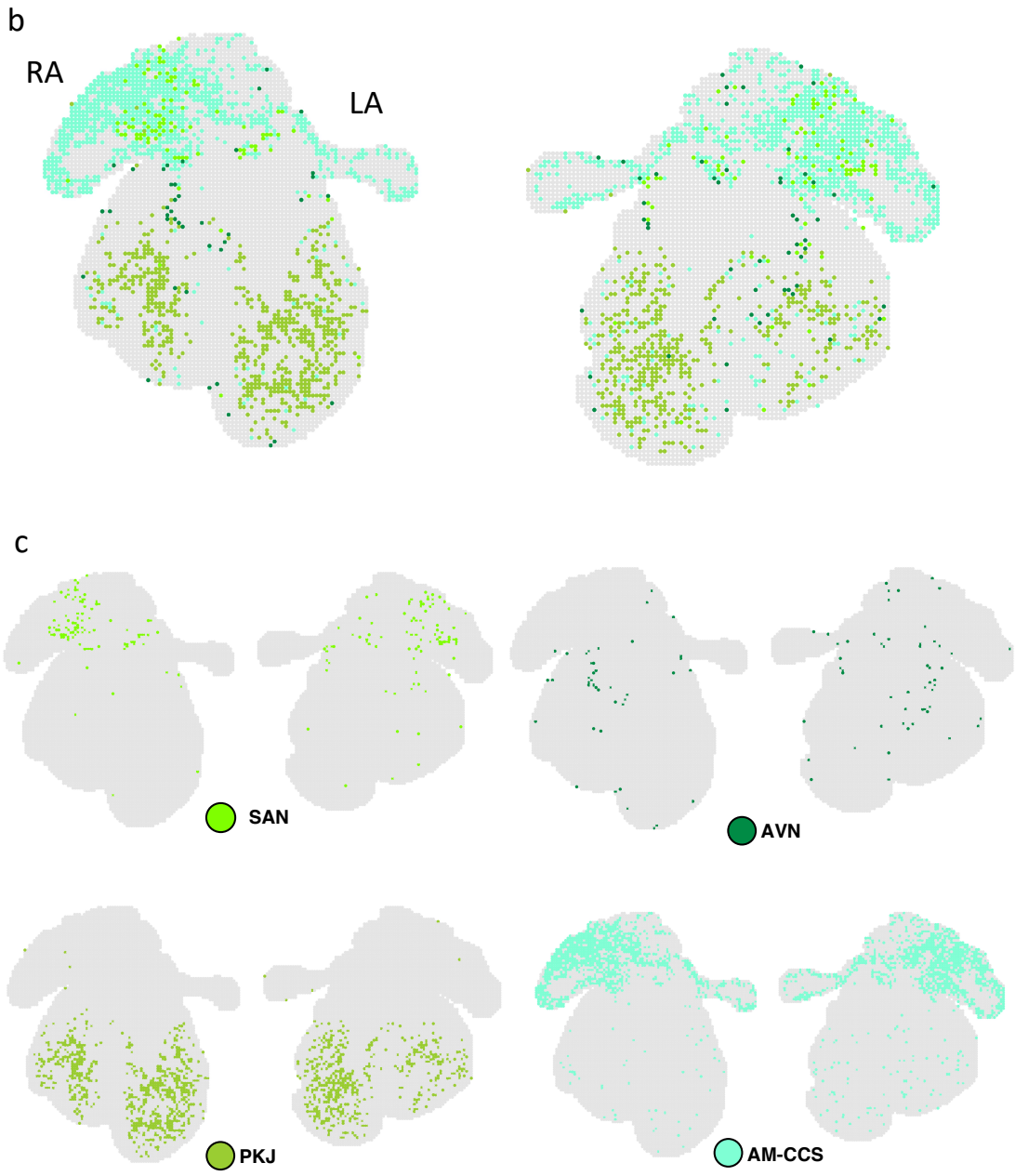

Figure 4.2.4 Integrated single-cell and spatial transcriptomics resolves cell types across the heart at E12.5.

a. Two representative slices from E12.5, coloured by cell type identified through RCTD predicted cell type and corresponding to cell labels at the figure base.

b. Two representative slices from E12.5 showing the merged major cardiac conduction system cell types identified through RCTD predicted cell type.

c. Two representative slices from E12.5 showing the SAN, AVN, PKJ and AM-CCS cell

types separately identified through RCTD predicted cell type and corresponding to cell labels at the figure base.

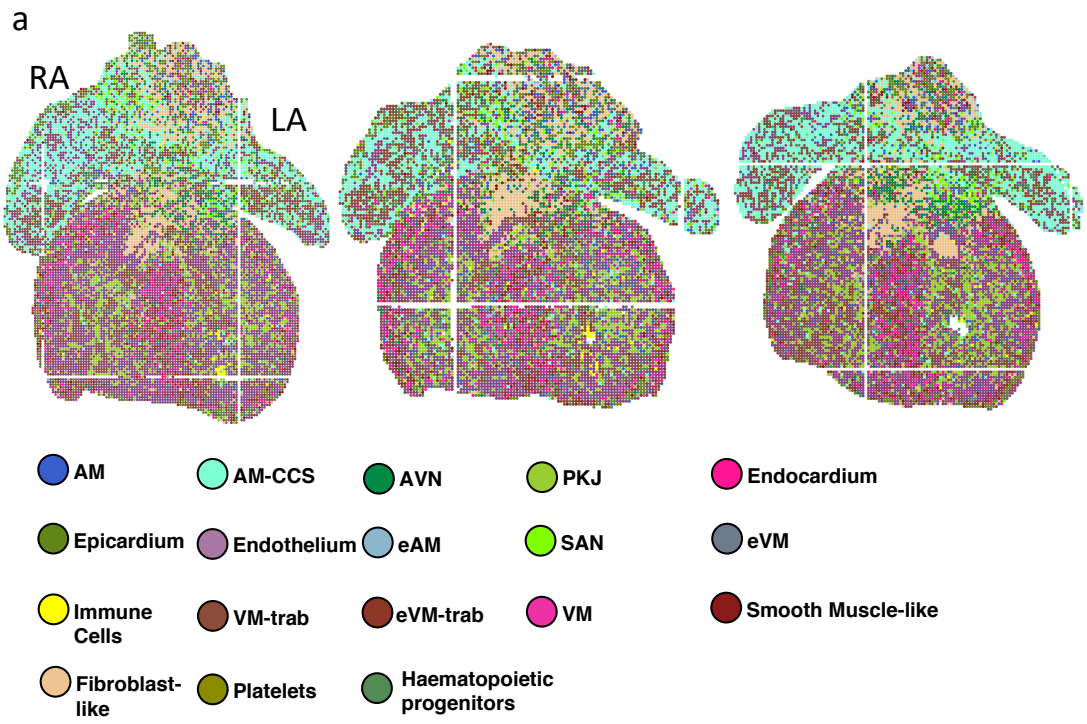

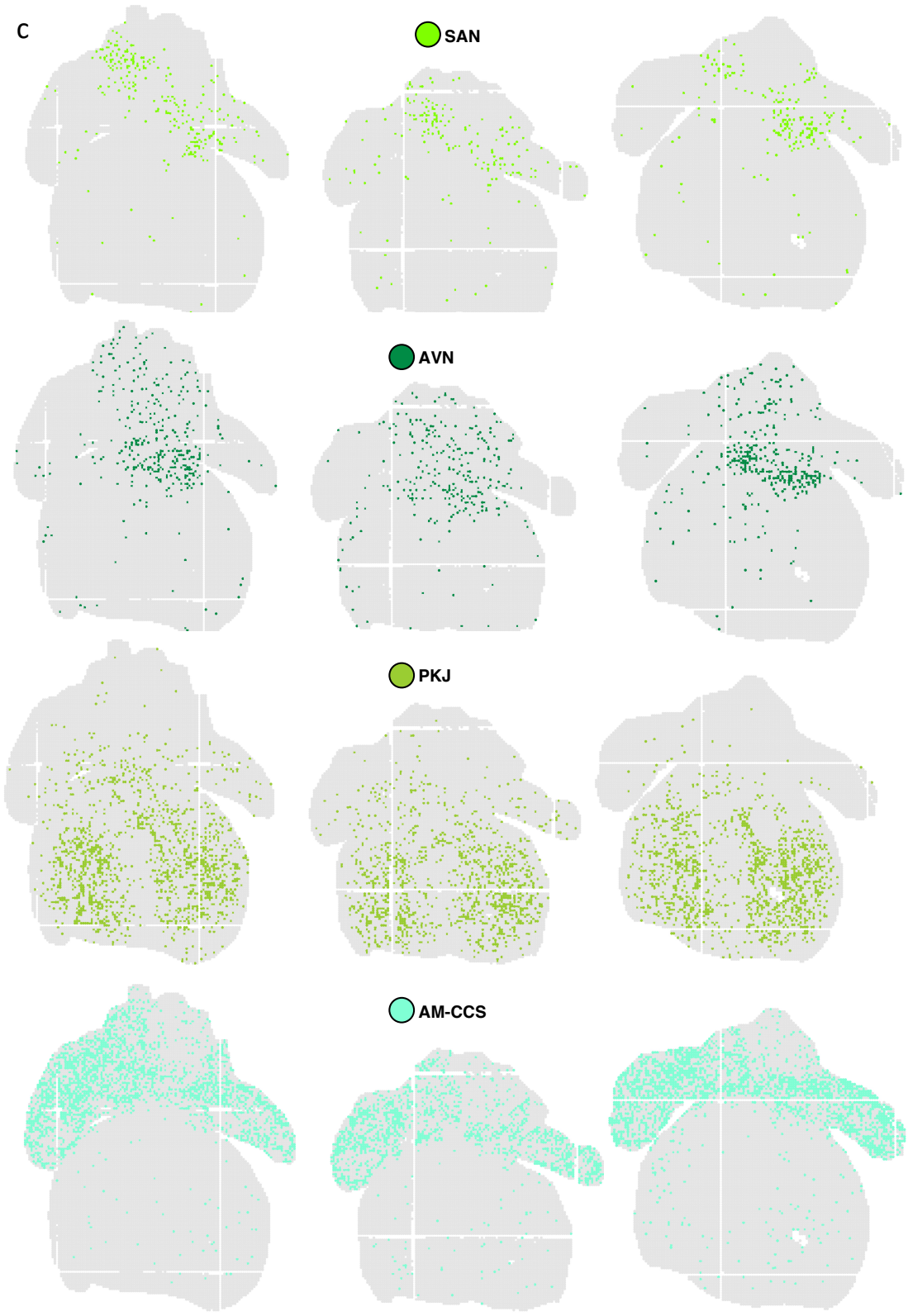

Figure 4.2.5 Integrated single-cell and spatial transcriptomics resolves cell types across the heart at E14.5.

a. Three representative slices from E14.5, coloured by cell type identified through RCTD predicted cell type and corresponding to cell labels at the figure base.

b. Three representative slices from E14.5 showing the merged major cardiac conduction system cell types identified through RCTD predicted cell type.

c. Three representative slices from E14.5 showing the SAN, AVN, PKJ and AM-CCS cell types separately identified through RCTD predicted cell type and corresponding to cell labels at the figure base.

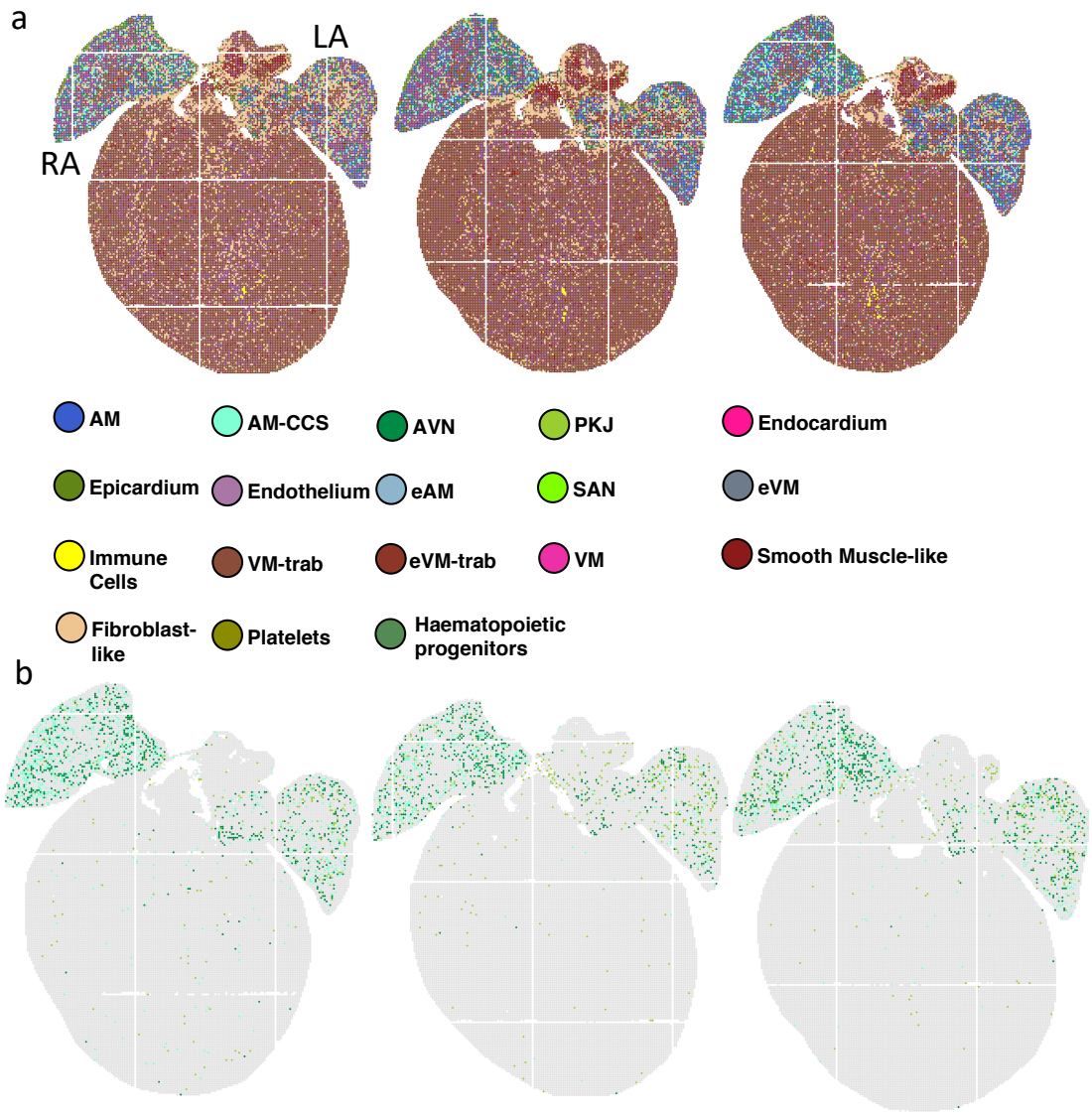

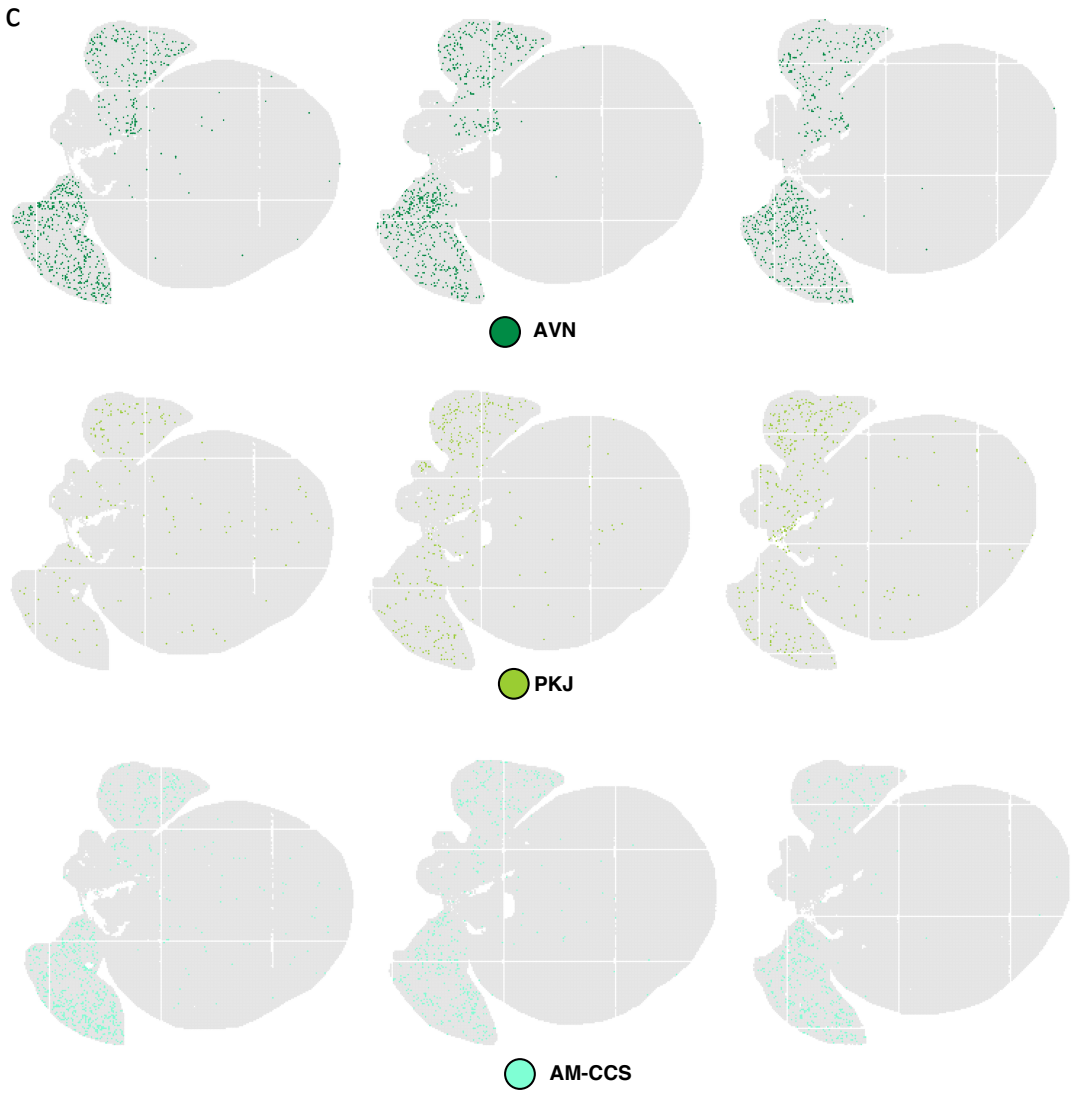

Figure 4.2.6. Integrated single-cell and spatial transcriptomics resolves cell types across the heart at P3.

a. Three representative slices from P3, coloured by cell type identified through RCTD predicted cell type and corresponding to cell labels at the figure base.

b. Three representative slices from P3 showing the merged major cardiac conduction system cell types identified through RCTD predicted cell type.

c. Three representative slices from P3 showing the AVN, PKJ and AM-CCS cell types separately identified through RCTD predicted cell type and corresponding to cell

labels at the figure base.

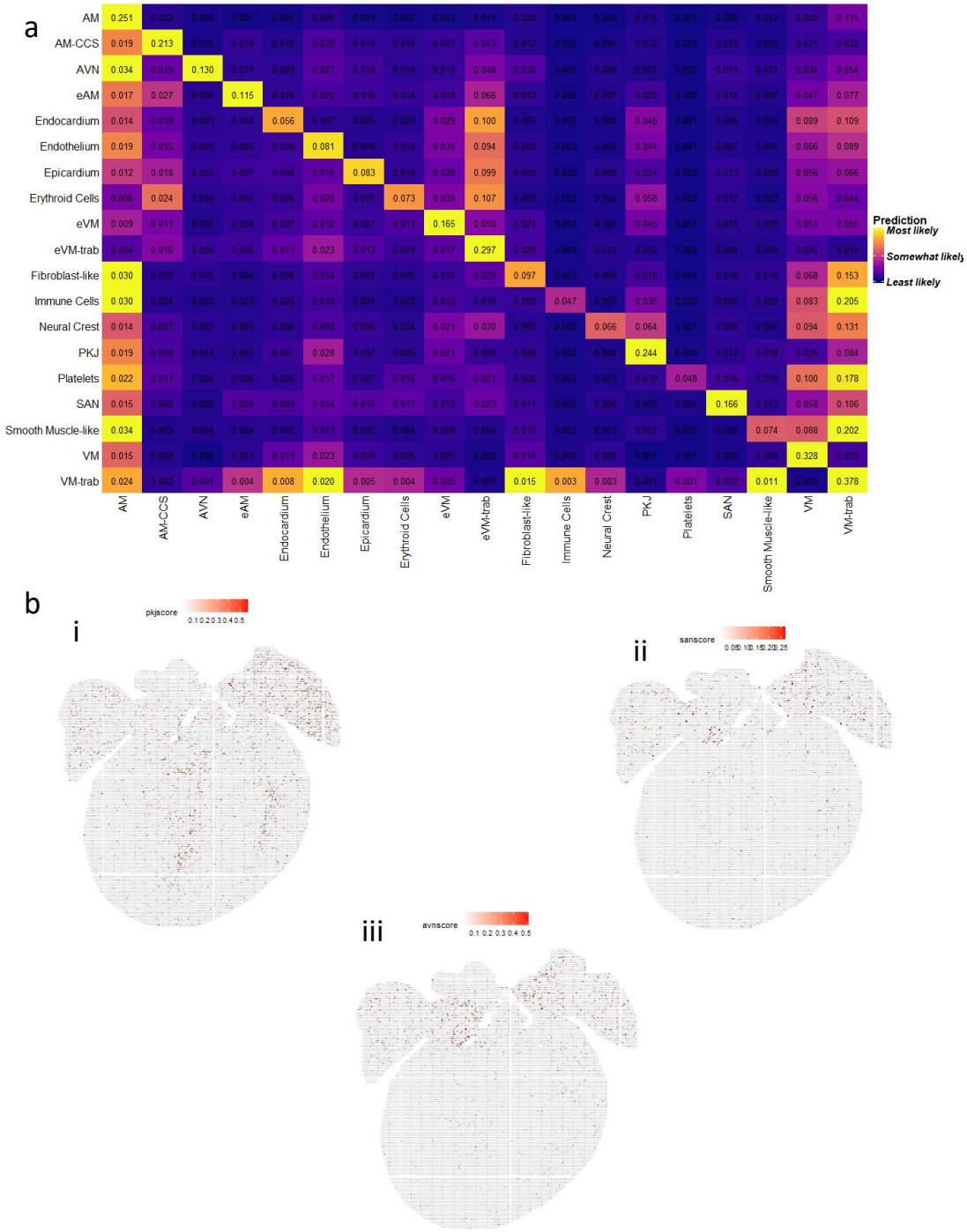

Figure 4.2.7. RCTD integrated single-cell and spatial transcriptomics still was able to

identify rare cell types, even if they were not considered the primary cell type in a pixel.

a. A heatmap demonstrating prediction scores from RCTD across all 3 developmental stages. Pixels were aggregated by their primary (most likely) predicted cell type label from RCTD, and the mean prediction scores for these cell type clusters then identified. Rows represent the primary cell type labels, and the columns represent additional predicted labels.

b. i) Slices from P3 hearts, coloured by the RCTD predicted score for Purkinje fibres, with red indicating higher likelihood. ii) Slices from P3 hearts, coloured by the RCTD predicted score for the sinoatrial node, with red indicating higher likelihood. iii) Slices from P3 hearts, coloured by the RCTD predicted score for the atrioventricular node, with red indicating higher likelihood.

Abbreviations: VM - ventricular cardiomyocytes; eAM –immature atrial cardiomyocytes; AM – atrial cardiomyocytes; eVM-trab – early trabecular ventricular cardiomyocytes; PKJ – Purkinje fibres; SAN – sinoatrial node; AM-CCS – atrial cardiac conduction system; eVM – immature ventricular cardiomyocytes; VM-trab – trabecular ventricular cardiomyocytes; AVN – atrioventricular node.

4.3 SrT analysis showing the spatio-temporal transcripts of *Dbh*$^{+}$-derived cardiomyocytes

E14.5 slices contained the most robust populations for the major cell types identified in both unsupervised clustering and RCTD method (Figure 4.3.1 and Figure 4.3.4). Therefore, in E14.5 slices it is verified that *Dbh* expression was identified across the myocardium, and in the CCS, as previous scRNAseq data suggested (Figure 4.3.1). In the a.i and b.i of Figure 4.3.1, selected cell types were labelled and a similar pattern was compared and displayed in the unsupervised analysis that, at E14.5, *Dbh* expression was strongest in the ventricular cardiac conduction system, but also expressed in the atrial and ventricular working cardiomyocytes (Figures 4.3.1 a.ii, b.ii). In contrast, *Wpre* was strongly expressed in the atrial cardiac conduction system and working atrial cell types at E14.5, but less in the ventricular cardiac conduction system or working ventricular cardiomyocytes (Figures 4.3.1 a.ii, b.ii). *Wpre* expression indicates a cell that is either expressing *Dbh* or whose ancestors expressed *Dbh*. *Wpre* appeared to be more strongly expressed in the atrial CCS in SrT, whereas *Dbh* appeared more strongly expressed in the ventricular CCS. The temporal discrepancy between *Dbh* and *Wpre* suggests that although *Dbh* expression is stronger in the ventricular CCS in the more developed CCS, during earlier development *Dbh* expression occurred in the atrial CCS, or their cellular ancestors, before the ventricular CCS: producing the stronger *Wpre* signal from the atrial CCS, not yet robustly mapped to the ventricular CCS.

To confirm where the newly identified cardiomyocyte populations were located within the maturing perinatal CCS, neonatal hearts with SrT were further examined. *Dbh* expression partially overlaps with a range of CCS markers, including *Id2*(Moskowitz et al., 2007), *Hcn4, Gja5, and Cacna2d2*(van Eif et al., 2020) (Figure 4.3.2a). To confirm whether these developmental *Dbh*$^{+}$- and/or *Wpre*$^{+}$-cardiomyocyte populations persisted into adulthood, adult (P56) heart slices were prepared and examined from the *Dbh*Cre/R26-tdTomato mice through SrT. By the adult stage, *Wpre* was enriched in the right atrium, SAN, AVN, and His-Purkinje network similar to neonatal heart (Figure 4.3.2b). Besides, *Wpre* expression has expanded from the overlap with CCS markers, to expression across the myocardium, although with relative enrichment in the ventricles in regions overlapping with CCS markers, particularly in the basal heart (Figure 4.3.2b). However, *Wpre*$^{+}$-cardiomyocytes were more abundant in adult than in neonatal heart with a greater abundance in the RA in particular (Figure 4.3.2b). A smaller number of *Dbh*$^{+}$-CMs were also identified by SrT, with similar spatial expression profiles as *Hcn4* and *Cacna2d2* (Figure 4.3.2c), the two key marker genes for the central CCS(van Eif et al., 2020), confirming persistence of *Dbh*$^{+}$-CMs in the mature postnatal heart.

We further analysed the abundance of *Dbh*$^{+}$- and *Wpre*$^{+}$-cardiomyocyte populations in developing and adult hearts and their coexpressing with four key CCS marker genes *Id2, Hcn4, Gja5, Cacna2d2* by examining heart sections prepared from *Dbh*Cre/R26-

tdTomato mice through SrT. The percentage of *Dbh*$^{+}$- and *Wpre*$^{+}$-cardiomyocytes in the heart were fairly constant, 0.4% and 18.2% at E12.5, 0.59% and 7.4% at P3, and 0.93% and 11.45% at adult, respectively.

Dbh and *Wpre* share similar spatial expression profiles with all four major CCS marker genes in all stages (Figure 4.3.2a,b), however the degree of overlap differs between the individual CCS marker genes (Figure 4.3.2d). At E12.5, the majority of *Dbh*$^{+}$ (51%) and *Wpre*$^{+}$ (50.6%) cells expressed the *Id2* gene, compared to *Cacna2d2* (21.6% in *Dbh*$^{+}$, 23% in *Wpre*$^{+}$), and *Gja5* (15.7% in *Dbh*$^{+}$, 17.9% in *Wpre*$^{+}$). Id2 expression in *Dbh*$^{+}$- and *Wpre*$^{+}$-cardiomyocytes declines at E14.5 and then remain constant to adult heart with an average of ~12%. Gja5, Cacna2d2 expression in *Dbh*$^{+}$- and *Wpre*$^{+}$ -cardiomyocytes is similar at E12.5, E14.5 and adult (~20%). However, *Hcn4* is much lower within both *Dbh*$^{+}$- and *Wpre*$^{+}$ -cardiomyocytes at E12.5 (3.92 in *Dbh*$^{+}$, 7.5% in *Wpre*$^{+}$) and the other stages, suggesting that *Dbh*$^{+}$-CMs and their derived cardiomyocytes in CCS have different physiological function from the majority of Hcn4+ cells.

Together, our SrT and combinatorial marker gene expression analyses allowed us to localize *Dbh*$^{+}$- and *Wpre*$^{+}$-cardiomyocytes to the CCS and strengthened the implied association with the CCS from our scRNA-seq interrogation. The lower abundance in expression of Hcn4 in *Dbh*$^{+}$- and *Wpre*$^{+}$-cardiomyocytes may suggest that *Dbh*$^{+}$- and *Wpre*$^{+}$-cardiomyocytes are from a different lineage to those Hcn4 expressing CCS cells, however they may share a similar lineage to *Id2/Gja5/Cacna2d2* expressing CCS cells,

which further support that composition of CCS cell populations, in particular in the atrial CCS, is highly heterogeneous.

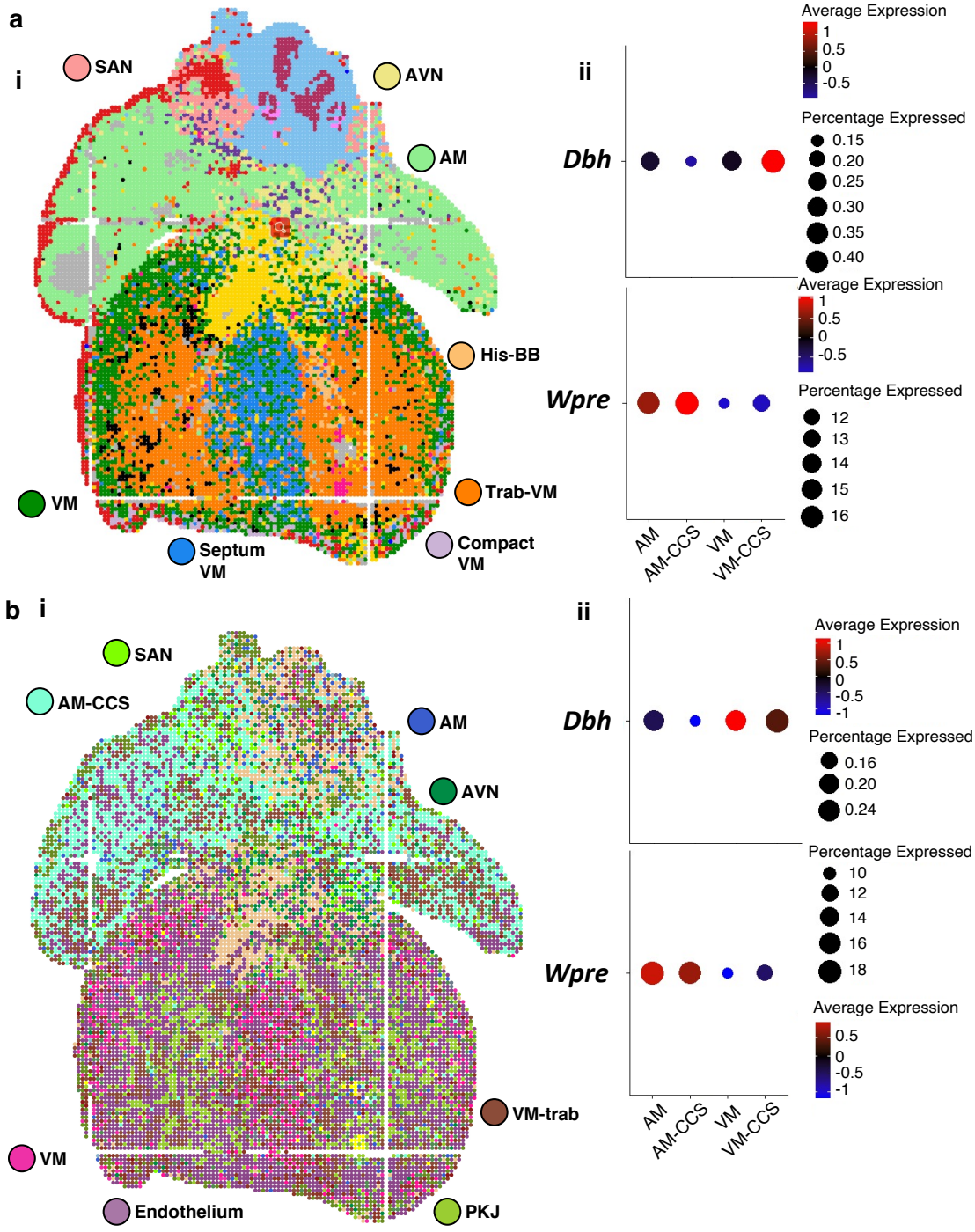

Figure 4.3.1. *Dbh* is expressed dynamically across the developing heart, as resolved with novel high resolution spatial transcriptomic techniques.

a. i) A plot of spatial transcriptomic pixels identified in a slice of E14.5 mouse heart, coloured by cell type identified through unsupervised clustering and with major cell types labelled. ii) Dot plots describing *Dbh* and *Wpre* (a more stable tdTomato-derived transcript) expression across major cardiomyocyte populations identified through unsupervised clustering of E14.5 spatial transcriptomics data.

b. i) A plot of spatial transcriptomic pixels identified in a slice of E14.5 mouse heart, coloured by cell type identified through integration of scRNA-Seq cell types and with major cell types labelled. ii) Dot plots describing *Dbh* and *Wpre* (a more stable tdTomato-derived transcript) expression across major cardiomyocyte populations identified through integration of scRNA-Seq cell types and E14.5 spatial transcriptomics data.

Abbreviations: VM – ventricular myocardium; Trab-VM – trabecular ventricular myocardium; SAN – sinoatrial node; AVN –atrioventricular node; AVJ – atrioventricular junction; AM – atrial myocardium; His-BB – His-bundle branch; AM-CCS – atrial cardiac conduction system; PKJ – purkinje fibres; VM-CCS – ventricular cardiac conduction system.

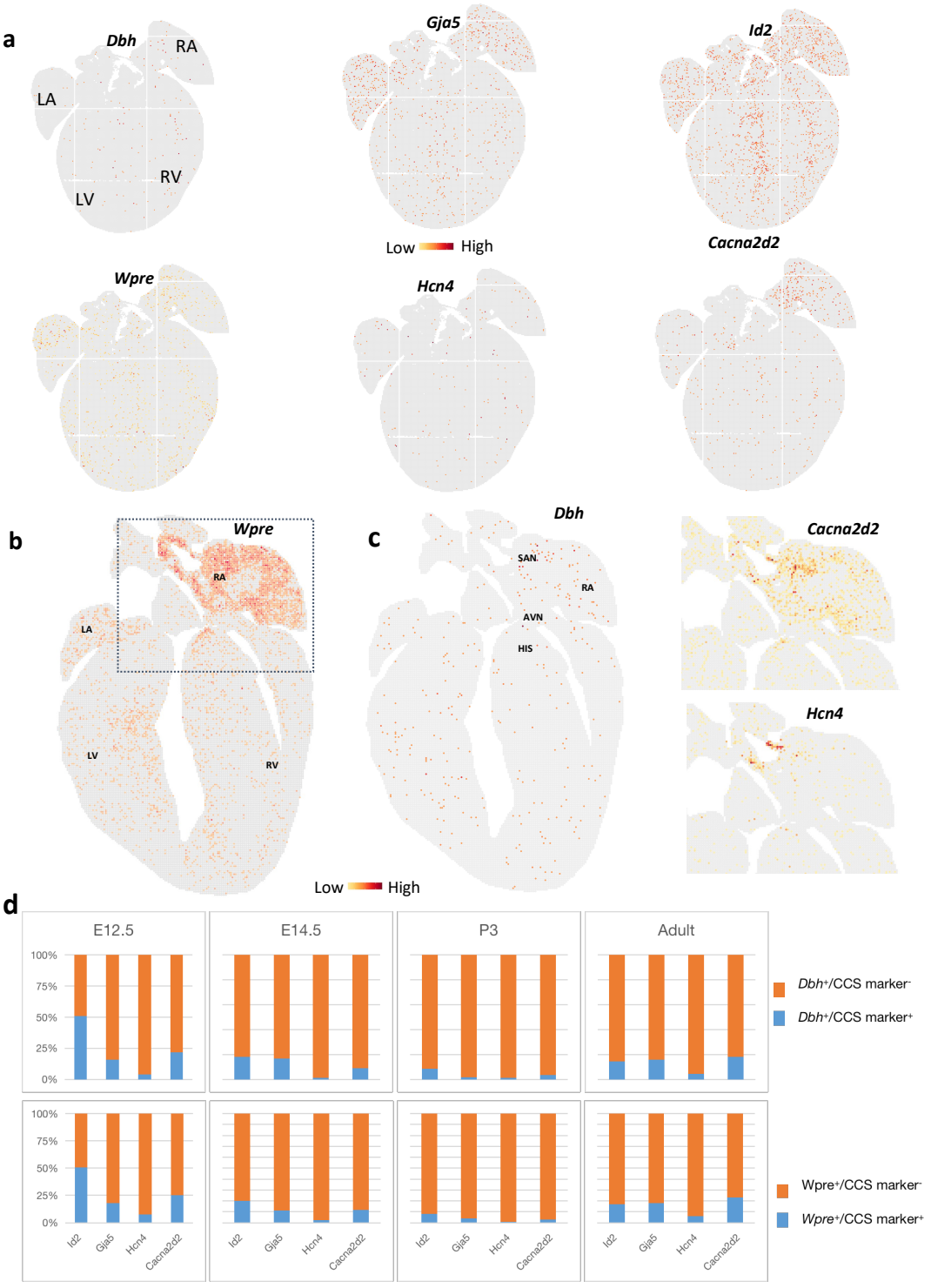

Figure 4.3.2. Expression of *Dbh, Wpre* and typical CCS markers was revealed by spatially resolved transcriptomics in postnatal and adult stage.

a. Spatially resolved *Wpre, Dbh* gene expressions in P3 heart section combined with the distribution of cardiac conduction system markers *Gja5, Hcn4, Id2* and *Cacna2d2*.

b. Spatially resolved *Wpre* gene expression in adult heart section.

c. Spatially resolved CCS marker gene expression of *Dbh, Cacna2d2, Hcn4* in adult heart section.

d. Percentage of Dbh^+ and $Wpre^+$ cells that express the CCS marker genes including *Id2, Gja5, Hcn4* and *Cacna2d2* across the developmental and adult stages.

Chapter 5: Lineage tracing analysis reveals the contribution of *Dbh*$^{+}$-derived cardiomyocytes (Dd-CMs) in developmental morphogenesis of murine heart

Recent refinement of transcriptomic technologies including Single-cell RNA sequencing (scRNA-seq) and spatial transcriptomics has facilitated the interrogation of cell populations with increasing classification power, revealing and characterizing novel cell types(Goodyer & Wu, 2018b; Lescroart et al., 2018; G. Li et al., 2016; Tyser et al., 2021; Xiong et al., 2019). Chapters 3 and 4 have demonstrated such approaches, particularly scRNA-seq and spatially resolved transcriptomic analysis to investigate cardiogenesis, development and maturation of cardiac conduction system, as well as novel findings of *Dbh*$^{+}$ derived cardiomyocytes. However, both scRNA-seq and spatially resolved transcriptomic analysis relied more on computation and data interpretation, but lack biological evidence. Lineage tracing is an essential biological tool to identify, track and map the cell type of interest in vivo(Kretzschmar & Watt, 2012). In this chapter, by performing genetic lineage tracing, the *Dbh*$^{+}$ derived cardiomyocytes were fated throughout the developmental stages to adult, and the association with cardiac conduction system and sympathetic innervation were appropriately revealed.

5.1 Lineage tracing fating the distribution of *Dbh*$^{+}$-CMs and Dd-CMs throughout different developmental stages and showing their association with CCS and sympathetic innervation.

To validate the transcriptomically identified Dbh^{+} cardiomyocyte population and elucidate their spatial localisation and temporal changes in the context of the developing heart, genetic fate mapping was also conducted using the Dbh^{Cre}/R26-tdTomato line shown in Figure 5.1.1a.

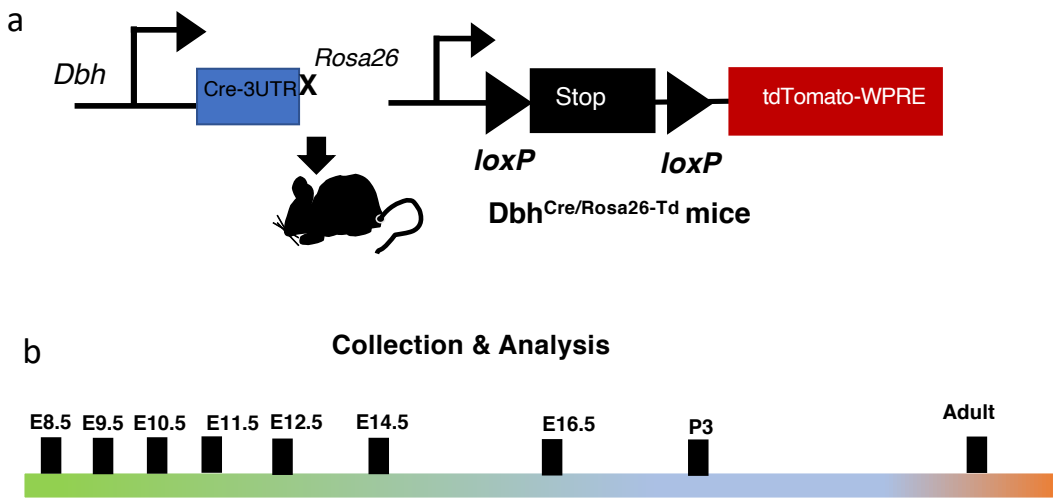

Figure 5.1.1 a. Schematic of *Dbh*-tdTomato reporter line creation. b. Collection and Analysis of embryos and embryonic hearts for lineage tracing study.

Whole embryos (E8.5, E9.5, E10.5, E11.5, E12.5, n=5 embryos per stage) or isolated hearts (E12.5, E13.5, E14.5, E16.5, P3, n=5 hearts per stage) were collected and analyzed by multiplex nucleic acid in situ hybridization (RNAscope),

immnuohistological staining and confocal microscopic imaging (Figure 5.1.1b). The whole embryos at E8.5 and E9.5 were dissected and checked but no tdTomato signals were found (Figure 5.1.2), revealing no Dbh+ cells appeared at this stage. Expression of tdTomato was first observed, through confocal microscopic imaging of the fluorescent protein, in the dorsal neural tube at E10.5 and then branched into groups migrating to the heart region via the pharyngeal arches between E10.5 to E12.5 (Figure 5.1.3a). At E12.5, tdTomato-expressing cells were observed in the sympathetic ganglion chain (SG) adjacent to the spinal cord, sinus venosus (SV, the tissue SAN develops from) and right atrium (RA) (Figure 5.1.3b and Figure 5.1.4a). Interestingly, it is worth mentioning that there is a typical migration trend from SG to SV and RA bypassing the lung, indicating the potential origins of *Dbh*$^{+}$ cells shown in Figure 5.1.3b and Figure 5.1.4a. In E12.5 embryos, abundant *Hcn4* mRNA signal was detected by RNAscope in the SV and RA, and partially overlapped with the *Dbh* mRNA signal, indicating some of *Dbh* expressing cells are likely cardiac pacemaker cells (Figure 5.1.3c and Figure 5.1.4c). Tyrosine hydroxylase (*Th*) mRNA signal was also detected by RNAscope in the SV region (Figure 5.1.3c) and RA (Figure 5.1.4b), but more abundantly in SV region, denoting the sympathetic innervation of the primordial atria at E12.5 (Figure 5.1.3c and Figure 5.1.4c).

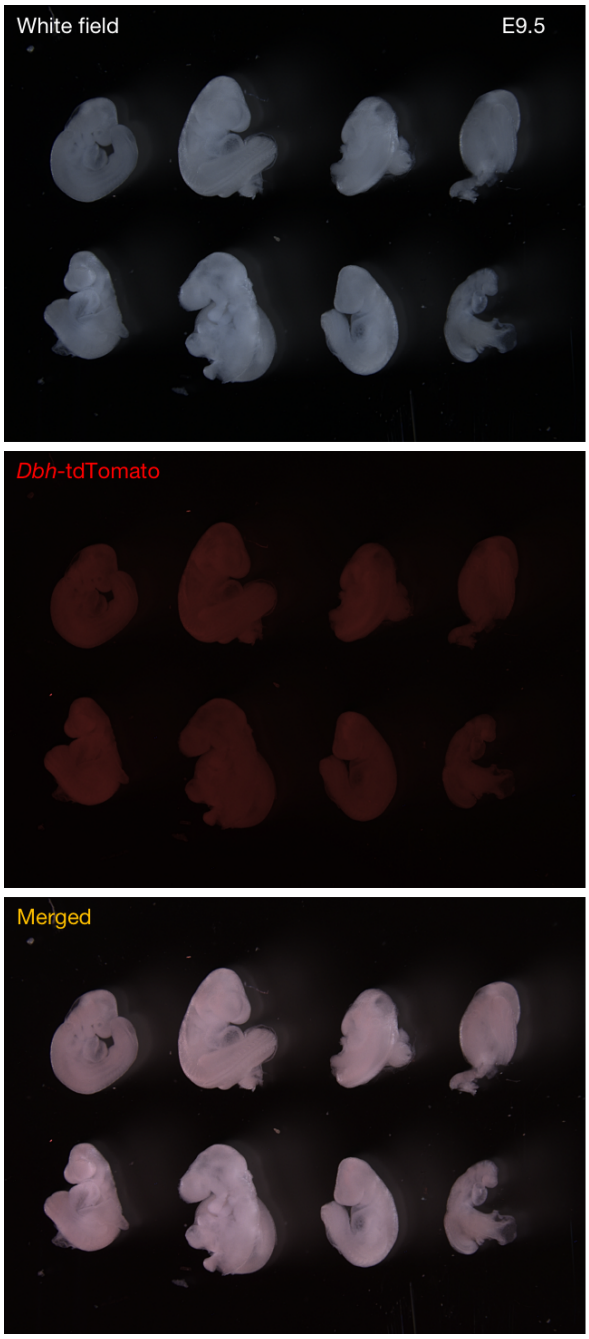

Figure 5.1.2 whole field images of E9.5 embryos revealing no tdTomato signals were found at E9.5.

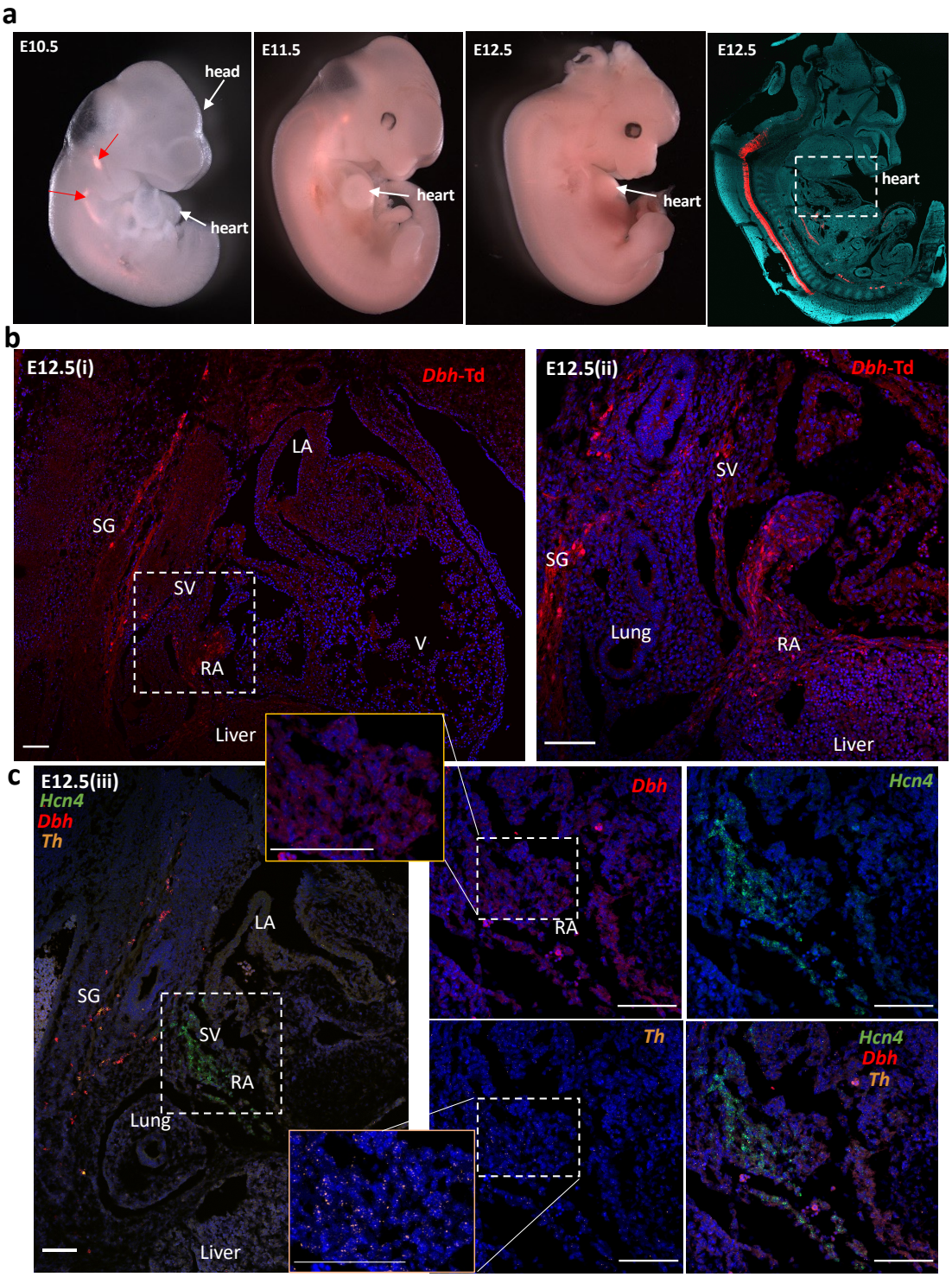

Figure 5.1.3 Prospective Cre fate mapping analysis of DbhCre/Rosa26-Td heart throughout the developmental stages.

a. Anatomic whole mount embryos revealing the location of Dbh+ cells from E10.5 to E12.5 murine embryos.

b. Genetic fluorescence showing the tdTomato-expressing cells in E12.5.

E12.5(i) showing the expression of tdTomato-expressing cells in heart region. E12.5(ii) showing the details of dotted square in E12.5(i).

c. RNAscope ISH technology showing the relationships between tdTomato-expressing cells with CCS and sympathetic innervation.

E12.5(iii) showing the *Hcn4*(Green), *Dbh*(Red) and *Th*(Orange) expression in the tdTomato-expressing cell positive region in the adjacent section of E12.5(i-ii), indicating the association with CCS and sympathetic innervation

Scale bar: 100μm; Red Arrowed: tdTomato-expressing cells

Abbreviations: SG: Sympathetic Ganglia; SV: Sinus Venosus; LA: Left Atrium; RA: Right Atrium; V: Ventricle

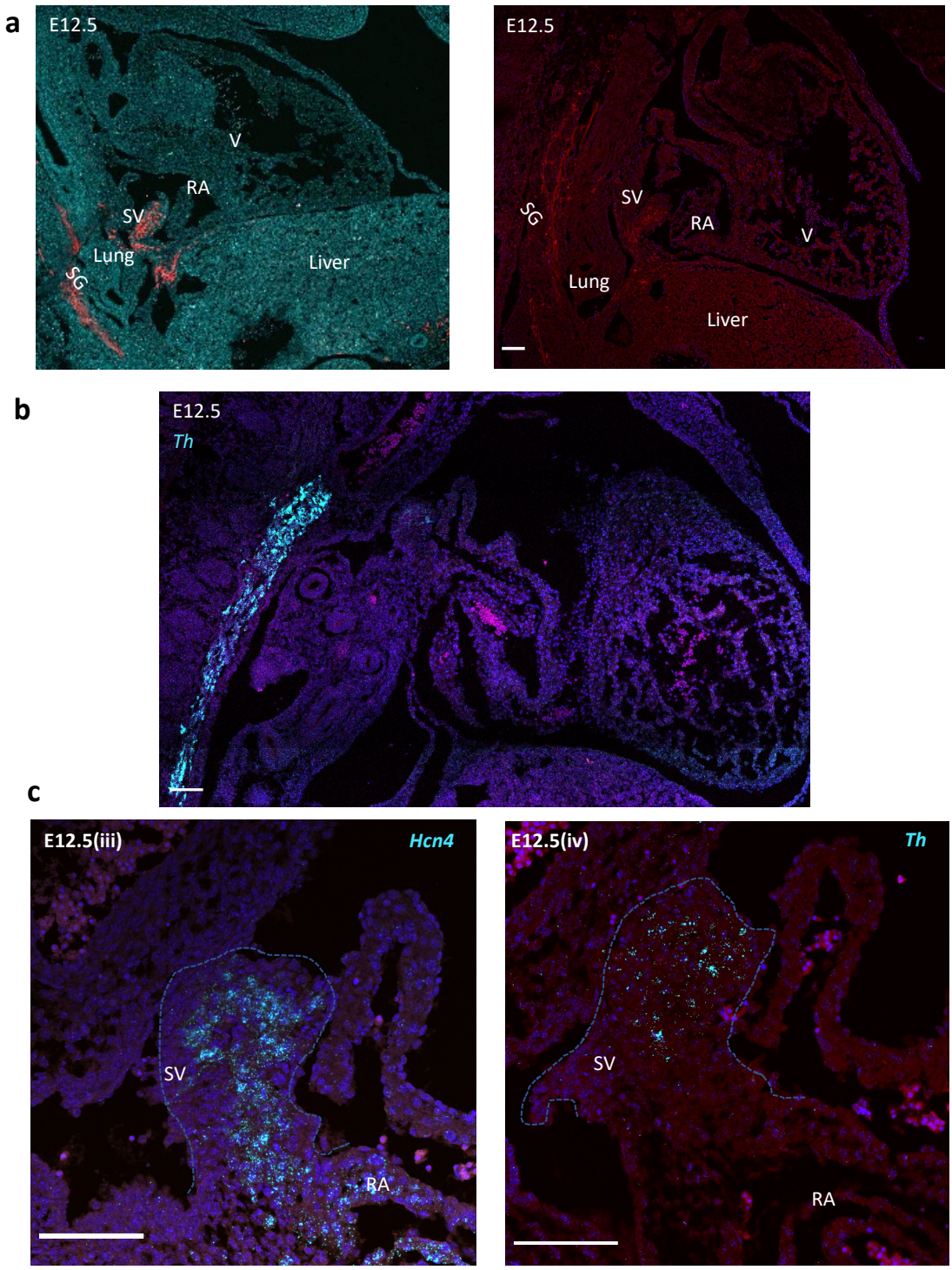

Figure 5.1.4. RNAscope ISH technology showing the relationships between tdTomato-expressing cells with CCS and sympathetic innervation.

a. Genetic fluorescence showing the tdTomato-expressing cells at E12.5.

b. E12.5 embryo section showing the Hcn4 (Cyan) expression in the tdTomato-expressing cell positive region, indicating the association with CCS.

c. E12.5 embryo section showing the Th (Cyan) expression in the tdTomato-expressing cell positive region, suggesting the association with sympathetic innervation.

Scale bar: 100μm

Abbreviations: SG: Sympathetic Ganglia; SV: Sinus Venosus; LA: Left Atrium; RA: Right Atrium; V: Ventricle.

The cell type identity and localisation of the *Dbh*$^{+}$-derived cells were further determined and delineated at E14.5, E16.5 and postnatal stages by RNAscope and immunofluorescence staining with various markers in heart sections of Dbh^{Cre}/Rosa26-tdTomato mice. It has been found that tdTomato-expressing cells mainly concentrated in the cardiac conduction system and ventricular trabecular regions throughout these stages (n=5 hearts examined per stage). tdTomato-expressing cells were detected in the central CCS including SAN, AVN, His bundle regions (Figure 5.1.5b), and many cells also express Hcn4 transcript (Figure 5.1.5b). TdTomato-expressing cells were also detected in ventricular trabecular cardiomyocytes where Hcn4 transcript is not expressed at E14.5. By staining with the myocyte marker, α-actinin, it has been further confirmed that the majority of tdTomato-expressing cells to be cardiomyocytes, these cells were thus defined as *Dbh*$^{+}$-derived cardiomyocytes (Dd- CMs) (Figure 5.1.6a).

Additionally, at E14.5, Th proteins were detected in the AVN, His bundle region and ventricular trabecular region indicating that sympathetic innervation occurred concurrently with CCS formation and illustrated the potential association with Dd- CMs (Figure 5.1.6b).

Moreover, *Bmp10* expression (a marker of developing ventricular trabecular cardiomyocytes and atrial cardiogenesis) extensively overlapped with *Wpre* expression (yellow dots) in the SAN and ventricular trabecular regions, as detected by SrT (Figure 5.1.7a) and RNAscope (Figure 5.1.7b), suggesting the Dd-CMs (tdTomato-expressing cardiomyocytes) contribute to trabeculation as well as CCS formation at this stage. In the Figure 5.1.7b, it is of note that Dd- CMs in the RA extensively overlap with either Hcn4 or Bmp10 expression but fewer in triple overlapped, indicating that there are possibly two sub-populations of Dd- CMs that contribute to atrial cardiogenesis and CCS formation respectively.

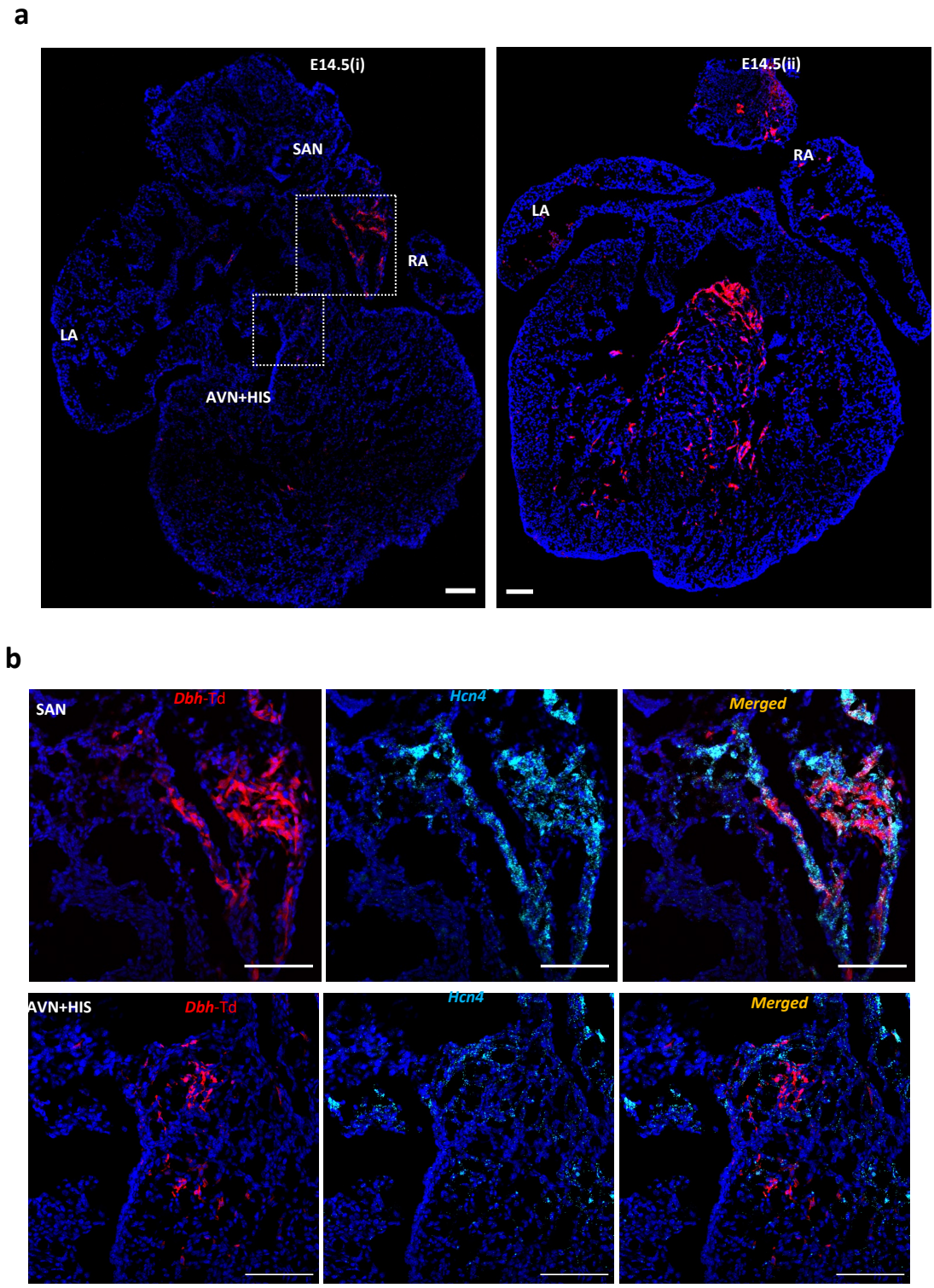

Figure 5.1.5 Spatio-temporal lineage tracing identified the distribution of tdTomato-expressing cells in murine heart at E14.5.

a. The spatial distribution profile of tdTomato-expressing cells in E14.5 embryonic murine heart. E14.5(i) and E14.5(ii) showing the whole field of the distribution of tdTomato-expressing cells.

b. RNAscope labelled the SAN, AVN and HIS bundle regions with Hcn4 (cyan) probe showing the co-expression with tdTomato-expressing cells (red).

Scale Bar:100μm

Abbreviations: RA: Right Atrium; LA: Left Atrium; SAN: Sinoatrial node; AVN: Atrioventricular node; HIS: Bundle of His

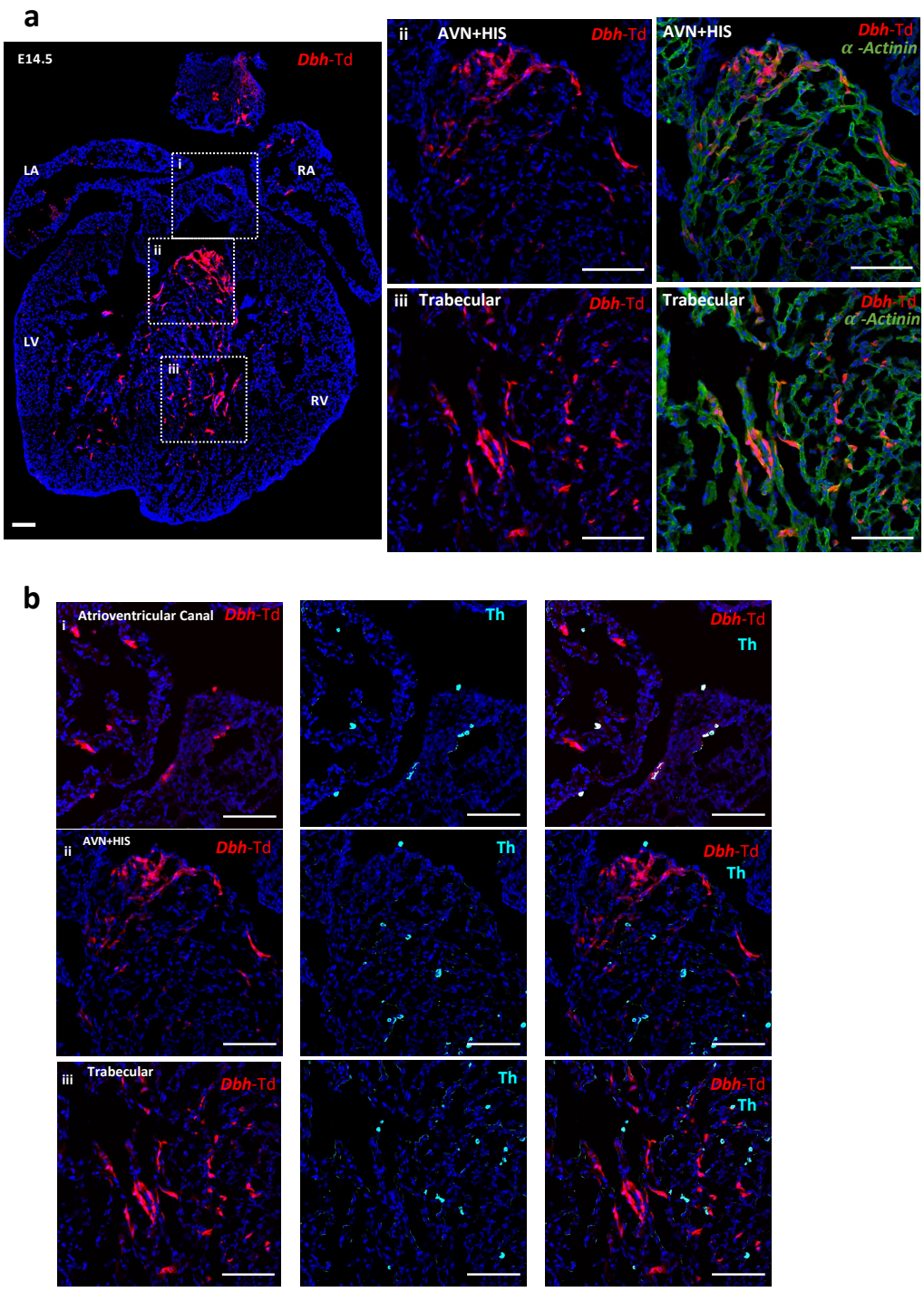

Figure 5.1.6. The spatial distribution profile of tdTomato-expressing cells in E14.5 embryonic murine heart and their association with sympathetic innervation.

a. Immunofluorescence of tdTomato-expressing cells in AVN+HIS bundle and Trabecular regions stained α-actinin (green) revealing the Dbh+ CMs at E14.5.

b. Immunofluorescence of Dbh+ CMs in Atrioventricular Canal, AVN+HIS bundle and Trabecular regions-stained Th (cyan) revealing the association between Dbh+ CMs with sympathetic innervation at E14.5.

scale bar: 100μm

Abbreviations: LA: Left Atrium; RA: Right Atrium; LV: Left Ventricle; RV: Right Ventricle; AVN: Atrioventricular node; HIS: Bundle of His.

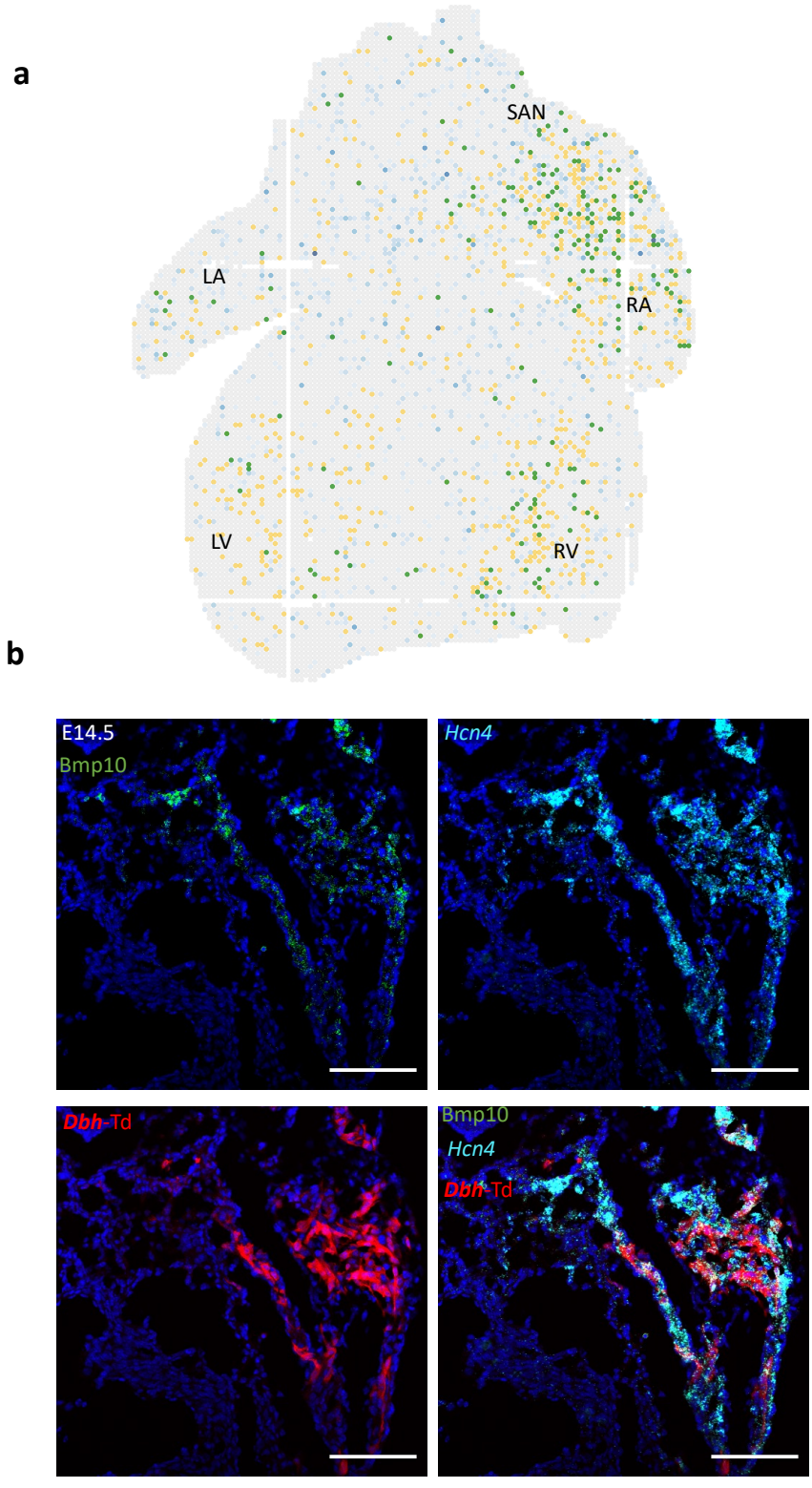

Figure 5.1.7. Spatio-temporal lineage tracing identified the correlation of expression of Bmp10 in tdTomato-expressing cells in murine heart at E14.5 stage.

a. Spatially resolved transcriptomics revealing the correlation between Bmp10 (yellow) gene expression and tdTomato-expressing cells (blue) in murine heart at E14.5 stage. Green dots show the overlap between Bmp10 expression and tdTomato-expressing cells.

b. RNAscope labelling the SAN region with Bmp10 (green), Hcn4 (cyan) probes showing the co-expression with tdTomato-expressing cells (red) which is consistent with spatially resolved transcriptomics at E14.5 stage.

Scale bar: 100μm

At E16.5, Dd-CMs (tdTomato-expressing cardiomyocytes) were markedly increased in number in ventricular myocardium in addition to their abundance in the central CCS shown in a series of whole field images in Figure 5.1.8. The central CCS was delineated by *Hcn4* expression detected by RNAscope (Figure 5.1.9). At this stage (E16.5), the RA expands to express *Bmp10*, concomitantly with the increase in Dd-CMs within the RA (Figure 5.1.9). Interestingly, most Dd-CMs in the trabecular ventricular myocardium, defined by co-expression of α-actinin, also coexpressed *Bmp10*, confirming these cells are ventricular trabecular myocytes (Figure 5.1.9 and Figure 5.1.10). Additionally, immunostaining demonstrated that Th protein expression occurred predominantly in the Dd-CMs abundant regions including SAN, AVN, HIS and trabecular regions, implying the potential interaction between Dd-CMs and sympathetic innervation (Figure 5.1.10).

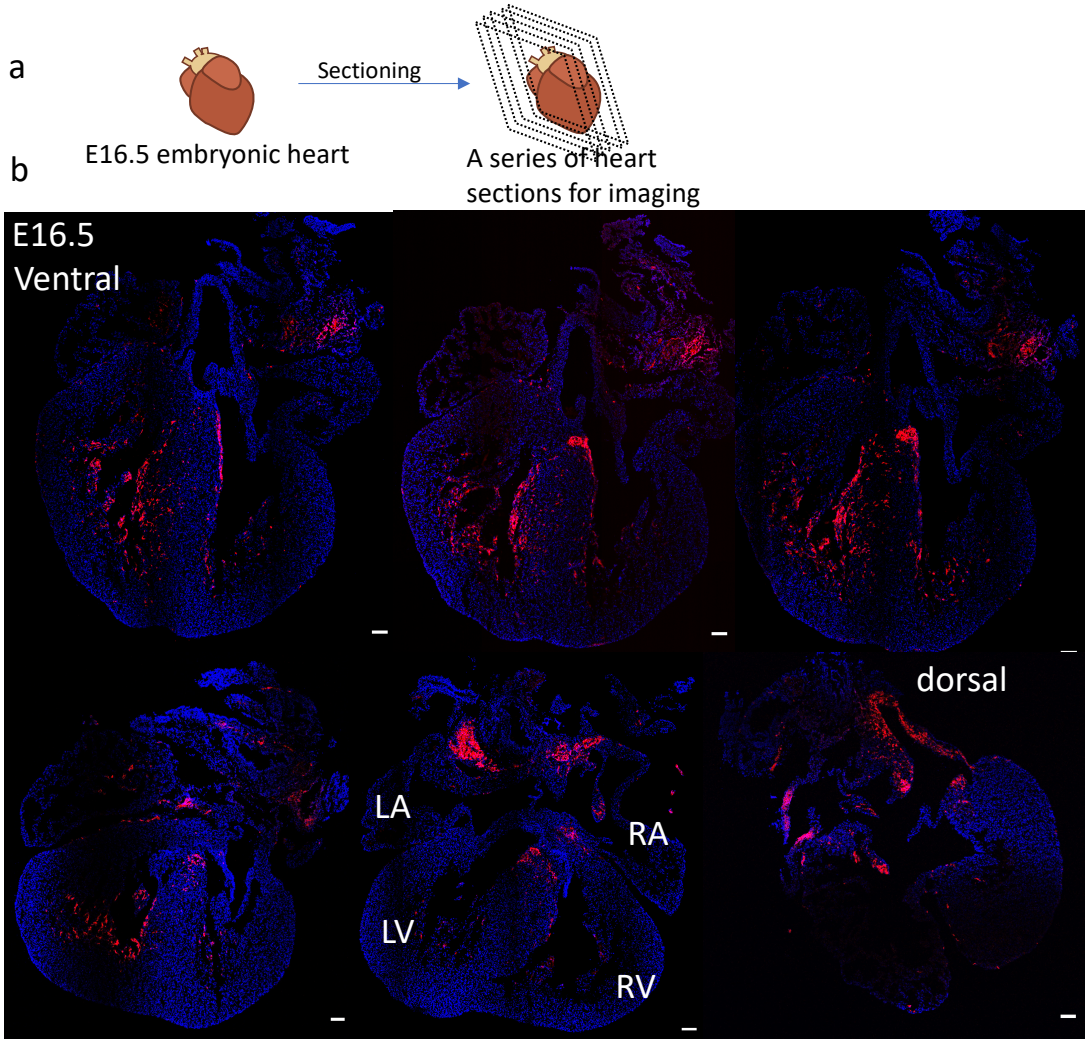

Figure 5.1.8. The spatial distribution profile of tdTomato-expressing cells in E16.5 embryonic murine heart.

a. A schematic graph showing the sectioning direction.

b. a series of selected global heart sections showing the distribution of Dd- CMs at E16.5 embryonic murine heart from the ventral to dorsal viewing.

Scale bar: 100μm

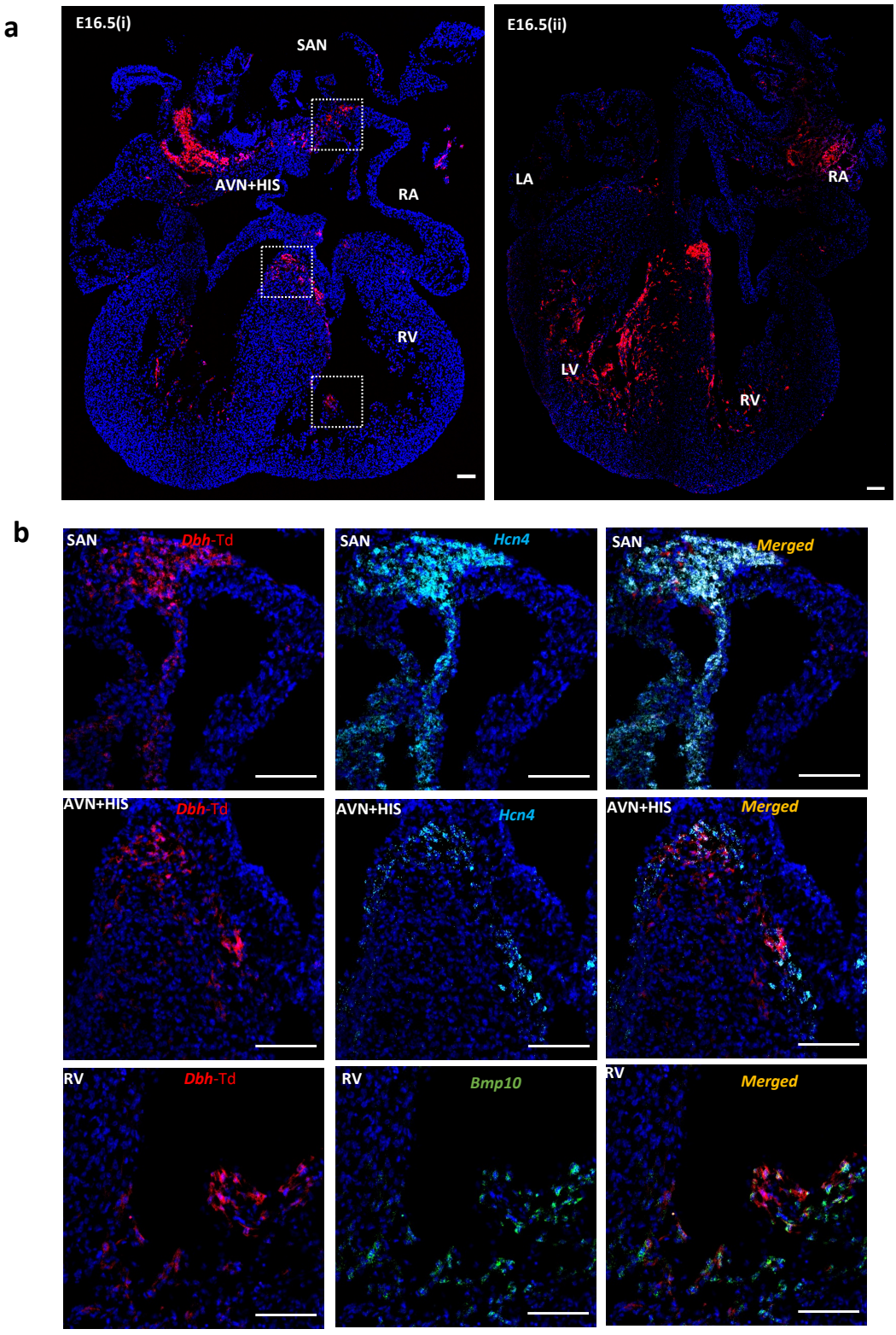

Figure 5.1.9. Spatio-temporal lineage tracing identified the distribution of tdTomato-expressing cells in murine heart at E16.5.

a. The distribution profile of tdTomato-expressing cells in E16.5 embryonic murine heart. E16.5(i) and E16.5(ii) showing the whole field of the distribution of tdTomato-expressing cells.

b. RNAscope labelled the SAN, AVN and His regions with Hcn4 (cyan) probe and RV with Bmp10 probe (green) showing the co-expression of tdTomato-expressing cells (red) in cardiac conduction system and trabecular regions.

Scale Bar:100μm

Abbreviations: RA: Right Atrium; LA: Left Atrium; SAN: Sinoatrial node; AVN: Atrioventricular node; HIS: Bundle of His

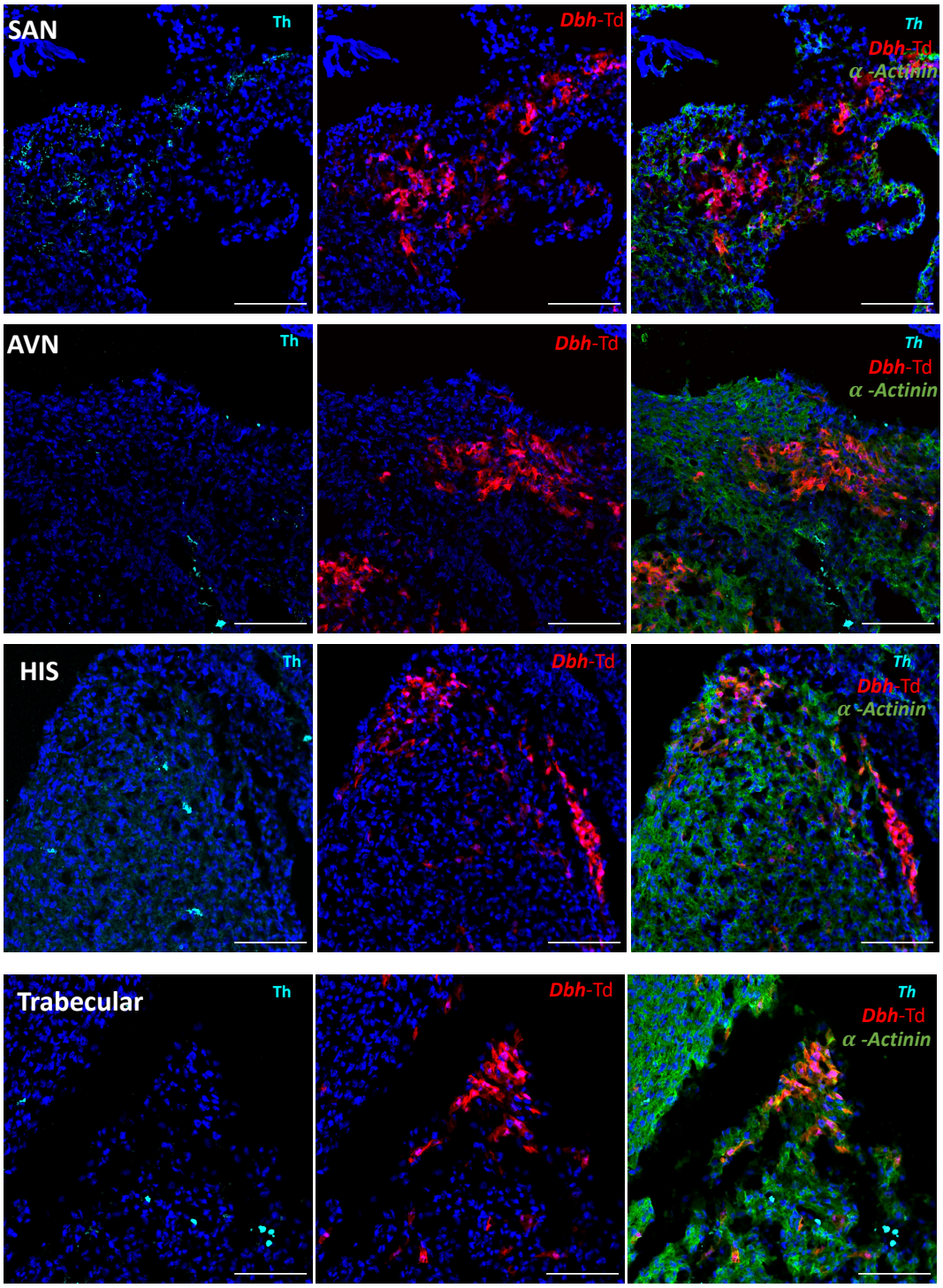

Figure 5.1.10 Immunofluorescence of tdTomato-expressing cells in SAN, AVN, HIS bundle and Trabecular regions stained α-actinin (green) and Th(cyan) revealing the Dd-CMs and their association with sympathetic innervation at E16.5 stage. Scale bar: 100μm

Afterwards, the detailed distribution of Dd-CMs was examined in relation to the sympathetic innervation across different regions of the hearts at P3 and adult. A series of whole field images followed by systemic sectioning showed the locus of dynamic expression of Dd-CMs at P3 (Figure 5.1.11). A clear distribution pattern of Dd-CMs is observed in the major CCS components from SAN, AVN to HIS and Purkinje fiber network (Figure 5.1.11 and Figure 5.1.12). Costaining with α-actinin antibody further validated the identity of Dd-CMs though some Dbh+ cells are α-actinin negative suggesting the potential existence of ICA cells (Figure 5.1.12). The SrT plot showed the abundant overlap between *Bmp10* expression and *Wpre* expression in the CCS components, especially in the SAN region and ventricular trabecular regions at P3 (Figure 5.1.13a). Consistently, multiplex in Situ hybridization of *Hcn4, Bmp10* with tdTomato signals further proved the expression of Dd-CMs in SAN. A pertinent observation is that two distinct subpopulations of Dd-CMs were illustrated for their independent functions as speculated (Figure 5.1.13b). Compared to P3 heart, Dd-CMs are more abundant in the adult heart in general with even more concentration in CCS and RA (Figure 5.1.14). Dd-CMs were abundant in areas with sympathetic innervation, as detected by Th immunostaining, particularly so in the adult heart (Figure 5.1.15). Furthermore, Dd-CMs and sympathetic varicosities can be observed in close proximity (Figure 5.1.15). Thus, there is the necessary anatomical substrate for a range of interactions between Dd-CMs and the sympathetic innervation of the heart.

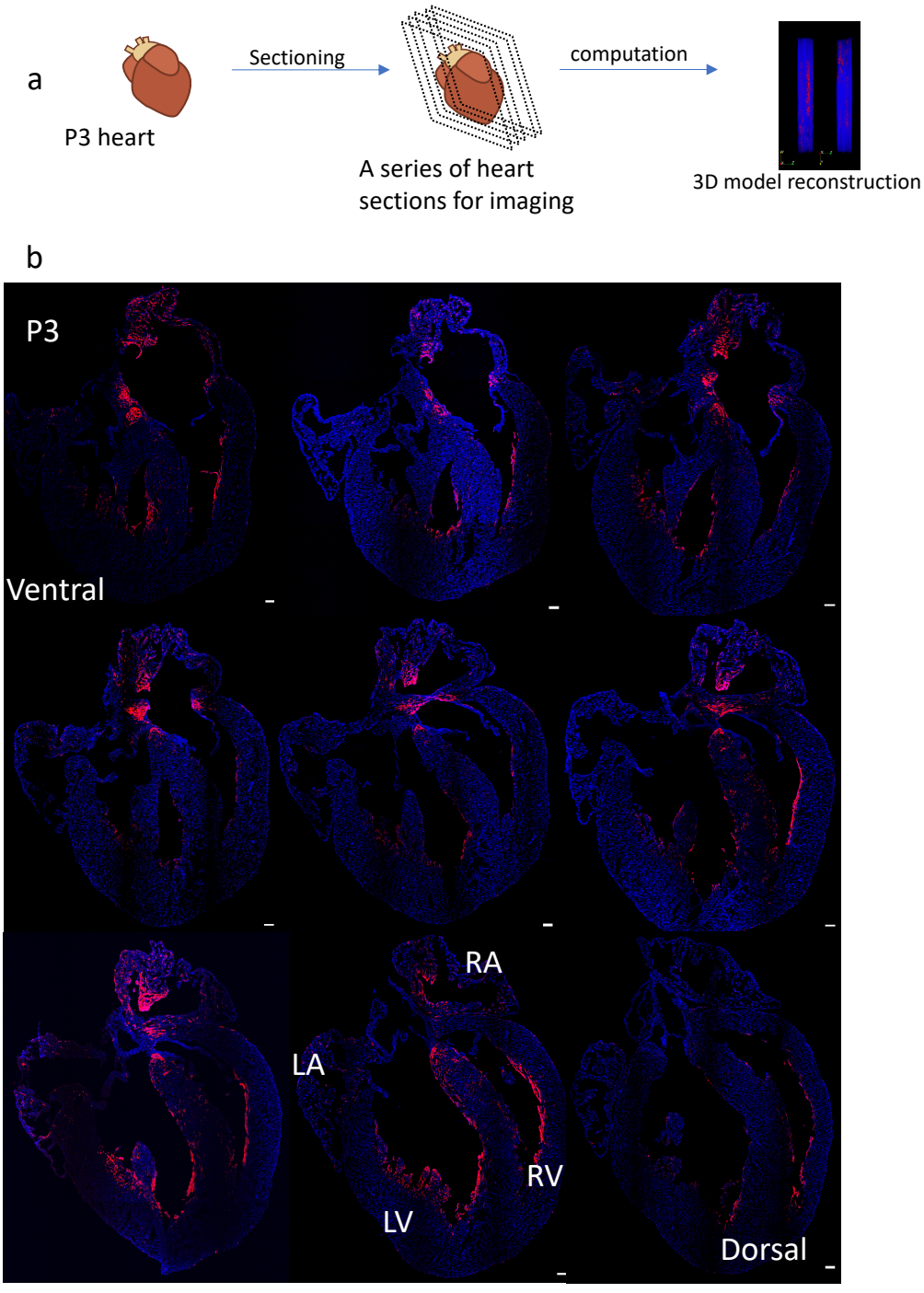

Figure 5.1.11. The spatial distribution profile of tdTomato-expressing cells at P3 murine heart.

a. A schematic graph showing the sectioning direction and 3D model reconstruction.

b. a series of selected global heart sections showing the distribution of Dbh+ CMs at

P3 murine heart from the ventral to dorsal viewing.

Scale bar:100μm

Abbreviations: LA: Left Atrium; RA: Right Atrium; LV: Left Ventricle; RV: Right Ventricle

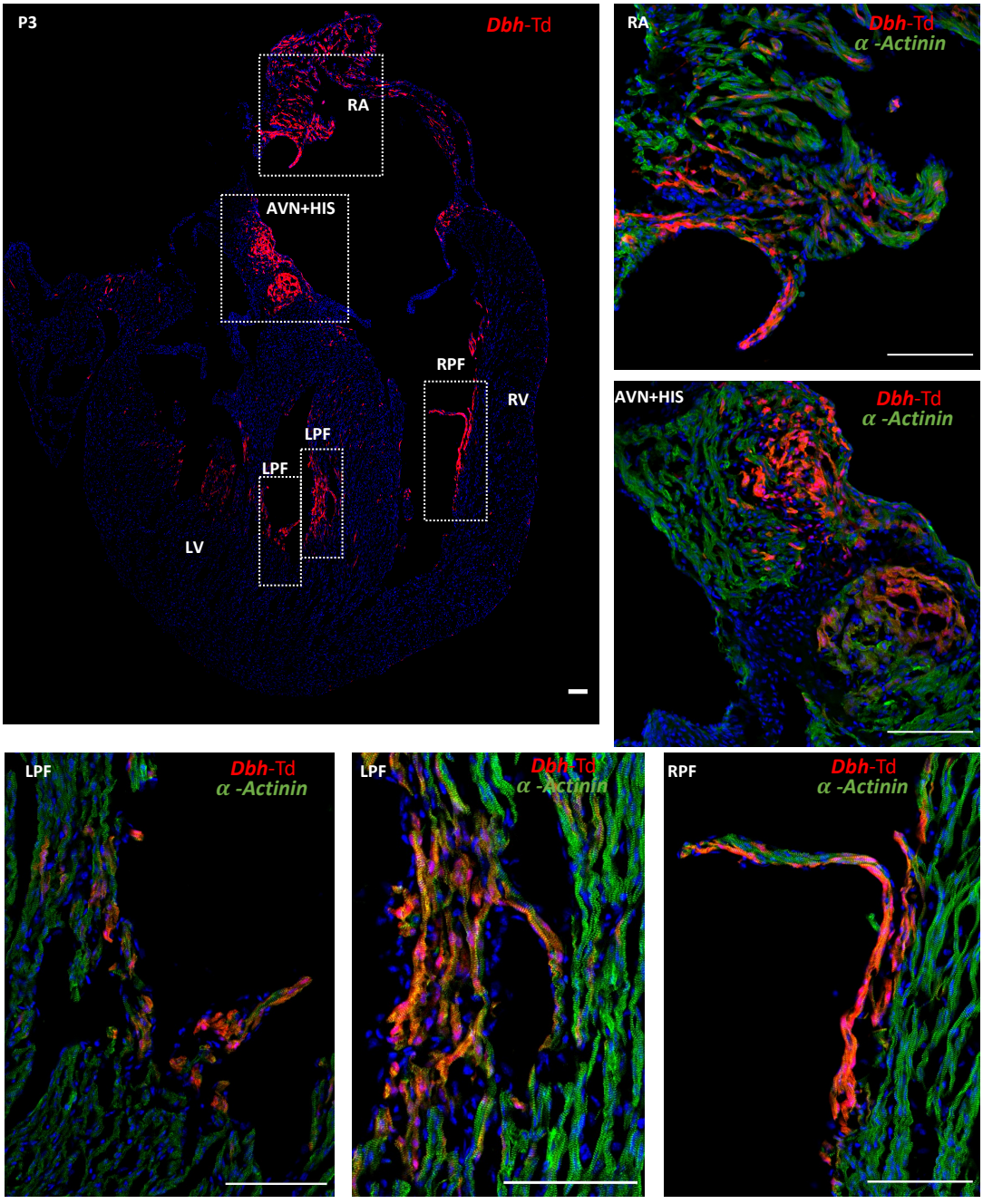

Figure 5.1.12. Immunofluorescence of tdTomato-expressing cells in RA, AVN and HIS bundle, LPF and RPF regions stained α-actinin (green) revealing the Dbh+ CM at P3 stage.

Scale Bar:100 µm,

Abbreviations: SAN: Sinoatrial node; AVN: Atrioventricular node; HIS: Bundle of His; LPF: Left ventricular Purkinje fibers; RPF: Right ventricular Purkinje fibers.

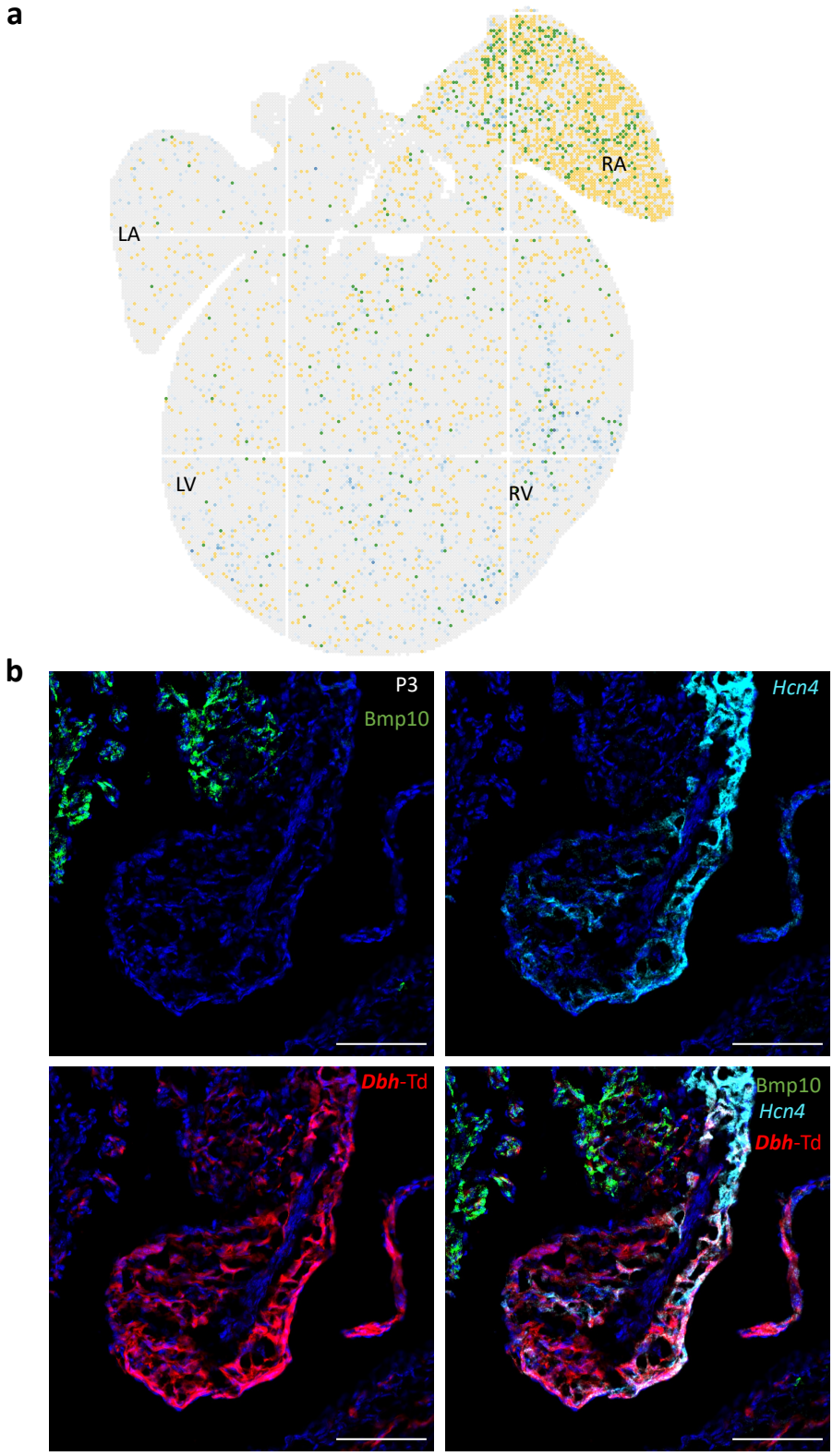

Figure 5.1.13 Spatio-temporal lineage tracing identified the correlation of expression of Bmp10 in the tdTomato-expressing cells in murine heart at postnatal stages.

a. Spatially resolved transcriptomics revealing the correlation between Bmp10 (yellow) gene expression and tdTomato-expressing cells (blue) in murine heart at postnatal stage. Green dots show the overlap between Bmp10 expression and tdTomato-expressing cells.

b. RNAscope labelling the SAN region with Bmp10 (green), Hcn4 (cyan) probes showing the co-expression with tdTomato-expressing cells (red) which is consistent with spatially resolved transcriptomics at postnatal stage.

   Scale bar: 100μm

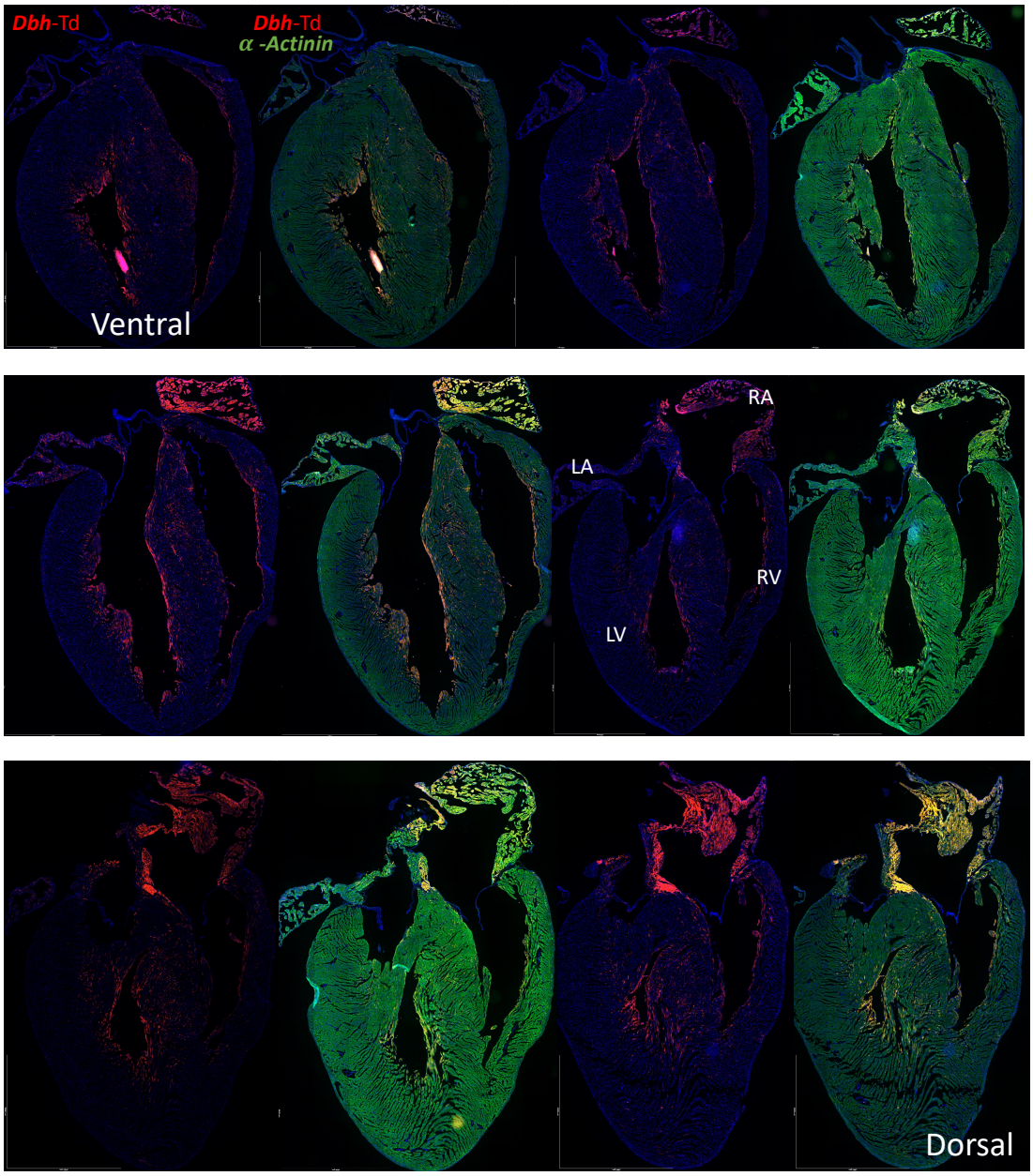

Figure 5.1.14. A series of selected global heart sections showing the distribution of Dbh+ CMs (red) stained the α-actinin (green) at adult murine heart from the ventral to dorsal viewing.

Scale Bar:100 μm,

Abbreviations: SAN: Sinoatrial node; RA: Right Atrium; LA: Left Atrium; LV: Left Ventricle; RV: Right Ventricle.

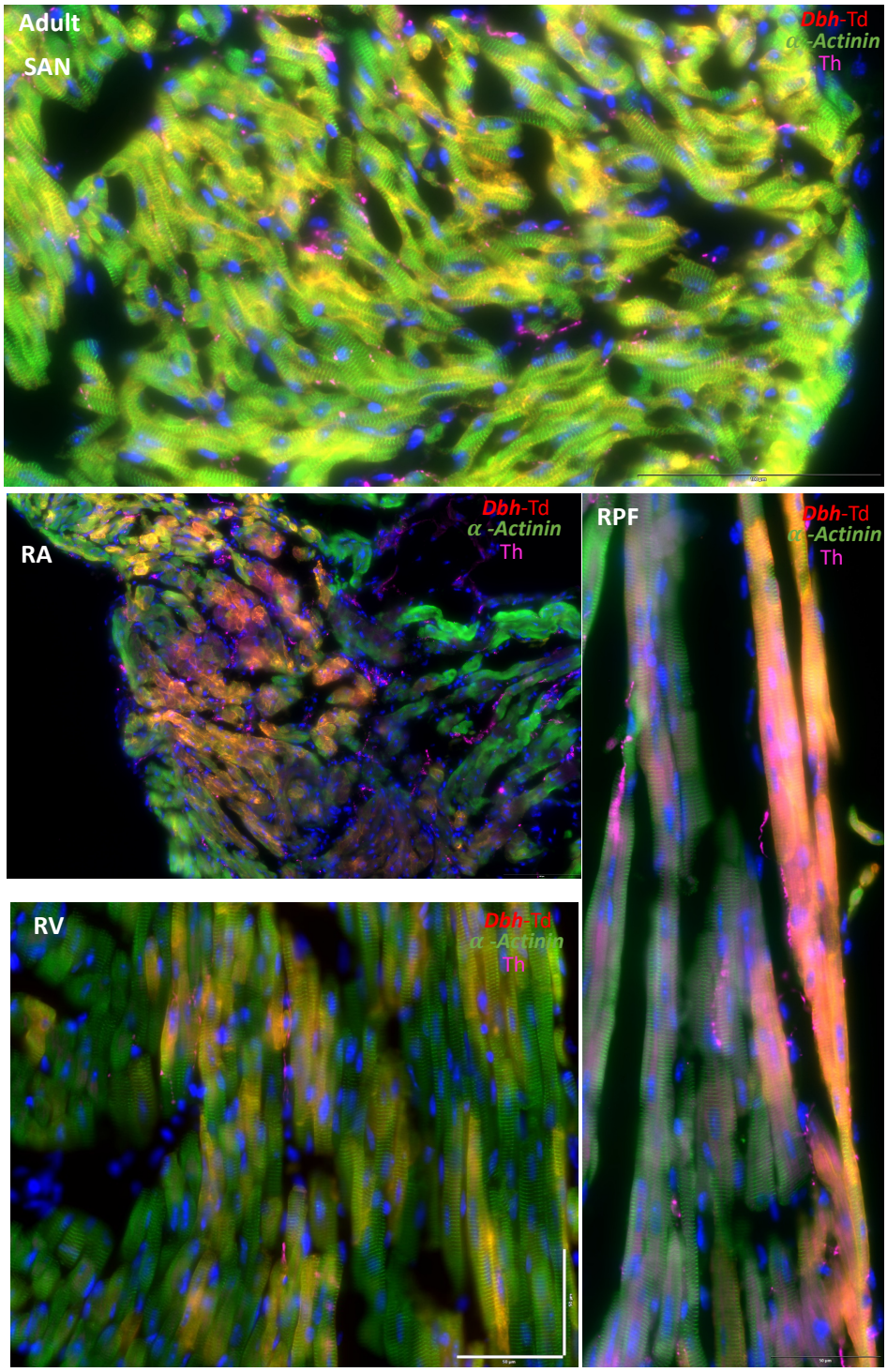

Figure 5.1.15. Immunofluorescence of Dbh+ CMs in SAN, RA,RV and RPF regions stained α-actinin (green) and Th (magenta) revealling the Dbh+ CMs and the association with sympathetic innervation at adult stage.

Scale Bar:100 µm,

Abbreviations: SAN: Sinoatrial node; RA: Right Atrium; RV: Right Ventricle; RPF: Right ventricular Punkinje fibers.

5.2 Anatomical characterization of *Dd-CMs* in the Purkinje fiber network

To further ascertain if Dd-CMs contribute to PKJ network formation, I then developed a new mouse model $Cx40^{EGFP/+}/Dbh^{Cre/Rosa26\text{-}Td/+}$ by crossing a $Dbh^{Cre/Rosa26\text{-}Td/+}$ reporter line with Cx40 transgenic eGFP ($Cx40^{EGFP/+}$) line that demarcates the PKJ network(Miquerol et al., 2004). A clear co-localization of tdTomato and $Cx40^{EGFP}$ signals was observed in both left and right ventricular Purkinje fibre networks (Fig.6b) in $Cx40^{EGFP/+}/Dbh^{Cre/Rosa26\text{-}Td/+}$ neonatal hearts (n=5 hearts examined). Notably, the Dd-CMs (tdTomato-expressing cells) are more extensive than $Cx40^{EGFP/+}$ cells in the ventricular endomyocardium. The result suggests that Dd-CMs form cardiomyocyte populations more than Purkinje conductive cells, which is in agreement with our earlier transcriptomic analyses (Figure 3.4.1, Figure 4.3.1 a.ii, b.ii, Figure 4.3.2 a,b).

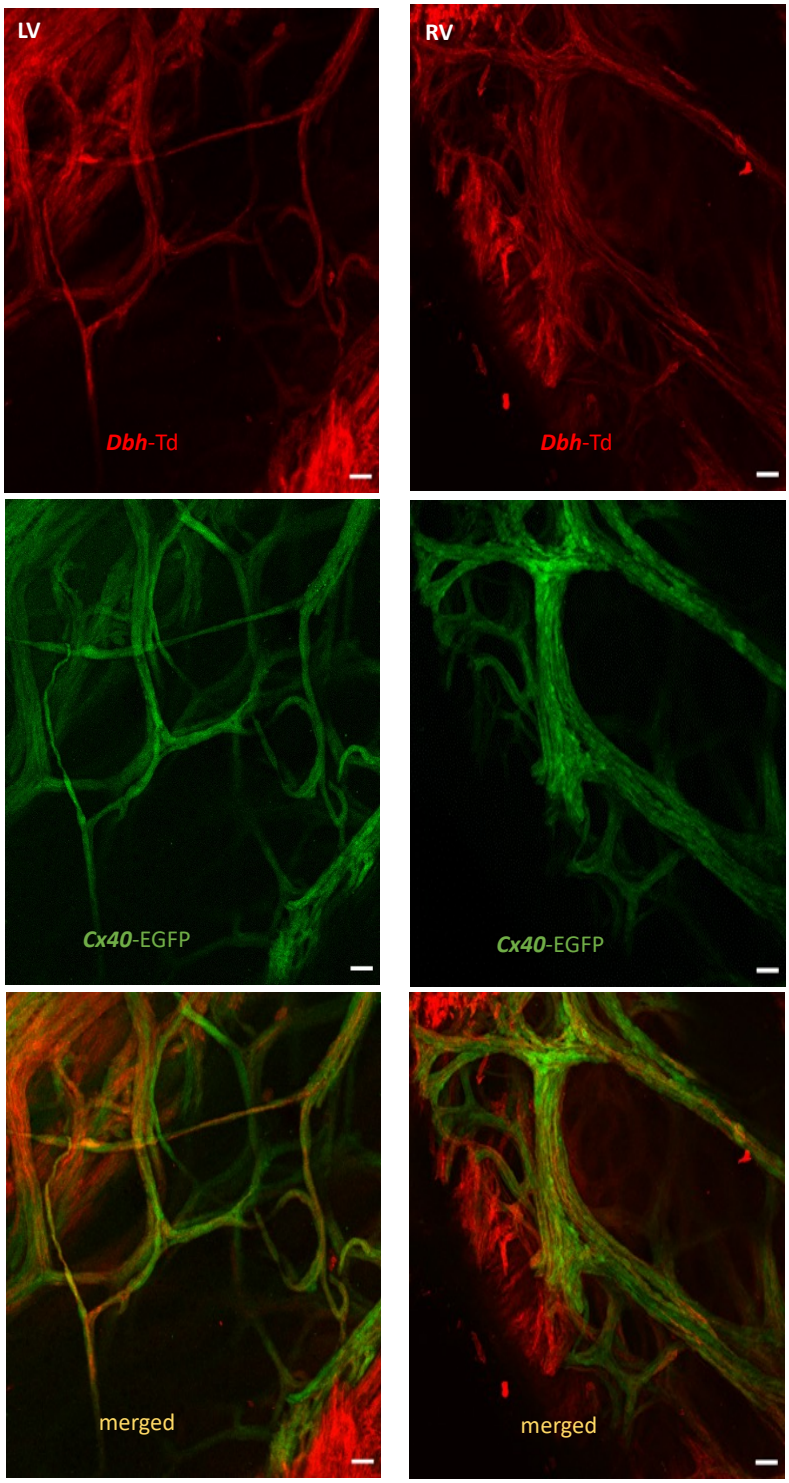

Figure 5.2.2 Co-expression of Dbh and Cx40 protein in PKF network in both left and right ventricle in $Cx40^{EGFP/+}/Dbh^{Cre/Rosa26\text{-}Td/+}$ neonatal mouse heart sections.

5.3 3D reconstruction of Dbh^{Cre}/R26-tdTomato mouse heart mapping the distribution of *Dd-CMs* at P3 and adult stage

In order to characterize the spatial distribution of Dd-CMs across the whole heart in neonatal (P3) and adult hearts (2-month-old), a three-dimensional (3D) computational image reconstruction was developed based on two series of microscopic histological images (Ni et al., 2017b). After the preparation and collection of series of images from P3 and adult hearts, the reconstruction was conducted by Prof. Zhang and his co-workers in the University of Manchester. Dd-CMs in P3 and adult hearts showed spatial distribution characteristics consistent with the CCS (i.e SAN, AVN, and His-Purkinje network, consistent with our earlier SrT analyses shown in Figure 4.4.2.

Reconstruction approach developed by Ni's group(Ni et al., 2017b) was further improved by optimizing holes restoration measure and image enhancement strategy, and then the histogram calculation process in the evaluation of pixel values between the original image and based image were included. To realize the controllability of the cardiac rhythm among singe cell, isolated tissue and whole heart level, this study exploited tdTomato fluorescence in multiple coronal slices of adult and neonatal murine cardiac cells selectively under 470 nm wavelength, 2 ms duration LED blue light. To establish an elaborate three-dimensional (3D) heart positive and negative cells distribution of cardiac cells, we computed each two-dimensional (2D) image by utilizing the OpenCV library and MATLAB software.

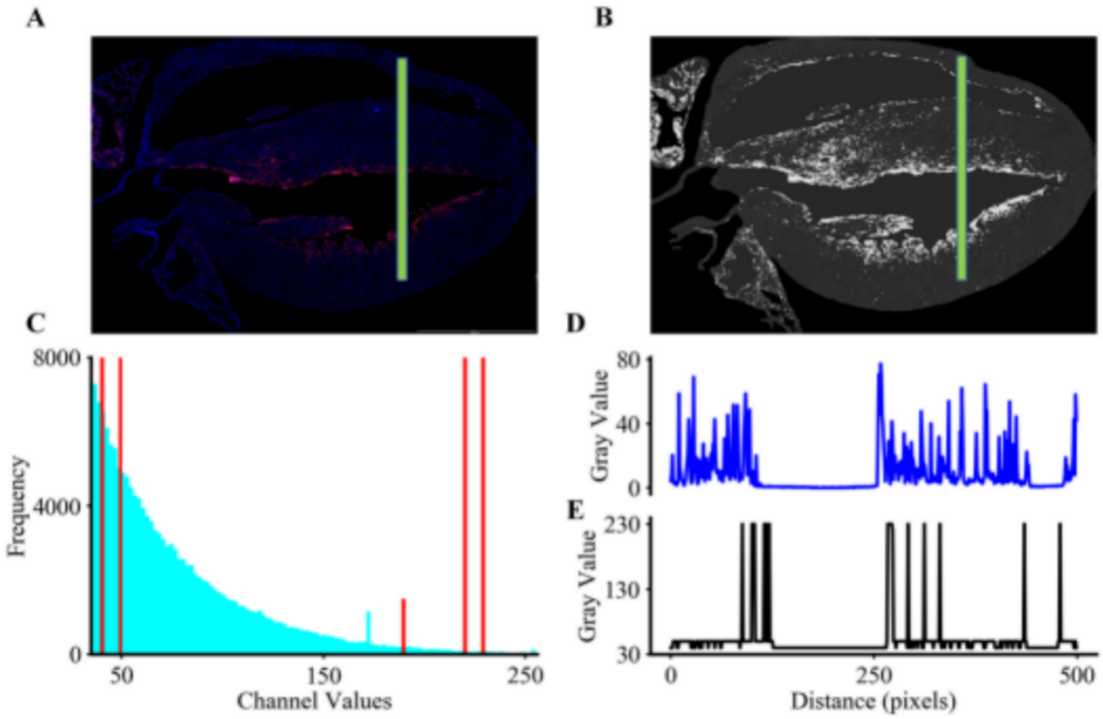

Figure 5.3.1. Frequency distribution histograms and radial grayscale distribution map for the intuitive analysis of adult mouse heart slice. A: Raw image; B: Preprocessed image by our method; C: Frequency distribution histograms of raw image (blue color) and preprocessed image (red color); D and E: Radial grayscale distribution along with the raw image (blue line) and preprocessed image (black line).

Figure 5.3.1 illustrates the analysis of a raw (Figure 5.3.1A) and its correspondingly preprocessed slice image (Figure 5.3.1B, after image merge step), the pixel value frequency distribution histograms (Figure 5.3.1C), and the radial grayscale distribution map (Figure 5.3.1D and Figure 5.3.1E). In the frequency distribution histograms as shown in Fig 5.3.1C, an intrinsic feature of the data demonstrates that our processing method has concentrated on several major channel values and filtered erratic and voluminous data. The advantage of the presented method is at that instead of using a

standard filter or channel enhancement method, a base-profile re-building and staining cells overlay strategy was used, such that the massive feature distribution in the raw image (blue color in Figure 5.3.1C) was integrated into three classes of features but with five-channel values in the preprocessed image (values marked by the red vertical lines in Figure 5.3.1C).

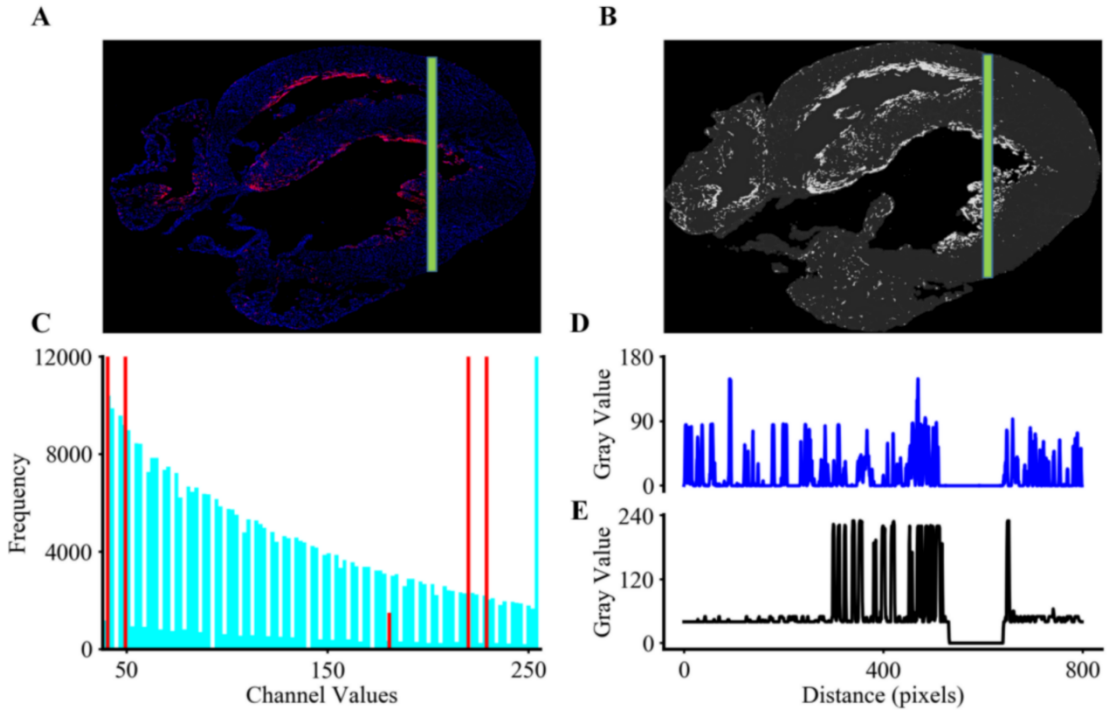

Figure 5.3.2. Frequency distribution histograms and radial grayscale distribution map for the intuitive analysis of neonatal mouse heart slice. A: Raw image; B: Preprocessed image by our method; C: Frequency distribution histograms of raw image (blue color) and preprocessed image (red color); D and E: Radial grayscale distribution along with the raw image (blue line) and preprocessed image (black line).

After validating the pixels' overall spatial distribution, we further investigated the invariance of the regional spatial displacement. We used the radial grayscale

distribution map to implement the gray analysis in the same location of the raw image and preprocessed image (green strip labels in Figure 5.3.1 and Figure 5.3.2). With comparison of the two images, it was shown there is a significant number of bristles in the raw image because of various regional holes and diverse grey values in the same color. For the preprocessed image, grey values were concentrated in five distinct clusters, which again enhanced the contrast of the whole image. Meanwhile, there was a similar trend of the grey value distributions in the regions marked by the green bar between the raw image and preprocessed image: the positive red cells distributed largely in the edge of the left and right ventricles, but it was more clearly classified in the pre-proceeded image as shown in its radial grayscale distribution map. Nevertheless, the negative cell distributed rather unevenly and had more holes in the histogram analysis of the neonatal mouse heart, which can be seen in Figure 5.3.2C.

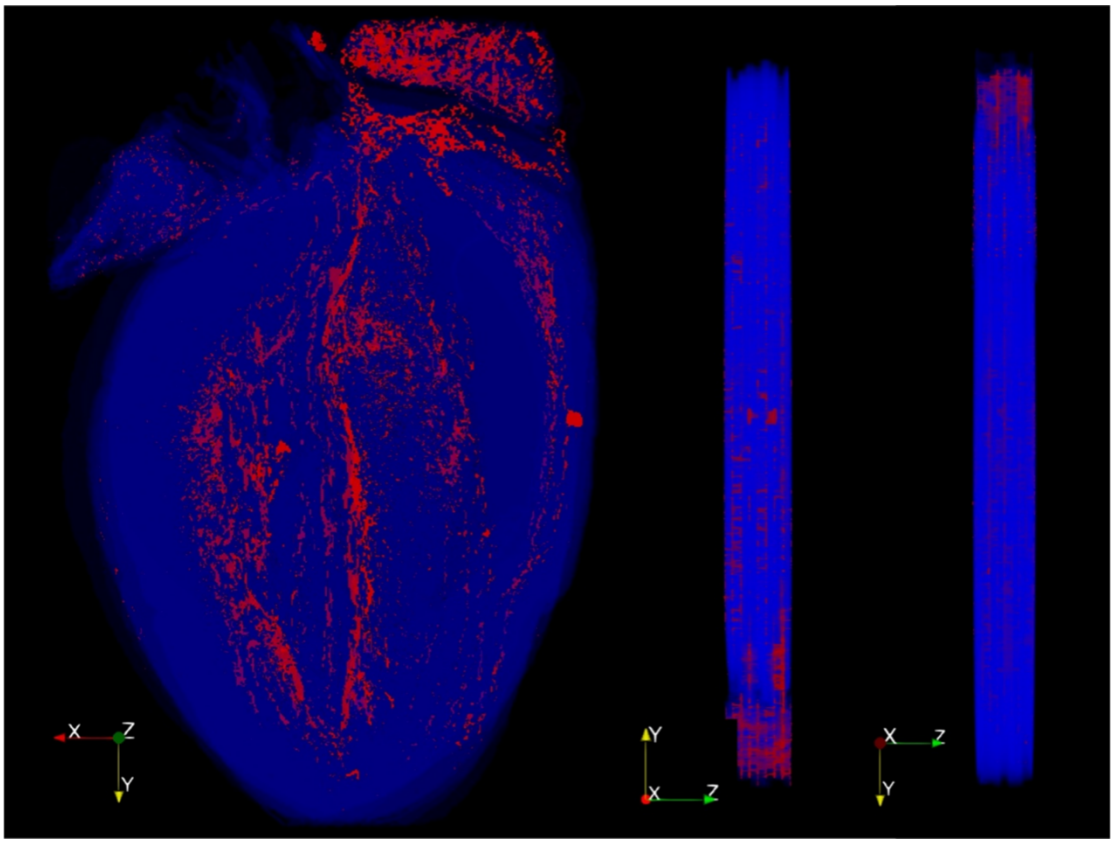

Figure 5.3.3. Multi-angle hyperspectral three-dimensional reconstruction results for tdTomato fluorescence cells of the adult mouse heart. All results write into VTK file format.

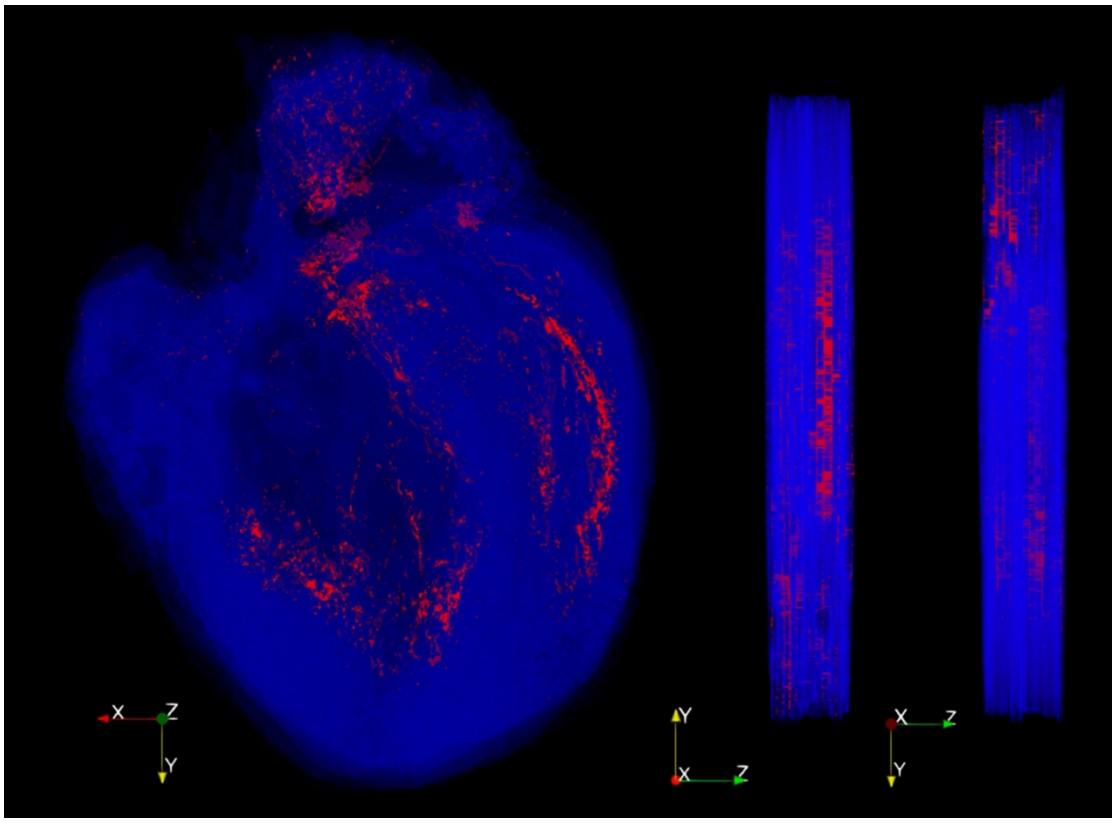

Figure 5.3.4. Multi-angle hyperspectral three-dimensional reconstruction results for tdTomato fluorescence cells of the neonatal mouse heart. All results write into VTK file format.

In this study, OpenCV and Matlab were utilized in combination to achieve an extended 3D reconstruction method, which can allow scientists to merge various components of the cell class into the same fundamental cardiac profile. The final 3D reconstruction result of adult and neonatal mouse heart is shown in Figure 5.3.3 and Figure 5.3.4, and the positive red cells are mostly observed in the RA and the surrounding areas of right

and left ventricle, but less detected in LA. To summarize, our method not only improved Ni.et.al's method(Ni et al., 2017b), but also incorporated an efficient computer vision analysis method to assess the 3D reconstruction process.

Chapter 6: Developing high-resolution three-dimension models of spatial distribution of cardiomyocyte subpopulation

Biological tissues are naturally three-dimensional (3D) opaque structures, which poses a major challenge for deep imaging of the spatial distribution and localization of specific cell types in organs in biomedical research. In this chapter, combining an improved heart tissue-clearing technique with high resolution light sheet fluorescence microscopy (LSFM), I conducted three-dimensional and multi-scale volumetric imaging of ultra-thin planes of murine hearts and obtained up to 2, 000 ultra-thin plane images per heart in three (x-, y- and z) directions and subsequently constructed high resolution 3-D volume heart models. I showed detailed three-dimensional spatial distributions of two specific cardiomyocyte populations, Hcn4 expression pacemaker cells and Pnmt+ cell-derived cardiomyocytes. The 3-D models presented allow for further geometrical and topological analysis of these cell types and the correlation with their physiological function in specific regions of the murine heart.

6.1 Improvements of tissue clearing method and high-resolution light sheet fluorescence microscopy

Biological tissues are naturally three-dimensional (3-D) structures and are usually opaque. This causes a major problem in deep imaging for defining the spatial distribution and positioning of specific cell types in intact organs, especially in highly

complex tissues such as the heart and brain. While modern fluorescent microscopic platforms, such as wide-field fluorescent microscopy or confocal scanning microscopy, have a high spatial resolution for imaging cellular structures, they suffer from insufficient axial resolution, as well as phototoxic damage if prolonged imaging is required(Sanderson et al., 2014). An alternative approach is to combine traditional histological sectioning approach to produce thin sliced tissue specimen (e.g. immunohistological staining on sectioned tissue samples) with post-imaging 3D reconstruction through computation. Histological sectioning also has significant limitations including tissue structure distortion and displacement, destruction of cell connections, and low spatial resolution when slicing samples.

Recently emerged tissue-clearing approaches provide an exciting opportunity to solve such problems by allowing efficient fluorescent labelling and rapid 3-D volumetric imaging of intact tissues, organs, and even entire organisms(Muntifering et al., 2018; Susaki & Ueda, 2016; Ueda et al., 2020). After clearance, the tissue becomes transparent, so the imaging depth may be less attenuated by the tissue sample. Such deep tissue visibility enables the interrogation of whole organ and even whole organisms without the need for sectioning the target tissue(Ueda et al., 2020). Clearing also removes strongly light-scattering and light-absorbing components of a tissue and equalizes the refractive index of the imaging medium to that of the tissue(Muntifering et al., 2018; Susaki & Ueda, 2016; Ueda et al., 2020). When tissue clearing is combined with light-sheet fluorescence microscopy (LSFM), 3D imaging of biological samples with high speed and

low photo-bleaching can be achieved. Hence, this approach has emerged as a powerful tool for biological research(Ueda et al., 2020; Verveer et al., 2007). LSFM itself provides higher speed, better signal-to-noise ratio, a lower level of photo-bleaching, and improved optical penetration depth than conventional wide-field fluorescent microscopy or confocal microscopy(Tomer et al., 2013). Further, it has an ability to selectively illuminate an ultra-thin plane of the sample via application of a sheet of light orthogonal to the detection path(Tomer et al., 2013).

In this chapter, I present a dataset of 3D murine heart volume models of spatial distribution of specific cell types obtained by combining an improved heart tissue clearing method with high resolution LSFM. Figure 6.1 illustrates a schematic overview of the study design and experimental procedure. The study has three major steps. Firstly, the heart sample is perfused by physiological solution in a Langendorff perfusion system allowing effective clearance of blood and tissue clearing. Such step is critical for reducing cardiac tissue auto fluorescence background. Secondly, the heart then undergoes a number of methodological interventions enabling efficient tissue clearing. Thirdly, high resolution LSFM is used for imaging the transparent heart. Finally, post-acquisition image reconstruction is performed to render the detailed 3D models. The detail explanations for each step are shown below.

Step 1: Whole heart clearing

The general procedure has been demonstrated in Figure 6.1A. The mouse underwent

intraperitoneal injection with 1.2% Avertin solution (0.5mL I.P) and heparin (200 units) for 10 minutes aiming for anesthetization and anticoagulation respectively. Afterwards, the heart was dissected and cannulated via the aorta for perfusion as follows. The heart was first perfused with cold PBS to remove blood to reduce the blood blocking, followed by 4% paraformaldehyde (PFA) phosphate buffer solution for fixation for 2 hours. After 15mL wash of PBS, the whole heart was then immediately perfused with CUBIC-P for 30 minutes, which is a chemical allowing efficient perfusion-fixation compatibility with downstream steps(Tainaka et al., 2018). This CUBIC-P is specially designed for organs with cavity structures such as hearts. After washing out the remaining PFA and CUBIC-P with PBS, the heart was treated with a lipid-removal chemical named CUBIC-L for delipidation. This process was conducted at 37°C for 5 to 7 days. Perfusion is crucial at this stage to convey the reagent, enabling a better clearing. Because the mouse model I used has genetically-encoded fluorescence labelling of the cells of interest, no staining is required. Otherwise, staining procedures are carried out at this time point. Followed by washing, the heart was then treated with CUBIC-L reagent to adjust the refractive index of the organs for at least 3 days.

Step 2: Transparent heart imaging

The transparent heart was illuminated by advanced Zeiss 7 light sheet fluorescent microscopy (LSFM). The adult murine heart (8 weeks old) is approximately 1.3cm x 0.7cm x 0.7cm in height, width and thickness. This LSFM with dedicated optics, enhanced sample chambers and designated sample holders enables high quality whole field imaging of the murine heart. LSFM separates the fluorescence of excitation

and detection into two solo light paths. In this case, the axis of illumination is perpendicular to the detection axis as shown in Figure 6.1B, allowing the illumination of a single thin section of heart at one point and thus generating inherent sections from the focus plane by merely exciting the fluorescence(Matsumoto et al., 2019). As a result, no pinhole or image processing procedures are needed. Unlike normal confocal fluorescent microscopes, LSFM is able to collect the light from the focus plane on the pixels rather than pixel by pixel, infinitely improving the resolution for the subsequent 3D reconstruction.

Step 3: 3D murine heart reconstruction

After imaging, the features and details of the heart were captured and reconstructed for the 3D model by using Zeiss Zen Blue software (Figure 6.1C). Fluorescent mode and depth code mode were selected to demonstrate the distribution of cell subpopulations of interest at 3-dimensional presentation. A series of image galleries were collected at certain interval of layers to show the distribution at 2-dimensional presentation.

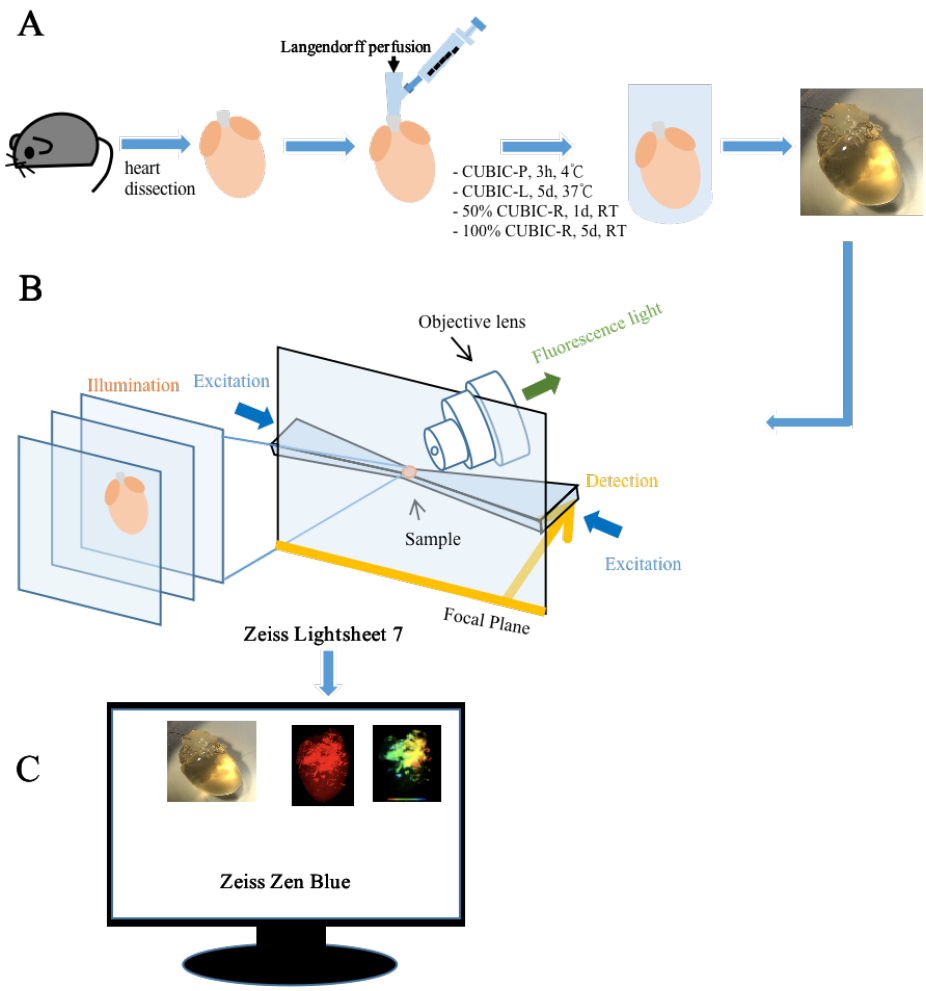

Figure 6.1 A schematic flowchart showing the process of the whole experiment. A. Sample preparation; B. Lightsheet imaging for transparent heart; C. 3D model reconstruction.

6.2 Verification of the improved method by 3D model reconstructions of Hcn4 expression pacemaker cells and Pnmt+ cell-derived cardiomyocytes

To verify this method, I successfully developed series of 3D volume models to define the spatial distributions of specific cardiomyocyte populations, which is comparable to the computational 3D models based on the histological images. This approach is efficient, not necessitating tissue sectioning, maintaining optimal tissue structure and organization, and has much higher axial and spatial resolution.

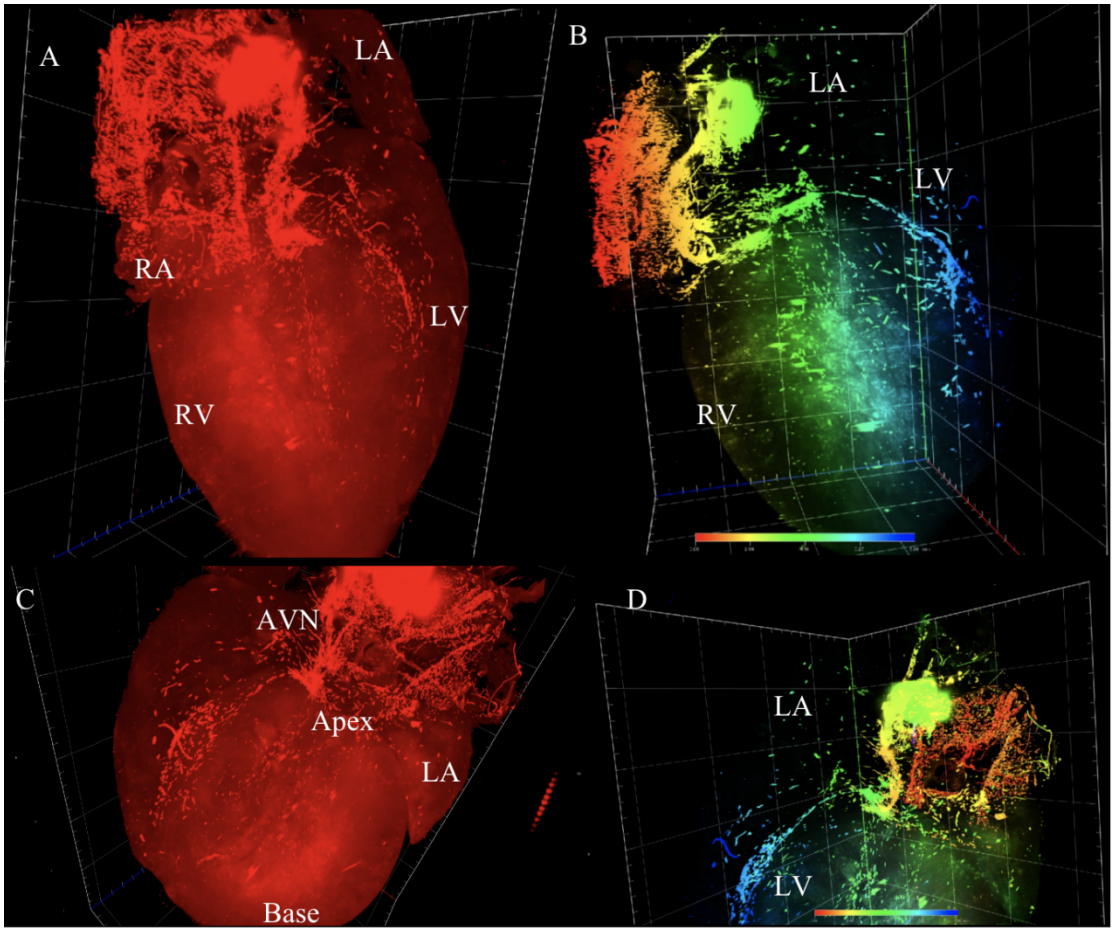

Figure 6.2.1 Fluorescent images and depth code images showed the distribution of Hcn4+ cells in adult mouse heart. A-B: The Tdtomato fluorescence and depth code

image showed the distribution of Hcn4+ cells from the ventral view respectively. C-D: The Tdtomato fluorescence and depth code image showed the distribution of Hcn4+ cells from the top left side respectively.

In the first set of data, I determined the spatial distribution of cardiac pacemaker cells by using potassium/sodium hyperpolarization-activated cyclic nucleotide-gated channel 4 (Hcn4) as a marker. Figure 6.2.1 presents the 3D volume reconstruction of spatial distribution Hcn4 positive pacemaker cells in the heart. Hcn4 is distributed throughout the right atrium with heavy staining localized in right atrial nodal regions (i.e., sinoatrial and atrioventricular nodes). Distribution of Hcn4 along the superior-inferior vena cava axis is in line with recent observations by Brennan et al(Brennan et al., 2020) and supports the wandering pacemaker hypothesis with 2 competing right atrial pacemakers localized near the superior vena cava and the inferior vena cava. Selected images captured by LSFM imaging representing coronal sections from an adult tdTomato mouse heart show the distribution of Hcn4+ pacemaker cells in adult Hcn4-Dre/tdTomato mice from ventral to dorsal, allowing visualization of the regional distribution of Hcn4 positive pacemaker cells in two dimension (Figure 6.2.2). The concurrent use of a programmed high resolution LSFM imaging allowed for the capture of ~ 2,000 ultra-thin plane images from a single murine heart with spatial resolution 1.54 µm × 1.54 µm × 4.01µm per pixel respectively in the x-, y- and z-direction, in corresponding to 5113 × 7325 × 1254 pixels in scaled image size. In online video 3, the multiple views are given and detailed structure and localization and depth of the Hcn4

positive cells are shown.

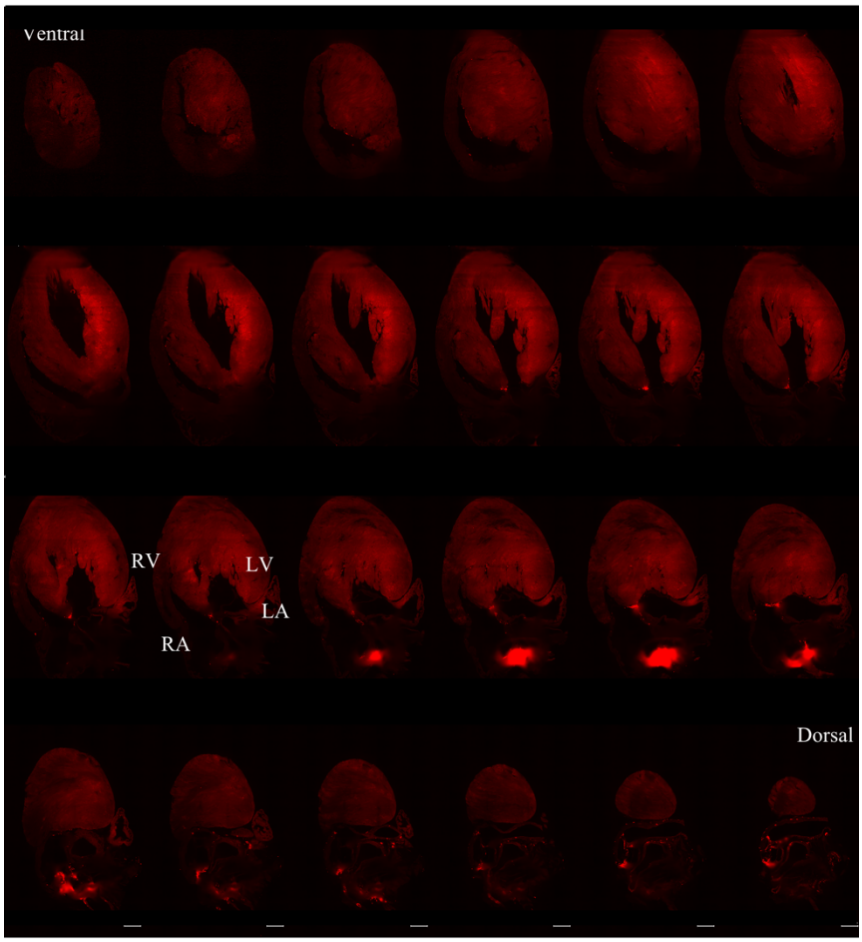

Figure 6.2.2 a systemic section views showed the distribution of Hcn4+ cells from ventral side to dorsal side in adult mouse heart. Scale bar: 1000 µm.

In the second series of models, I determined the spatial distribution of Pnmt+ cell-derived cardiomyocytes (PdCMs) that we discovered recently (Grassam-Rowe et al., 2020; Ni et al., 2017c; Y. Wang et al., 2017a). Figure 6.2.3 presents examples of two 3D volume reconstruction models of spatial distribution of Pnmt+ cell derived cardiomyocytes (PdCMs) in adult PnmtCre/ChR2-tdTomato heart. The use of the same programmed high resolution LSFM imaging for the capture of ~ 2,000 ultra-thin plane images from a single murine heart with similar spatial resolution in the x-, y- and z-

direction as obtained in Hcn4Dre/tdTomato hearts. The 3D volume model illustrates the reconstruction of spatial distribution of Pnmt+ cell derived cardiomyocytes (PdCMs) in adult PnmtCre/ChR2-tdTomato heart. The tdTomato fluorescence present from ventral, left and dorsal views respectively (Figure 6.2.3A-C). I also used depth code showing the localization of PdCMs in the heart from ventral, left side and dorsal side respectively (Figure 6.2.3D-F). The localization of PdCMs has not been shown previously in a computational 3D representation with such high spatial resolution. In online video 4, multiple views are given and detailed structure and localization and depth of the PdCMs are shown. Figure 6.2.4 presents images captured by LSFM imaging representing coronal sections from an adult ChR2/tdTomato mouse heart. This shows the distribution of PdCMs from ventral side to dorsal side, allowing visualizing of the regional distribution of PdCMs in a two-dimensional manner.

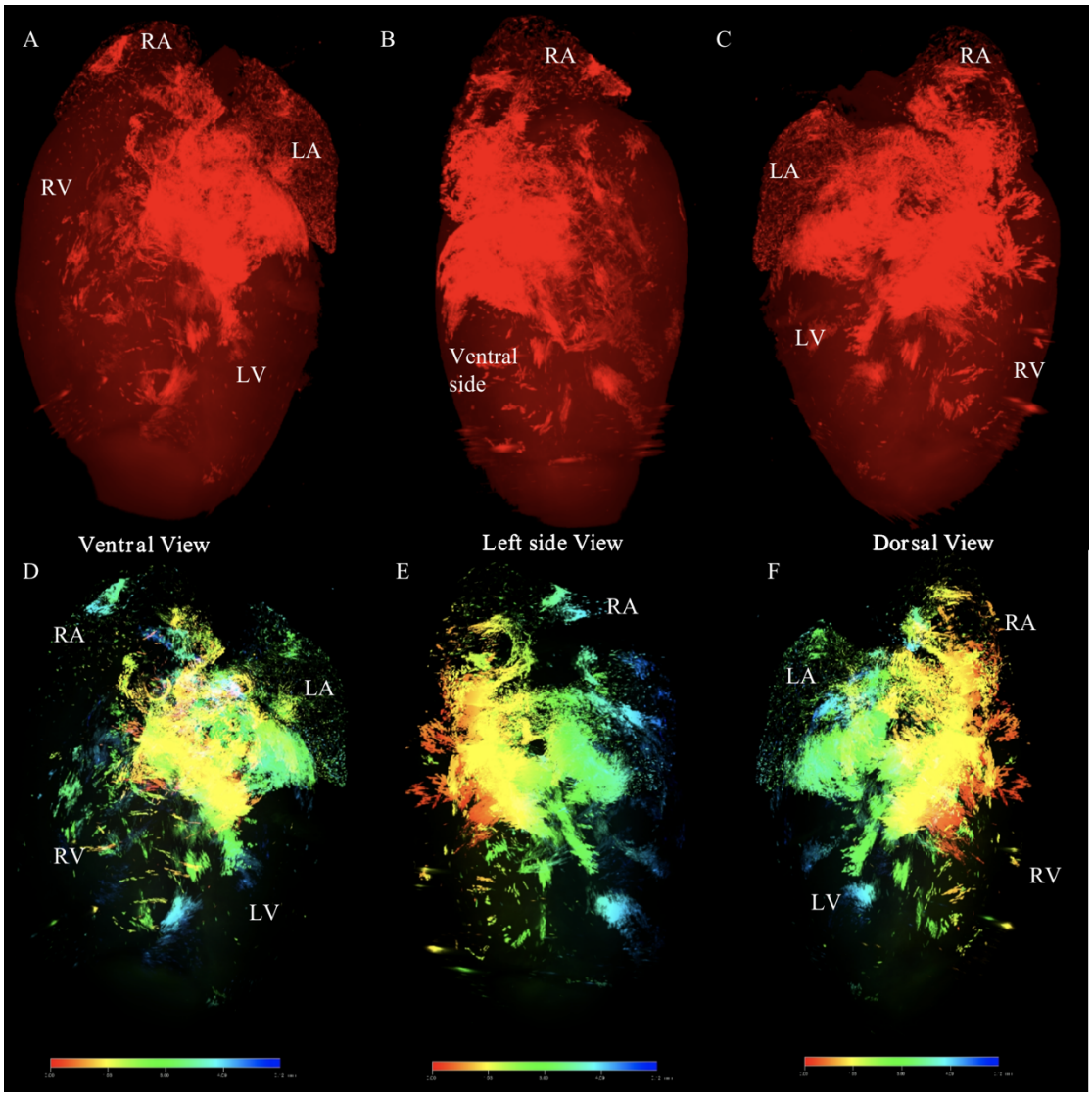

Figure 6.2.3 Fluorescent images and depth code images showed the distribution of Pnmt+ cell-derived cardiomyocytes (PdCMs) in adult mouse heart. A-C: The Tdtomato fluorescence was present from ventral, left side and dorsal side respectively. D-F: The depth code showed the depth of the fluorescence in adult mouse heart from ventral, left side and dorsal side respectively.

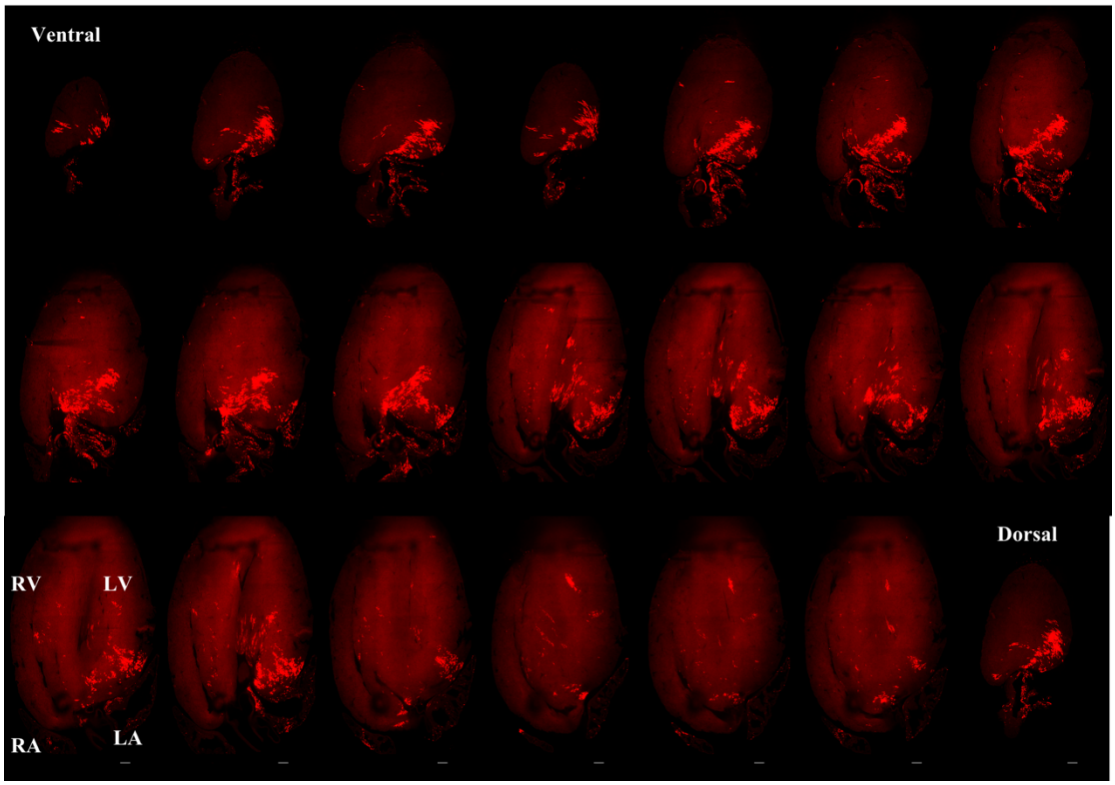

Figure 6.2.4 a systemic section views showed the distribution of Pnmt+cells derived cardiomyocytes (PdCMs) from ventral side to dorsal side in adult mouse heart. Scale bar: 500 μm

6.3 Technique validation for high-resolution three-dimension method

In order to validate this high-resolution three-dimension method, the genotypes of the mice were used for verification to confirm the accuracy of subsequent results. The $Hcn4^{DreER/tdTomato}$ mice were genotyped using PCR to detect the presence of the $Hcn4^{e(kozak\text{-}DreER\text{-}WPRE\text{-}A)1}$ gene (wild type: forward primer: AGCGAAGGACGCGTCCTCACTG, reverse primer: ACCGTTGGTGCTGGACTT GCCG; Mutant: forward primer: CGGGCCCG GGAGGAGGTG, reverse primer: GGTAGAGGCCAGGTCAGCATCGTG) and $H11^{CAG\text{-}RSR\text{-}}$

^{tdTomato} gene (wild type: forward primer: ATAAGCCATTCTCCATTTCA, reverse primer: GACACATCCTG CCCTTACCTTA; Mutant: forward primer: GACACATCCTGCCCTTACCTTA, reverse primer: GCGGGCCATTTACCGTCATT). The Pnmt$^{Cre/ChR2\text{-}tdTomato}$ mice were genotyped using PCR to detect the presence of the Cre-recombinase gene (forward primer: GACGGAAATCCATCG CT CGAC, reverse primer: GACATGTTCAGGGA TCGCCAG) and ChR2 gene (wild type: forward primer: AAGGGAGCAGTGGAG TA, reverse primer: CCGAAAATCTGTGGGAAGTC; Mutant: forward primer: GG CATTAAAGCAGCGTATCC, reverse primer: CTGTTCCTGTACGGCATGG).

Further validation of the model was performed by immunohistochemistry on Hcn4$^{DreER/\ tdTomato}$ mouse heart tissue. Figure 6.3 shows similar expression of distribution patterns specifically within the SAN of (A) the Hcn4^{+} cells in Hcn4$^{DreER/tdTomato}$ heart and (B) Pnmt^{+}/Tdtomato positive cells in Pnmt$^{Cre/ChR2\text{-}tdTomato}$ heart.

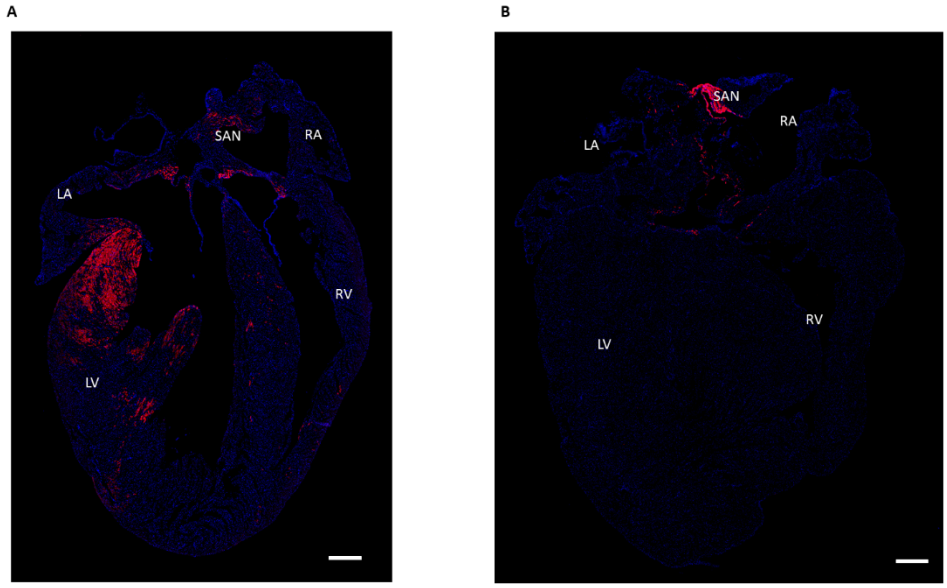

Figure 6.3 Histological section confocal microscopic images of expression of distribution patterns of the $Hcn4^{+}$ cells in $Hcn4^{DreER/tdTomato}$ heart (A) and $Pnmt^{+}$/Tdtomato positive cells in $Pnmt^{Cre/ChR2\text{-}tdTomato}$ heart (B). Tdtomato fluorescence signal indicating $Pnmt^{+}$ myocytes were observed on the left side of heart and SAN region. B: Tdtomato fluorescence signal was mainly observed in the SAN and AVN regions in $Hcn4^{DreER/tdTomato}$ heart. Scale bar: 500 μm.

6.4 3D model reconstruction of *Dbh*$^{+}$ cells in murine heart

This approach was also applied to the Dbh-Cre/ChR2-tdTomato mouse model, revealing *Dbh* expression spatially and temporarily. As identified by the scRNA seq and spatial transcriptome analysis, the *Dbh*$^{+}$ cells are concentrated in the right atrium and cardiac conduction system. Demonstrated in Figure 6.4.1, two 3D volume reconstruction models of *Dbh*$^{+}$ cell in adult by using Dbh-Cre/ChR2-tdTomato heart to indicate the width and depth of *Dbh*$^{+}$ cells. Figure 6.4.1(A-B) shows *Dbh*$^{+}$ cell distribution in the whole heart, sparse in the ventricular but concentrated in the right atrium. As more closely illustrated in Figure 6.4.1(C-D), DBH+ cells take up the central cardiac conduction system like SAN, AVN and HIS bundle regions, consistent with our scRNA seq and spatial transcriptomes. The depth code model (Figure 6.4.1 D) also suggested the expression of DBH at superficial and internal level.

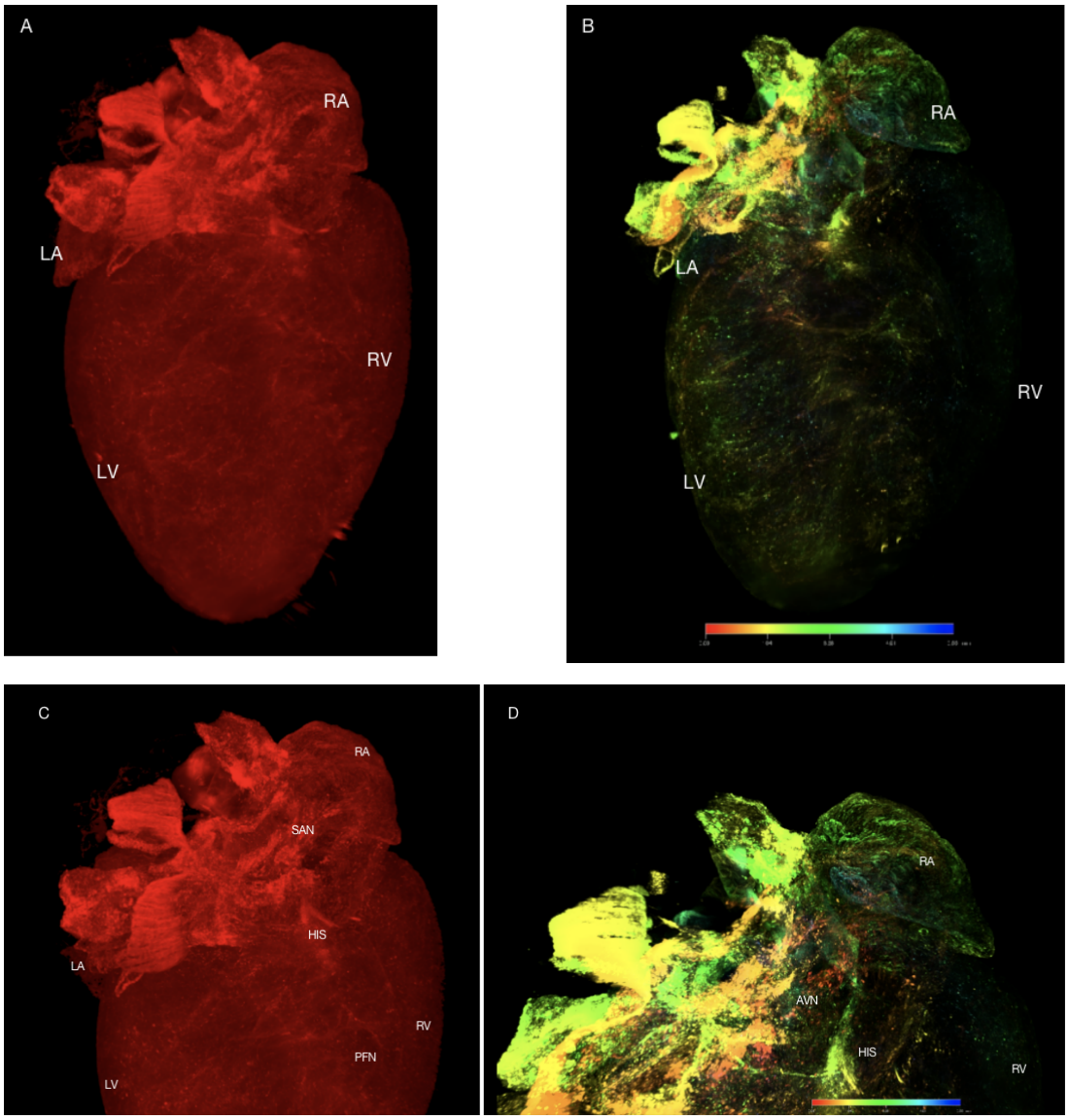

Figure 6.4.1 Fluorescent images and depth code images showed the distribution of DBH+ cells in adult mouse heart. A-B: The Tdtomato fluorescence and depth code image showed the distribution of DBH+ cells from the dorsal view respectively. C-D: The Tdtomato fluorescence and depth code image showed the distribution of *Dbh*$^{+}$ cells from the atrial region respectively.

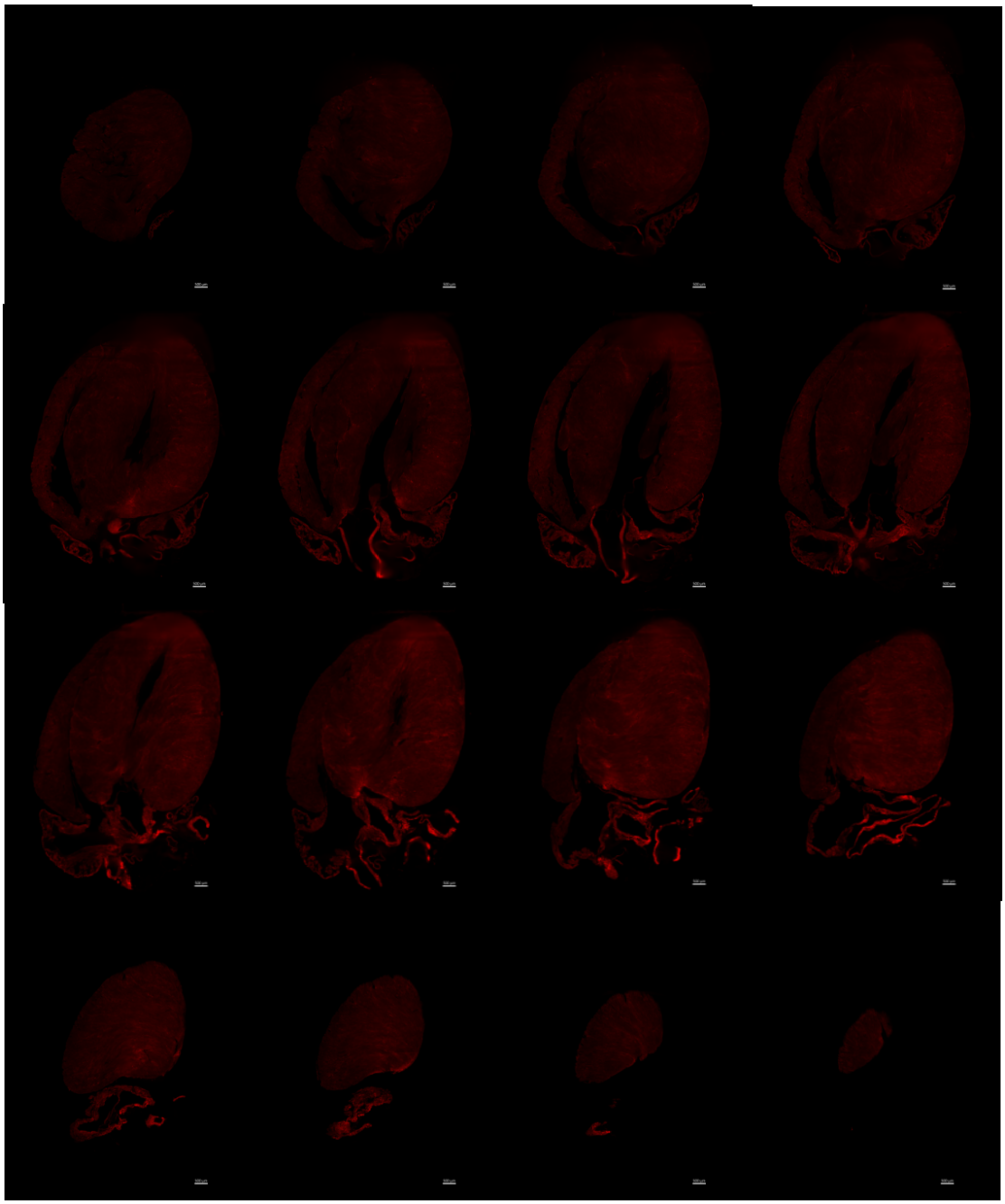

Figure 6.4.2 Systemic section views showed the distribution of *Dbh*$^{+}$ cells from ventral side to dorsal side in adult mouse heart. Scale bar: 1000 μm.

Figure 6.4.2 exhibits images captured by LSFM imaging representing coronal sections from an adult Dbh-Cre/ChR2-tdTomato mouse heart. This shows the distribution of Dbh+ cells from ventral side to dorsal side, allowing visualizing of the regional

distribution of *Dbh*$^{+}$ cells in a two-dimensional manner.

To conclude, the combination of an improved heart tissue-clearing technique with high-resolution light sheet fluorescence microscopy (LSFM) has several advantages and features. Firstly, I used mouse models with conditional cell type specific overexpression of fluorescent protein allowing cell-type-specific visualization. These models provide the unique advantage of using tissue clearing for studying specific cell types without the requirement of using immunostaining with antibodies. Secondly, I modified the clearing approach to achieve high-quality transparent heart tissue with reduced auto-fluorescent background for optical imaging. Thirdly, imaging by a high-resolution light sheet system allows global heart view and cellular visualization achieved by rapid changing in optical lens and is integrated with 3D reconstruction without the requirement of additional mathematical modeling. Finally, the 3D reconstruction allows for detailed geometrical and topological analysis. The datasets presented here thus offer a means for reuse and a basis for further development of functional models of the heart by incorporating physiological data in the future.

However, the requirement for the microscope is high and the machine itself is costly even though the sample preparation is simple and feasible. The method elucidated in chapter 5.3 is a good alternative. The method is well-established and unambiguously unveiled the specific cell type distribution. One drawback of this method is that the quality of 3D reconstruction is largely dependent on single slice imaging, given that

every image should give a relatively high and comparable resolution, moreover the imaging process is time-consuming. Even tiny unmatched pixels between adjacent images make a difference. A better and unrestricted method needs to be developed for future study.

Chapter 7: Characterising electrophysiological and endocrine properties of *Dd-CM*s

Based on the findings presented in Chapters 3-5, the genetic profiles and spatial distribution of Dbh+-derived cardiomyocytes (Dd-CMs) were revealed and elucidated. As a key enzyme in the process of catecholamine biosynthesis, Dbh protein is likely to exert functions during the development of maturation of the heart, which accounts for its existence in specific cardiomyocytes. In this chapter, I explored the potential electrophysiological properties and endocrine function of Dd-CM in adult murine heart.

7.1 Generation of mouse models

To explore the electrophysiological function of Dbh+ cells, a new mouse line was generated by crossing the Dbh-Cre mice with B6.Cg-Gt (ROSA) 26Sortm27.1(CAG-COP4*H134R/tdTomato) Hze/J strain (Stock No. 012567, Jackson Labs) reporter line. Channelrhodopsin-2 is a subfamily of retinylidene proteins, functioning as a light-gate ion channel. Serving as a sensory photoreceptor on the cell surface, ChR2 can control the electrical excitability by influx of calcium and other ions in response to light. The hChR2(H134R)-tdTomato is a fusion protein consisting of a mammalian codon-optimized channelrhodopsin-2 that secretes a gain-of-function H134R substitution with a tdTomato fluorescent reporter protein. The hChR2(H134R)-tdTomato is designated to give rise to bigger stationary photocurrents compared with pure ChR2.

The hChR2(H134R)-tdTomato is to exert function when driven by blue ligh(450-490nm), forcing the open of cation channels and thus depolarizing the cells and fire the action potentials.

In this new optogenetic line, a loxP STOP loxP cassette stop transcription of the downstream of HChR2(H134R)-tdTomato fusion protein, thus no fluorescence is observed in mouse heart. This can be explained by the fact that the HChR2(H134R)-tdTomato driven by the CAG promoter was targeted for insertion in the Gt(ROSA)26Sor region, it is Cre recombinase expressed in the cells of interest that determines the expression of fusion protein. When we crossed the Dbh-Cre heterozygous mice with this reporter line, the offspring will delete the STOP cassette in Cre-expressing Dbh cells, finally causing the expression of fusion protein.

This new line provides an effective tool for optogenetic study of these Dbh+ cells. Combined with the tdTomato labelling, we can visualise these cells and study their electrophysiological properties.

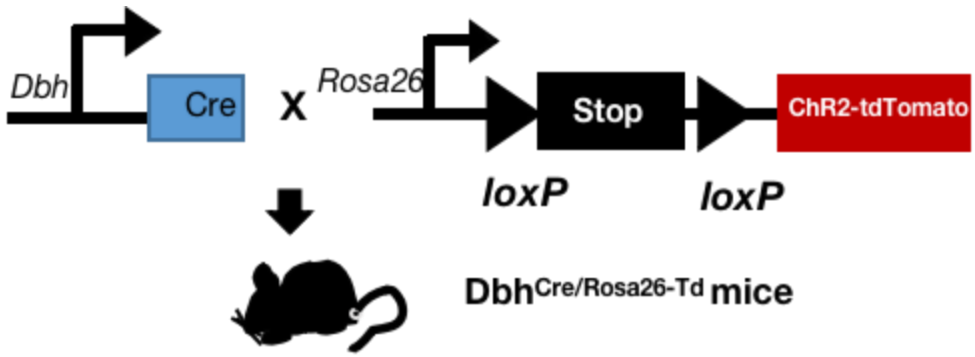

Figure 7.1 The strategy of DbhCre/ChR2-Td mouse model

7.2 Optical mapping reveals the fast conduction property of *Dd-CM*s

I explored the electrophysiological properties of *Dbh*$^{+}$-derived cardiomyocytes corresponding to their specific location across the heart by using above optogenetic mouse line DbhCre/ChR2-tdTomato obtained by crossing DbhCre mouse line with ChR2-tdTomato mice. This line allows to achieve cell type specific activation of *Dbh*$^{+}$-derived cardiomyocytes with light wavelength ~470 nm for optogenetic activation of ChR2. Figure 7.2.1a shows the recordings of optical Vm recorded in DbhCre/ChR2-tdTomato hearts under conditions of sinus rhythm or optogenetic stimulation by light pacing positioned in different epicardial regions of the heart, as shown in Figure 7.2.1b. Both electrical and light pacing resulted in an anisotropic propagation of action potentials when pacing ventricle from the epicardium or endocardium side. The light intensity required for overdriving sinus rhythm, with directed optogenetic stimulation is highly correlated to the distribution pattern of Dd-CMs (RA<LA<RV<LV) shown in Figure 7.2.2a. Then electrical and light pacing to evoke ventricular conduction properties was compared. Both electrical and light pacing resulted in an anisotropic propagation of action potentials when endocardial pacing of either the left or right ventricle (Figure 7.2.2b). However, compared to non-cell-type-specific electrical stimulation, Dd-CMs cell type-specific light stimulation evoked a significantly faster action potential conduction with endocardial pacing of either the left or right ventricle (Figure 7.2.2a) demonstrated by isochronal activation maps of action potentials in Dbh^{Cre}/ChR2-Td hearts (Figure 7.2.2b-c). The faster conduction velocity indicates that

selective Dd-CM activation may be activating the fast conductive ventricular CCS, suggesting a close association of Dd-CM with the ventricular CCS.

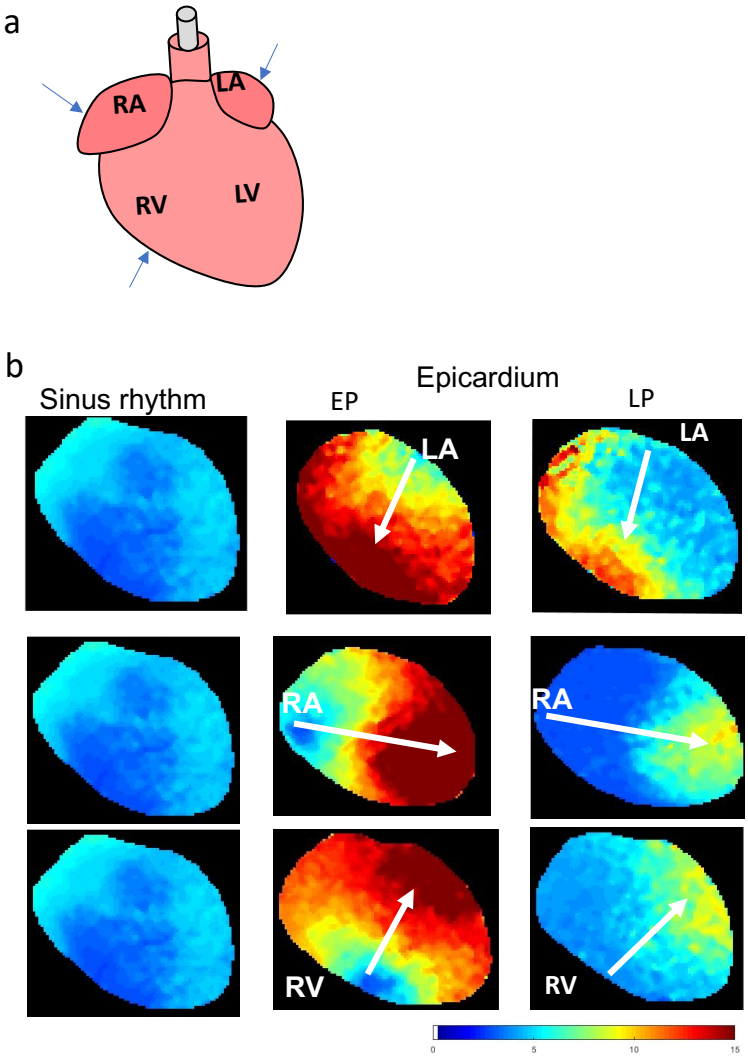

Figure 7.2.1 The optical mapping of *Dbh*$^{+}$-derived cardiomyocytes in adult murine hearts

a) A schematic graph showing the pacing location in adult murine hearts

b) Isochronal activation maps of action potentials obtained from sinus rhythm, electrical pacing and light-pacing from *Dbh*Cre/ChR2-Td hearts recorded from

epicardium. Light pulses evoked action potentials in a 1:1 manner (n=4 hearts). Light intensity: 0.6–0.8mW/mm2. Light pacing resulted in an anisotropic propagation spread from RV-LV.

Scale bar: 100 µm

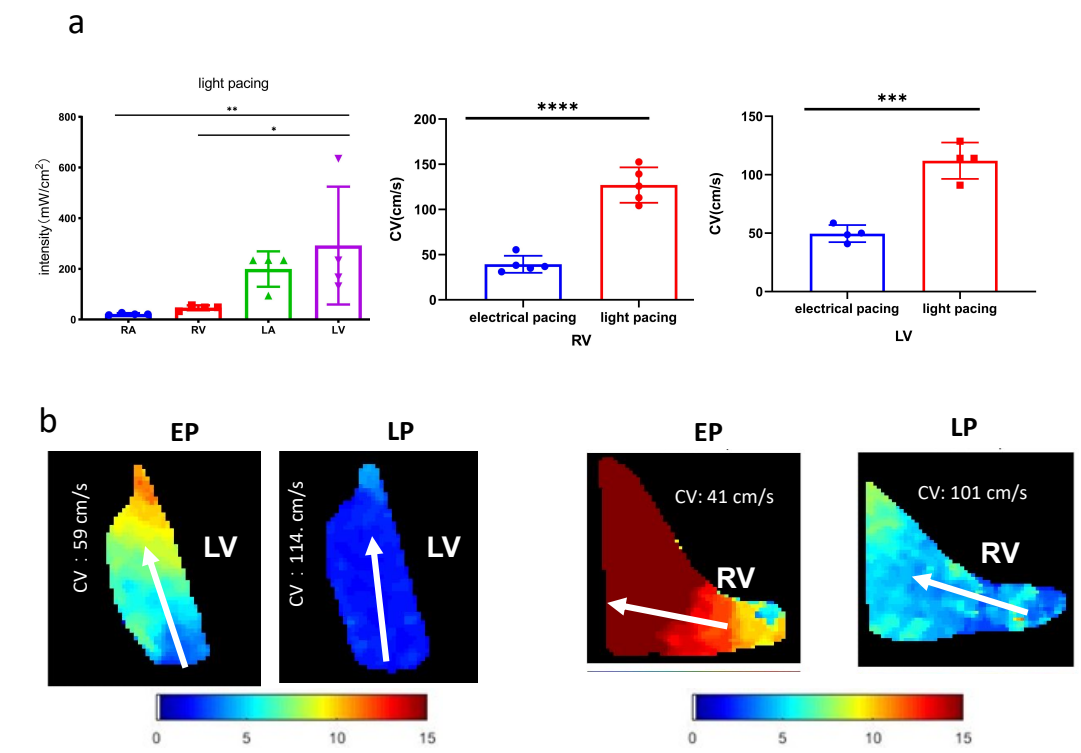

Figure 7.2.2 Correlation of conduction properties of *Dbh*$^{+}$-derived cardiomyocytes in adult murine hearts

a) Comparison of light intensities of LP thresholds in different pacing sites and comparison of conduction velocity (CV) of action potential propagation of RV and LV. Light pulses evoked action potentials in a 1:1 manner (n=4 hearts). Light intensity: 0.6–0.8mW/mm^2.

b) Isochronal activation maps of action potentials obtained from endocardium of Dbh^{Cre}/ChR2-Td hearts recorded under conditions of 1) electrical pacing (EP)

2) light-pacing (LP) in both left and right ventricles.

7.3 NE trace showing the potential endocrine functions

The GO analysis was previously conducted and demonstrated that Dbh+ derived cardiomyocytes possess a high potential of catecholaminergic functions though varies in different regions in chapter 3.5. To interrogate this putative catecholaminergic function ex vivo, I then used a fluorescent false neurotransmitter 270 (FFN270), a fluorescent tracer recently developed by Dunn et al(Dunn et al., 2018) as a fluorescent substrate of the norepinephrine and vesicular monoamine transporter (VMAT2) enabling an intuitive way to visualize the location and activity of sympathetic neurons in the place of interest. Wild type mice were used for the first trial. I treated adult mouse hearts with FFN270 by Langendorf perfusion in for 30 mins (n = 3, 8 weeks old examined). Then the SAN and right atrium were dissected for imaging.

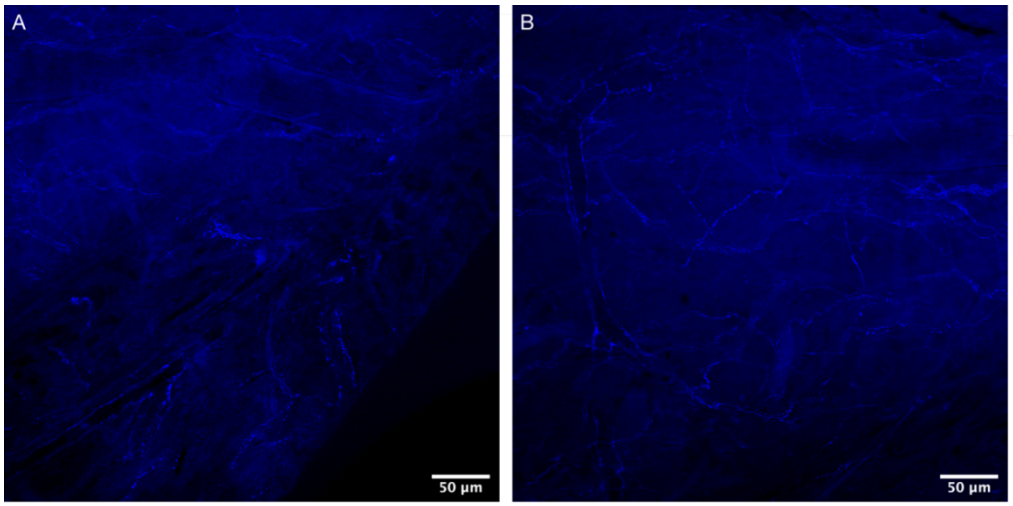

Figure 7.3.1 A and B showing NE trace (blue) signals on the SAN region of wild type mice heart. Scale bar: 50µm.

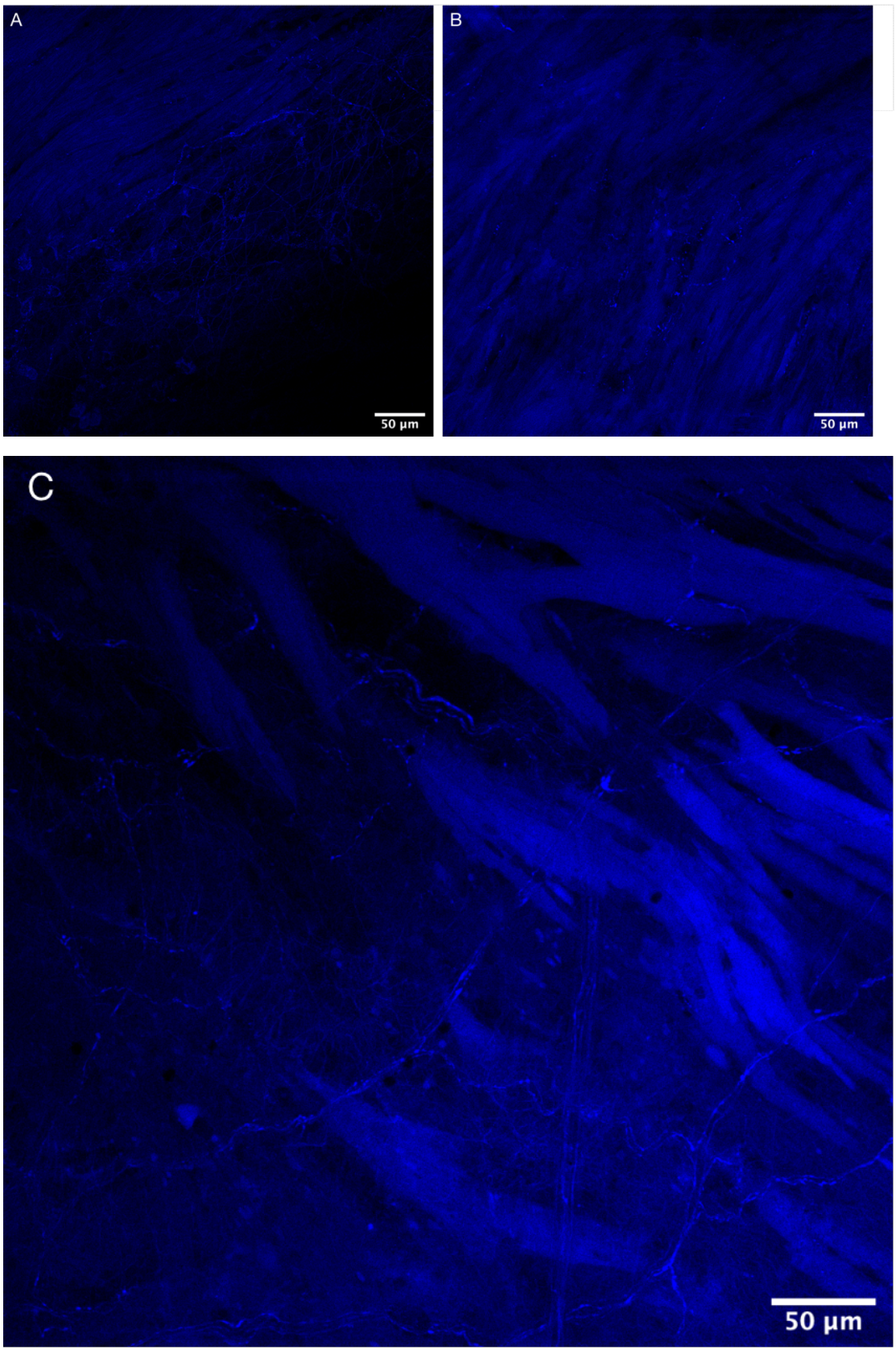

Figure 7.3.2 A-C showing NE trace (blue) signals on the right atrial region of wild type mice heart. Scale bar: 50µm.

FFN270 signal presented as punctate fluorescence in cardiac sympathetic nerve fibers as exemplified in the image taken from SAN region (Figure7.3.1A-B). FFN270 presented a bright cluster of punctate fluorescence in the SAN and right atrium which are abundant with the cardiac sympathetic innervation. This is consistent with the previous report that SAN is in high density of sympathetic innervation correlated to its physiological function as a pacemaker. An unambiguous sympathetic nervous network is depicted in the SAN region that identified the effectiveness of this method. Compared to the SAN region, the sympathetic nerve fiber in the right atrial region is less enhanced but elicit three patterns with cardiomyocytes. Some sympathetic nerve fibers extend along with the elongated cardiomyocytes whilst some cross the adjacent cardiomyocytes (Figure 7.3.2A-B) While trans-membrane signals are also observed in right atrial suggesting uptake and release function of NE occurred at this time (Figure 7.3.2C). Interestingly, I found there are some brighter cells that concentrated in the right atrial region (Figure 7.3.2C). Given the nature of FFN270 as a fluorescent substrate of the norepinephrine and vesicular monoamine transporter (VMAT2), fluorescence on the cell surface probably results from either the NE release from the vesicle to the intracellular and extracellular or reuptake of NE. This finding implies that there is a subpopulation of cells in the right atrium that are capable of release and uptake of catecholamine. To explore the identity of this subpopulation, I tried PNMT+ derived cardiomyocytes and Dbh+ derived cardiomyocytes since these two subpopulations both historically and temporally contain catecholaminergic enzymes.

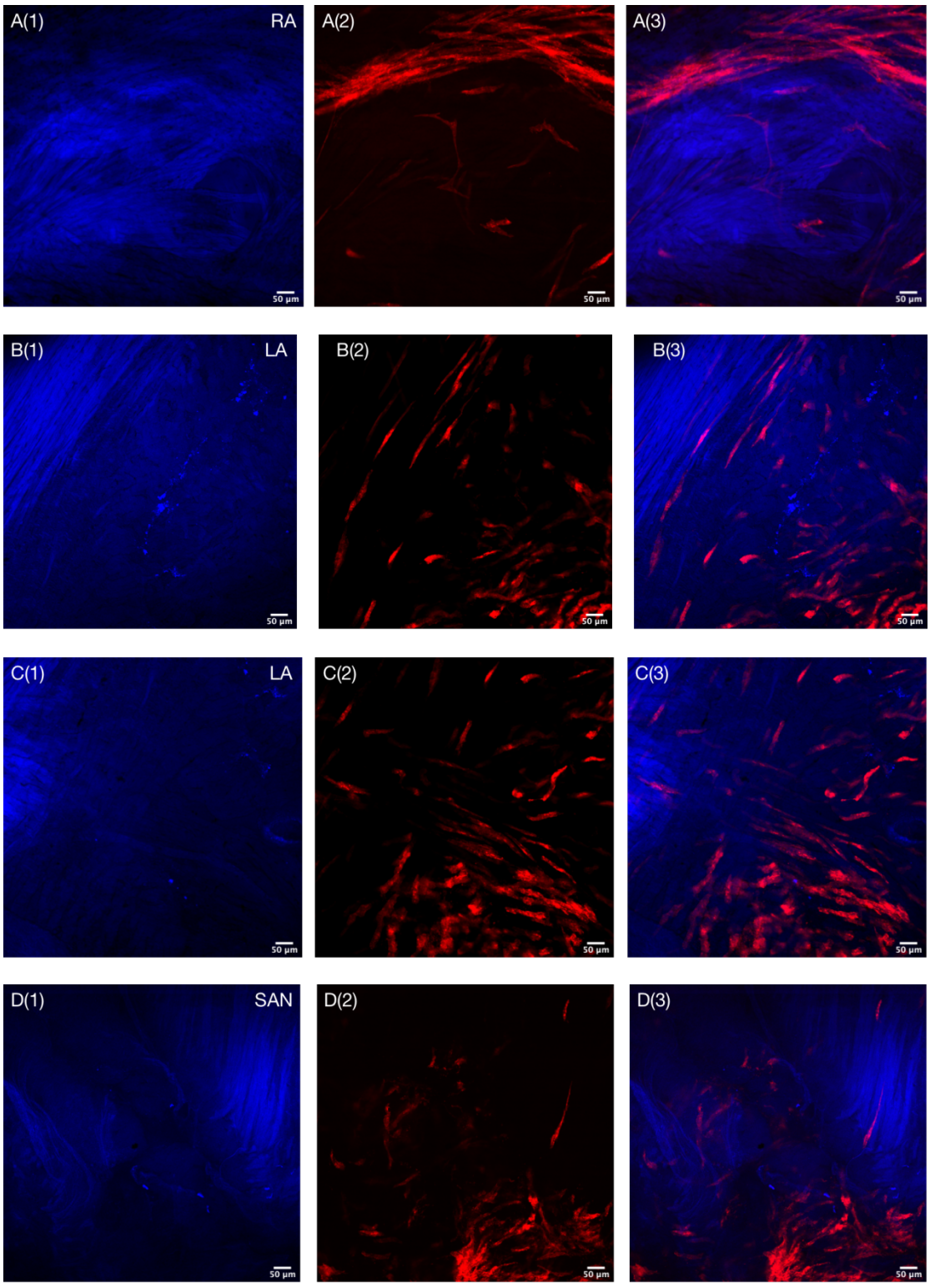

Figure 7.3.3 A-D showing NE trace (blue) signals in RA, LA and SAN regions on PdCM (red) mouse hearts. Scale bar: 50µm.

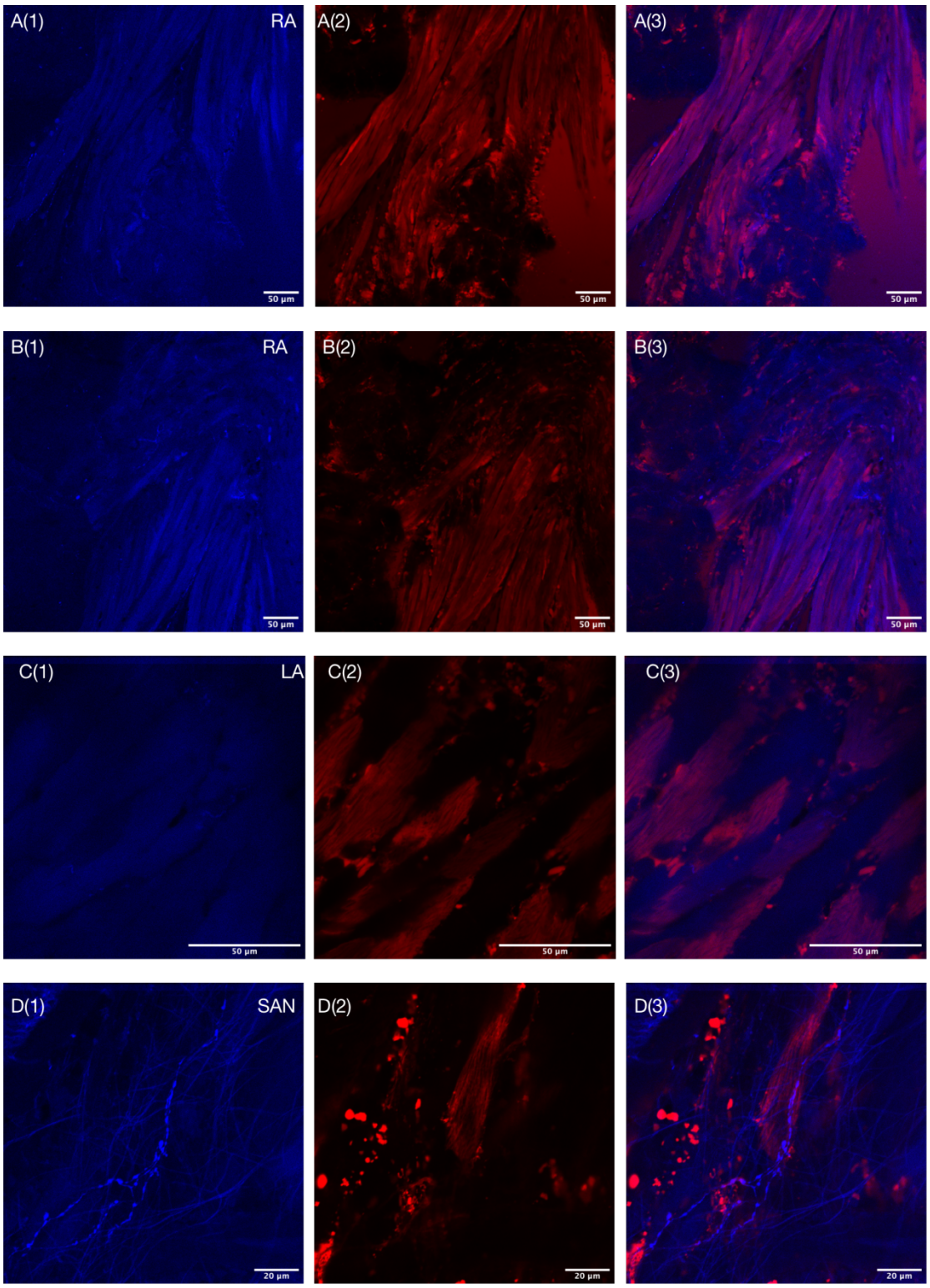

Figure 7.3.4 A-D showing NE trace (blue) signals in RA, LA and SAN regions on Dbh-Cre/tdTomato (red) mouse hearts. Scale bar: A-C: 50µm; D: 20µm.

The NE trace was conducted in both PdCM mouse model and Dbh-Cre/tdTomato mouse model. Shown in Figure 7.3.3A-D, consistent with previous reports that PNMT+ derived cardiomyocytes were found mainly located in the left atrium and some in SAN nodal region but less in right atrium. Those bright cells of interest were also detected in both right and left atria, plus a few in SAN region, after NE trace loading. However, almost no overlap was observed with Pnmt-tdTomato signal, suggesting the loss or silence of related catecholaminergic function. In contrast, distinct overlaps between brighter cells and Dbh-tdTomato were revealed notably in right atrium with a few in left atrial and SAN region, indicating that most of the brighter cells are Dbh-tdTomato cells (Figure 7.3.4A-D). This fraction of Dbh+ derived cardiomyocytes cells labelled with FFN270 further proves the possibility that NE transporter and synaptic vesicles exist in these cells.

To further verify, we applied a NET inhibitor, nomifensine, as a control. Nomifensine inhibit the reuptake of NE and dopamine. Significantly, nomifensine decreased in FFN270 signal in both SAN and atrial preparations, indicating the uptake and release activities in sympathetic innervation fibers and Dbh-derived cardiomyocytes were suppressed (Figure 7.3.5). Taken together, Dbh+ derived cardiomyocytes, unlike the PdCMs, are likely to still hold the ability of release and uptake of catecholaminergic substance.

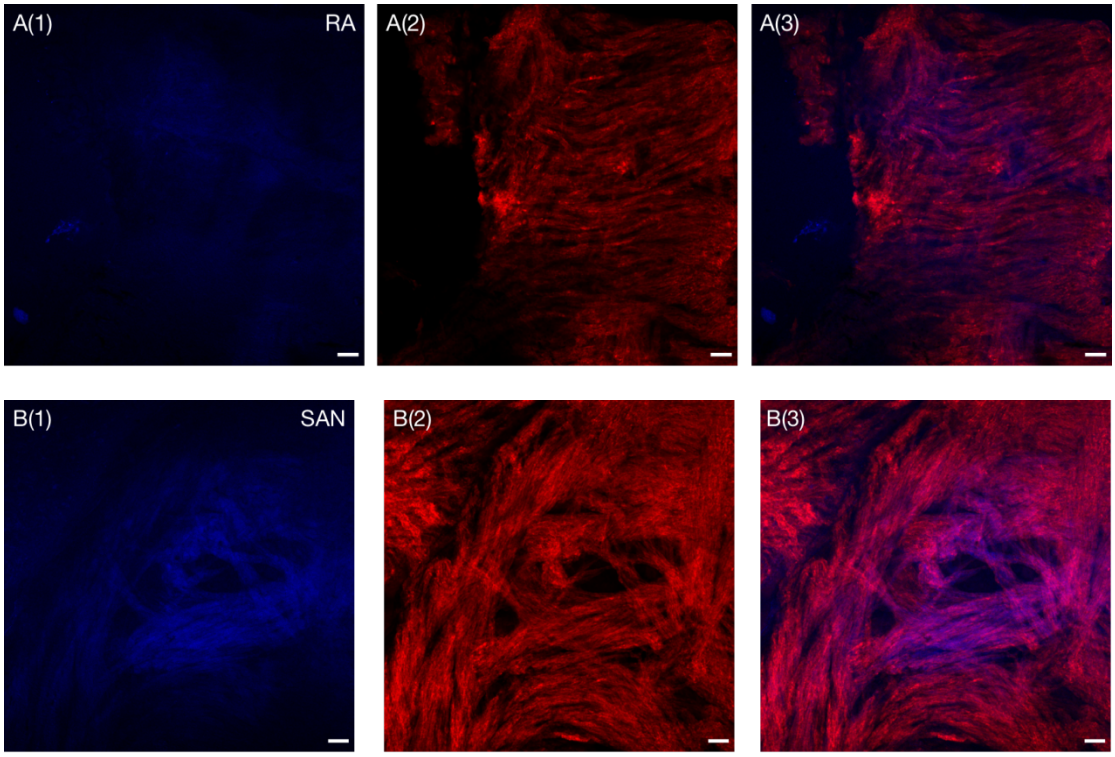

Figure 7.3.5 A-B showing NE trace (blue) signals after the treatment of NET inhibitor in RA, and SAN regions on Dbh-Cre/tdTomato (red) mouse hearts. Scale bar: 100μm

7.4 TEM study indicating the structurally potential of endocrine functions

I further dissected Dbh+Td positive right atrial tissue and conducted TEM image and EDS analysis of chromium signal in comparison with adrenal medullary chromaffin cells. As shown in Figure 7.4, Dbh+ cardiomyocyte contains high electron density vesicles as seen in adrenal medullary chromaffin cells. Dbh+ cardiomyocytes have much fewer and weaker chromium signal in these vesicles than those of medullary chromaffin cells. This finding is strong evidence to prove the potential uptake and

release function of Dd-CMs. However, more investigation is required for further validation.

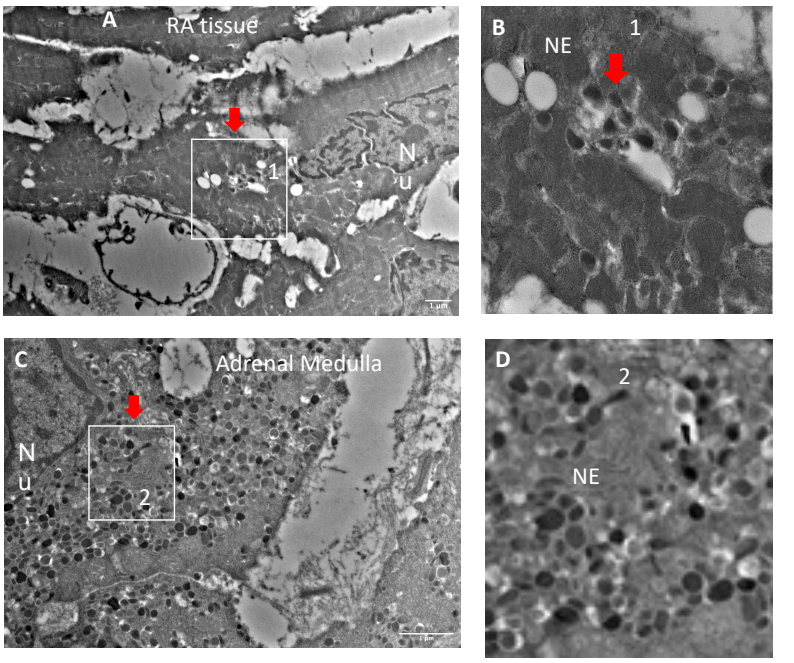

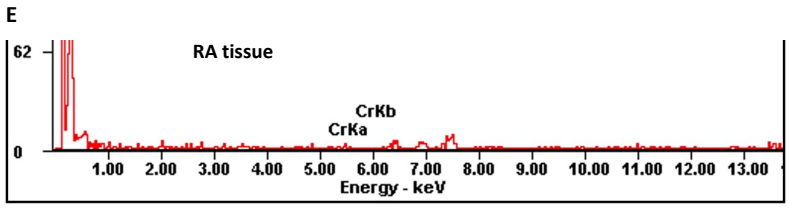

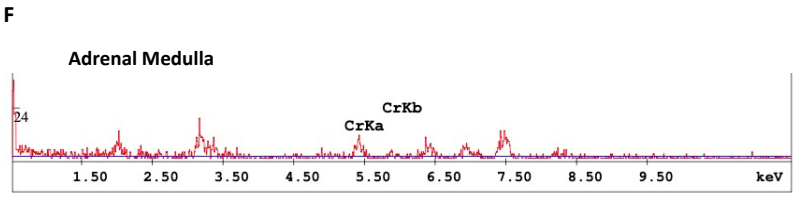

Figure 7.4 Illustration of TEM image and EDS mapping to analyze chromaffin cells. A. Cardiomyocytes containing high electron density vesicles (red arrow). B. The region within the white frame is selected for EDS analysis of chromium. C. Adrenal medullary cells from the same mouse containing large number of high electron density vesicles (red arrow). D. The region within the white frame is selected for EDS analysis of

chromium. E. The CrKa and CrKb peaks in EDS spectrum were barely detectable which showed very weak Chromium signals in the RA region. F. The CrKa and CrKb peaks in EDS spectrum confirmed chromium within the adrenal medulla tissue.

Chapter 8. Discussion and Conclusion

This thesis focuses on the development of the cardiac conduction system in murine heart by applying various state of the art techniques to investigate their characterization from development to maturation. By utilising advanced and complementary transcriptomic analyses, genetic fate mapping, optogenetics, imaging and 3D computational image reconstruction, my study has interrogated developing and adult murine hearts, providing new insights into the development and physiology of the mammalian CCS through discovery and characterisation of a novel *Dbh* expressing and *Dbh*$^{+}$-derived cardiomyocyte populations (Dd-CMs). There are several notable findings from my study:

Firstly, by undertaking integrated scRNAseq and spatially resolved transcriptomic analyses of the developing heart, a comprehensive transcriptional landscape of cell types is established to populate the developing murine heart. The dataset spans a large number of single cell transcriptomes from six mid-to-late developmental stages by scRNAseq (175237 cells) and spatial transcriptomics (~25000 cells) from 3 developmental stages. Through meaningful cardiomyocyte-focused quality control and utilizing a novel local and global structure-preserving dimensionality reduction technique (PHATE); this allows to discriminate rarer cardiac cell types, such as the CCS. The spatially resolved transcriptomic Stereo-seq investigation identified major cardiac cell populations and structures through both unsupervised and supervised machine

learning techniques. However, it is noted that there were some imperfect, but logical, predictions of cell types. Integration of scRNAseq and SrT data remains a nascent field, and future computational work is expected to produce more accurate integration, perhaps through inclusion of prior knowledge and combinatorial scoring based on a cell's given cassette of initially predicted labels. The utilization of the nanoscale SrT technology Stereo-seq with high resolution (center-to-center spots distance of 500-715 nm) and larger capture size (1 cm x 1 cm) provides the leading resolution and tissue capture area compared to other reported spatial transcriptomic techniques, with sequencing depth and breadth comparable to many single-cell sequencing techniques, but with spatial information to further advance understanding(A. Chen et al., 2021). The adoption of these novel technologies integrated into a 'traditional' biological workflow at the hardware and software level helps advance the integration of bioinformatics-led discovery, reducing resource consumption in hypothesis generation.

Secondly, I revealed a novel cardiomyocyte population, *Dbh*$^{+}$-CMs, and their association with the CCS was defined. My investigation demonstrated that tdTomato-expressing cells first appeared in the neural tube at E10.5 and then branched into groups migrating to the heart between E10.5 to E12.5, which most likely reflects neural crest cell migration and their respective formation of sympathetic ganglia (SG)(George et al., 2021; Minoux & Rijli, 2010). Given the speculation and debate about the involvement of neural crest in cardiac and CCS morphogenesis, I believe this

represents an interesting potential link between cardiomyocytes and neural crest for further investigation. The transcriptomic analyses indicate that although *Dbh*$^{+}$-CMs represented only small percentages of the total working cardiomyocyte populations, the CCS appeared to be over-represented in *Dbh*$^{+}$ cardiomyocytes as percentages of their respective total cardiomyocyte lineage numbers (PKJ: 12.76%, AVN: 12.14%, SAN: 8.39%, and AM-CCS: 3.82%). My experimental results demonstrate that ex vivo *Dbh*$^{+}$-derived CMs mainly populated the cardiac conduction system and ventricular trabecular regions throughout E14.5, E16.5, and postnatal stages (Figures in Chapter5). Collectively, these results indicate that *Dbh*$^{+}$-derived trabecular ventricular cardiomyocytes and *Dbh*$^{+}$-derived ventricular PKJ myocytes likely share some common progenitor, although it is difficult to specify at what stage of development this progenitor arises or when its progeny specify to differential cell fates. The SrT and combinatorial marker gene expression analyses also suggest *Dbh*$^{+}$- and *Wpre*$^{+}$-cardiomyocytes are from different lineages than those *Hcn4* expressing CCS cells.

It is a pertinent observation that a significant fraction of *Dbh*$^{+}$-derived cardiomyocytes (Dd-CMs) also express *Bmp10* in right atrium and ventricular trabeculae from E14.5 onwards. *Bmp10* is a known key regulator of cardiac morphogenesis, and myocardial trabecular formation and chamber maturation(H. Chen et al., 2004b; Neuhaus et al., 1999). It has also been shown that Bmp10-mediated signaling interacts with key cardiogenic factors, such as Nkx2.5, Mef2C, and Tbx20, in the developing myocardium(H. Chen et al., 2004b) and promotes endocardium

development(Mikryukov et al., 2021). This finding may suggest a previously unexpected role of *Bmp10* in either specification or maintenance of catecholaminergic cardiomyocytes and function, which mandates further exploration in the future.

Thirdly, I found that *Dbh*$^{+}$-CM-associated CCS formation occurred concurrently with sympathetic innervation. It is known that sympathetic innervation occurs concurrently with the development of the cardiovascular system(Durães Campos et al., 2018b). However, so far there is very limited information about how the sympathetic innervation is coordinated with CCS formation(Manousiouthakis et al., 2014) despite their close anatomical and functional association mapped the overall structure of the sympathetic ganglia and their projections to the heart. They found that the stellate ganglia located bilaterally in the upper thorax initiate axonal extension starting around E14. Later, sympathetic axons from the right stellate ganglia descends dorsally (with respect to the heart) along the right superior vena cava, some of this projection extends laterally to reach the SAN and further extends into the right atrium by E15.5(Manousiouthakis et al., 2014). Thus, their study suggests that sympathetic innervation occurs in murine embryonic heart after the CCS has formed at E14.5. Interestingly, I identified Th expression in murine heart at E12.5 in the SV (primordial SAN) region (Chapter 5). From E14.5 onwards, the Th positive nerve fibers were clearly identified and they extended to the AV junction, His-Bundle and part of the ventricular myocardium. This outgrowth occurred concurrently with *Dbh*$^{+}$-CM-associated CCS formation. This may suggest an important role of sympathetic innervation in CCS

formation, or vice versa. The importance of the sympathetic nervous system, or some other catecholaminergic source, is supported by the evidence of embryonic death with cardiac developmental defects due to two most important catecholamine synthetic enzymes, Th-deficient(Zhou et al., 1995) and *Dbh*-deficient mice(Thomas et al., 1995, 1998). The relationship between sympathetic innervation and cardiac pathology in the adult(C. Y. Li & Li, 2015) and the perseverance of *Dbh*$^{+}$-CMs into adult hearts, raises important pre-clinical questions about any putative interaction between the sympathetic innervation of the heart and *Dbh*$^{+}$-CMs or Dd-CMs.

Furthermore, the functional characterizations demonstrated that compared to non-cell-type-specific electrical stimulation: directed optogenetic light stimulation evoked a much faster conduction velocity in both epicardium and endocardium demonstrated by isochronal activation maps of action potentials in Dbh^{Cre}/ChR2-Td hearts (Chapter 7). The apparent activation of rapid conduction pathways is consistent with the functional aspects expected from association of Dd-CMs with the fast conductive ventricular Purkinje system (Chapter 5). My study also provides the evidence of high electron density catecholaminergic-type vesicles adult cardiomyocyte located in right atrium (the region is rich of Dd-CMs) similar to those seen in adrenal medullary chromaffin cells – confirming one aspect of previously computational gene ontology predictions, of which many remain for future investigation. However, further experimentation is required to ascertain how extensive these catecholaminergic functions are, and any influence they have on normal cardiac function or dysfunction.

That the catecholamine signal is richer in chromaffin cells, which are the main producers of endocrine catecholamines for the entire organism, is not surprising, given that it would be theoretically unlikely for any catecholamine production from the heart to be significantly more than autocrine or paracrine production. Others have previously reported cardiomyocytes may be involved in cardiac parasympathetic nervous system signaling, through the canonical parasympathetic neurotransmitter acetylcholine(Zaglia & Mongillo, 2017). The parasympathetic and sympathetic nervous system are, canonically, antagonistic for regulating cardiac function. That the parenchymal cells of the heart themselves may play a role in regulating the balance between stimulatory and suppressive signaling independent of higher neural control, seems an attractive suggestion from an evolutionary perspective. Recently, evidence suggested that intercellular signaling between cardiac sympathetic neurons and cardiomyocytes may be channeled through elementary units, represented by the neuro-cardiac junctions “NCJs”, where a ‘quasi-synaptic’ communication takes place, and whose properties fit well with those of neurogenic regulation of cardiac function (Prando et al., 2018; Zaglia & Mongillo, 2017). My lineage tracing data also show that Dd-CMs are abundant in areas enriched in sympathetic innervation. That Dd-CMs are enriched in the same anatomical regions (endomyocardially) in the ventricles supports that Dd-CMs are associated with the ventricular CCS, as sympathetic innervation of the ventricles is known to be restricted to the ventricular CCS. Moreover, the close proximity of Dd-CMs and sympathetic varicosities opens a huge interest for future studies to elucidate the communication mechanism of the sympathetic nervous

system and *Dbh*$^{+}$-CMs and any physiological and pathophysiological implications.

Furthermore, I also developed a high resolution three-dimension models by using optimized tissue clearing method to visualize cell subpopulations of interest. This method was verified by known Hcn4 mouse model and previously reported PdCM mouse model, plus validation of immunostaining on Hcn4+ and PdCM mouse heart sections. This method provided a tool for further geometrical and topological analysis of distinct cell types and the correlation with their physiological function in specific regions of the murine heart.

In conclusion, I have studied the development and function of the murine cardiac conduction system by applying a sophisticated approach integrating single cell RNA sequencing, high resolution spatial resolved transcriptomics, unsupervised and supervised machine learning techniques, lineage tracing, multi-modal imaging, and optogenetics. My results provide new insights into the mid-to-late development of the mammalian CCS through identification of previously unreported cardiac catecholaminergic cardiomyocytes.

The thesis aims were fulfilled throughout the project, however, the research in this field never ends. First, the origin of this novel subpopulation *Dbh*$^{+}$-CMs has not been confirmed yet. The relationships between *Dbh*$^{+}$-CMs and other catecholaminergic cells such as ICA cells and PdCMs are unknown. Also, we hope to optimize the existing

protocol of embryo culture to trace and visualize this lineage thoroughly and in a real-time way. Second, the electrophysiological functions as well as pathophysiological functions are not completely explored. A knock-out mouse model is indispensable as a particularly useful tool to investigate the potential role of *Dbh*$^{+}$-CMs in heart development and maturation. Studies on the performance of *Dbh*$^{+}$-CMs in disease models such as the ischemia-reperfusion model will have significant clinical implications, indicating their potential roles as a therapeutic target.

Publications

Journal articles

T. Sun, A. Grassam Rowe, X. Tan, H. Ren, Z. Pu, Y. An, X. Guo, W. Hu, Y. Liu, Z. Liu, K. Kou, X. Ou, T. Chen, X. Fan, Y. Liu, T. Shu, Y. He, Y. Ren, A. Chen, Z. Shang, Z. Xia, N. Smart, H. Zhang, W. Shou, M. Lei, Integrated transcriptome and lineage analyses reveal novel catecholaminergic cardiomyocytes contributing to cardiac conduction system in murine heart. Nature Cardiovascular Research (Under Review)

T. Sun, H. Ren, Z. Pu, T. Chen, L. Liu, C. O'Shea, D. Pavlovic, X. Tan, M. Lei, A Dataset of High Resolution 3-D Heart Models of Cardiomyocyte Subpopulations in Cleared Murine Heart. Front. Physiol. (Under Revision)

T. Sun, X. Fan, W. Crawford, X.Q. Tan, X. Ou, D.A. Terrar, M. Lei, Pnmt-derived cardiomyocytes: Anatomical localization, function and future perspectives, Front. Physiol. 10 (2019) 1–6. doi:10.3389/fphys.2019.00713.

Conferences

Physiological Society Conference 2019, Liverpool, UK (Oral presentation)

Oxford BHF Centre of Research Excellence Annual Symposium, UK (Poster)

Bibliography

A, P., F, G., & JF, B. (2006). Delays in neuronal differentiation in Mash1/Ascl1 mutants. *Developmental Biology*, *295*(1), 67–75. https://doi.org/10.1016/J.YDBIO.2006.03.008

Aanhaanen, W. T. J., Boukens, B. J. D., Sizarov, A., Wakker, V., de Gier-De Vries, C., van Ginneken, A. C., Moorman, A. F. M., Coronel, R., & Christoffels, V. M. (2011). Defective Tbx2-dependent patterning of the atrioventricular canal myocardium causes accessory pathway formation in mice. *The Journal of Clinical Investigation*, *121*(2), 534–544. https://doi.org/10.1172/JCI44350

Aanhaanen, W. T. J., Brons, J. F., Domínguez, J. N., Rana, M. S., Norden, J., Airik, R., Wakker, V., de Gier-De Vries, C., Brown, N. A., Kispert, A., Moorman, A. F. M., & Christoffels, V. M. (2009). The Tbx2+ primary myocardium of the atrioventricular canal forms the atrioventricular node and the base of the left ventricle. *Circulation Research*, *104*(11), 1267–1274. https://doi.org/10.1161/CIRCRESAHA.108.192450

Aanhaanen, W. T. J., Mommersteeg, M. T. M., Norden, J., Wakker, V., de Gier-De Vries, C., Anderson, R. H., Kispert, A., Moorman, A. F. M., & Christoffels, V. M. (2010). Developmental origin, growth, and three-dimensional architecture of the atrioventricular conduction axis of the mouse heart. *Circulation Research*, *107*(6), 728–736. https://doi.org/10.1161/CIRCRESAHA.110.222992

Abboud, F. M. (1996). An intrinsic cardiac adrenergic system can regulate cardiac development and function. *The Journal of Clinical Investigation*, *98*(6), 1275–1276. https://doi.org/10.1172/JCI118912

Abu-Issa, R. (2014). Heart Fields: Spatial Polarity and Temporal Dynamics. *The Anatomical Record*, *297*(2), 175–182. https://doi.org/10.1002/AR.22831

Abu-Issa, R., Waldo, K., & Kirby, M. L. (2004). Heart fields: one, two or more? *Developmental Biology*, *272*(2), 281–285. https://doi.org/10.1016/J.YDBIO.2004.05.016

Allen, E., Coote, J. H., Grubb, B. D., Batten, T. F. C., Pauza, D. H., Ng, G. A., & Brack, K. E. (2018). Electrophysiological effects of nicotinic and electrical stimulation of intrinsic cardiac ganglia in the absence of extrinsic autonomic nerves in the rabbit heart. *Heart Rhythm*, *15*(11), 1698. https://doi.org/10.1016/J.HRTHM.2018.05.018

Anderson, M. E. (2001). Ca2+-dependent regulation of cardiac L-type Ca2+ channels: is a unifying mechanism at hand? *Journal of Molecular and Cellular Cardiology*, *33*(4), 639–650. https://doi.org/10.1006/JMCC.2000.1354

Ardell, J. L., & Armour, J. A. (2016). Neurocardiology: Structure-Based Function. *Comprehensive Physiology*, *6*(4), 1635–1653. https://doi.org/10.1002/CPHY.C150046

Armour, J. A. (2008). Potential clinical relevance of the “little brain” on the mammalian heart. *Experimental Physiology*, *93*(2), 165–176. https://doi.org/10.1113/EXPPHYSIOL.2007.041178

Baker, C., Taylor, D. G., Osuala, K., Natarajan, A., Molnar, P. J., Hickman, J., Alam, S., Moscato, B., Weinshenker, D., & Ebert, S. N. (2012). Adrenergic deficiency leads to impaired electrical conduction and increased arrhythmic potential in the embryonic mouse heart. *Biochemical and Biophysical Research Communications*, *423*(3), 536–541. https://doi.org/10.1016/J.BBRC.2012.05.163

Bakker, M. L., Boukens, B. J., Mommersteeg, M. T. M., Brons, J. F., Wakker, V., Moorman, A. F. M., &

Christoffels, V. M. (2008). Transcription factor Tbx3 is required for the specification of the atrioventricular conduction system. *Circulation Research*, *102*(11), 1340–1349. https://doi.org/10.1161/CIRCRESAHA.107.169565

Batulevicius, D., Skripka, V., Pauziene, N., & Pauza, D. H. (2008). Topography of the porcine epicardiac nerve plexus as revealed by histochemistry for acetylcholinesterase. *Autonomic Neuroscience : Basic & Clinical*, *138*(1–2), 64–75. https://doi.org/10.1016/J.AUTNEU.2007.10.005

Bell, D., Schluter, K. D., Zhou, X. J., McDermott, B. J., & Piper, H. M. (1995). Hypertrophic effects of calcitonin gene-related peptide (CGRP) and amylin on adult mammalian ventricular cardiomyocytes. *Journal of Molecular and Cellular Cardiology*, *27*(11), 2433–2443. https://doi.org/10.1006/jmcc.1995.0231

Bhattacharyya, S., & Munshi, N. v. (2020). Development of the Cardiac Conduction System. *Cold Spring Harbor Perspectives in Biology*, *12*(12), a037408. https://doi.org/10.1101/CSHPERSPECT.A037408

Blaschke, R. J., Hahurij, N. D., Kuijper, S., Just, S., Wisse, L. J., Deissler, K., Maxelon, T., Anastassiadis, K., Spitzer, J., Hardt, S. E., Schöler, H., Feitsma, H., Rottbauer, W., Blum, M., Meijlink, F., Rappold, G., & Gittenberger-De Groot, A. C. (2007). Targeted mutation reveals essential functions of the homeodomain transcription factor Shox2 in sinoatrial and pacemaking development. *Circulation*, *115*(14), 1830–1838. https://doi.org/10.1161/CIRCULATIONAHA.106.637819

Brack, K. E. (2015). The heart's 'little brain' controlling cardiac function in the rabbit. *Experimental Physiology*, *100*(4), 348. https://doi.org/10.1113/EXPPHYSIOL.2014.080168

Brennan, J. A., Chen, Q., Gams, A., Dyavanapalli, J., Mendelowitz, D., Peng, W., & Efimov, I. R. (2020). Evidence of Superior and Inferior Sinoatrial Nodes in the Mammalian Heart. *JACC: Clinical Electrophysiology*, *6*(14), 1827–1840. https://doi.org/10.1016/J.JACEP.2020.09.012

Bressan, M., Liu, G., & Mikawa, T. (2013). Early mesodermal cues assign avian cardiac pacemaker fate potential in a tertiary heart field. *Science (New York, N.Y.)*, *340*(6133), 744–748. https://doi.org/10.1126/SCIENCE.1232877

Brionne, A., Juanchich, A., & Hennequet-Antier, C. (2019). ViSEAGO: A Bioconductor package for clustering biological functions using Gene Ontology and semantic similarity. *BioData Mining*, *12*(1), 1–13. https://doi.org/10.1186/S13040-019-0204-1/FIGURES/5

Bruneau, B. G. (2008). The developmental genetics of congenital heart disease. *Nature*, *451*(7181), 943–948. https://doi.org/10.1038/NATURE06801

Bruneau, B. G. (2013). Signaling and Transcriptional Networks in Heart Development and Regeneration. *Cold Spring Harbor Perspectives in Biology*, *5*(3), a008292. https://doi.org/10.1101/CSHPERSPECT.A008292

Bruneau, B. G., Nemer, G., Schmitt, J. P., Charron, F., Robitaille, L., Caron, S., Conner, D. A., Gessler, M., Nemer, M., Seidman, C. E., & Seidman, J. G. (2001). A murine model of Holt-Oram syndrome defines roles of the T-box transcription factor Tbx5 in cardiogenesis and disease. *Cell*, *106*(6), 709–721. https://doi.org/10.1016/S0092-8674(01)00493-7

Buckingham, M., Meilhac, S., & Zaffran, S. (2005). Building the mammalian heart from two sources of myocardial cells. *Nature Reviews. Genetics*, *6*(11), 826–835. https://doi.org/10.1038/NRG1710

Burkhard, S., van Eif, V., Garric, L., Christoffels, V. M., & Bakkers, J. (2017). On the Evolution of the

Cardiac Pacemaker. *Journal of Cardiovascular Development and Disease*, *4*(2). https://doi.org/10.3390/JCDD4020004

C, S., H, W., J, E., M, W., & H, R. (1999). Bone morphogenetic proteins are required in vivo for the generation of sympathetic neurons. *Neuron*, *24*(4), 861–870. https://doi.org/10.1016/S0896-6273(00)81033-8

Cable, D. M., Murray, E., Zou, L. S., Goeva, A., Macosko, E. Z., Chen, F., & Irizarry, R. A. (2021). Robust decomposition of cell type mixtures in spatial transcriptomics. *Nature Biotechnology*. https://doi.org/10.1038/S41587-021-00830-W

Cai, C. L., Liang, X., Shi, Y., Chu, P. H., Pfaff, S. L., Chen, J., & Evans, S. (2003). Isl1 identifies a cardiac progenitor population that proliferates prior to differentiation and contributes a majority of cells to the heart. *Developmental Cell*, *5*(6), 877–889. https://doi.org/10.1016/S1534-5807(03)00363-0

Cardiac Electrophysiology: From Cell to Bedside | ScienceDirect. (n.d.). Retrieved August 28, 2021, from https://www.sciencedirect.com/book/9780323447331/cardiac-electrophysiology-from-cell-to-bedside

Carmeliet, E. (1999). Cardiac ionic currents and acute ischemia: from channels to arrhythmias. *Physiological Reviews*, *79*(3), 917–1017. https://doi.org/10.1152/PHYSREV.1999.79.3.917

Chen, A., Liao, S., Cheng, M., Ma, K., Wu, L., Lai, Y., Yang, J., Li, W., Xu, J., Hao, S., Lu, H., Chen, X., Liu, X., Huang, X., Lin, F., Tang, X., Li, Z., Hong, Y., Fu, D., … Wang, J. (2021). *Large field of view-spatially resolved transcriptomics at nanoscale resolution*. https://doi.org/10.1101/2021.01.17.427004

Chen, H., Shi, S., Acosta, L., Li, W., Lu, J., Bao, S., Chen, Z., Yang, Z., Schneider, M. D., Chien, K. R., Conway, S. J., Yoder, M. C., Haneline, L. S., Franco, D., & Shou, W. (2004a). BMP10 is essential for maintaining cardiac growth during murine cardiogenesis. *Development (Cambridge, England)*, *131*(9), 2219–2231. https://doi.org/10.1242/DEV.01094

Chen, H., Shi, S., Acosta, L., Li, W., Lu, J., Bao, S., Chen, Z., Yang, Z., Schneider, M. D., Chien, K. R., Conway, S. J., Yoder, M. C., Haneline, L. S., Franco, D., & Shou, W. (2004b). BMP10 is essential for maintaining cardiac growth during murine cardiogenesis. *Development (Cambridge, England)*, *131*(9), 2219–2231. https://doi.org/10.1242/DEV.01094

Chen, K. H., Boettiger, A. N., Moffitt, J. R., Wang, S., & Zhuang, X. (2015). RNA imaging. Spatially resolved, highly multiplexed RNA profiling in single cells. *Science (New York, N.Y.)*, *348*(6233). https://doi.org/10.1126/SCIENCE.AAA6090

Cheng, C. F., Kuo, H. C., & Chien, K. R. (2003). Genetic modifiers of cardiac arrhythmias. *Trends in Molecular Medicine*, *9*(2), 59–66. https://doi.org/10.1016/S1471-4914(03)00004-2

Choate, J. K., Klemm, M., & Hirst, G. D. S. (1993). Sympathetic and parasympathetic neuromuscular junctions in the guinea-pig sino-atrial node. *Journal of the Autonomic Nervous System*, *44*(1), 1–15. https://doi.org/10.1016/0165-1838(93)90374-4

Choquet, C., Kelly, R. G., & Miquerol, L. (2020). Nkx2-5 defines distinct scaffold and recruitment phases during formation of the murine cardiac Purkinje fiber network. *Nature Communications*, *11*(1). https://doi.org/10.1038/s41467-020-19150-9

Christoffels, V. M., Habets, P. E. M. H., Franco, D., Campione, M., de Jong, F., Lamers, W. H., Bao, Z. Z., Palmer, S., Biben, C., Harvey, R. P., & Moorman, A. F. M. (2000). Chamber formation and morphogenesis in the developing mammalian heart. *Developmental Biology*, *223*(2), 266–278. https://doi.org/10.1006/DBIO.2000.9753

Christoffels, V. M., Keijser, A. G. M., Houweling, A. C., Clout, D. E. W., & Moorman, A. F. M. (2000). Patterning the embryonic heart: identification of five mouse Iroquois homeobox genes in the developing heart. *Developmental Biology*, *224*(2), 263–274. https://doi.org/10.1006/DBIO.2000.9801

Christoffels, V. M., Mommersteeg, M. T. M., Trowe, M. O., Prall, O. W. J., de Gier-De Vries, C., Soufan, A. T., Bussen, M., Schuster-Gossler, K., Harvey, R. P., Moorman, A. F. M., & Kispert, A. (2006). Formation of the venous pole of the heart from an Nkx2-5-negative precursor population requires Tbx18. *Circulation Research*, *98*(12), 1555–1563. https://doi.org/10.1161/01.RES.0000227571.84189.65

Christoffels, V. M., & Moorman, A. F. M. (2009). Development of the cardiac conduction system why are some regions of the heart more arrhythmogenic than others? In *Circulation: Arrhythmia and Electrophysiology* (Vol. 2, Issue 2, pp. 195–207). https://doi.org/10.1161/CIRCEP.108.829341

CLAPHAM, D. E., & KEATING, M. T. (2006). Cardiac Excitability and Heritable Arrhythmias. *Nadas' Pediatric Cardiology*, 891–906. https://doi.org/10.1016/B978-1-4160-2390-6.50066-0

Crick, S. J., Sheppard', M. N., Anderson3, R. H., Polak2, J. M., & Wharton2, J. (1996). A quantitative study of nerve distribution in the conduction system of the guinea pig heart. *Journal of Anatomy*, *188*(Pt 2), 403. /pmc/articles/PMC1167577/?report=abstract

Cv Tyser, R., Ma Miranda, A., Chen, C.-M., Davidson, S. M., Srinivas, S., & Riley, P. R. (2016). *Calcium handling precedes cardiac differentiation to initiate the first heartbeat*. https://doi.org/10.7554/eLife.17113.001

Davis, D. L., Edwards, A. v., Juraszek, A. L., Phelps, A., Wessels, A., & Burch, J. B. E. (2001). A GATA-6 gene heart-region-specific enhancer provides a novel means to mark and probe a discrete component of the mouse cardiac conduction system. *Mechanisms of Development*, *108*(1–2), 105–119. https://doi.org/10.1016/S0925-4773(01)00500-7

de Boer, B. A., van den Berg, G., de Boer, P. A. J., Moorman, A. F. M., & Ruijter, J. M. (2012). Growth of the developing mouse heart: an interactive qualitative and quantitative 3D atlas. *Developmental Biology*, *368*(2), 203–213. https://doi.org/10.1016/J.YDBIO.2012.05.001

de La Cruz, M. v., Markwald, R. R., Krug, E. L., Rumenoff, L., Gómez, C. S., Sadowinski, S., de Galicia, T. J., Gómez, F., García, M. S., Guzmán, L. V., Angeles, L. R., & Moreno-Rodriguez, R. A. (2001). Living morphogenesis of the ventricles and congenital pathology of their component parts. *Cardiology in the Young*, *11*(6), 588–600. https://doi.org/10.1017/S1047951101000932

Delorme, B., Dahl, E., Jarry-Guichard, T., Briand, J. P., Willecke, K., Gros, D., & Théveniau-Ruissy, M. (1997). Expression pattern of connexin gene products at the early developmental stages of the mouse cardiovascular system. *Circulation Research*, *81*(3), 423–437. https://doi.org/10.1161/01.RES.81.3.423

Devine, W. P., Wythe, J. D., George, M., Koshiba-Takeuchi, K., & Bruneau, B. G. (2014a). Early patterning and specification of cardiac progenitors in gastrulating mesoderm. *ELife*, *3*. https://doi.org/10.7554/ELIFE.03848

Devine, W. P., Wythe, J. D., George, M., Koshiba-Takeuchi, K., & Bruneau, B. G. (2014b). Early patterning and specification of cardiac progenitors in gastrulating mesoderm. *ELife*, *3*. https://doi.org/10.7554/ELIFE.03848

Dickerson, L. W., Rodak, D. J., Fleming, T. J., Gatti, P. J., Massari, V. J., McKenzie, J. C., & Gillis, R. A. (1998). Parasympathetic neurons in the cranial medial ventricular fat pad on the dog heart

selectively decrease ventricular contractility. *Journal of the Autonomic Nervous System*, *70*(1–2), 129–141. https://doi.org/10.1016/S0165-1838(98)00048-4

Domínguez, J. N., Meilhac, S. M., Bland, Y. S., Buckingham, M. E., & Brown, N. A. (2012). Asymmetric fate of the posterior part of the second heart field results in unexpected left/right contributions to both poles of the heart. *Circulation Research*, *111*(10), 1323–1335. https://doi.org/10.1161/CIRCRESAHA.112.271247

Dunn, M., Henke, A., Clark, S., Kovalyova, Y., Kempadoo, K. A., Karpowicz, R. J., Kandel, E. R., Sulzer, D., & Sames, D. (2018). Designing a norepinephrine optical tracer for imaging individual noradrenergic synapses and their activity in vivo. *Nature Communications 2018 9:1*, *9*(1), 1–13. https://doi.org/10.1038/s41467-018-05075-x

Durães Campos, I., Pinto, V., Sousa, N., & Pereira, V. H. (2018a). A brain within the heart: A review on the intracardiac nervous system. *Journal of Molecular and Cellular Cardiology*, *119*, 1–9. https://doi.org/10.1016/J.YJMCC.2018.04.005

Durães Campos, I., Pinto, V., Sousa, N., & Pereira, V. H. (2018b). A brain within the heart: A review on the intracardiac nervous system. *Journal of Molecular and Cellular Cardiology*, *119*, 1–9. https://doi.org/10.1016/J.YJMCC.2018.04.005

Ebert, S. N., Baden, J. M., Mathers, L. H., Siddall, B. J., & Wong, D. L. (1996). Expression of phenylethanolamine n-methyltransferase in the embryonic rat heart. *Journal of Molecular and Cellular Cardiology*, *28*(8), 1653–1658. https://doi.org/10.1006/JMCC.1996.0155

Ebert, S. N., Rong, Q., Boe, S., & Pfeifer, K. (2008a). CATECHOLAMINE SYNTHESIZING CELLS IN THE EMBRYONIC MOUSE HEART. *Annals of the New York Academy of Sciences*, *1148*, 317. https://doi.org/10.1196/ANNALS.1410.008

Ebert, S. N., Rong, Q., Boe, S., & Pfeifer, K. (2008b). Catecholamine-synthesizing cells in the embryonic mouse heart. *Annals of the New York Academy of Sciences*, *1148*(407), 317–324. https://doi.org/10.1196/annals.1410.008

Ebert, S. N., Rong, Q., Boe, S., Thompson, R. P., Grinberg, A., & Pfeifer, K. (2004). Targeted insertion of the Cre-recombinase gene at the phenylethanolamine n-methyltransferase locus: A new model for studying the developmental distribution of adrenergic cells. *Developmental Dynamics*, *231*(4), 849–858. https://doi.org/10.1002/dvdy.20188

Ebert, S. N., & Taylor, D. G. (2006). Catecholamines and development of cardiac pacemaking: An intrinsically intimate relationship. *Cardiovascular Research*, *72*(3), 364–374. https://doi.org/10.1016/j.cardiores.2006.08.013

Ebert, S. N., & Thompson, R. P. (2001a). Embryonic epinephrine synthesis in the rat heart before innervation: Association with pacemaking and conduction tissue development. *Circulation Research*, *88*(1), 117–124. https://doi.org/10.1161/01.RES.88.1.117

Ebert, S. N., & Thompson, R. P. (2001b). Embryonic Epinephrine Synthesis in the Rat Heart Before Innervation. *Circulation Research*, *88*(1), 117–124. https://doi.org/10.1161/01.RES.88.1.117

Eng, C. H. L., Lawson, M., Zhu, Q., Dries, R., Koulena, N., Takei, Y., Yun, J., Cronin, C., Karp, C., Yuan, G. C., & Cai, L. (2019). Transcriptome-scale super-resolved imaging in tissues by RNA seqFISH+. *Nature 2019 568:7751*, *568*(7751), 235–239. https://doi.org/10.1038/s41586-019-1049-y

Enomoto, H., Heuckeroth, R. O., Golden, J. P., Johnson, E. M., & Milbrandt, J. (2000). Development of cranial parasympathetic ganglia requires sequential actions of GDNF and neurturin. *Development*, *127*(22), 4877–4889. https://doi.org/10.1242/DEV.127.22.4877

Espinoza-Lewis, R. A., Liu, H., Sun, C., Chen, C., Jiao, K., & Chen, Y. P. (2011). Ectopic expression of

Nkx2.5 suppresses the formation of the sinoatrial node in mice. *Developmental Biology*, *356*(2), 359–369. https://doi.org/10.1016/J.YDBIO.2011.05.663

Espinoza-Lewis, R. A., Yu, L., He, F., Liu, H., Tang, R., Shi, J., Sun, X., Martin, J. F., Wang, D., Yang, J., & Chen, Y. P. (2009). Shox2 is essential for the differentiation of cardiac pacemaker cells by repressing Nkx2-5. *Developmental Biology*, *327*(2), 376–385. https://doi.org/10.1016/J.YDBIO.2008.12.028

Evans, S. M., Yelon, D., Conlon, F. L., & Kirby, M. L. (2010). Myocardial lineage development. *Circulation Research*, *107*(12), 1428–1444. https://doi.org/10.1161/CIRCRESAHA.110.227405

F, G., LC, L., JE, J., A, A., DJ, A., & AL, J. (1993). Mammalian achaete-scute homolog 1 is required for the early development of olfactory and autonomic neurons. *Cell*, *75*(3), 463–476. https://doi.org/10.1016/0092-8674(93)90381-Y

FAWCETT, D. W., & SELBY, C. C. (1958). Observations on the Fine Structure of the Turtle Atrium. *The Journal of Biophysical and Biochemical Cytology*, *4*(1), 63. https://doi.org/10.1083/JCB.4.1.63

Fedele, L., & Brand, T. (2020). The intrinsic cardiac nervous system and its role in cardiac pacemaking and conduction. In *Journal of Cardiovascular Development and Disease* (Vol. 7, Issue 4, pp. 1–33). MDPI AG. https://doi.org/10.3390/jcdd7040054

Frank, D. U., Carter, K. L., Thomas, K. R., Burr, R. M., Bakker, M. L., Coetzee, W. A., Tristani-Firouzi, M., Bamshad, M. J., Christoffels, V. M., & Moon, A. M. (2012). Lethal arrhythmias in Tbx3-deficient mice reveal extreme dosage sensitivity of cardiac conduction system function and homeostasis. *Proceedings of the National Academy of Sciences of the United States of America*, *109*(3). https://doi.org/10.1073/PNAS.1115165109/-/DCSUPPLEMENTAL/PNAS.201115165SI.PDF

Galow, A. M., Kussauer, S., Wolfien, M., Brunner, R. M., Goldammer, T., David, R., & Hoeflich, A. (2021). Quality control in scRNA-Seq can discriminate pacemaker cells: the mtRNA bias. *Cellular and Molecular Life Sciences*, *78*(19–20), 6585–6592. https://doi.org/10.1007/S00018-021-03916-5/FIGURES/2

Garcia-Frigola, C., Shi, Y., & Evans, S. M. (2003). Expression of the hyperpolarization-activated cyclic nucleotide-gated cation channel HCN4 during mouse heart development. *Gene Expression Patterns : GEP*, *3*(6), 777–783. https://doi.org/10.1016/S1567-133X(03)00125-X

Gassmann, M., Casagranda, F., Orloli, D., Simon, H., Lai, C., Kleint, R., & Lemke, G. (1995). Aberrant neural and cardiac development in mice lacking the ErbB4 neuregulin receptor. *Nature*, *378*(6555), 390–394. https://doi.org/10.1038/378390A0

Gatti, P. J., Johnson, T. A., Phan, P., Jordan, I. K., Coleman, W., & Massari, V. J. (1995). The physiological and anatomical demonstration of functionally selective parasympathetic ganglia located in discrete fat pads on the feline myocardium. *Journal of the Autonomic Nervous System*, *51*(3), 255–259. https://doi.org/10.1016/0165-1838(94)00139-B

George, R. M., Maldonado-Velez, G., & Firulli, A. B. (2021). The heart of the neural crest: Cardiac neural crest cells in development and regeneration. *Development (Cambridge)*, *147*(20). https://doi.org/10.1242/DEV.188706/225875

Gladka, M. M., Molenaar, B., de Ruiter, H., van der Elst, S., Tsui, H., Versteeg, D., Lacraz, G. P. A., Huibers, M. M. H., van Oudenaarden, A., & van Rooij, E. (2018). Single-Cell Sequencing of the Healthy and Diseased Heart Reveals Cytoskeleton-Associated Protein 4 as a New Modulator of Fibroblasts Activation. *Circulation*, *138*(2), 166–180.

https://doi.org/10.1161/CIRCULATIONAHA.117.030742

Goodyer, W. R., Beyersdorf, B. M., Paik, D. T., Tian, L., Li, G., Buikema, J. W., Chirikian, O., Choi, S., Venkatraman, S., Adams, E. L., Tessier-Lavigne, M., Wu, J. C., & Wu, S. M. (2019). Transcriptomic Profiling of the Developing Cardiac Conduction System at Single-Cell Resolution. *Circulation Research*, *125*(4), 379–397. https://doi.org/10.1161/CIRCRESAHA.118.314578

Goodyer, W. R., & Wu, S. M. (2018a). Fates Aligned: Origins and Mechanisms of Ventricular Conduction System and Ventricular Wall Development. *Pediatric Cardiology*, *39*(6), 1090–1098. https://doi.org/10.1007/S00246-018-1869-9

Goodyer, W. R., & Wu, S. M. (2018b). Fates Aligned: Origins and Mechanisms of Ventricular Conduction System and Ventricular Wall Development. *Pediatric Cardiology*, *39*(6), 1090. https://doi.org/10.1007/S00246-018-1869-9

Gorza, L., Schiaffino, S., & Vitadello, M. (1988). Heart conduction system: a neural crest derivative? *Brain Research*, *457*(2), 360–366. https://doi.org/10.1016/0006-8993(88)90707-X

Gourdie, R. G., Harris, B. S., Bond, J., Edmondson, A. M., Cheng, G., Sedmera, D., O'Brien, T. X., Mikawa, T., Thompson, R. P., Watanabe, Burch, Rosen, Moorman, & Markwald. (2003). His–Purkinje Lineages and Development. *Novartis Foundation Symposium*, *250*, 110–124. https://doi.org/10.1002/0470868066.CH7

Gourdie, R. G., Wei, Y., Kim, D., Klatt, S. C., & Mikawa, T. (1998). *Endothelin-induced conversion of embryonic heart muscle cells into impulse-conducting Purkinje fibers* (Vol. 95). www.pnas.org.

Grant, A. O. (2009). Cardiac ion channels. In *Circulation: Arrhythmia and Electrophysiology* (Vol. 2, Issue 2, pp. 185–194). https://doi.org/10.1161/CIRCEP.108.789081

Grassam-Rowe, A., Ou, X., & Lei, M. (2020). Novel cardiac cell subpopulations: Pnmt-derived cardiomyocytes. *Open Biology*, *10*(8). https://doi.org/10.1098/RSOB.200095

Gray, A. L., Johnson, T. A., Ardell, J. L., & Massari, V. J. (2004). Parasympathetic control of the heart. II. A novel interganglionic intrinsic cardiac circuit mediates neural control of heart rate. *Journal of Applied Physiology (Bethesda, Md. : 1985)*, *96*(6), 2273–2278. https://doi.org/10.1152/JAPPLPHYSIOL.00616.2003

Grego-Bessa, J., Luna-Zurita, L., del Monte, G., Bolós, V., Melgar, P., Arandilla, A., Garratt, A. N., Zang, H., Mukouyama, Y. suke, Chen, H., Shou, W., Ballestar, E., Esteller, M., Rojas, A., Pérez-Pomares, J. M., & de la Pompa, J. L. (2007). Notch signaling is essential for ventricular chamber development. *Developmental Cell*, *12*(3), 415–429. https://doi.org/10.1016/J.DEVCEL.2006.12.011

Hafemeister, C., & Satija, R. (2019). Normalization and variance stabilization of single-cell RNA-seq data using regularized negative binomial regression. *Genome Biology*, *20*(1), 1–15. https://doi.org/10.1186/S13059-019-1874-1/FIGURES/6

HALL, E. K. (1957). Acetylcholine and epinephrine effects on the embryonic rat heart. *Journal of Cellular and Comparative Physiology*, *49*(2), 187–200. https://doi.org/10.1002/JCP.1030490203

Harrelson, Z., Kelly, R. G., Goldin, S. N., Gibson-Brown, J. J., Bollag, R. J., Silver, L. M., & Papaioannou, V. E. (2004). Tbx2 is essential for patterning the atrioventricular canal and for morphogenesis of the outflow tract during heart development. *Development (Cambridge, England)*, *131*(20), 5041–5052. https://doi.org/10.1242/DEV.01378

Hoffmann, S., Berger, I. M., Glaser, A., Bacon, C., Li, L., Gretz, N., Steinbeisser, H., Rottbauer, W.,

Just, S., & Rappold, G. (2013). Islet1 is a direct transcriptional target of the homeodomain transcription factor Shox2 and rescues the Shox2-mediated bradycardia. *Basic Research in Cardiology*, *108*(2). https://doi.org/10.1007/S00395-013-0339-Z

Hoogaars, W. M. H., Engel, A., Brons, J. F., Verkerk, A. O., de Lange, F. J., Wong, L. Y. E., Bakker, M. L., Clout, D. E., Wakker, V., Barnett, P., Ravesloot, J. H., Moorman, A. F. M., Verheijck, E. E., & Christoffels, V. M. (2007). Tbx3 controls the sinoatrial node gene program and imposes pacemaker function on the atria. *Genes & Development*, *21*(9), 1098–1112. https://doi.org/10.1101/GAD.416007

Hoogaars, W. M. H., Tessari, A., Moorman, A. F. M., de Boer, P. A. J., Hagoort, J., Soufan, A. T., Campione, M., & Christoffels, V. M. (2004). The transcriptional repressor Tbx3 delineates the developing central conduction system of the heart. *Cardiovascular Research*, *62*(3), 489–499. https://doi.org/10.1016/J.CARDIORES.2004.01.030

Hou, Y., Scherlag, B. J., Lin, J., Zhou, J., Song, J., Zhang, Y., Patterson, E., Lazzara, R., Jackman, W. M., & Po, S. S. (2007). Interactive atrial neural network: Determining the connections between ganglionated plexi. *Heart Rhythm*, *4*(1), 56–63. https://doi.org/10.1016/J.HRTHM.2006.09.020

Huang, M. H., Bahl, J. J., Wu, Y., Hu, F., Larson, D. F., Roeske, W. R., & Ewy, G. A. (2005). Neuroendocrine properties of intrinsic cardiac adrenergic cells in fetal rat heart. *American Journal of Physiology - Heart and Circulatory Physiology*, *288*(2 57-2), 497–503. https://doi.org/10.1152/ajpheart.00591.2004

Huang, M. H., Friend, D. S., Sunday, M. E., Singh, K., Haley, K., Austen, K. F., Kelly, R. A., & Smith, T. W. (1996). An intrinsic adrenergic system in mammalian heart. *Journal of Clinical Investigation*, *98*(6), 1298–1303. https://doi.org/10.1172/JCI118916

Huang, M. H., Lui, C. Y., Abusaid, G. H., Poh, K. K., Barbagelata, A. N., Uretsky, B. F., & Fujise, K. (2010). Cardiac calcitonin gene-related peptide and left ventricular hypertrophy in the cardiac allograft. *Journal of Heart and Lung Transplantation*, *29*(4), 487–488. https://doi.org/10.1016/j.healun.2009.11.002

Huang, M. H., Nguyen, V., Wu, Y., Rastogi, S., Lui, C. Y., Birnbaum, Y., Wang, H. Q., Ware, D. L., Chauhan, M., Garg, N., Poh, K. K., Ye, L., Omar, A. R., Tan, H. C., Uretsky, B. F., & Fujise, K. (2009). Reducing ischaemia/reperfusion injury through δ-opioid-regulated intrinsic cardiac adrenergic cells: Adrenopeptidergic co-signalling. *Cardiovascular Research*, *84*(3), 452–460. https://doi.org/10.1093/cvr/cvp233

Huang, M. H., Wang, H. Q., Roeske, W. R., Birnbaum, Y., Wu, Y., Yang, N. P., Lin, Y., Ye, Y., McAdoo, D. J., Hughes, M. G., Lick, S. D., Boor, P. J., Lui, C. Y., & Uretsky, B. F. (2007). Mediating δ-opioid-initiated heart protection via the β2-adrenergic receptor: Role of the intrinsic cardiac adrenergic cell. *American Journal of Physiology - Heart and Circulatory Physiology*, *293*(1), 376–384. https://doi.org/10.1152/ajpheart.01195.2006

Ibrahim, S. F., & van den Engh, G. (2007). Flow cytometry and cell sorting. *Advances in Biochemical Engineering/Biotechnology*, *106*, 19–39. https://doi.org/10.1007/10_2007_073

Ieda, M., Kanazawa, H., Kimura, K., Hattori, F., Ieda, Y., Taniguchi, M., Lee, J.-K., Matsumura, K., Tomita, Y., Miyoshi, S., Shimoda, K., Makino, S., Sano, M., Kodama, I., Ogawa, S., & Fukuda, K. (2007). Sema3a maintains normal heart rhythm through sympathetic innervation patterning. *Nature Medicine 2007 13:5*, *13*(5), 604–612. https://doi.org/10.1038/nm1570

Ignarro, L. J., & Shideman, F. E. (1968). APPEARANCE AND CONCENTRATIONS OF CATECHOLAMINES

AND THEIR BIOSYNTHESIS IN THE EMBRYONIC AND DEVELOPING CHICK. *Journal of Pharmacology and Experimental Therapeutics*, *159*(1).

Ivanovitch, K., Temiño, S., & Torres, M. (2017). Live imaging of heart tube development in mouse reveals alternating phases of cardiac differentiation and morphogenesis. *ELife*, *6*. https://doi.org/10.7554/ELIFE.30668

JL, A., MC, A., JA, A., GE, B., PS, C., RD, F., N, H., DS, O., HN, S., HD, S., K, S., & IH, Z. (2016). Translational neurocardiology: preclinical models and cardioneural integrative aspects. *The Journal of Physiology*, *594*(14), 3877–3909. https://doi.org/10.1113/JP271869

Kasemeier-Kulesa, J. C., Bradley, R., Pasquale, E. B., Lefcort, F., & Kulesa, P. M. (2006). Eph/ephrins and N-cadherin coordinate to control the pattern of sympathetic ganglia. *Development*, *133*(24), 4839–4847. https://doi.org/10.1242/DEV.02662

Kaufman, M. H., & Bard, J. B. L. (1999). *The Anatomical Basis of Mouse Development.* 305.

Kelly, R. G., Buckingham, M. E., & Moorman, A. F. (2014). Heart fields and cardiac morphogenesis. *Cold Spring Harbor Perspectives in Medicine*, *4*(10). https://doi.org/10.1101/CSHPERSPECT.A015750

Kitajima, S., Miyagawa-Tomita, S., Inoue, T., Kanno, J., & Saga, Y. (2006). Mesp1-nonexpressing cells contribute to the ventricular cardiac conduction system. *Developmental Dynamics*, *235*(2), 395–402. https://doi.org/10.1002/dvdy.20640

Kretzschmar, K., & Watt, F. M. (2012). Lineage Tracing. *Cell*, *148*(1), 33–45. https://doi.org/10.1016/J.CELL.2012.01.002

Kvetnansky, R., Kubovcakova, L., Tillinger, A., Micutkova, L., Krizanova, O., & Sabban, E. L. (2006). Gene expression of phenylethanolamine N-methyltransferase in corticotropin-releasing hormone knockout mice during stress exposure. *Cellular and Molecular Neurobiology*, *26*(4–6), 735–754. https://doi.org/10.1007/s10571-006-9063-7

Kvetnansky, R., Micutkova, L., Kubovcakova, L., Sabban, E. L., Palkovits, M., & Krizanova, O. (2004). Localization and regulation of phenylethanolamine N-methyltransferase gene expression in the heart of rats and mice during stress. *Annals of the New York Academy of Sciences*, *1018*(4212), 405–417. https://doi.org/10.1196/annals.1296.050

Lafzi, A., Moutinho, C., Picelli, S., & Heyn, H. (2018). Tutorial: guidelines for the experimental design of single-cell RNA sequencing studies. *Nature Protocols*, *13*(12), 2742–2757. https://doi.org/10.1038/S41596-018-0073-Y

Langdon, R. J., Yousefi, P. D., Relton, C. L., & Suderman, M. J. (1992). Calcium channels in the heart: an overview. *Heart Disease and Stroke : A Journal for Primary Care Physicians*, *1*(6), 398–403. https://doi.org/10.2/JQUERY.MIN.JS

Lee, J. H., Daugharthy, E. R., Scheiman, J., Kalhor, R., Yang, J. L., Ferrante, T. C., Terry, R., Jeanty, S. S. F., Li, C., Amamoto, R., Peters, D. T., Turczyk, B. M., Marblestone, A. H., Inverso, S. A., Bernard, A., Mali, P., Rios, X., Aach, J., & Church, G. M. (2014). Highly multiplexed subcellular RNA sequencing in situ. *Science*, *343*(6177), 1360–1363. https://doi.org/10.1126/SCIENCE.1250212

Lescroart, F., Chabab, S., Lin, X., Rulands, S., Paulissen, C., Rodolosse, A., Auer, H., Achouri, Y., Dubois, C., Bondue, A., Simons, B. D., & Blanpain, C. (2014). Early lineage restriction in temporally distinct populations of Mesp1 progenitors during mammalian heart development. *Nature Cell Biology*, *16*(9), 829–840. https://doi.org/10.1038/NCB3024

Lescroart, F., Hamou, W., Francou, A., Théveniau-Ruissy, M., Kelly, R. G., & Buckingham, M. (2015).

Clonal analysis reveals a common origin between nonsomite-derived neck muscles and heart myocardium. *Proceedings of the National Academy of Sciences of the United States of America*, *112*(5), 1446–1451. https://doi.org/10.1073/PNAS.1424538112/-/DCSUPPLEMENTAL

Lescroart, F., Kelly, R. G., le Garrec, J. F., Nicolas, J. F., Meilhac, S. M., & Buckingham, M. (2010). Clonal analysis reveals common lineage relationships between head muscles and second heart field derivatives in the mouse embryo. *Development (Cambridge, England)*, *137*(19), 3269–3279. https://doi.org/10.1242/DEV.050674

Lescroart, F., Wang, X., Lin, X., Swedlund, B., Gargouri, S., Sànchez-Dànes, A., Moignard, V., Dubois, C., Paulissen, C., Kinston, S., Göttgens, B., & Blanpain, C. (2018). Defining the earliest step of cardiovascular lineage segregation by single-cell RNA-seq. *Science (New York, N.Y.)*, *359*(6380), 1177–1181. https://doi.org/10.1126/SCIENCE.AAO4174

Li, C. Y., & Li, Y. G. (2015). Cardiac Sympathetic Nerve Sprouting and Susceptibility to Ventricular Arrhythmias after Myocardial Infarction. *Cardiology Research and Practice*, *2015*. https://doi.org/10.1155/2015/698368

Li, G., Xu, A., Sim, S., Priest, J. R., Tian, X., Khan, T., Quertermous, T., Zhou, B., Tsao, P. S., Quake, S. R., & Wu, S. M. (2016). Transcriptomic Profiling Maps Anatomically Patterned Subpopulations among Single Embryonic Cardiac Cells. *Developmental Cell*, *39*(4), 491–507. https://doi.org/10.1016/J.DEVCEL.2016.10.014

Liang, D., Xue, J., Geng, L., Zhou, L., Lv, B., Zeng, Q., Xiong, K., Zhou, H., Xie, D., Zhang, F., Liu, J., Liu, Y., Li, L., Yang, J., Xue, Z., & Chen, Y. H. (2021). Cellular and molecular landscape of mammalian sinoatrial node revealed by single-cell RNA sequencing. *Nature Communications 2021 12:1*, *12*(1), 1–15. https://doi.org/10.1038/s41467-020-20448-x

Liang, X., Wang, G., Lin, L., Lowe, J., Zhang, Q., Bu, L., Chen, Y., Chen, J., Sun, Y., & Evans, S. M. (2013). HCN4 dynamically marks the first heart field and conduction system precursors. *Circulation Research*, *113*(4), 399–407. https://doi.org/10.1161/CIRCRESAHA.113.301588

Liang, X., Zhang, Q., Cattaneo, P., Zhuang, S., Gong, X., Spann, N. J., Jiang, C., Cao, X., Zhao, X., Zhang, X., Bu, L., Wang, G., Chen, H. S. V., Zhuang, T., Yan, J., Geng, P., Luo, L., Banerjee, I., Chen, Y., … Evans, S. M. (2015). Transcription factor ISL1 is essential for pacemaker development and function. *The Journal of Clinical Investigation*, *125*(8), 3256–3268. https://doi.org/10.1172/JCI68257

Liu, J., Dobrzynski, H., Yanni, J., Boyett, M. R., & Lei, M. (2007). Organisation of the mouse sinoatrial node: structure and expression of HCN channels. *Cardiovascular Research*, *73*(4), 729–738. https://doi.org/10.1016/j.cardiores.2006.11.016

Liu, Y., Yang, M., Deng, Y., Su, G., Enninful, A., Guo, C. C., Tebaldi, T., Zhang, D., Kim, D., Bai, Z., Norris, E., Pan, A., Li, J., Xiao, Y., Halene, S., & Fan, R. (2020). High-Spatial-Resolution Multi-Omics Sequencing via Deterministic Barcoding in Tissue. *Cell*, *183*(6), 1665-1681.e18. https://doi.org/10.1016/J.CELL.2020.10.026

Loher, P., & Karathanasis, N. (2020). Machine Learning Approaches Identify Genes Containing Spatial Information From Single-Cell Transcriptomics Data. *Frontiers in Genetics*, *11*, 612840. https://doi.org/10.3389/fgene.2020.612840

López-Sánchez, C., Bártulos, Ó., Martínez-Campos, E., Gañán, C., Valenciano, A. I., García-Martínez, V., de Pablo, F., & Hernández-Sánchez, C. (2010). Tyrosine hydroxylase is expressed during early heart development and is required for cardiac chamber formation. *Cardiovascular*

Research, *88*(1), 111–120. https://doi.org/10.1093/CVR/CVQ179

Ma, L., Lu, M. F., Schwartz, R. J., & Martin, J. F. (2005). Bmp2 is essential for cardiac cushion epithelial-mesenchymal transition and myocardial patterning. *Development (Cambridge, England)*, *132*(24), 5601–5611. https://doi.org/10.1242/DEV.02156

Macosko, E. Z., Basu, A., Satija, R., Nemesh, J., Shekhar, K., Goldman, M., Tirosh, I., Bialas, A. R., Kamitaki, N., Martersteck, E. M., Trombetta, J. J., Weitz, D. A., Sanes, J. R., Shalek, A. K., Regev, A., & McCarroll, S. A. (2015). Highly Parallel Genome-wide Expression Profiling of Individual Cells Using Nanoliter Droplets. *Cell*, *161*(5), 1202–1214. https://doi.org/10.1016/J.CELL.2015.05.002

Manousiouthakis, E., Mendez, M., Garner, M. C., Exertier, P., & Makita, T. (2014). Venous endothelin guides sympathetic innervation of the developing mouse heart. *Nature Communications*, *5*. https://doi.org/10.1038/NCOMMS4918

Mantri, M., Scuderi, G. J., Abedini-Nassab, R., Wang, M. F. Z., McKellar, D., Shi, H., Grodner, B., Butcher, J. T., & de Vlaminck, I. (2021). Spatiotemporal single-cell RNA sequencing of developing chicken hearts identifies interplay between cellular differentiation and morphogenesis. *Nature Communications*, *12*(1). https://doi.org/10.1038/s41467-021-21892-z

Matsumoto, K., Mitani, T. T., Horiguchi, S. A., Kaneshiro, J., Murakami, T. C., Mano, T., Fujishima, H., Konno, A., Watanabe, T. M., Hirai, H., & Ueda, H. R. (2019). Advanced CUBIC tissue clearing for whole-organ cell profiling. *Nature Protocols 2019 14:12*, *14*(12), 3506–3537. https://doi.org/10.1038/s41596-019-0240-9

ME, N., SG, R., & A, C. (2021). *SMaSH: A scalable, general marker gene identification framework for single-cell RNA sequencing and Spatial Transcriptomics*. https://doi.org/10.1101/2021.04.08.438978

Meilhac, S. M., Esner, M., Kelly, R. G., Nicolas, J. F., & Buckingham, M. E. (2004). The clonal origin of myocardial cells in different regions of the embryonic mouse heart. *Developmental Cell*, *6*(5), 685–698. https://doi.org/10.1016/S1534-5807(04)00133-9

Meyer, D., & Birchmeier, C. (1995). Multiple essential functions of neuregulin in development. *Nature*, *378*(6555), 386–390. https://doi.org/10.1038/378386A0

Meysen, S., Marger, L., Hewett, K. W., Jarry-Guichard, T., Agarkova, I., Chauvin, J. P., Perriard, J. C., Izumo, S., Gourdie, R. G., Mangoni, M. E., Nargeot, J., Gros, D., & Miquerol, L. (2007). Nkx2.5 cell-autonomous gene function is required for the postnatal formation of the peripheral ventricular conduction system. *Developmental Biology*, *303*(2), 740–753. https://doi.org/10.1016/j.ydbio.2006.12.044

Mikryukov, A. A., Mazine, A., Wei, B., Yang, D., Miao, Y., Gu, M., & Keller, G. M. (2021). BMP10 Signaling Promotes the Development of Endocardial Cells from Human Pluripotent Stem Cell-Derived Cardiovascular Progenitors. *Cell Stem Cell*, *28*(1), 96-111.e7. https://doi.org/10.1016/j.stem.2020.10.003

Minoux, M., & Rijli, F. M. (2010). Molecular mechanisms of cranial neural crest cell migration and patterning in craniofacial development. *Development*, *137*(16), 2605–2621. https://doi.org/10.1242/DEV.040048

Miquerol, L., Meysen, S., Mangoni, M., Bois, P., van Rijen, H. V. M., Abran, P., Jongsma, H., Nargeot, J., & Gros, D. (2004). Architectural and functional asymmetry of the His-Purkinje system of the murine heart. *Cardiovascular Research*, *63*(1), 77–86.

https://doi.org/10.1016/J.CARDIORES.2004.03.007/2/63-1-77-FIG5.GIF

Miquerol, L., Moreno-Rascon, N., Beyer, S., Dupays, L., Meilhac, S. M., Buckingham, M. E., Franco, D., & Kelly, R. G. (2010). Biphasic development of the mammalian ventricular conduction system. *Circulation Research*, *107*(1), 153–161. https://doi.org/10.1161/CIRCRESAHA.110.218156

ML, K. (1988). Nodose placode contributes autonomic neurons to the heart in the absence of cardiac neural crest. *The Journal of Neuroscience : The Official Journal of the Society for Neuroscience*, *8*(4), 1089–1095. https://doi.org/10.1523/JNEUROSCI.08-04-01089.1988

Mohan, R. A., Boukens, B. J., & Christoffels, V. M. (2018). Developmental Origin of the Cardiac Conduction System: Insight from Lineage Tracing. *Pediatric Cardiology*, *39*(6), 1107–1114. https://doi.org/10.1007/S00246-018-1906-8

Mommersteeg, M. T. M., Domínguez, J. N., Wiese, C., Norden, J., de Gier-De Vries, C., Burch, J. B. E., Kispert, A., Brown, N. A., Moorman, A. F. M., & Christoffels, V. M. (2010). The sinus venosus progenitors separate and diversify from the first and second heart fields early in development. *Cardiovascular Research*, *87*(1), 92–101. https://doi.org/10.1093/CVR/CVQ033

Moon, K. R., van Dijk, D., Wang, Z., Gigante, S., Burkhardt, D. B., Chen, W. S., Yim, K., Elzen, A. van den, Hirn, M. J., Coifman, R. R., Ivanova, N. B., Wolf, G., & Krishnaswamy, S. (2019). Visualizing structure and transitions in high-dimensional biological data. *Nature Biotechnology 2019 37:12*, *37*(12), 1482–1492. https://doi.org/10.1038/s41587-019-0336-3

Moorman, A. F. M., Christoffels, V. M., Anderson, R. H., & van den Hoff, M. J. B. (2007). The heart-forming fields: one or multiple? *Philosophical Transactions of the Royal Society B: Biological Sciences*, *362*(1484), 1257–1265. https://doi.org/10.1098/RSTB.2007.2113

Mori, A. D., Zhu, Y., Vahora, I., Nieman, B., Koshiba-Takeuchi, K., Davidson, L., Pizard, A., Seidman, J. G., Seidman, C. E., Chen, X. J., Henkelman, R. M., & Bruneau, B. G. (2006). Tbx5-dependent rheostatic control of cardiac gene expression and morphogenesis. *Developmental Biology*, *297*(2), 566–586. https://doi.org/10.1016/J.YDBIO.2006.05.023

Moskowitz, I. P. G., Kim, J. B., Moore, M. L., Wolf, C. M., Peterson, M. A., Shendure, J., Nobrega, M. A., Yokota, Y., Berul, C., Izumo, S., Seidman, J. G., & Seidman, C. E. (2007). A molecular pathway including Id2, Tbx5, and Nkx2-5 required for cardiac conduction system development. *Cell*, *129*(7), 1365–1376. https://doi.org/10.1016/J.CELL.2007.04.036

Müller, F., & Rohrer, H. (2002). Molecular control of ciliary neuron development: BMPs and downstream transcriptional control in the parasympathetic lineage. *Development*, *129*(24), 5707–5717. https://doi.org/10.1242/DEV.00165

Muntifering, M., Castranova, D., Gibson, G. A., Meyer, E., Kofron, M., & Watson, A. M. (2018). Clearing for Deep Tissue Imaging. *Current Protocols in Cytometry*, *86*(1). https://doi.org/10.1002/CPCY.38

Natarajan, A. R., Rong, Q., Katchman, A. N., & Ebert, S. N. (2004). Intrinsic cardiac catecholamines help maintain beating activity in neonatal rat cardiomyocyte cultures. *Pediatric Research*, *56*(3), 411–417. https://doi.org/10.1203/01.PDR.0000136279.80897.4C

Nelson, M. E., Riva, S. G., & Cvejic, A. (2021). SMaSH: A scalable, general marker gene identification framework for single-cell RNA sequencing and Spatial Transcriptomics. *BioRxiv*, 2021.04.08.438978. https://doi.org/10.1101/2021.04.08.438978

Neuhaus, H., Rosen, V., & Thies, R. S. (1999). Heart specific expression of mouse BMP-10 a novel member of the TGF-beta superfamily. *Mechanisms of Development*, *80*(2), 181–184.

https://doi.org/10.1016/S0925-4773(98)00221-4

Ng, G. A., Brack, K. E., & Coote, J. H. (2001). Effects of direct sympathetic and vagus nerve stimulation on the physiology of the whole heart--a novel model of isolated Langendorff perfused rabbit heart with intact dual autonomic innervation. *Experimental Physiology*, *86*(3), 319–329. https://doi.org/10.1113/EPH8602146

Ni, H., Wang, Y., Crawford, W., Zhang, S., Cheng, L., Zhang, H., & Lei, M. (2017a). *cell-derived cells in murine heart Background & Summary*. 1–7. https://doi.org/10.1038/sdata.2017.134

Ni, H., Wang, Y., Crawford, W., Zhang, S., Cheng, L., Zhang, H., & Lei, M. (2017b). Three-dimensional image reconstruction of distribution of Pnmt+ cell-derived cells in murine heart. *Scientific Data 2017 4:1*, *4*(1), 1–7. https://doi.org/10.1038/sdata.2017.134

Ni, H., Wang, Y., Crawford, W., Zhang, S., Cheng, L., Zhang, H., & Lei, M. (2017c). Three-dimensional image reconstruction of distribution of Pnmt+ cell-derived cells in murine heart. *Scientific Data 2017 4:1*, *4*(1), 1–7. https://doi.org/10.1038/sdata.2017.134

Nygaard, V., Rødland, E. A., & Hovig, E. (2016). Methods that remove batch effects while retaining group differences may lead to exaggerated confidence in downstream analyses. *Biostatistics (Oxford, England)*, *17*(1), 29–39. https://doi.org/10.1093/BIOSTATISTICS/KXV027

Osuala, K., Telusma, K., Khan, S. M., Wu, S., Shah, M., Baker, C., Alam, S., Abukenda, I., Fuentes, A., Seifein, H. B., & Ebert, S. N. (2011). Distinctive Left-Sided distribution of Adrenergic-Derived cells in the adult mouse heart. *PLoS ONE*, *6*(7). https://doi.org/10.1371/journal.pone.0022811

Oudit, G. Y., Kassiri, Z., Sah, R., Ramirez, R. J., Zobel, C., & Backx, P. H. (2001). The molecular physiology of the cardiac transient outward potassium current (I(to)) in normal and diseased myocardium. *Journal of Molecular and Cellular Cardiology*, *33*(5), 851–872. https://doi.org/10.1006/JMCC.2001.1376

Pattyn, A., Morin, X., Cremer, H., Goridis, C., & Brunet, J.-F. (1999). The homeobox gene Phox2b is essential for the development of autonomic neural crest derivatives. *Nature 1999 399:6734*, *399*(6734), 366–370. https://doi.org/10.1038/20700

PAUZIENE, N., PAUZA, D. H., & STROPUS, R. (2000). Morphology of human intracardiac nerves: an electron microscope study. *Journal of Anatomy*, *197 Pt 3*(Pt 3), 437–459. https://doi.org/10.1046/J.1469-7580.2000.19730437.X

Pauziene, N., Rysevaite-Kyguoliene, K., Alaburda, P., Pauza, A. G., Skukauskaite, M., Masaityte, A., Laucaityte, G., Saburkina, I., Inokaitis, H., Plisiene, J., & Pauza, D. H. (2017). Neuroanatomy of the Pig Cardiac Ventricles. A Stereomicroscopic, Confocal and Electron Microscope Study. *Anatomical Record (Hoboken, N.J. : 2007)*, *300*(10), 1756–1780. https://doi.org/10.1002/AR.23619

PM, W., SJ, M., K, O., CJ, K., JM, V., & DJ, A. (2001). Neural crest stem cells undergo cell-intrinsic developmental changes in sensitivity to instructive differentiation signals. *Neuron*, *29*(1), 57–71. https://doi.org/10.1016/S0896-6273(01)00180-5

Prall, O. W. J., Menon, M. K., Solloway, M. J., Watanabe, Y., Zaffran, S., Bajolle, F., Biben, C., McBride, J. J., Robertson, B. R., Chaulet, H., Stennard, F. A., Wise, N., Schaft, D., Wolstein, O., Furtado, M. B., Shiratori, H., Chien, K. R., Hamada, H., Black, B. L., … Harvey, R. P. (2007). An Nkx2-5/Bmp2/Smad1 negative feedback loop controls heart progenitor specification and proliferation. *Cell*, *128*(5), 947–959. https://doi.org/10.1016/J.CELL.2007.01.042

Prando, V., da Broi, F., Franzoso, M., Plazzo, A. P., Pianca, N., Francolini, M., Basso, C., Kay, M. W.,

Zaglia, T., & Mongillo, M. (2018). Dynamics of neuroeffector coupling at cardiac sympathetic synapses. *The Journal of Physiology*, *596*(11), 2055–2075. https://doi.org/10.1113/JP275693

PRICE, Z., EIDE, B., PRINTZMETAL, M., & CARPENTER, C. (1959). Ultrastructure of the dog cardiac muscle cell. *Circulation Research*, *7*, 858–865. https://doi.org/10.1161/01.RES.7.6.858

Puskaric, S., Schmitteckert, S., Mori, A. D., Glaser, A., Schneider, K. U., Bruneau, B. G., Blaschke, R. J., Steinbeisser, H., & Rappold, G. (2010). Shox2 mediates Tbx5 activity by regulating Bmp4 in the pacemaker region of the developing heart. *Human Molecular Genetics*, *19*(23), 4625–4633. https://doi.org/10.1093/HMG/DDQ393

Ren, Z., Yu, P., Li, D., Li, Z., Liao, Y., Wang, Y., Zhou, B., & Wang, L. (2020). Single-Cell Reconstruction of Progression Trajectory Reveals Intervention Principles in Pathological Cardiac Hypertrophy. *Circulation*, 1704–1719. https://doi.org/10.1161/CIRCULATIONAHA.119.043053

Rentschler, S., Zander, J., Meyers, K., France, D., Levine, R., Porter, G., Rivkees, S. A., Morley, G. E., & Fishman, G. I. (2002). Neuregulin-1 promotes formation of the murine cardiac conduction system. *Proceedings of the National Academy of Sciences*, *99*(16), 10464–10469. https://doi.org/10.1073/PNAS.162301699

Rodriques, S. G., Stickels, R. R., Goeva, A., Martin, C. A., Murray, E., Vanderburg, C. R., Welch, J., Chen, L. M., Chen, F., & Macosko, E. Z. (2019). Slide-seq: A scalable technology for measuring genome-wide expression at high spatial resolution. *Science (New York, N.Y.)*, *363*(6434), 1463–1467. https://doi.org/10.1126/SCIENCE.AAW1219

Rysevaite, K., Saburkina, I., Pauziene, N., Noujaim, S. F., Jalife, J., & Pauza, D. H. (2011). Morphologic pattern of the intrinsic ganglionated nerve plexus in mouse heart. *Heart Rhythm*, *8*(3), 448–454. https://doi.org/10.1016/J.HRTHM.2010.11.019

Rysevaite, K., Saburkina, I., Pauziene, N., Vaitkevicius, R., Noujaim, S. F., Jalife, J., & Pauza, D. H. (2011). Immunohistochemical characterization of the intrinsic cardiac neural plexus in whole-mount mouse heart preparations. *Heart Rhythm*, *8*(5), 731–738. https://doi.org/10.1016/J.HRTHM.2011.01.013

Saburkina, I., Rysevaite, K., Pauziene, N., Mischke, K., Schauerte, P., Jalife, J., & Pauza, D. H. (2010). Epicardial neural ganglionated plexus of ovine heart: anatomic basis for experimental cardiac electrophysiology and nerve protective cardiac surgery. *Heart Rhythm*, *7*(7), 942–950. https://doi.org/10.1016/J.HRTHM.2010.02.036

Sampaio, K. N., Mauad, H., Spyer, K. M., & Ford, T. W. (2003). Differential chronotropic and dromotropic responses to focal stimulation of cardiac vagal ganglia in the rat. *Experimental Physiology*, *88*(3), 315–327. https://doi.org/10.1113/EPH8802525

Sanderson, M. J., Smith, I., Parker, I., & Bootman, M. D. (2014). Fluorescence Microscopy. *Cold Spring Harbor Protocols*, *2014*(10), pdb.top071795. https://doi.org/10.1101/PDB.TOP071795

Satija, R., Farrell, J. A., Gennert, D., Schier, A. F., & Regev, A. (2015). Spatial reconstruction of single-cell gene expression data. *Nature Biotechnology 2015 33:5*, *33*(5), 495–502. https://doi.org/10.1038/nbt.3192

Savolainen, S. M., Foley, J. F., & Elmore, S. A. (n.d.). *Histology Atlas of the Developing Mouse Heart with Emphasis on E11.5 to E18.5*. https://doi.org/10.1177/0192623309335060

Savolainen, S. M., Foley, J. F., & Elmore, S. A. (2009). Histology atlas of the developing mouse heart with emphasis on E11.5 to E18.5. *Toxicologic Pathology*, *37*(4), 395–414. https://doi.org/10.1177/0192623309335060

Shekhar, A., Lin, X., Liu, F. Y., Zhang, J., Mo, H., Bastarache, L., Denny, J. C., Cox, N. J., Delmar, M.,

Roden, D. M., Fishman, G. I., & Park, D. S. (2016). Transcription factor ETV1 is essential for rapid conduction in the heart. *The Journal of Clinical Investigation*, *126*(12), 4444–4459. https://doi.org/10.1172/JCI87968

Shigenobu, K., Tanaka, H., & Kasuya, Y. (1988). Changes in Sensitivity of Rat Heart to Norepinephrine and Isoproterenol during Pre- and Postnatal Development and Its Relation to Sympathetic Innervation. *Developmental Pharmacology and Therapeutics*, *11*(4), 226–236. https://doi.org/10.1159/000457693

Singh, R., Hoogaars, W. M., Barnett, P., Grieskamp, T., Sameer Rana, M., Buermans, H., Farin, H. F., Petry, M., Heallen, T., Martin, J. F., Moorman, A. F. M., Hoen, P. A. C., Kispert, A., & Christoffels, V. M. (2012). Tbx2 and Tbx3 induce atrioventricular myocardial development and endocardial cushion formation. *Cellular and Molecular Life Sciences : CMLS*, *69*(8), 1377–1389. https://doi.org/10.1007/S00018-011-0884-2

Srivastava, D. (2006). Making or breaking the heart: from lineage determination to morphogenesis. *Cell*, *126*(6), 1037–1048. https://doi.org/10.1016/J.CELL.2006.09.003

Ståhl, P. L., Salmén, F., Vickovic, S., Lundmark, A., Navarro, J. F., Magnusson, J., Giacomello, S., Asp, M., Westholm, J. O., Huss, M., Mollbrink, A., Linnarsson, S., Codeluppi, S., Borg, Å., Pontén, F., Costea, P. I., Sahlén, P., Mulder, J., Bergmann, O., … Frisén, J. (2016). Visualization and analysis of gene expression in tissue sections by spatial transcriptomics. *Science*, *353*(6294), 78–82. https://doi.org/10.1126/SCIENCE.AAF2403/SUPPL_FILE/AAF2403_STAHL_SM.PDF

Sun, T., Fan, X., Crawford, W., Tan, X. Q., Ou, X., Terrar, D. A., & Lei, M. (2019). Pnmt -derived cardiomyocytes: Anatomical localization, function and future perspectives. *Frontiers in Physiology*, *10*(MAY), 1–6. https://doi.org/10.3389/fphys.2019.00713

Susaki, E. A., & Ueda, H. R. (2016). Whole-body and Whole-Organ Clearing and Imaging Techniques with Single-Cell Resolution: Toward Organism-Level Systems Biology in Mammals. *Cell Chemical Biology*, *23*(1), 137–157. https://doi.org/10.1016/J.CHEMBIOL.2015.11.009

Tainaka, K., Murakami, T. C., Susaki, E. A., Shimizu, C., Saito, R., Takahashi, K., Hayashi-Takagi, A., Sekiya, H., Arima, Y., Nojima, S., Ikemura, M., Ushiku, T., Shimizu, Y., Murakami, M., Tanaka, K. F., Iino, M., Kasai, H., Sasaoka, T., Kobayashi, K., … Ueda, H. R. (2018). Chemical Landscape for Tissue Clearing Based on Hydrophilic Reagents. *Cell Reports*, *24*(8), 2196-2210.e9. https://doi.org/10.1016/J.CELREP.2018.07.056/ATTACHMENT/04EEF9D8-5AE3-4208-870C-62C8E11D221B/MMC3.XLSX

Tamura, Y., Sano, M., Nakamura, H., Ito, K., Sato, Y., Shinmura, K., Ieda, M., Fujita, J., Kurosawa, H., Ogawa, S., Nakano, S., Matsuzaki, M., & Fukuda, K. (2016). Neural crest-derived resident cardiac cells contribute to the restoration of adrenergic function of transplanted heart in rodent. *Cardiovascular Research*, *109*(3), 350–357. https://doi.org/10.1093/cvr/cvv267

Teitelman, G., Baker, H., Joh, T. H., & Reis, D. J. (1979). Appearance of catecholamine-synthesizing enzymes during development of rat sympathetic nervous system: Possible role of tissue environment. *Proceedings of the National Academy of Sciences*, *76*(1), 509–513. https://doi.org/10.1073/PNAS.76.1.509

Tessadori, F., van Weerd, J. H., Burkhard, S. B., Verkerk, A. O., de Pater, E., Boukens, B. J., Vink, A., Christoffels, V. M., & Bakkers, J. (2012). Identification and Functional Characterization of Cardiac Pacemaker Cells in Zebrafish. *PLOS ONE*, *7*(10), e47644. https://doi.org/10.1371/JOURNAL.PONE.0047644

Thomas, S. A., Marck, B. T., Palmiter, R. D., & Matsumoto, A. M. (1998). Restoration of

norepinephrine and reversal of phenotypes in mice lacking dopamine beta-hydroxylase. *Journal of Neurochemistry*, *70*(6), 2468–2476. https://doi.org/10.1046/J.1471-4159.1998.70062468.X

Thomas, S. A., Matsumoto, A. M., & Palmiter, R. D. (1995). Noradrenaline is essential for mouse fetal development. *Nature*, *374*(6523), 643–646. https://doi.org/10.1038/374643A0

Tomer, R., Khairy, K., & Keller, P. J. (2013). Light sheet microscopy in cell biology. *Methods in Molecular Biology (Clifton, N.J.)*, *931*, 123–137. https://doi.org/10.1007/978-1-62703-056-4_7

Tran, H. T. N., Ang, K. S., Chevrier, M., Zhang, X., Lee, N. Y. S., Goh, M., & Chen, J. (2020). A benchmark of batch-effect correction methods for single-cell RNA sequencing data. *Genome Biology*, *21*(1), 1–32. https://doi.org/10.1186/S13059-019-1850-9/TABLES/1

Tyser, R. C. V., Ibarra-Soria, X., McDole, K., Jayaram, S. A., Godwin, J., Brand, T. A. H. V. den, Miranda, A. M. A., Scialdone, A., Keller, P. J., Marioni, J. C., & Srinivas, S. (2021). Characterization of a common progenitor pool of the epicardium and myocardium. *Science*, *371*(6533). https://doi.org/10.1126/SCIENCE.ABB2986/SUPPL_FILE/PAPV2.PDF

Ueda, H. R., Ertürk, A., Chung, K., Gradinaru, V., Chédotal, A., Tomancak, P., & Keller, P. J. (2020). Tissue clearing and its applications in neuroscience. *Nature Reviews Neuroscience 2020 21:2*, *21*(2), 61–79. https://doi.org/10.1038/s41583-019-0250-1

V, H., S, W., L, B., NA, B., RH, A., & DJ, H. (2008). Cells migrating from the neural crest contribute to the innervation of the venous pole of the heart. *Journal of Anatomy*, *212*(1), 1–11. https://doi.org/10.1111/J.1469-7580.2007.00833.X

van den Boogaard, M., Wong, L. Y. E., Tessadori, F., Bakker, M. L., Dreizehnter, L. K., Wakker, V., Bezzina, C. R., 'T Hoen, P. A. C., Bakkers, J., Barnett, P., & Christoffels, V. M. (2012). Genetic variation in T-box binding element functionally affects SCN5A/SCN10A enhancer. *Journal of Clinical Investigation*, *122*(7), 2519–2530. https://doi.org/10.1172/JCI62613

van Eif, V. W. W., Devalla, H. D., Boink, G. J. J., & Christoffels, V. M. (2018). Transcriptional regulation of the cardiac conduction system. *Nature Reviews Cardiology*, *15*(10), 617–630. https://doi.org/10.1038/S41569-018-0031-Y

van Eif, V. W. W., Stefanovic, S., Mohan, R. A., & Christoffels, V. M. (2020). Gradual differentiation and confinement of the cardiac conduction system as indicated by marker gene expression. *Biochimica et Biophysica Acta (BBA) - Molecular Cell Research*, *1867*(3), 118509. https://doi.org/10.1016/J.BBAMCR.2019.07.004

Vedantham, V., Galang, G., Evangelista, M., Deo, R. C., & Srivastava, D. (2015). RNA sequencing of mouse sinoatrial node reveals an upstream regulatory role for Islet-1 in cardiac pacemaker cells. *Circulation Research*, *116*(5), 797–803. https://doi.org/10.1161/CIRCRESAHA.116.305913

Végh, A. M. D., Duim, S. N., Smits, A. M., Poelmann, R. E., Harkel, A. D. J. ten, DeRuiter, M. C., Goumans, M. J., & Jongbloed, M. R. M. (2016). Part and Parcel of the Cardiac Autonomic Nerve System: Unravelling Its Cellular Building Blocks during Development. *Journal of Cardiovascular Development and Disease*, *3*(3), 28. https://doi.org/10.3390/JCDD3030028

Végh, A. M. D., Duim, S. N., Smits, A. M., Poelmann, R. E., ten Harkel, A. D. J., Deruiter, M. C., Goumans, M. J., & Jongbloed, M. R. M. (2016). Part and Parcel of the Cardiac Autonomic Nerve System: Unravelling Its Cellular Building Blocks during Development. *Journal of Cardiovascular Development and Disease*, *3*(3). https://doi.org/10.3390/JCDD3030028

Verveer, P. J., Swoger, J., Pampaloni, F., Greger, K., Marcello, M., & Stelzer, E. H. K. (2007). High-resolution three-dimensional imaging of large specimens with light sheet-based microscopy. *Nature Methods*, *4*(4), 311–313. https://doi.org/10.1038/NMETH1017

Vicente-Steijn, R., Passier, R., Wisse, L. J., Schalij, M. J., Poelmann, R. E., Gittenberger-De Groot, A. C., & Jongbloed, M. R. M. (2011). Funny current channel HCN4 delineates the developing cardiac conduction system in chicken heart. *Heart Rhythm*, *8*(8), 1254–1263. https://doi.org/10.1016/J.HRTHM.2011.03.043

Virágh, S., & Challice, C. E. (1980). The development of the conduction system in the mouse embryo heart. *Developmental Biology*, *80*(1), 28–45. https://doi.org/10.1016/0012-1606(80)90496-0

W, H. (2013). Autonomic cardiac innervation: development and adult plasticity. *Organogenesis*, *9*(3), 176–193. https://doi.org/10.4161/ORG.24892

Wake, E., & Brack, K. (2016). Characterization of the intrinsic cardiac nervous system. *Autonomic Neuroscience : Basic & Clinical*, *199*, 3–16. https://doi.org/10.1016/J.AUTNEU.2016.08.006

Walker, C. A., & Spinale, F. G. (1999). The structure and function of the cardiac myocyte: A review of fundamental concepts. *The Journal of Thoracic and Cardiovascular Surgery*, *118*(2), 375–382. https://doi.org/10.1016/S0022-5223(99)70233-3

Wang, X., Allen, W. E., Wright, M. A., Sylwestrak, E. L., Samusik, N., Vesuna, S., Evans, K., Liu, C., Ramakrishnan, C., Liu, J., Nolan, G. P., Bava, F. A., & Deisseroth, K. (2018). Three-dimensional intact-tissue sequencing of single-cell transcriptional states. *Science (New York, N.Y.)*, *361*(6400). https://doi.org/10.1126/SCIENCE.AAT5691

Wang, Y., Lin, W. K., Crawford, W., Ni, H., Bolton, E. L., Khan, H., Shanks, J., Bub, G., Wang, X., Paterson, D. J., Zhang, H., Galione, A., Ebert, S. N., Terrar, D. A., & Lei, M. (2017a). Optogenetic Control of Heart Rhythm by Selective Stimulation of Cardiomyocytes Derived from Pnmt+ Cells in Murine Heart. *Scientific Reports 2017 7:1*, *7*(1), 1–10. https://doi.org/10.1038/srep40687

Wang, Y., Lin, W. K., Crawford, W., Ni, H., Bolton, E. L., Khan, H., Shanks, J., Bub, G., Wang, X., Paterson, D. J., Zhang, H., Galione, A., Ebert, S. N., Terrar, D. A., & Lei, M. (2017b). Optogenetic Control of Heart Rhythm by Selective Stimulation of Cardiomyocytes Derived from Pnmt + Cells in Murine Heart. *Scientific Reports*, *7*. https://doi.org/10.1038/srep40687

Wang, Z., Fermini, B., & Nattel, S. (1993). Sustained depolarization-induced outward current in human atrial myocytes. Evidence for a novel delayed rectifier K+ current similar to Kv1.5 cloned channel currents. *Circulation Research*, *73*(6), 1061–1076. https://doi.org/10.1161/01.RES.73.6.1061

Webb, S., Brown, N. A., & Andersen, R. H. (1998). Formation of the atrioventricular septal structures in the normal mouse. *Circulation Research*, *82*(6), 645–656. https://doi.org/10.1161/01.RES.82.6.645

Webb, S., Qayyum, S. R., Anderson, R. H., Lamers, W. H., & Richardson, M. K. (2003). Septation and separation within the outflow tract of the developing heart. *Journal of Anatomy*, *202*(4), 327–342. https://doi.org/10.1046/J.1469-7580.2003.00168.X

Wessels, A., Vermeulen, J. L. M., Verbeek, F. J., Viragh, S. Z., Kalman, F., Lamers, W. H., & Moorman, A. F. M. (1992). Spatial Distribution of "Tissue-Specific" Antigens in the Developing Human Heart and Skeletal Muscle Ill. AN IMMUNOHISTOCHEMICAL ANALYSIS OF THE DISTRIBUTION OF THE NEURAL TISSUE ANTIGEN G1 N2 IN THE EMBRYONIC HEART; IMPLICATIONS FOR THE

DEVELOPMENT OF THE ATRIOVENTRICULAR CONDUCTION SYSTEM. In *THE ANATOMICAL RECORD* (Vol. 232).

Winter, J., Tanko, A. S., Brack, K. E., Coote, J. H., & Ng, G. A. (2012). Differential cardiac responses to unilateral sympathetic nerve stimulation in the isolated innervated rabbit heart. *Autonomic Neuroscience : Basic & Clinical*, *166*(1–2), 4–14. https://doi.org/10.1016/J.AUTNEU.2011.08.004

Wu, M., Peng, S., Yang, J., Tu, Z., Cai, X., Cai, C. L., Wang, Z., & Zhao, Y. (2014). Baf250a orchestrates an epigenetic pathway to repress the Nkx2.5-directed contractile cardiomyocyte program in the sinoatrial node. *Cell Research*, *24*(10), 1201–1213. https://doi.org/10.1038/CR.2014.113

Xia, J., Meng, Z., Ruan, H., Yin, W., Xu, Y., & Zhang, T. (2020). Heart Development and Regeneration in Non-mammalian Model Organisms. *Frontiers in Cell and Developmental Biology*, *8*, 1249. https://doi.org/10.3389/FCELL.2020.595488/BIBTEX

Xiong, H., Luo, Y., Yue, Y., Zhang, J., Ai, S., Li, X., Wang, X., Zhang, Y. L., Wei, Y., Li, H. H., Hu, X., Li, C., & He, A. (2019). Single-Cell Transcriptomics Reveals Chemotaxis-Mediated Intraorgan Crosstalk During Cardiogenesis. *Circulation Research*, *125*(4), 398–410. https://doi.org/10.1161/CIRCRESAHA.119.315243

Y, M., A, Z., E, M., C, D., MD, S., Y, M., & P, C. (2009). BMP signaling regulates sympathetic nervous system development through Smad4-dependent and -independent pathways. *Development (Cambridge, England)*, *136*(21), 3575–3584. https://doi.org/10.1242/DEV.038133

Yamada, S., & Nomura, S. (2020). Review of Single-Cell RNA Sequencing in the Heart. *International Journal of Molecular Sciences 2020, Vol. 21, Page 8345*, *21*(21), 8345. https://doi.org/10.3390/IJMS21218345

Yekelchyk, M., Guenther, S., Preussner, J., & Braun, T. (2019). Mono- and multi-nucleated ventricular cardiomyocytes constitute a transcriptionally homogenous cell population. *Basic Research in Cardiology*, *114*(5). https://doi.org/10.1007/S00395-019-0744-Z

Yuan, B. -X, Ardell, J. L., Hopkins, D. A., Losier, A. M., & Armour, J. A. (1994). Gross and microscopic anatomy of the canine intrinsic cardiac nervous system. *The Anatomical Record*, *239*(1), 75–87. https://doi.org/10.1002/ar.1092390109

Yuan, S., & Schoenwolf, G. C. (2000). Islet-1 Marks the Early Heart Rudiments and is Asymmetrically Expressed During Early Rotation of the Foregut in the Chick Embryo. *Anat Rec*, *260*, 204–207. https://doi.org/10.1002/1097-0185

Zaffran, S., Kelly, R. G., Meilhac, S. M., Buckingham, M. E., & Brown, N. A. (2004). Right ventricular myocardium derives from the anterior heart field. *Circulation Research*, *95*(3), 261–268. https://doi.org/10.1161/01.RES.0000136815.73623.BE

Zaglia, T., & Mongillo, M. (2017). Cardiac sympathetic innervation, from a different point of (re)view. *The Journal of Physiology*, *595*(12), 3919–3930. https://doi.org/10.1113/JP273120

Zarzoso, M., Rysevaite, K., Milstein, M. L., Calvo, C. J., Kean, A. C., Atienza, F., Pauza, D. H., Jalife, J., & Noujaim, S. F. (2013). Nerves projecting from the intrinsic cardiac ganglia of the pulmonary veins modulate sinoatrial node pacemaker function. *Cardiovascular Research*, *99*(3), 566–575. https://doi.org/10.1093/CVR/CVT081

Zhang, S. S., Kim, K. H., Rosen, A., Smyth, J. W., Sakuma, R., Delgado-Olguiń, P., Davis, M., Chi, N. C., Puviindran, V., Gaborit, N., Sukonnik, T., Wylie, J. N., Brand-Arzamendi, K., Farman, G. P., Kim, J., Rose, R. A., Marsden, P. A., Zhu, Y., Zhou, Y. Q., … Backx, P. H. (2011). Iroquois homeobox gene 3 establishes fast conduction in the cardiac His-Purkinje network. *Proceedings of the*

National Academy of Sciences of the United States of America, *108*(33), 13576–13581. https://doi.org/10.1073/PNAS.1106911108

Zhao, Q., Sun, Q., Zhou, L., Liu, K., & Jiao, K. (2019). Complex regulation of mitochondrial function during cardiac development. *Journal of the American Heart Association*, *8*(13). https://doi.org/10.1161/JAHA.119.012731

Zhou, Q. Y., Quaife, C. J., & Palmiter, R. D. (1995). Targeted disruption of the tyrosine hydroxylase gene reveals that catecholamines are required for mouse fetal development. *Nature 1995 374:6523*, *374*(6523), 640–643. https://doi.org/10.1038/374640a0